Electronic Structure Theory of Magnetoresistive Effects in Atomic-Scale Junctions induced by Spin-Orbit Coupling and Spin Non-Collinearity

Dissertation
zur Erlangung des Doktorgrades
der Mathematisch-Naturwissenschaftlichen Fakultät der
Christian-Albrechts-Universität zu Kiel

vorgelegt von

Fabian Otte

aus Kiel

Kiel

2016

Erster Gutachter:	Prof. Dr. Stefan Heinze
Zweiter Gutachter:	Prof. Dr. Yuriy Mokrousov
Tag der mündlichen Prüfung:	13.1.2016
Zum Druck genehmigt:	13.1.2016

gez. Prof. Dr. Wolfgang J. Duschl, Dekan

Zusammenfassung

In dieser Arbeit werden magnetoresistive Effekte auf der atomaren Skala, die durch die Spin-Bahn-Kopplung und nicht-kollineare Spinstrukturen verursacht werden, mittels der Theorie der elektronischen Struktur untersucht. Dazu wird die "Full potential linearized augmented plane wave" (FLAPW) Methode benutzt, die auf der Dichtefunktionaltheorie (DFT) basiert. Die elektronische Struktur wird auf Wannier-Funktionen projiziert, mit deren Hilfe eine "Tight-Binding" (TB) ähnliche Hamiltonmatrix konstruiert wird. Diese Hamiltonmatrix wird in einem Formalismus basierend auf Greenschen Funktionen verwendet, um die Transmissionsfunktion mittels der Landauer-Büttiker-Formel zu gewinnen.

Der anisotrope magnetoresistive Effekt (AMR) von symmetrischen, einatomigen Ni-Kontakten mit Co-, Rh- und Ir-Endatomen wird als Funktion des Abstandes zwischen den Endatomen untersucht. Eine nicht-triviale Abstandsabhängigkeit des AMR, der Werte von bis zu 150 % erreicht, wird gefunden und sogar Vorzeichenwechsel treten auf. Das durch die Spin-Bahn-Kopplung verursachte Mischen und der Abfall der Übergangsmatrixelemente der Orbitale über das Vakuum zwischen den Endatomen hängt von der Symmetrie der Orbitale ab. Daher dominieren räumlich delokalisierte Orbitale den AMR im Tunnelregime und lokalisierte Orbitale im Kontaktregime. Diese Erkenntnisse erlauben es Rastertunnelmikroskopie-Experimente der Abstandsabhängigkeit des AMR von Co und Ir Adatomen, die auf Domänen und Domänenwänden der Doppellage Fe auf W(110) platziert sind, zu erklären. Dabei wird gezeigt, dass der AMR in Einzelatomen stark beeinflusst werden kann.

Weiterhin werden Kontakte mit einzelnen Molekülen bestehend aus Metall-Benzol-Komplexen, die von einatomigen Ni- und Co-Ketten kontaktiert werden, studiert. Die Hybridisierung der Molekülorbitale mit den Orbitalen des benachbarten Metallatoms resultiert in einer Filterung der Transmissionsfunktion anhand der Orbitalsymmetrie, die zu einem gigantischen molekularen AMR führt.

Anschließend wird über die idealisierte Struktur basierend auf einatomigen Ketten hinausgegangen und der AMR in Pt-Bruchkontakten untersucht. Es wurde theoretisch vorhergesagt, dass Pt in niedrigdimensionalen Systemen ein magnetisches Moment entwickelt und jüngste experimentelle Ergebnisse des AMR von Pt-Bruchkontakten liefern starke Indizien für diesen aufkommendem Magnetismus. Von bcc-(001) Elektroden kontaktierte Pt-Trimere werden studiert und ein AMR von bis zu 20 % in Übereinstimmung mit den experimentellen Daten wird gefunden.

Schließlich wird der Ursprung des nicht-kollinearen magnetischen Tunnelwiderstands (TNCMR) erläutert, der in Rastertunnelmikroskopie-Experimenten entdeckt wurde, bei denen Skyrmionen in der PdFe/Ir(111)-Oberfläche von nicht-magnetischen Spitzen

sondiert werden. Basierend auf TB und DFT Rechnungen wird gezeigt, dass die Änderung des Tunnelstroms von der Mischung der Spinkanäle herrührt, die durch die nicht-kollineare Spinstruktur verursacht wird. Dieses Mischen führt zu einer Verschiebung eines Peaks in der Vakuumzustandsdichte, die einen TNCMR von bis zu 100 % verursachen kann. Dieser Effekt könnte in zukünftigen Bauteilen zur elektronischen Detektion von Skyrmion ohne zusätzliche magnetische Elemente genutzt werden.

Abstract

In this thesis magnetoresistive effects caused by spin-orbit coupling (SOC) and spin non-collinearity are studied on the atomic scale based on electronic structure theory. The full-potential linearized augmented plane wave method is applied, which is based on density functional theory (DFT). The electronic structure is projected on Wannier functions from which a tight-binding (TB) like Hamiltonian is constructed. This Hamiltonian is used in a Green's function formalism to obtain the transmission function of single-atom and single-molecule junctions within the Landauer approach.

The anisotropic magnetoresistance (AMR) of symmetric Ni monowire junctions terminated by Co, Rh and Ir apex atoms is investigated as a function of the distance between the apex atoms. A non-trivial distance dependence of the AMR is found, which can reach values of up to 150 % and can even change sign. The orbital mixing due to SOC and the decay of the transition-matrix element across the gap between the apex atoms depends on the orbital symmetries. Therefore, spatially localized and delocalized orbitals dominate the AMR in the contact and tunneling regime, respectively. These findings allow to explain scanning tunneling microscopy (STM) experiments of the distance dependence of AMR in Co and Ir adatoms located on domains and domain walls of a double layer of Fe on W(110). It is shown that the AMR can be tuned on the single-atom level.

Furthermore, single-molecule junctions consisting of metal-benzene complexes contacted by Ni and Co monowires are studied. The hybridization of the molecular orbitals with the orbitals of the adjacent metal atom results in an orbital-symmetry filtering effect on the transmission function, which leads to a giant molecular AMR.

Going beyond the idealized monowire geometry, the AMR is investigated in Pt break junctions. Pt is expected to become magnetic in low-dimensional systems and recent experimental results on the AMR of Pt break junctions strongly indicate this emergent magnetism. Pt trimers contacted by bulk-like bcc-(001) electrodes are studied finding an AMR of up to 20 % in agreement with the experimental results.

Finally, the origin of the tunneling non-collinear magnetoresistance (TNCMR) is explained, which has been discovered in STM experiments probing magnetic skyrmions in PdFe/Ir(111) with non-magnetic tips. It is demonstrated based on TB and DFT that the change of the tunnel conductance is due to spin mixing caused by the non-collinearity of the spin structure. This mixing leads to a peak shift in the vacuum density of states, which can result in a TNCMR of up to 100 %. This effect may be used for an all-electrical detection of skyrmions in future devices.

Contents

1 Introduction

Today, spintronics is a research focus of condensed matter physics. Its key idea to use not only the charge but also the spin degree of freedom of electrons opens the route to a vast number of potential applications. One type of effects that is already exploited in today's information technology are the magnetoresistive effects. In particular, magnetoresistances are one key ingredient of ultra-dense magnetic data storage devices. Before 1990, inductive read heads, which measure the magnetic flux from a stored bit, were used in hard disk drives. Since the size of the bit determines the magnetic flux, the limiting bit size is comparably large. Magnetoresistive effects have been found to be ideally suited to further increase the data storage density. Magnetoresistance originates from the interdependencies between the conductance and the alignment of the magnetization. In general, the magnetoresistance (MR) is defined as the ratio of the conductance between two configurations of the magnetization, here labeled with 1 and 2:

$$\mathrm{MR} = 100\% \cdot \frac{G_1 - G_2}{G_2}. \tag{1.1}$$

Starting in 1990, IBM introduced the first hard disk drive (HDD) using MR. In particular, the read head was based on the anisotropic magnetoresistance (AMR). The AMR was discovered by Lord Kelvin in 1854 [2] and relies on the difference between the conductance for a parallel ($G_{\parallel}$) and for a perpendicular ($G_{\perp}$) orientation of the magnetization of the sample with respect to the current direction. It is caused by the relativistic spin-orbit coupling (SOC), which changes the scattering properties of the electrons constituting the current depending on the magnetization direction, and

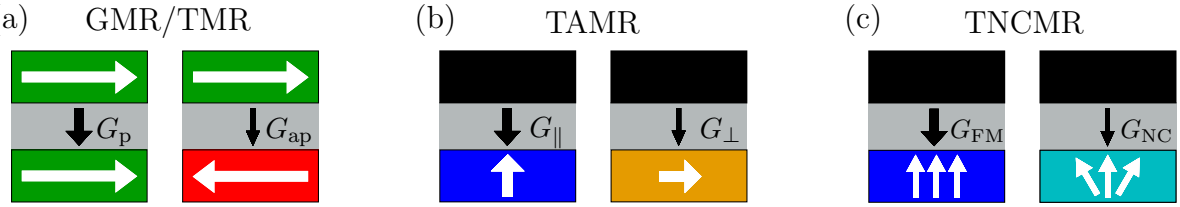

Figure 1.1: Sketch of the (a) giant magnetoresistance/tunneling magnetoresistance, (b) tunneling anisotropic magnetoresistance and (c) tunneling non-collinear magnetoresistance. Black boxes represent non-magnetic electrodes while colored boxes represent magnetic electrodes with a magnetization direction represented by the white arrows. Gray boxes represent insulators or in case of the GMR non-magnetic metals. The figure is adapted from Fig. 1 of Ref. [1].

reaches values of up to 5 % [3]. The magnitude of the MR limits the size of the bits at which the signal-to-noise ratio is still large enough for exploitation in devices.

In 1997, HDDs using the giant magnetoresistance (GMR) were introduced. For the GMR, discovered in 1988 by Peter Grünberg [4] and Albert Fert [5], who were awarded the Nobel prize in Physics 2007, two magnetic layers separated by a non-magnetic metal are considered as sketched in Fig. 1.1 (a). If the magnetizations of the two layers are aligned antiparallel (G_{ap}), electrons of spin-up and spin-down character undergo the same scattering processes. However, if the magnetizations of the two layers are aligned parallel (G_{p}), the scattering properties differ for spin-up and spin-down electrons enhancing the total current compared to the case of antiparallel alignment of the magnetizations. The magnitude of the GMR obtained in devices is about 10 % [6].

Larger MR values of more than 100 % can be reached in tunnel junctions, which in similarity to the GMR consist of two magnetic electrodes and an insulating barrier. The tunneling magnetoresistance (TMR) was discovered by M. Julliere in 1975 [7]. The first HDD utilizing the TMR, which is nowadays used in all HDD read heads, was introduced in 2004.

Recently, the AMR was discovered in the tunneling geometry, consisting of a magnetic and a non-magnetic electrode separated by an insulating barrier as sketched in Fig. 1.1 (b), using planar tunnel junctions with ferromagnetic semiconductors [8]. The tunneling anisotropic magnetoresistance (TAMR) is thereby defined according to Eq. (1.1) for a conductance with a parallel ($G_{\parallel}$) and perpendicular ($G_{\perp}$) orientation of the magnetization with respect to the tunneling current. In the TAMR geometry only one magnetic electrode is needed, which is advantageous since in contrast to the GMR and TMR spin coherence is not necessary. However, as already mentioned above, the limited magnitude of the (tunneling) AMR found in mesoscopic samples of 2-3 % limits the achievable bit size.

New interest in the AMR also arose concerning its enhancement in low-dimensional systems. Low-dimensional systems often show very different properties compared to the bulk case. Regarding the electric properties, one can no longer use Ohm's law since quantization effects occur. If one considers the ballistic regime, i.e., the absence of electron scattering, the resistance is determined by the spin-degenerate conductance quantum $G_0 = 2e^2/h = (12.9\ \mathrm{k\Omega})^{-1}$ divided by the number of available modes. In the ballistic regime, the AMR has been predicted to reach values of nearly 20 % [9] and at the single-atom limit of the TAMR values of 10 % have been found experimentally [10]. The origin of this enhancement compared to the bulk case lies in the fact that only a few modes are affected by SOC, while the remaining modes constitute a background conductance. Therefore, the fewer "background modes" present the larger the AMR, which means constrictions on the atomic-scale lead to the largest effects.

Unfortunately, reducing the dimensionality of the junction complicates the experimental and theoretical investigation of these systems. However, the formidable development of the scanning tunneling microscopy (STM), invented by Binning and Rohrer in 1981 [11], who were honored with the Nobel prize in Physics in 1986, and of the spin-polarized STM [12] provided sophisticated state-of-the-art experimental techniques allowing one to resolve electronic and magnetic structures on the atomic scale.

Complementary on the theory side, electronic structure methods have been developed without which detailed understanding of these experiments would not be possible. One of the most successful methods is the density functional theory (DFT) developed by Hohenberg, Kohn [13], who was awarded the Nobel Prize in Chemistry in 1998, and Sham [14]. To make practical use of the DFT, numerous implementations have been developed and one of the most precise implementations is the full-potential linearized augmented plane wave (FLAPW) method [15, 16], which takes into account all electrons and the full shape of the electrostatic potential.

The size of the system which can be described by DFT methods is limited by the speed of the supercomputers used for the calculations. The present-day frontiers are reached by describing, for example, realistic break junctions, junctions of a full STM geometry or huge non-collinear magnetic structures such as skyrmions consisting of hundreds of atoms. Furthermore, not all materials can be described accurately with current approximations of the exchange-correlation potential.

Therefore, and since human nature demands for intuitive, picturesque understanding from which new ideas can spark, effective models are very useful. For the electronic structure one approach is the tight-binding (TB) model based on easy-to-interpret atomic orbitals or more sophisticated Wannier functions.

In this thesis, which is primarily concerned with MR, a combined approach is used. On the one hand, FLAPW calculations post-processed with a Green's function formalism [17] based on Wannier functions [18] are performed to determine the transmission function and conductance from DFT and, on the other hand, simple TB models are devised to describe the underlying physical origin of the properties of interest.

The conductance is obtained starting with calculations using the `FLEUR` code [19]. The `FLEUR` code is an implementation of the FLAPW method developed at the Forschungszentrum Jülich. It offers real two-dimensional and one-dimensional [20] geometries using an optimized basis set to describe the vacuum region, which allows for faster calculations compared to the usual super cell approach. The Green's function formalism needs a description of the electronic structure in localized orbitals. Therefore, the electronic structure obtained by `FLEUR` is projected on Wannier functions, which in contrast to the delocalized basis in FLAPW are localized in real-space and preserve the accuracy of the FLAPW calculation including complex electronic effects due to SOC. From the Wannier functions a tight-binding like Hamiltonian matrix for open quantum systems is constructed, which allows to apply the Green's function formalism to obtain the transmission function.

The thesis starts with a description of the Green's function formalism to calculate the transmission function and conductance within the Landauer approach [21] to coherent transport in chapter 2. A short introduction to DFT and the FLAPW method and its implementation in `FLEUR` is given in chapter 3. The Wannier functions and the setup of the Hamiltonian matrices for the transport calculations are described in chapter 4.

In chapter 5, the AMR in single-atom junctions is studied from the tunneling to the contact regime. For this purpose, the conductance of symmetric Ni monowires terminated by Co, Rh and Ir apex atoms is calculated for a gap of variable size between the apex atoms to mimic distance-dependent STM experiments. We find that the

AMR is enhanced for heavier apex atoms due to the larger SOC to up to 150 %. As a function of the gap size the AMR varies drastically and can even change its sign. This distance dependence can be explained via the SOC induced orbital mixing and the decay constants of the transition matrix elements between the orbitals at the apex atoms on each side of the gap, which depend on the orbital symmetry. Therefore, the AMR is dominated by spatially delocalized and localized orbital types in the tunneling and contact regime, respectively.

The insight gained from the idealized junctions considered in chapter 5 allows to explain STM experiments of Co and Ir adatoms on a double layer of Fe on W(110) as discussed in chapter 6. The double layer of Fe exhibits domains and domain walls with a magnetization pointing parallel and perpendicular to the surface, respectively. The magnetic moments of adatoms located on domains and domain walls are aligned to the moments of the underlying Fe atoms by the strong exchange interaction. Their conductances are probed with a non-magnetic W tip and the distance between the tip and the adatom is varied. This setup resembles the AMR geometry sketched in Fig. 1.1 (b). A non-trivial distance dependence of the AMR is found for both Co and Ir apex atoms. Motivated by DFT calculations, these results are explained with a TB model, the key ingredients of which consist of the SOC induced orbital hybridization at the adatom and the different decay constants of the transition matrix elements between the adatom and the apex atom of the STM tip of orbitals of different symmetry. Furthermore, the Green's function formalism can be used to derive an analytical form of the distance dependence of the conductance, which results in an excellent fit of the experimental data.

In chapter 7, a new way of enhancing the AMR is introduced: orbital-symmetry filtering by organic materials contacted by metallic leads. We find that the AMR in monowires can be enhanced to gigantic values of about 100000 % by contacting metal-benzene complexes. The origin of this giant AMR is an orbital-symmetry filtering effect on the transmission function caused by the hybridization of the molecule with the adjacent metal atoms, which reduces the number of modes contributing to the transmission function. The quality of the orbital-symmetry filtering is thereby sensitive to the energetic position of the molecular orbitals, which is shown by contacting Bz, VBz_2, $NbBz_2$, $TaBz_2$, and V_2Bz_3. In addition, the energy landscape of this so-called molecular anisotropic magnetoresistance (MAMR) is analyzed by using Ni and Co monowires as contacting leads. Eventually, a generic TB model is used to show that the effect might also be found for molecules on surfaces.

In chapter 8, we shift from idealized monowire structures to geometries which are closer to experimental ones. The AMR of a break junction consisting of a Pt trimer between two bcc(001)-leads is analyzed, whereby the junction is elongated to several distances. In such nanoscale junctions, Pt has been predicted to become ferromagnetic due to the reduced coordination number, which leads to an increased density of states at the Fermi level fulfilling the Stoner criterion for ferromagnetism.

Direct experimental verification of this emergent magnetism is extremely difficult. Therefore, one tries to detect it indirectly by measuring the AMR, which relies on a spontaneous magnetization. Recent experiments reporting on the AMR of Pt break

junctions [22] strongly indicate an emergent magnetism in these low-dimensional Pt systems. However, this interpretation is not unambiguous due to the complexity of the structure and the unknown exact atomic arrangement. Therefore, complementary calculations of the conductance in such junctions are necessary [22], which we provide in this chapter. We find conductances in the range of 0.75 to $0.9\,G_0$ and an AMR of up to 20 %. During elongation these values vary, which can be attributed to changes in the electronic structure induced by the emergent magnetism and the bonding characteristics for the different elongations. Qualitatively, our findings agree well with the experimental data.

In chapter 9, the origin of a newly discovered magnetoresistance effect is explained, which is not caused by SOC but by non-collinear spin structures. This tunneling non-collinear magnetoresistance (TNCMR) has been observed experimentally in STM experiments on skyrmions in the PdFe/Ir(111) system [23, 24] probed by a non-magnetic tip. A sketch of the principle analogous to the TMR/GMR and TAMR can be seen in Fig. 1.1 (c). The TNCMR measures the difference of the conductance for a ferromagnetic (G_{FM}) or non-collinear (G_{NC}) arrangement of the spin structure of the magnetic electrode. These findings are explained using two-orbital TB models adapted to results from DFT calculations of spin-spiral states incorporating the full spin structure, resulting in very well agreement with the experimental findings. The mixing of orbitals of majority and minority spin character induced by the non-collinearity [25] leads to a pronounced peak shift in the vacuum density of states compared to the ferromagnetic case, which can constitute a TNCMR of up to 100 %. The TNCMR provides a possibility to easily detect non-collinear magnetic structures without the need of a magnetic read-out electrode.

Finally, the thesis is concluded in chapter 10.

2 Coherent Transport

In macroscopic dimensions the resistance of a conductor can be described by Ohm's law

$$R = (\sigma A/L)^{-1}, \tag{2.1}$$

where σ is the material specific conductivity, and A and L are the cross-sectional area and the length of the conductor, respectively. However, if the dimensions of the conductor are reduced from macroscopic to microscopic length scales, Ohm's law breaks down and new effects emerge. Firstly, even if the conductor is perfect, i.e., no scattering of the conducting electrons occurs, a resistance due to the interface of the contacts with the conductor arises independently of the length L. Secondly, the resistance does not scale with A^{-1} anymore but depends on the number of transverse modes in the conductor and changes in discrete steps. The characteristic lengths at which these effects occur are the mean free path l_{mfp} and the phase relaxation length l_ϕ.

The mean free path is the length that an electron can travel without changing its momentum. The momentum can be changed by scattering due to impurities and interfaces or any other scattering event that does not change the phase of the electron. The regime where only phase-conserving scattering occurs is called coherent transport. If no scattering is present at all, the regime is called ballistic. The mean free path is strongly material dependent. In magnetic transition metals it is of the order of $l_{\mathrm{mfp}} = 10 - 20\,\text{Å}$ [26].

If scattering events are present which change the energy and the phase, one speaks of incoherent transport. This can be caused by electron-phonon or electron-electron scattering. The phase relaxation length is the length an electron travels without changing its energy and is of the order of $l_\phi = 100 - 200\,\text{Å}$ [27].

In this work, we regard the coherent transport regime. In the following, we will briefly derive the basic equations and properties of the coherent transport regime following the book from Datta [28].

2.1 Conductance Quantum and Ballistic Contact Resistance

We consider a three-dimensional conductor of a free electron gas with dimensions $\Omega = L_x \times L_y \times L_z$ where $L_x \gg L_y = L_z$ and periodic boundary conditions. This leads to wave functions

$$\psi(\mathbf{r}) = \frac{1}{\sqrt{\Omega}} \exp(i\mathbf{kr}) \tag{2.2}$$

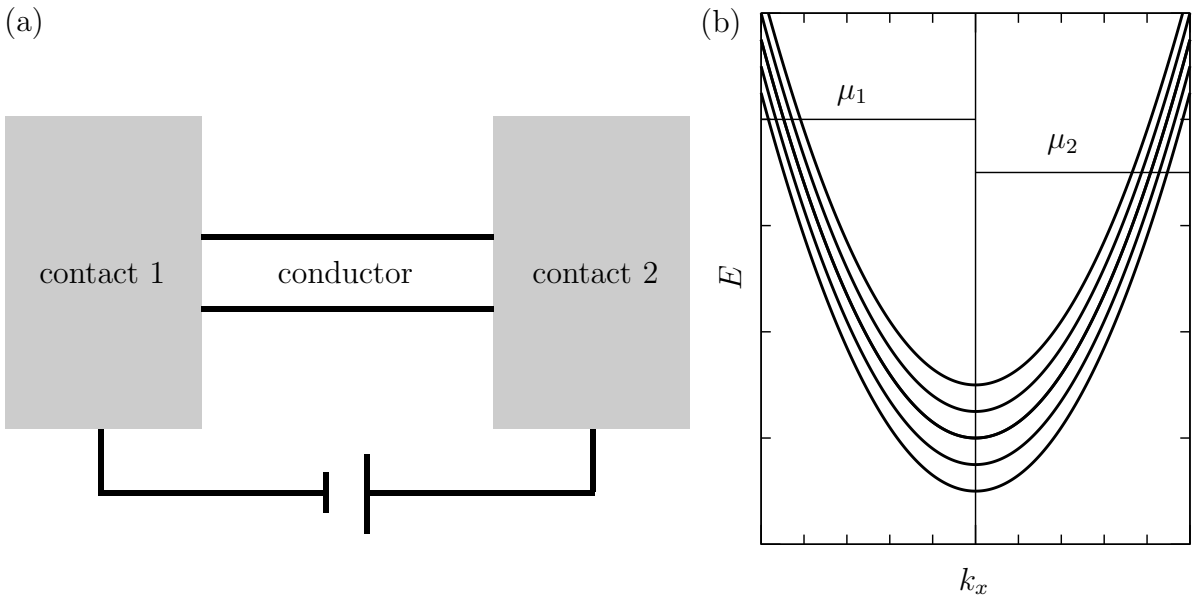

Figure 2.1: (a) Sketch of a conductor connected to contact 1 with chemical potential μ_1 and contact 2 with chemical potential μ_2. (b) Sketch of the dispersion relation for a free $3D$ electron gas in dependence of k_x. k_y and k_z give rise to the transverse modes.

with the conditions

$$k_x = \frac{2\pi}{L}\nu_x, \quad k_y = \frac{2\pi}{L_y}\nu_y, \quad k_z = \frac{2\pi}{L_z}\nu_z \quad \text{with} \quad \nu_x, \nu_y, \nu_z \in \mathbb{Z}. \tag{2.3}$$

The energy dispersion is

$$E = \frac{\hbar^2}{2m}(k_x^2 + k_y^2 + k_z^2) =: \frac{\hbar^2 k_x^2}{2m} + \epsilon_0(k_y, k_z). \tag{2.4}$$

The conductor is connected to two contacts at the left and right side as sketched in Fig. 2.1 (a). The contacts are assumed to be reflectionless, meaning that electrons can enter the contacts from the conductor with a negligible probability of being reflected.

Since one is interested in the transverse current in x direction, one regards the energy dispersion as a function of k_x, while k_y and k_z give rise to the different transverse modes as sketched in Fig. 2.1 (b). The current density of one of the positive k_x modes, which occupation shall be described by $f^+(E(k_x))$, can be described by

$$j^+ = envf, \tag{2.5}$$

where e is the charge of the electron, $n = \frac{1}{\Omega}$ is the electron density, and $v = \frac{1}{\hbar}\frac{\partial E}{\partial k_x}$ is the velocity of the electron. The total current of the positive k_x modes then is

$$I^+ = j^+ \cdot (L_y \cdot L_z) = \frac{e}{L_x} \sum_{k_x \geq 0} \frac{1}{\hbar}\frac{\partial E}{\partial k_x} f^+(E). \tag{2.6}$$

Since the k_x states are very dense, it is convenient to change to an integral representation

$$I^+ = \frac{e}{L}\int_{\epsilon_0(k_y,k_z)}^{\infty} \frac{1}{\hbar}\frac{\partial E}{\partial k_x} f^+(E)\frac{\mathrm{d}k_x}{(2\pi/L_x)} = \frac{e}{h}\int_{\epsilon_0(k_y,k_z)}^{\infty} f^+(E)\mathrm{d}E. \tag{2.7}$$

To get the current for all modes, one now simply has to count the number of modes at energy E

$$M(E) = \sum_{k_y,k_z} \theta(E - \epsilon_0(k_y, k_z)), \tag{2.8}$$

which then gives

$$I^+ = \frac{e}{h}\int_{-\infty}^{\infty} f^+(E)M(E)\mathrm{d}E. \tag{2.9}$$

From the above equation one can see that the current carried by each mode per energy is the conductance quantum e/h.

If one now applies a bias voltage so that contact 1 and 2 have a chemical potential of μ_1 and μ_2, respectively, the current carried by the $-k_x$ and $+k_x$ states does not cancel out anymore as indicated in Fig. 2.1 (b). If the number of modes $M(E) \equiv M$ is constant in the energy range $\mu_1 \geq E \geq \mu_2$ and the occupation function of the left and right contact $f_\mathrm{L}(E)$ and $f_\mathrm{R}(E)$ are simple step-functions ($T = 0\,\mathrm{K}$) one can write:

$$I = I^+ + I^- = \frac{e}{h}\int_{-\infty}^{\infty} (\theta(\mu_2 - E) - \theta(\mu_1 - E))M(E)\mathrm{d}E \tag{2.10}$$

$$= \frac{|e|}{h}\int_{\mu_2}^{\mu_1} M\mathrm{d}E = \frac{|e|^2}{h}M\frac{\mu_2 - \mu_1}{|e|}. \tag{2.11}$$

Analogous to Ohm's law one can define a contact resistance G_C from Eq. (2.11) given by

$$G_C^{-1} = \frac{h}{e^2 M} \approx \frac{6.45\,\mathrm{k\Omega}}{M}, \tag{2.12}$$

which is created by the finite number of modes in the conductor. When the dimensions of the conductor L_y and L_z become macroscopic, the number of modes will be large so that the contact resistance tends to zero.

2.2 The Landauer-Büttiker Formula

If one now considers conductors which exhibit elastic scattering of the electrons, one has to take into account the probability $T(E)$ for electrons with energy E originating from the left lead to be scattered into the right lead and vice versa as sketched in Fig. 2.2. One can regard the conductor as being partitioned into a scattering region and two

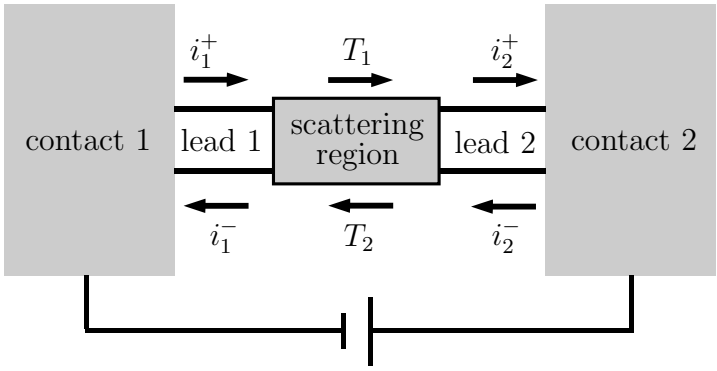

Figure 2.2: Sketch of a conductor consisting of a scattering region which is connected to contact 1 by the ballistically conducting lead 1 and contact 2 by the ballistically conducting lead 2. The probability of an electron originating from contact 1 and contact 2 to be transmitted by the scattering region is T_1 and T_2, respectively.

perfectly conducting leads connecting the scattering region to the contacts. The influx of electrons per unit energy from lead 1 and 2 (cf. with Fig. 2.2) can be written as:

$$i_1^+(E) = \frac{e}{h} M_1(E) f_1(E) \tag{2.13}$$

$$i_2^-(E) = \frac{e}{h} M_2(E) f_2(E). \tag{2.14}$$

The outflux from lead 2 is

$$i_2^+(E) = T_1(E) i_1^+(E) + (1 - T_2(E)) i_2^-(E) \tag{2.15}$$

and from lead 1 it is

$$i_1^-(E) = (1 - T_1(E)) i_1^+(E) + T_2(E) i_2^-(E). \tag{2.16}$$

The net current per energy is then given by

$$i(E) = i_1^+ - i_1^- = i_2^+ - i_2^- \tag{2.17}$$

$$= T_1 i_1^+ - T_2 i_2^- \tag{2.18}$$

$$= \frac{e}{h} [M_1(E) T_1(E) f_1(E) - M_2(E) T_2(E) f_2(E)]. \tag{2.19}$$

Defining the transmission function as $\bar{T}(E) = M(E)T(E)$ and assuming $\bar{T} = \bar{T}_1 = \bar{T}_2$, which holds if no incoherent scattering is present, one ends up with the Landauer-Büttiker formula [21, 29]:

$$I = \frac{e}{h} \int \bar{T}(E) [f_1(E) - f_2(E)] \mathrm{d}E. \tag{2.20}$$

The transmission function $\bar{T}$ is the sum of all the transmission probabilities T_{mn} between every mode m in lead 1 and every mode n in lead 2:

$$\bar{T}(E) = \sum_m \sum_n T_{mn}(E). \tag{2.21}$$

Büttiker has shown that the formula can be generalized to multi-terminal devices [30].

In this work, it is assumed that the electronic structure of the conductor does not change with the applied bias, which means that the transmission function does not change as a function of the applied bias.

2.3 Obtaining the Transmission Function with Green's Functions

To calculate the transport properties we now have to calculate the transmission function $\bar{T}(E)$. The transmission probabilities T_{mn} can be calculated from the scattering matrix, which relates the outgoing wave amplitudes b_i to the incoming wave amplitudes a_i of the electrons in lead 1 and lead 2, for example, for n modes the scattering matrix $\mathbf{S}$ can be described by

$$\begin{pmatrix} b_1 \\ b_2 \\ \vdots \\ b_n \end{pmatrix} = \begin{pmatrix} s_{11} & s_{12} & \cdots & s_{1n} \\ s_{21} & s_{22} & \cdots & s_{2n} \\ \vdots & \vdots & \ddots & \vdots \\ s_{n1} & s_{n2} & \cdots & s_{nn} \end{pmatrix} \begin{pmatrix} a_1 \\ a_2 \\ \vdots \\ a_n \end{pmatrix}. \tag{2.22}$$

The transmission probabilities T_{mn} are obtained from the scattering matrix by

$$T_{mn} = |s_{mn}|^2. \tag{2.23}$$

A more general and computationally more powerful concept are Green's functions. Green's functions give the response at any point in the conductor due to an excitation at any other point. The Green's function is related to the scattering matrix by the Fisher-Lee relation [31].

2.3.1 Green's Functions

The transport through a conductor can be described by an incident wave originating from the contacts, which leads to an excitation S in the conductor. The response Ψ to this excitation in the conductor is connected to the excitation by the Hamilton operator

$$\hat{H} = -\frac{\hbar^2}{2m}\Delta + U(\mathbf{r}), \tag{2.24}$$

where $U(\mathbf{r})$ represents the potential in the conductor. The problem can be expressed as

$$\left[E - \hat{H}\right] \Psi = S. \tag{2.25}$$

To calculate Ψ, the Green's function

$$G = \left[E - \hat{H}\right]^{-1} \tag{2.26}$$

has to be calculated.

It is instructive to regard the simple case of a one-dimensional wire with $U(\mathbf{r}) \equiv U_0$. Then Eq. (2.25) reads

$$\left(E - U_0 + \frac{\hbar^2}{2m}\frac{\partial^2}{\partial x^2}\right) G(x, x') = \delta(x - x'). \tag{2.27}$$

The solution to this differential equation are outgoing or incoming plane waves:

$$G^{\mathrm{R}}(x,x') = -\frac{1}{\hbar\nu}\exp\left[ik|x-x'|\right] \tag{2.28}$$

$$G^{\mathrm{A}}(x,x') = +\frac{1}{\hbar\nu}\exp\left[-ik|x-x'|\right], \tag{2.29}$$

where $k = \frac{\sqrt{2m(E-U_0)}}{\hbar}$ and $\nu = \frac{\hbar k}{m}$. The retarded Green's function G^{R} corresponds to outgoing waves and the advanced Green's function G^{A} to incoming plane waves. Which solution is adequate to the problem has to be determined by the boundary conditions.

The boundary conditions can be incorporated into Eq. (2.27) by adding an infinitesimal $+i\eta$ ($\eta > 0$) to the energy:

$$\left(E - U_0 + \frac{\hbar^2}{2m}\frac{\partial^2}{\partial x^2} + i\eta\right)\tilde{G}(x,x') = \delta(x-x'). \tag{2.30}$$

This leads to an imaginary component in the wave vector

$$\tilde{k} = \frac{\sqrt{2m(E-U_0}}{\hbar}\sqrt{1+\frac{i\eta}{E-U_0}} \approx k\left(1+\frac{i\eta}{2(E-U_0)}\right), \tag{2.31}$$

which makes the retarded Green's function the only solution since the advanced Green's function would grow indefinitely for $|x-x'| \to \infty$. The inverse behavior can be obtained if $-i\eta$ is added to the energy.

In general, the retarded and advanced Green's functions are defined as

$$G^{\mathrm{R}} = \left[E - \hat{H} + i\eta\right]^{-1} \quad (\eta \to 0^+) \tag{2.32}$$

$$G^{\mathrm{A}} = \left[E - \hat{H} - i\eta\right]^{-1} \quad (\eta \to 0^+). \tag{2.33}$$

The Green's function can be expanded in the eigenfunctions of the Hamilton operator

$$\hat{H}\Psi_\alpha = \epsilon_\alpha \psi_\alpha(\mathbf{r}) \tag{2.34}$$

yielding [28]:

$$G^{\mathrm{R}} = \sum_\alpha \frac{\psi_\alpha(\mathbf{r})\psi_\alpha^*(\mathbf{r}')}{E-\epsilon_\alpha+i\eta} \tag{2.35}$$

$$G^{\mathrm{A}} = \sum_\alpha \frac{\psi_\alpha(\mathbf{r})\psi_\alpha^*(\mathbf{r}')}{E-\epsilon_\alpha-i\eta}, \tag{2.36}$$

therefore

$$G^{\mathrm{A}}(\mathbf{r},\mathbf{r}') = [G^{\mathrm{R}}(\mathbf{r},\mathbf{r}')]^* \to G^{\mathrm{A}} = [G^{\mathrm{R}}]^\dagger. \tag{2.37}$$

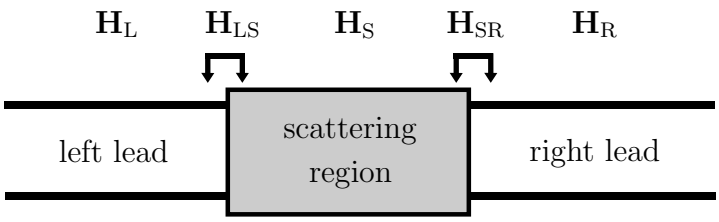

Figure 2.3: Sketch of the partitioning of the conductor in the left and right lead and the scattering region used to calculate the Green's function of the scattering region.

2.3.2 Matrix Representation of the Green's Function

If one now discretizes space or switches to a tight-binding description of the wave functions defined by matrix $\mathbf{H}$, one ends up with a matrix equation for the Green's function:

$$[(E+i\eta)\mathbf{1}-\mathbf{H}]\mathbf{G}^\mathrm{R}=\mathbf{1}\Leftrightarrow\mathbf{G}^\mathrm{R}=[(E+i\eta)\mathbf{1}-\mathbf{H}]^{-1}. \tag{2.38}$$

To calculate the Green's function, the matrix $[(E+i\eta)\mathbf{1}-\mathbf{H}]$ has to be inverted[1]. Since the conductor is connected to semi-infinite leads, the matrix is of infinite dimensions. This problem can be solved by the use of surface Green's functions. To do that the matrix is partitioned into submatrices:

$$[(E+i\eta)\mathbf{1}-\mathbf{H}]=\begin{bmatrix}(E+i\eta)\mathbf{1}-\mathbf{H}_\mathrm{L} & \mathbf{H}_\mathrm{LS} & 0\\ \mathbf{H}_\mathrm{SL} & E\mathbf{1}-\mathbf{H}_\mathrm{S} & \mathbf{H}_\mathrm{SR}\\ 0 & \mathbf{H}_\mathrm{RS} & (E+i\eta)\mathbf{1}-\mathbf{H}_\mathrm{R}\end{bmatrix}. \tag{2.39}$$

The matrices $[(E+i\eta)\mathbf{1}-\mathbf{H}_{\mathrm{L/R}}]$ and $[E\mathbf{1}-\mathbf{H}_\mathrm{S}]$ represent the isolated leads and scattering region, respectively, as sketched in Fig. 2.3. It is assumed that the interactions between the leads are negligible and also the coupling matrices $\mathbf{H}_\mathrm{LS}$ and $\mathbf{H}_\mathrm{RS}$ are chosen non-zero only in the vicinity of the interface of the conductor with the left and right lead. Furthermore, it is enough to add the $i\eta$ in the leads to determine the boundary conditions for the Green's function [28].

One can now also define submatrices of the Green's function:

$$\begin{bmatrix}\mathbf{G}_\mathrm{L} & \mathbf{G}_\mathrm{LS} & \mathbf{G}_\mathrm{LR}\\ \mathbf{G}_\mathrm{SL} & \mathbf{G}_\mathrm{S} & \mathbf{G}_\mathrm{SR}\\ \mathbf{G}_\mathrm{RL} & \mathbf{G}_\mathrm{RS} & \mathbf{G}_\mathrm{R}\end{bmatrix}\equiv\begin{bmatrix}(E+i\eta)\mathbf{1}-\mathbf{H}_\mathrm{L} & \mathbf{H}_\mathrm{LS} & 0\\ \mathbf{H}_\mathrm{SL} & E\mathbf{1}-\mathbf{H}_\mathrm{S} & \mathbf{H}_\mathrm{SR}\\ 0 & \mathbf{H}_\mathrm{RS} & (E+i\eta)\mathbf{1}-\mathbf{H}_\mathrm{R}\end{bmatrix}^{-1}=\mathbf{G}. \tag{2.40}$$

Eq. (2.38) yields

$$\mathbf{H}_\mathrm{SL}\mathbf{G}_\mathrm{LS}+[E\mathbf{1}-\mathbf{H}_\mathrm{S}]\mathbf{G}_\mathrm{S}+\mathbf{H}_\mathrm{RS}\mathbf{G}_\mathrm{RS}=\mathbf{1} \tag{2.41}$$

$$\mathbf{H}_\mathrm{LS}\mathbf{G}_\mathrm{S}+[(E+i\eta)\mathbf{1}-\mathbf{H}_\mathrm{L}]\mathbf{G}_\mathrm{LS}=\mathbf{0} \tag{2.42}$$

$$\mathbf{H}_\mathrm{RS}\mathbf{G}_\mathrm{S}+[(E+i\eta)\mathbf{1}-\mathbf{H}_\mathrm{R}]\mathbf{G}_\mathrm{RS}=\mathbf{0}. \tag{2.43}$$

[1]Because we are looking at the retarded Green's function we will drop the index R from hereon until otherwise noted.

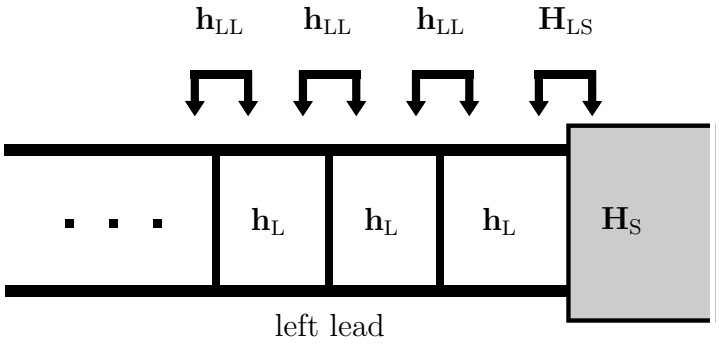

Figure 2.4: Sketch of the partitioning of the leads (here exemplary for the left lead) to calculate the surface Green's function of the leads.

Using the Green's function of the isolated, semi-infinite leads

$$\mathbf{g}_{\mathrm{L/R}} = [(E + i\eta)\mathbf{1} - \mathbf{H}_{\mathrm{L/R}}]^{-1} \tag{2.44}$$

and Eqs. (2.42) and (2.43) one obtains

$$\mathbf{G}_{\mathrm{LS/RS}} = -\mathbf{g}_{\mathrm{L/R}}\mathbf{H}_{\mathrm{LS/RS}}\mathbf{G}_{\mathrm{S}}. \tag{2.45}$$

Substituting this in Eq. (2.41) and taking into account that $\mathbf{H}_{\mathrm{SL/RS}} = \mathbf{H}^{\dagger}_{\mathrm{LS/SR}}$ yields an expression for the Green's function of the conductor

$$\mathbf{G}_{\mathrm{S}} = \left[E\mathbf{1} - \mathbf{H}_{\mathrm{S}} - \mathbf{\Sigma}_{\mathrm{L}} - \mathbf{\Sigma}_{\mathrm{R}}\right]^{-1}. \tag{2.46}$$

The terms

$$\mathbf{\Sigma}_{\mathrm{L/R}} = \mathbf{H}^{\dagger}_{\mathrm{LS/RS}}\mathbf{g}_{\mathrm{L/R}}\mathbf{H}_{\mathrm{LS/RS}} \tag{2.47}$$

are called (retarded) self-energies and take into account the effect of the leads on the propagation of the electrons in the conductor. Following from Eq. (2.37) the advanced self-energy can be obtained by taking the adjoint of the retarded self-energy:

$$\mathbf{\Sigma}^{\mathrm{A}}_{\mathrm{L/R}} = [\mathbf{\Sigma}^{\mathrm{R}}_{\mathrm{L/R}}]^{\dagger}. \tag{2.48}$$

2.3.3 Surface Green's Function

To determine the self-energies of the leads one still would need to invert the semi-infinite matrix $[(E + i\eta)\mathbf{1} - \mathbf{H}_{\mathrm{L/R}}]$. There are several methods to solve this problem. We here follow the decimation technique described in Ref. [32]. To do that the Hamiltonian of the leads are also divided into submatrices taking into account only a limited number of nearest-neighbor hoppings, which have to be chosen in a way that the leads are still well described. The partitioning of the left lead is sketched in Fig. 2.4. The Hamiltonian of the left lead then states:

$$\mathbf{H}_{\mathrm{L}} = \begin{pmatrix} \ddots & \mathbf{h}_{\mathrm{LL}} & \mathbf{0} & \mathbf{0} \\ \mathbf{h}^{\dagger}_{\mathrm{LL}} & \mathbf{h}_{\mathrm{L}} & \mathbf{h}_{\mathrm{LL}} & \mathbf{0} \\ \mathbf{0} & \mathbf{h}^{\dagger}_{\mathrm{LL}} & \mathbf{h}_{\mathrm{L}} & \mathbf{h}_{\mathrm{LL}} \\ \mathbf{0} & \mathbf{0} & \mathbf{h}^{\dagger}_{\mathrm{LL}} & \mathbf{h}_{\mathrm{L}} \end{pmatrix} \tag{2.49}$$

The equation defining the Green's function can be written as:

$$\begin{pmatrix} \ddots & -\mathbf{h}_{\mathrm{LL}} & \mathbf{0} & \mathbf{0} \\ -\mathbf{h}_{\mathrm{LL}}^{\dagger} & \omega\mathbf{1}-\mathbf{h}_{\mathrm{L}} & -\mathbf{h}_{\mathrm{LL}} & \mathbf{0} \\ \mathbf{0} & -\mathbf{h}_{\mathrm{LL}}^{\dagger} & \omega\mathbf{1}-\mathbf{h}_{\mathrm{L}} & -\mathbf{h}_{\mathrm{LL}} \\ \mathbf{0} & \mathbf{0} & -\mathbf{h}_{\mathrm{LL}}^{\dagger} & \omega\mathbf{1}-\mathbf{h}_{\mathrm{L}} \end{pmatrix} \cdot \begin{pmatrix} \ddots & \vdots & \vdots & \vdots \\ \cdots & \mathbf{g}_{22} & \mathbf{g}_{12} & \mathbf{g}_{02} \\ \cdots & \mathbf{g}_{21} & \mathbf{g}_{11} & \mathbf{g}_{01} \\ \cdots & \mathbf{g}_{20} & \mathbf{g}_{10} & \mathbf{g}_{00} \end{pmatrix} = \mathbf{1}, \tag{2.50}$$

where $\omega = E + i\eta$. Multiplying the rows of the first matrix with the last column of the second matrix yields:

$$(\omega\mathbf{1}-\mathbf{h}_{\mathrm{L}})\mathbf{g}_{00} - \mathbf{h}_{\mathrm{LL}}^{\dagger}\mathbf{g}_{01} = \mathbf{1} \tag{2.51}$$

$$-\mathbf{h}_{\mathrm{LL}}\mathbf{g}_{00} + (\omega\mathbf{1}-\mathbf{h}_{\mathrm{L}})\mathbf{g}_{01} - \mathbf{h}_{\mathrm{LL}}^{\dagger}\mathbf{g}_{02} = \mathbf{0} \tag{2.52}$$

$$-\mathbf{h}_{\mathrm{LL}}\mathbf{g}_{01} + (\omega\mathbf{1}-\mathbf{h}_{\mathrm{L}})\mathbf{g}_{02} - \mathbf{h}_{\mathrm{LL}}^{\dagger}\mathbf{g}_{03} = \mathbf{0} \tag{2.53}$$

$$-\mathbf{h}_{\mathrm{LL}}\mathbf{g}_{0m-1} + (\omega\mathbf{1}-\mathbf{h}_{\mathrm{L}})\mathbf{g}_{0m} - \mathbf{h}_{\mathrm{LL}}^{\dagger}\mathbf{g}_{0m+1} = \mathbf{0}. \tag{2.54}$$

Solving for $\mathbf{g}_{0m}$ and using $\mathbf{W} = \omega\mathbf{1} - \mathbf{h}_{\mathrm{L}}$ leads to:

$$\mathbf{g}_{0m} = \mathbf{W}^{-1}(\mathbf{h}_{\mathrm{LL}}\mathbf{g}_{0m-1} + \mathbf{h}_{\mathrm{LL}}^{\dagger}\mathbf{g}_{0m+1}). \tag{2.55}$$

Plugging $\mathbf{g}_{01}$ into Eq. (2.51), $\mathbf{g}_{01}$ and $\mathbf{g}_{03}$ into Eq. (2.53), as well as $\mathbf{g}_{03}$ and $\mathbf{g}_{05}$ in Eq. (2.54) for $m = 4$ and using the abbreviations

$$\widetilde{\mathbf{W}}_{\mathrm{S}} = (\mathbf{W} + \mathbf{h}_{\mathrm{LL}}^{\dagger}\mathbf{W}^{-1}\mathbf{h}_{\mathrm{LL}}) \tag{2.56}$$

$$\widetilde{\mathbf{W}}_{\mathrm{B}} = (\mathbf{W} + \mathbf{h}_{\mathrm{LL}}^{\dagger}\mathbf{W}^{-1}\mathbf{h}_{\mathrm{LL}} + \mathbf{h}_{\mathrm{LL}}\mathbf{W}^{-1}\mathbf{h}_{\mathrm{LL}}^{\dagger}) \tag{2.57}$$

$$\widetilde{\mathbf{h}}_{\mathrm{LL}} = -(\mathbf{h}_{\mathrm{LL}}\mathbf{W}^{-1}\mathbf{h}_{\mathrm{LL}}) \tag{2.58}$$

$$\widetilde{\mathbf{h}}_{\mathrm{LL}\dagger} = -(\mathbf{h}_{\mathrm{LL}}^{\dagger}\mathbf{W}^{-1}\mathbf{h}_{\mathrm{LL}}^{\dagger}) \tag{2.59}$$

yields a formally identical set of equations as Eqs. (2.51)-(2.54):

$$\widetilde{\mathbf{W}}_{\mathrm{S}}\mathbf{g}_{00} - \widetilde{\mathbf{h}}_{\mathrm{LL}\dagger}\mathbf{g}_{02} = \mathbf{1} \tag{2.60}$$

$$-\widetilde{\mathbf{h}}_{\mathrm{LL}}\mathbf{g}_{00} + \widetilde{\mathbf{W}}_{\mathrm{B}}\mathbf{g}_{02} - \widetilde{\mathbf{h}}_{\mathrm{LL}\dagger}\mathbf{g}_{04} = \mathbf{0} \tag{2.61}$$

$$-\widetilde{\mathbf{h}}_{\mathrm{LL}}\mathbf{g}_{02} + \widetilde{\mathbf{W}}_{\mathrm{B}}\mathbf{g}_{04} - \widetilde{\mathbf{h}}_{\mathrm{LL}\dagger}\mathbf{g}_{06} = \mathbf{0} \tag{2.62}$$

$$-\widetilde{\mathbf{h}}_{\mathrm{LL}}\mathbf{g}_{0(2m-2)} + \widetilde{\mathbf{W}}_{\mathrm{B}}\mathbf{g}_{0(2m)} - \widetilde{\mathbf{h}}_{\mathrm{LL}\dagger}\mathbf{g}_{0(2m+2)} = \mathbf{0} \tag{2.63}$$

Iterating this procedure yields after p steps:

$$\widetilde{\mathbf{W}}_{\mathrm{S}}^{(p)} = \mathbf{W}_{\mathrm{S}}^{(p-1)} + \widetilde{\mathbf{h}}_{\mathrm{LL}\dagger}^{(p-1)}\left[\mathbf{W}_{\mathrm{B}}^{(p-1)}\right]^{-1}\widetilde{\mathbf{h}}_{\mathrm{LL}}^{(p-1)} \tag{2.64}$$

$$\widetilde{\mathbf{W}}_{\mathrm{B}}^{(p)} = \mathbf{W}_{\mathrm{B}}^{(p-1)} + \widetilde{\mathbf{h}}_{\mathrm{LL}\dagger}^{(p-1)}\left[\mathbf{W}_{\mathrm{B}}^{(p-1)}\right]^{-1}\widetilde{\mathbf{h}}_{\mathrm{LL}}^{(p-1)} + \widetilde{\mathbf{h}}_{\mathrm{LL}}^{(p-1)}\left[\mathbf{W}_{\mathrm{B}}^{(p-1)}\right]^{-1}\widetilde{\mathbf{h}}_{\mathrm{LL}\dagger}^{(p-1)} \tag{2.65}$$

$$\widetilde{\mathbf{h}}_{\mathrm{LL}\dagger}^{(p)} = \widetilde{\mathbf{h}}_{\mathrm{LL}\dagger}^{(p-1)}\left[\mathbf{W}_{\mathrm{B}}^{(p-1)}\right]^{-1}\widetilde{\mathbf{h}}_{\mathrm{LL}\dagger}^{(p-1)} \tag{2.66}$$

$$\widetilde{\mathbf{h}}_{\mathrm{LL}}^{(p)} = \widetilde{\mathbf{h}}_{\mathrm{LL}}^{(p-1)}\left[\mathbf{W}_{\mathrm{B}}^{(p-1)}\right]^{-1}\widetilde{\mathbf{h}}_{\mathrm{LL}}^{(p-1)}, \tag{2.67}$$

where the latter two equations yield the interactions between layer 0 and 2^p. The fact that the number of layers eliminated from the set of equations grows with an exponential of the number of steps makes this method very effective.

One can expect that the interactions $\widetilde{\mathbf{h}}_{\mathrm{LL}\dagger}^{(p_0)}$ and $\widetilde{\mathbf{h}}_{\mathrm{LL}}^{(p_0)}$ between layer 0 and 2^{p_0} become negligible for large enough p_0. Then Eqs. (2.64)−(2.67) do not change anymore for further iterations and one ends up with

$$\widetilde{\mathbf{W}}_{\mathrm{S}}^{(p_0)}\mathbf{g}_{00} = \mathbf{1}. \tag{2.68}$$

With this one can obtain the effective Green's function $\mathbf{g}_{\mathrm{L}} = \mathbf{g}_{00}$ for the surface of the lead, which is then coupled to the scattering region as described in the previous section.

We can now calculate the self-energies and, therefore, the Green's function according to Eq. (2.46). The Green's function gives access to all the quantities of interest like the transmission and spectral function.

2.3.4 Spectral Function and Transmission Function

From Eq. (2.46) an effective Schrödinger equation for the scattering region including the influence of the leads and the coupling to the contacts, i.e., of an open quantum system, can be obtained:

$$\left[\mathbf{H}_{\mathrm{S}} + \mathbf{\Sigma}_{\mathrm{L}} + \mathbf{\Sigma}_{\mathrm{R}}\right]\psi_\alpha = \epsilon_\alpha \psi_\alpha \tag{2.69}$$

The Hamiltonian $\mathbf{H}_{\mathrm{S}} + \mathbf{\Sigma}_{\mathrm{L}} + \mathbf{\Sigma}_{\mathrm{R}}$ is not Hermitian since the self-energies $\mathbf{\Sigma}_{\mathrm{L/R}}$ are not Hermitian and, therefore, the eigenvalues are complex. Using the eigenenergies of the isolated scattering region $\mathbf{H}_{\mathrm{S}}$

$$\mathbf{H}_{\mathrm{S}}\psi_{\alpha 0} = \epsilon_{\alpha 0}\psi_{\alpha 0} \tag{2.70}$$

one can write

$$\epsilon_\alpha = \epsilon_{\alpha 0} - \Delta_\alpha - i(\gamma_\alpha/2), \tag{2.71}$$

where Δ_α represents the shift in energy of the eigenstate of the isolated scattering region due to the interaction with the leads. γ_α reflects the finite lifetime of the state since it adds a time dependence to the probability density

$$|\psi_\alpha|^2 \exp\left(-2\gamma_\alpha t/\hbar\right). \tag{2.72}$$

$2\gamma_\alpha/\hbar$ is the average time an electron stays in state α before it exits the scattering region into the leads.

One can now again write the retarded Green's function in terms of the eigenfunctions of $[\mathbf{H}_{\mathrm{S}} + \mathbf{\Sigma}_{\mathrm{L}} + \mathbf{\Sigma}_{\mathrm{R}}]$ defined in Eq. (2.70) and of the eigenfunctions Φ_α of the adjoint operator[2] $[\mathbf{H}_{\mathrm{S}} + \mathbf{\Sigma}_{\mathrm{L}}^{\mathrm{A}} + \mathbf{\Sigma}_{\mathrm{R}}^{\mathrm{A}}]$ [28]:

$$G^{\mathrm{R}}(\mathbf{r}, \mathbf{r}') = \sum_\alpha \frac{\psi_\alpha(\mathbf{r})\Phi_\alpha^*(\mathbf{r}')}{E - \epsilon_\alpha}. \tag{2.73}$$

[2]For the eigenfunctions of the operator and its adjoint holds: $\int \Phi_\alpha \psi_\beta^*(\mathbf{r})\mathrm{d}^3\mathbf{r} = \delta_{\alpha\beta}$.

The so called spectral function $\mathbf{A}$ can now be expressed as:

$$\mathbf{A} \equiv i\left[\mathbf{G}^{\mathrm{R}} - \mathbf{G}^{\mathrm{A}}\right] \tag{2.74}$$

$$= \sum_{\alpha} \psi_{\alpha}(\mathbf{r})\Phi_{\alpha}^{*}(\mathbf{r}')\frac{\gamma_{\alpha}}{(E - \epsilon_{\alpha 0} - \Delta_{\alpha})^2 + (\gamma_{\alpha}/2)^2}. \tag{2.75}$$

The trace of the spectral function

$$\mathrm{Tr}[\mathbf{A}(E)] \equiv \int \mathbf{A}(\mathbf{r}, \mathbf{r}, E)\mathrm{d}^3\mathbf{r} = \sum_{\alpha} \frac{\gamma_{\alpha}}{(E - \epsilon_{\alpha 0} - \Delta_{\alpha})^2 + (\gamma_{\alpha}/2)^2} \tag{2.76}$$

yields the density of states

$$N(E) = \frac{1}{2\pi}\mathrm{Tr}[\mathbf{A}(E)] = \sum_{\alpha} \frac{1}{2\pi}\frac{\gamma_{\alpha}}{(E - \epsilon_{\alpha 0} - \Delta_{\alpha})^2 + (\gamma_{\alpha}/2)^2}. \tag{2.77}$$

For vanishingly small couplings ($\gamma_{\alpha}, \Delta_{\alpha} \to 0$) to the leads, one obtains the usual expression for the density of states

$$N(E) = \sum_{\alpha} \delta(E - \epsilon_{0\alpha}). \tag{2.78}$$

From the above equations one can see that for the simplest case of energy independent self-energies the coupling to the leads leads to a Lorentzian broadening

$$\frac{\gamma}{(E - \epsilon)^2 + (\gamma/2)^2} \tag{2.79}$$

for each peak in the density of states. However, in general the self-energies are energy dependent and, therefore, also the eigenenergies ϵ_{α}, which can lead to different peak shapes.

The diagonal elements of the spectral function yield the local density of states:

$$\rho(\mathbf{r}, E) = \frac{1}{2\pi}\mathbf{A}(\mathbf{r}, \mathbf{r}, E) = \sum_{\alpha} \frac{1}{2\pi}\frac{\gamma_{\alpha}}{(E - \epsilon_{\alpha 0} - \Delta_{\alpha})^2 + (\gamma_{\alpha}/2)^2}\psi_{\alpha}(\mathbf{r})\Phi_{\alpha}^{*}(\mathbf{r}). \tag{2.80}$$

The spectral function can be calculated more conveniently by [28]

$$\mathbf{A} = \mathbf{G}_{\mathrm{S}}\mathbf{\Gamma}_{\mathrm{L}}\mathbf{G}_{\mathrm{S}}^{\dagger} + \mathbf{G}_{\mathrm{S}}\mathbf{\Gamma}_{\mathrm{R}}\mathbf{G}_{\mathrm{S}}^{\dagger}, \tag{2.81}$$

whereby the so called broadening matrices $\mathbf{\Gamma}_{\mathrm{L/R}}$ of the left and right lead are defined as

$$\mathbf{\Gamma}_{\mathrm{L/R}}(E) = i\left[\mathbf{\Sigma}_{\mathrm{L/R}}(E) - \mathbf{\Sigma}_{\mathrm{L/R}}^{\dagger}(E)\right]. \tag{2.82}$$

Finally, we now can calculate the transmission function $T(E)$ from the Green's function

$$T(E) = \mathrm{Tr}\left[\mathbf{\Gamma}_{\mathrm{L}}(E)\mathbf{G}_{\mathrm{S}}(E)\mathbf{\Gamma}_{\mathrm{R}}(E)\mathbf{G}_{\mathrm{S}}^{\dagger}(E)\right]. \tag{2.83}$$

The equivalence to Eq. (2.23) can be obtained by the Fisher-Lee relation [31, 33], which connects the Green's function formalism with the scattering matrix $\mathbf{S}$:

$$s_{mn} = \frac{i}{\hbar}\frac{1}{\sqrt{|v_{m,<}||v_{n,>}|}}(\Phi^{\mathrm{L}}_{n,<})^{\dagger}\mathbf{\Gamma}_{\mathrm{L}}\mathbf{G}_{\mathrm{S}}\mathbf{\Gamma}_{\mathrm{R}}(\Phi^{\mathrm{R}}_{n,>}), \tag{2.84}$$

where $\Phi^{\mathrm{L}}_{n,<}$ and $\Phi^{\mathrm{R}}_{n,>}$ are incoming ($<$) and outgoing ($>$) waves in the left and right lead, respectively, and $v_{m,<}$ and $v_{n,>}$ are their group velocities. Furthermore, one can write [33]:

$$\mathbf{\Gamma}_{\mathrm{L}} = \sum_n \mathbf{\Gamma}_{\mathrm{L}}\Phi^{\mathrm{L}}_{n,<}\frac{1}{\hbar|v_{n,<}|}(\Phi^{\mathrm{L}}_{n,<})^{\dagger}\mathbf{\Gamma}_{\mathrm{L}} \tag{2.85}$$

$$\mathbf{\Gamma}_{\mathrm{R}} = \sum_n \mathbf{\Gamma}_{\mathrm{R}}\Phi^{\mathrm{R}}_{n,>}\frac{1}{\hbar|v_{n,>}|}(\Phi^{\mathrm{R}}_{n,>})^{\dagger}\mathbf{\Gamma}_{\mathrm{R}}, \tag{2.86}$$

which then yields:

$$T(E) = \mathrm{Tr}\left[\mathbf{\Gamma}_{\mathrm{L}}(E)\mathbf{G}_{\mathrm{S}}(E)\mathbf{\Gamma}_{\mathrm{R}}(E)\mathbf{G}^{\dagger}_{\mathrm{S}}(E)\right] \tag{2.87}$$

$$= \sum_{m,n}|s_{mn}|^2. \tag{2.88}$$

Extensive details on the derivation of the above equations can be found in [33]. Eq. (2.83) can be obtained more generally by the non-equilibrium Green's function formalism [17, 28, 33, 34, 35, 36, 37] in terms of second quantization, which in principle also allows to incorporate non-coherent and finite bias effects.

2.4 Numerically Efficient Formula for the Transmission Function

As stated above, only a limited number of sites in the scattering region is connected to the leads and also in the scattering region itself only hoppings up to a certain neighbor are taken into account. The matrix of the scattering region can then be divided into n principal layers and in this way becomes a block tridiagonal matrix

$$\mathbf{H}_{\mathrm{S}} = \begin{pmatrix} \mathbf{h}_{1,1} & \mathbf{h}_{1,2} & \mathbf{0} & \mathbf{0} & \mathbf{0} \\ \mathbf{h}^{\dagger}_{1,2} & \mathbf{h}_{2,2} & \ddots & \mathbf{0} & \mathbf{0} \\ \mathbf{0} & \ddots & \ddots & \ddots & \mathbf{0} \\ \mathbf{0} & \mathbf{0} & \ddots & \mathbf{h}_{n-1,n-1} & \mathbf{h}_{(n-1),n} \\ \mathbf{0} & \mathbf{0} & \mathbf{0} & \mathbf{h}^{\dagger}_{(n-1),n} & \mathbf{h}_{n,n} \end{pmatrix}. \tag{2.89}$$

Only the principal layers $\mathbf{h}_{1,1}$ and $\mathbf{h}_{n,n}$ are connected to the left and right lead via $\mathbf{\Sigma}_{\mathrm{L}}$ and $\mathbf{\Sigma}_{\mathrm{R}}$, respectively. This makes $\mathbf{\Gamma}_{\mathrm{L}}$ and $\mathbf{\Gamma}_{\mathrm{R}}$ only nonzero in the upper left and lower right corner, respectively. Following Ref. [35] one exploits this by rewriting the formula for the transmission (Eq. (2.83)) using Eq. (2.81) as:

$$T = \mathrm{Tr}\left[\mathbf{\Gamma}_{\mathrm{R}}(\mathbf{A} - \mathbf{G}^{\dagger}_{\mathrm{S}}\mathbf{\Gamma}_{\mathrm{R}}\mathbf{G}_{\mathrm{S}})\right]. \tag{2.90}$$

Since $\mathbf{\Gamma}_\mathrm{R}$ is only nonzero in the lower right corner, one only needs the last diagonal block of the matrices to calculate the transmission:

$$T = \mathrm{Tr}\left[(\mathbf{\Gamma}_\mathrm{R})_{n,n}(\mathbf{A}_{n,n} - (\mathbf{G}_\mathrm{S}^\dagger)_{n,n}(\mathbf{\Gamma}_\mathrm{R})_{n,n}(\mathbf{G}_\mathrm{S})_{n,n})\right]. \tag{2.91}$$

$\mathbf{A}$ is calculated via Eq. (2.74).

The block diagonal elements of the Green's function $\mathbf{G}_\mathrm{S}$ are calculated in a recursive scheme [37]: With $\mathbf{B} \equiv [E\mathbf{1} - \mathbf{H}_\mathrm{S} - \mathbf{\Sigma}_\mathrm{L} - \mathbf{\Sigma}_\mathrm{R}]$ the Green's function of the first q principal layer (only connected to the left lead indicated by index L) is defined by

$$\mathbf{B}_{1:q,1:q}\mathbf{g}^{Lq} = \mathbf{1}_{1:q,1:q}. \tag{2.92}$$

For the Green's function of the $(q+1)$th layer $\mathbf{g}^{Lq+1}$, one can write

$$\begin{pmatrix} \mathbf{B}_{1:q,1:q} & \mathbf{B}_{1:q,q+1} \\ \mathbf{B}_{q+1,1:q} & \mathbf{B}_{q+1,q+1} \end{pmatrix} \begin{pmatrix} \mathbf{g}^{Lq+1}_{1:q,1:q} & \mathbf{g}^{Lq+1}_{1:q,q+1} \\ \mathbf{g}^{Lq+1}_{q+1,1:q} & \mathbf{g}^{Lq+1}_{q+1,q+1} \end{pmatrix} = \begin{pmatrix} \mathbf{1}_{1:q,1:q} & \mathbf{0}_{1:q,q+1} \\ \mathbf{0}_{q+1,1:q} & \mathbf{1}_{q+1,q+1} \end{pmatrix}. \tag{2.93}$$

Dyson's equation states

$$\mathbf{g}^{Lq+1} = \mathbf{g}^0 + \mathbf{g}^0\mathbf{U}\mathbf{g}^{Lq+1} \tag{2.94}$$

with

$$\mathbf{g}^0 = \begin{pmatrix} \mathbf{B}^{-1}_{1:q,1:q} & \mathbf{0} \\ \mathbf{0} & \mathbf{B}^{-1}_{q+1,q+1} \end{pmatrix}, \tag{2.95}$$

$$\mathbf{U} = \begin{pmatrix} \mathbf{0} & -\mathbf{B}_{1:q,q+1} \\ -\mathbf{B}_{q+1,1:q} & \mathbf{0} \end{pmatrix}. \tag{2.96}$$

Using Eq. (2.94) and the fact that the only nonzero element of $\mathbf{B}_{1:q,q+1}$ and $\mathbf{B}_{q+1,1:q}$ is $\mathbf{B}_{q,q+1}$ and $\mathbf{B}_{q+1,q}$, respectively. One finds for the diagonal block of the lower right corner of $\mathbf{g}^{Lq+1}$:

$$\mathbf{g}^{Lq+1}_{q+1,q+1} = (\mathbf{B}_{q+1,q+1} - \mathbf{B}_{q+1,q}\mathbf{g}^{Lq}_{q,q}\mathbf{B}_{q,q+1})^{-1}. \tag{2.97}$$

$\mathbf{g}^{Ln}_{n,n}$ is then equal to the diagonal block of the lower right corner of the fully connected Green's function $(\mathbf{G}_\mathrm{S})_{n,n}$ needed in Eq. (2.91).

3 Density Functional Theory and FLAPW

To utilize the formalism introduced in the previous chapter, we need to determine the matrices $\mathbf{H}_{\mathrm{S}}$, $\mathbf{H}_{\mathrm{LS}}$, $\mathbf{H}_{\mathrm{SR}}$, $\mathbf{h}_{\mathrm{L}}$, $\mathbf{h}_{\mathrm{LL}}$, and the analogons for the right lead. To be able to do the partitioning of the matrices as described in the previous chapter, one needs to describe the system under investigation in terms of localized orbitals, so that the interactions between the orbitals are negligible at a certain separation.

In this work, we obtain these matrices using maximally localized Wannier functions. The Wannier functions are in turn obtained from a description of the system in terms of Bloch functions gained with the FLAPW method, which is based on density functional theory.

3.1 Density Functional Theory

For many-body problems, analytical solutions of the Schrödinger equation are only feasible for the hydrogen atom, while already for the helium atom only approximative solutions are possible. To still be able to effectively and precisely describe many-body problems like they appear in solid-state physics, numerous theories have been developed. One of the most successful approaches is DFT developed by Hohenberg, Kohn and Sham [13, 14]. DFT is computationally efficient and able to cover most of the effects arising in solids.

Its starting point is the Born-Oppenheimer approximation, which fixes the atomic nuclei positions and, therefore, reduces the problem to the positional variables of the electrons. The Schrödinger equation then states:

$$\left[-\frac{\hbar^2}{2m}\sum_{i=1}^{N}\nabla_i^2+\frac{1}{2}\sum_{i\neq j=1}^{N}\frac{e^2}{|\mathbf{r}_i-\mathbf{r}_j|}-\sum_{i=1}^{N}\sum_{\mu=1}^{M}\frac{e^2Z_\mu}{|\mathbf{r}_i-\boldsymbol{\tau}_\mu|}\right]\Psi(\mathbf{r}_1,...,\mathbf{r}_N)=E\Psi(\mathbf{r}_1,...,\mathbf{r}_N), \tag{3.1}$$

where N is the number of electrons, $\mathbf{r}_i$ is the position of the ith electron, M is the number of nuclei, and $\boldsymbol{\tau}_\mu$ and Z_μ are the position and charge of the μth nucleus. Since the system has $3N$ variables, the solution of Eq. (3.1) is computationally very demanding.

3.1.1 The Hohenberg-Kohn Theorem

The idea behind DFT is to relinquish the information of each individual electron and instead to focus on the electron density

$$n(\mathbf{r})=\langle\Psi|\sum_{i=1}^{N}\delta(\mathbf{r}-\mathbf{r}_i)|\Psi\rangle. \tag{3.2}$$

This reduces the number of variables to 3.

For systems with non-degenerate ground states, Hohenberg and Kohn proved the following two theorems [13]:

- For a given external potential $v(\mathbf{r}) = \sum_{\mu=1}^{M} \frac{e^2 Z_\mu}{|\mathbf{r}-\boldsymbol{\tau}_\mu|}$ created by the nuclei, the ground state energy and all other ground state properties of the system are unique functionals of the electron density $n(\mathbf{r})$.
- The ground state density $n_0(\mathbf{r})$ minimizes the energy functional $E[n]$:

$$E_0 = \min_n E_{v(\mathbf{r})}[n] = \min_n \left(F_{\mathrm{HK}}[n] + \int v(\mathbf{r}) n(\mathbf{r}) \mathrm{d}^3\mathbf{r} \right), \tag{3.3}$$

where the universal Hohenberg-Kohn functional is defined as the sum of the kinetic energy $\hat{T} = -\frac{\hbar^2}{2m} \sum_{i=1}^{N} \nabla_i^2$ and Coulomb interaction energy $\hat{U} = \frac{1}{2} \sum_{i \neq j=1}^{N} \frac{e^2}{|\mathbf{r}_i - \mathbf{r}_j|}$ of the electrons

$$F_{\mathrm{HK}}[n] = \langle \Psi[n] | \hat{T} + \hat{U} | \Psi[n] \rangle. \tag{3.4}$$

Therefore, the ground state density can be obtained by the minimization of the energy functional. It was further shown that the theorems mentioned above can also be proven for degenerate ground states [38]. Since the Hohenberg-Kohn functional is not known exactly, approximations have to be made to make practical use of the Hohenberg-Kohn theorem.

3.1.2 The Kohn-Sham Equations

The main idea of Kohn and Sham is to project the problem of interacting electrons on a problem of non-interacting electrons in an effective potential $v_{\mathrm{eff}}(\mathbf{r})$, which is chosen so that the ground state density is equivalent to the problem of interacting electrons. For each of the N electrons this leads to Schrödinger-like one-particle equations, the so called Kohn-Sham equations [14]:

$$\left(-\frac{\hbar^2}{2m} \nabla^2 + v_{\mathrm{eff}}(\mathbf{r}) \right) \psi_i(\mathbf{r}) = \epsilon_i \psi_i(\mathbf{r}). \tag{3.5}$$

The ground state density is calculated via

$$n(\mathbf{r}) = \sum_{i=1}^{N} |\psi_i(\mathbf{r})|^2 . \tag{3.6}$$

To determine v_{eff}, the Hohenberg-Kohn functional is expressed in terms of the kinetic energy T_{S} and Hartree energy U_{H} of the non-interacting many-body system:

$$T_{\mathrm{S}}[\psi[n]] = -\frac{\hbar^2}{2m_e} \sum_{i=1}^{N} \int \nabla \psi_i^*(\mathbf{r}) \nabla \psi_i(\mathbf{r}) \mathrm{d}^3\mathbf{r}, \tag{3.7}$$

$$U_{\mathrm{H}}[n] = \frac{e^2}{2} \int \frac{n(\mathbf{r}) n(\mathbf{r}')}{|\mathbf{r} - \mathbf{r}'|} \mathrm{d}^3\mathbf{r} \mathrm{d}^3\mathbf{r}', \tag{3.8}$$

$$F_{\mathrm{HK}} = T + U = T_{\mathrm{S}} + U_{\mathrm{H}} + E_{\mathrm{xc}}. \tag{3.9}$$

This equation defines the exchange-correlation functional, which includes all the unknown terms arising due to the interaction of the electrons. With this formulation the variation of the energy functional yields an explicit expression of the Kohn-Sham equations:

$$\left(-\frac{\hbar^2}{2m_e}\nabla^2 + e^2\int \mathrm{d}^3\mathbf{r}'\frac{n(\mathbf{r}')}{|\mathbf{r}-\mathbf{r}'|} + v(\mathbf{r}) + \frac{\delta E_{\mathrm{xc}}[n]}{\delta n(\mathbf{r})}\right)\psi_i(\mathbf{r}) = \epsilon_i\psi_i(\mathbf{r}). \tag{3.10}$$

Since the equations depend on the particle density n and, therefore, on ψ_i, this is a self-consistency problem, which has to be solved iteratively.

Starting from a guess for the starting density, which is usually constructed as a superposition of the charge density of isolated atoms, the Kohn-Sham equations are solved. The output density is then mixed with the input density constituting the starting density of the next iteration. This is done until the difference between input and output density is reasonably small.

To make the calculation of the total energy numerically convenient, the kinetic energy can be expressed as

$$T_{\mathrm{S}}(n(\mathbf{r})) = \sum_{i=1}^{N}\epsilon_i - \int v_{\mathrm{eff}}(\mathbf{r})n(\mathbf{r})\mathrm{d}^3\mathbf{r}, \tag{3.11}$$

which avoids the direct calculation of $\nabla\psi_i$ and which leads to

$$E[n] = \sum_{i=1}^{N}\epsilon_i - \int v_{\mathrm{eff}}(\mathbf{r})n(\mathbf{r})\mathrm{d}^3\mathbf{r} + \frac{e^2}{2}\int\frac{n(\mathbf{r})n(\mathbf{r}')}{|\mathbf{r}-\mathbf{r}'|}\mathrm{d}^3\mathbf{r}\mathrm{d}^3\mathbf{r}' + \int v(\mathbf{r})n(\mathbf{r})\mathrm{d}^3\mathbf{r} + E_{\mathrm{xc}}[n]. \tag{3.12}$$

3.1.3 Spin Density Functional Theory and Non-Collinearity

The Hohenberg-Kohn theorem also holds for spin-polarized systems. In this case, the minimization of the energy has to be done with respect to the particle density and, in addition, to the magnetization density $\mathbf{m}(\mathbf{r})$:

$$E[n_0(\mathbf{r}), \mathbf{m}_0(\mathbf{r})] \leq E[n(\mathbf{r}), \mathbf{m}(\mathbf{r})], \tag{3.13}$$

where $n(\mathbf{r})$ and $\mathbf{m}(\mathbf{r})$ are expressed in terms of Pauli spinors:

$$\boldsymbol{\psi}_i(\mathbf{r}) = \begin{pmatrix}\psi_{\uparrow,i}(\mathbf{r})\\ \psi_{\downarrow,i}(\mathbf{r})\end{pmatrix}, \tag{3.14}$$

$$n(\mathbf{r}) = \sum_{i=1}^{N}|\boldsymbol{\psi}_i(\mathbf{r})|^2, \tag{3.15}$$

$$\mathbf{m}(\mathbf{r}) = \mu_{\mathrm{B}}\sum_{i=1}^{N}\boldsymbol{\psi}_i^*\boldsymbol{\sigma}\boldsymbol{\psi}_i. \tag{3.16}$$

Variation of the energy functional then again leads to Kohn-Sham equations:

$$\left(-\frac{\hbar^2}{2m_e}\nabla^2 + v_{\text{eff}}(\mathbf{r}) + \boldsymbol{\sigma}\mathbf{B}_{\text{eff}}(\mathbf{r})\right)\boldsymbol{\psi}_i(\mathbf{r}) = \epsilon_i\boldsymbol{\psi}_i(\mathbf{r}), \tag{3.17}$$

where the effective magnetic field includes the applied external field and a term arising from the variation of the exchange-correlation energy with respect to the magnetization density:

$$\mathbf{B}_{\text{eff}}(\mathbf{r}) = \mathbf{B}_{\text{ext}}(\mathbf{r}) + \mathbf{B}_{\text{xc}}(\mathbf{r}) \tag{3.18}$$

$$\mathbf{B}_{\text{xc}}(\mathbf{r}) = \frac{\delta E_{\text{xc}}[n(\mathbf{r}), \mathbf{m}(\mathbf{r})]}{\delta \mathbf{m}(\mathbf{r})}. \tag{3.19}$$

In the case of collinear magnetism, where the global and the local spin axes coincide and $\mathbf{B}_{\text{xc}}(\mathbf{r}) = B_{\text{xc}}(\mathbf{r})\hat{e}_z$, the spin-up and spin-down channel decouple and the magnetization can be expressed by its absolute value $m(\mathbf{r}) = |\mathbf{m}(\mathbf{r})| = n_\uparrow - n_\downarrow$. One then obtains independent Kohn-Sham equations for each spinor component:

$$\left(-\frac{\hbar^2}{2m}\nabla^2 + v_{\text{eff}}(\mathbf{r}) + B_{\text{xc}}(\mathbf{r})\right)\psi_{\uparrow,i}(\mathbf{r}) = \epsilon_{\uparrow,i}\psi_{\uparrow,i}(\mathbf{r}), \tag{3.20}$$

$$\left(-\frac{\hbar^2}{2m}\nabla^2 + v_{\text{eff}}(\mathbf{r}) - B_{\text{xc}}(\mathbf{r})\right)\psi_{\downarrow,i}(\mathbf{r}) = \epsilon_{\downarrow,i}\psi_{\downarrow,i}(\mathbf{r}). \tag{3.21}$$

Non-collinear systems can be treated based on the density matrix ρ:

$$\rho = \frac{1}{2}n\mathbf{I}_2 + \boldsymbol{\sigma}\cdot\mathbf{m} = \frac{1}{2}\begin{pmatrix} n + m_z & m_x - im_y \\ m_x + im_y & n - m_z \end{pmatrix}, \tag{3.22}$$

where $\boldsymbol{\sigma}$ is vector of the Pauli matrices.

3.1.4 Exchange-Correlation Potentials

No exact expression for the exchange-correlation energy is known so far, which forces one to use approximations to describe these many-body effects. One of the most widespread approximation is the local density approximation (LDA), or, for the spin-polarized case, the local spin density approximation (LSDA). In LSDA the exchange-correlation energy is locally approximated by the exchange-correlation energy of a homogeneous electron gas $\epsilon_{\text{xc}}(n(\mathbf{r}), m(\mathbf{r}))$, which can be calculated numerically:

$$E_{\text{xc}}[n(\mathbf{r}), \mathbf{m}(\mathbf{r})] = \int n(\mathbf{r})\epsilon_{\text{xc}}(n(\mathbf{r}), |\mathbf{m}(\mathbf{r})|)\mathrm{d}^3\mathbf{r}. \tag{3.23}$$

The LSDA approximation, which in principle should be most suitable for systems with slowly varying particle densities, also proved its usefulness in inhomogeneous systems. Albeit, it fails to correctly describe the ground state of some systems, as, for example, the bulk crystal structure of Fe and its magnetic properties. Therefore, a number of additional approximations have been developed. The next logical step is to consider

non-local exchange-correlation effects by including the gradient of the particle density, which is called the generalized gradient approximation (GGA):

$$E_{\mathrm{xc}}^{\mathrm{GGA}}[n_\uparrow, n_\downarrow] = \int f(n_\uparrow, n_\downarrow, \nabla n_\uparrow, \nabla n_\downarrow) \mathrm{d}^3\mathbf{r}. \tag{3.24}$$

With the LDA and GGA approximations one is able to describe a wide range of systems.

3.2 The FLAPW Method

Solving the Kohn-Sham equations is not a straight forward task in practice, since the regions of space are highly inhomogeneous. While the wave functions oscillate fast near the atomic cores, between the atomic cores, in the so-called interstitial region, they are much smoother. This leads to a problem regarding the choice of the basis set in which the wave functions are expanded. The basis has to be chosen in a way that it is computationally feasible and still able to precisely describe all the regions of the system.

Plane waves are well suited as basis sets, since they are orthogonal, diagonal in any power of the momentum operator and, due to their simplicity, easy to implement. However, near the atomic cores plane waves with large wave vectors are needed to precisely describe the fast oscillating wave functions, which makes plane waves computationally inefficient.

The augmented plane wave (APW) method [39] uses optimized basis sets in the different regions of space, i.e., plane waves in the interstitial region and atomic-like orbitals near the atomic cores. A computationally more efficient advancement of the APW method is the linearized augmented plane wave (LAPW) method [40, 41, 42]. The method used in this thesis is the FLAPW method and is implemented in the `FLEUR` code [19], which treats the atomic cores self-consistently, and is, therefore, one of the most precise implementations of DFT.

The `FLEUR` code also offers implementations optimized for different geometries, such as bulk systems, surfaces, or, heavily used in this thesis, one-dimensional (1D) structures. Surfaces and 1D-structures introduce a third region, the vacuum, where exponentially decaying functions are used as basis functions.

In the following, we will briefly introduce the FLAPW method and the `FLEUR` code.

3.2.1 The APW Method

The APW method [39] divides space in two regions: the so-called muffin tins, which are spheres around the atom sites, and the interstitial region, which is the remaining space between the muffin tins. The potential is approximated as spherically symmetric in the muffin-tin spheres and as constant in the interstitial regions:

$$V(\mathbf{r}) = \begin{cases} V_{\mathrm{I}}^0 = \text{const.} & \text{interstitial region} \\ V_\mu(r) & \text{muffin tin } \mu \end{cases} . \tag{3.25}$$

These approximations to the potential are called shape approximations.

The basis functions are chosen as plane waves in the interstitial regions and spherical harmonics $Y_L(\hat{\mathbf{r}})$ in the muffin tins:

$$\varphi_{\mathbf{G}}(\mathbf{k},\mathbf{r}) = \begin{cases} \frac{1}{\sqrt{\Omega}} e^{i(\mathbf{G}+\mathbf{k})\mathbf{r}} & \text{interstitial region} \\ \sum_L A_L^{\mu\mathbf{G}}(\mathbf{k}) u_l(r) Y_L(\hat{\mathbf{r}}) & \text{muffin tin } \mu \end{cases}, \tag{3.26}$$

where $\mathbf{k}$ is the Bloch vector, $\mathbf{G}$ is a reciprocal vector, Ω is the cell volume, L is an abbreviation for the quantum numbers l and m, and $u_l(r)$ is the solution of the separated radial part of the Schrödinger equation for energy parameter ϵ_l:

$$\left(-\frac{\hbar^2}{2m}\frac{\mathrm{d}^2}{\mathrm{d}r^2} + \frac{\hbar^2}{2m}\frac{l(l+1)}{r^2} + V(r) - \epsilon_l\right) r u_l(r) = 0. \tag{3.27}$$

The coefficients $A_L^{\mu\mathbf{G}}$ are determined by the requirement that the basis functions have to be continuous at the boundary of the muffin-tin spheres. This leads to the fact that $A_L^{\mu\mathbf{G}} \propto \frac{1}{u_l(R_\mu)}$, which in turn leads to the so-called asymptotic problem, if $u_l(R_\mu)$ vanishes or becomes small.

Further problems arise due to the fact that the ϵ_l have to be set to the corresponding band energies to yield accurate results. Since the wave functions have to be known to determine the band energies, requiring the ϵ_l to equal the band energies turns the solution of the characteristic equation to a non-linear problem, which is computationally very demanding.

3.2.2 The LAPW Method

The limited variational freedom of the APW method can be extended by doing a Taylor expansion of u_l in terms of energy around ϵ_l [40, 41, 42]:

$$u_l(r,\epsilon) = u_l(r,\epsilon_l) + \frac{\partial}{\partial\epsilon} u_l(r,\epsilon)\bigg|_{\epsilon_l} (\epsilon - \epsilon_l) + O[(\epsilon-\epsilon_l)^2]. \tag{3.28}$$

The Taylor expansion is canceled after the linear term, introducing a quadratic error in the wave function. Due to the variational principle, this introduces an error of the order of $(\epsilon-\epsilon_l)^4$ to the band energies. Because of the high order, the linearization works very well over broad energy regions. The method is then called LAPW. The $\dot{u}_l = \frac{\partial}{\partial\epsilon} u_l$ can be calculated by differentiating Eq. (3.27):

$$\left(-\frac{\hbar^2}{2m}\frac{\mathrm{d}^2}{\mathrm{d}r^2} + \frac{\hbar^2}{2m}\frac{l(l+1)}{r^2} + V(r) - \epsilon_l\right) r\dot{u}_l(r) = r u_l(r). \tag{3.29}$$

To uniquely define u_l, it is useful to normalize u_l:

$$\langle u_l | u_l \rangle = \int_0^{R_\mu} u_l(r)^2 r^2 \mathrm{d}r = 1. \tag{3.30}$$

Taking the energy derivative of Eq. (3.30) shows that with this normalization u_l and $\dot{u}_l$ are orthogonal.

The basis functions in LAPW are chosen as:

$$\varphi_{\mathbf{G}}(\mathbf{k},\mathbf{r}) = \begin{cases} \frac{1}{\sqrt{\Omega}} e^{i(\mathbf{G}+\mathbf{k})\mathbf{r}} & \text{interstitial region} \\ \sum_L A_L^{\mu\mathbf{G}}(\mathbf{k}) u_l(r) Y_L(\hat{\mathbf{r}}) + B_L^{\mu\mathbf{G}}(\mathbf{k}) \dot{u}_l(r) Y_L(\hat{\mathbf{r}}) & \text{muffin tin } \mu \end{cases} . \quad (3.31)$$

The additional variational freedom due to the extra term with coefficients $B_L^{\mu\mathbf{G}}(\mathbf{k})$ now allows to request that not only the basis functions themselves but also theirs derivatives are continuous at the muffin-tin boundary. This also determines $B_L^{\mu\mathbf{G}}(\mathbf{k})$.

In the LAPW method, ϵ_l does not need to be set to the band energies anymore and is treated as a fixed parameter. In addition, the asymptotic problem is solved, since if u_l vanishes at the muffin-tin boundary, $\frac{\partial}{\partial r} u_l$ and $\dot{u}_l$ are in general nonzero. Finally, the LAPW method can be extended to non-spherical potentials due to the large variational freedom offered by the basis functions.

3.2.3 The FLAPW Method

LAPW methods, which use the shape approximation of the potential (Eq. (3.25)), yield accurate results for close-packed metal systems. However, for systems containing open structures, such as surfaces, clusters or monowires, the approximation of a constant potential in the interstitial region and a spherically-symmetric potential in the muffin-tin cores becomes inaccurate.

To handle these kind of systems, the full-potential LAPW method has been developed [15, 16], which does not assume any shape approximations to the potential. The coulomb potential consists of the contribution from the electrons, the Hartree potential V_{H}, and the contribution from the ionic cores V_{i}:

$$V(\mathbf{r}) = V_{\mathrm{H}} + V_{\mathrm{i}}. \quad (3.32)$$

The Hartree potential has to be determined by solving the Poisson equation

$$\Delta V_{\mathrm{H}} = 4\pi\rho(\mathbf{r}). \quad (3.33)$$

The charge density and the potential are represented differently in the different regions of space similar to the basis functions:

$$\rho(\mathbf{r}) = \begin{cases} \sum_{\mathbf{G}} \rho_{\mathbf{G}} e^{i\mathbf{G}\mathbf{r}} & \text{interstitial region} \\ \sum_L \rho_L^{\mu}(r) Y_L(\hat{\mathbf{r}}) & \text{muffin tin } \mu \end{cases} , \quad (3.34)$$

$$V(\mathbf{r}) = \begin{cases} \sum_{\mathbf{G}} V_{\mathbf{G}} e^{i\mathbf{G}\mathbf{r}} & \text{interstitial region} \\ \sum_L V_L^{\mu}(r) Y_L(\hat{\mathbf{r}}) & \text{muffin tin } \mu \end{cases} . \quad (3.35)$$

The potential is then calculated separately for each region of space. This is done by replacing the true muffin-tin charge by a convergent pseudo-charge density that leads to the same potential, i.e., it has the same multipole moments, outside the muffin tin. Then the interstitial potential can be calculated in reciprocal space. After that, the potential in the muffin tins can be computed by solving the Dirichlet boundary value problem defined by the true muffin-tin charge density and the interstitial potential on the muffin-tin boundaries.

3.2.4 Relativistic Effects

The Kohn-Sham equations in the relativistic density functional theory have the form of single-particle Dirac equations:

$$c\alpha\mathbf{p} + (\beta - \mathbf{1})mc^2 + V_{\text{eff}}(\mathbf{r})\mathbf{\Psi} = \epsilon\mathbf{\Psi}, \tag{3.36}$$

where c is the velocity of light,

$$\alpha = \begin{pmatrix} \mathbf{0} & \sigma \\ \sigma & \mathbf{0} \end{pmatrix}, \tag{3.37}$$

$$\beta = \begin{pmatrix} \mathbf{1} & \mathbf{0} \\ \mathbf{0} & -\mathbf{1} \end{pmatrix}, \tag{3.38}$$

and $\mathbf{\Psi}$ is the four-component Dirac spinors. In principle, Eq. (3.36) can be solved for each component utilizing the FLAPW basis. However, that would increase the computational time by a factor of 64.

Therefore, the scalar-relativistic (SR) approximation [43] has been developed, which initially omits the spin-orbit interaction but retains all other relativistic effects for the electrons in the muffin-tin spheres. This is justified by the fact that the kinetic energy of the electrons and, thus, relativistic effects are largest near the nuclei. The vacuum and interstitial region are treated non-relativistically, too.

For the limit of low velocities $v^2/c^2 \ll 1$ of the valence electrons, the Dirac equation can be reduced to the Pauli equation with Pauli Hamiltonian

$$\mathbf{H}_{\text{Pauli}} = \frac{\mathbf{p}^2}{2m} - e\Phi - \frac{\mathbf{p}^4}{8m^3c^2} + \frac{e\hbar^2}{8m^2c^2}\nabla\cdot\mathbf{E} + \frac{e\hbar}{4m^2c^2}\sigma(\mathbf{E}\times\mathbf{p}). \tag{3.39}$$

The first two contributions represent the non-relativistic kinetic and electrostatic energy. Together they form the non-relativistic Hamilton operator. The third and fourth term are the relativistic mass-velocity correction and the Darwin correction, respectively. These terms are independent of the spin $\mathbf{S} = \sigma/2$ and form in combination with the non-relativistic terms the SR Hamiltonian. The last term is the spin-orbit coupling H_{SO}, which can be interpreted as the coupling of the electron spin with the magnetic field created by its own orbital motion around the nucleus.

As mentioned before, SOC effects are strongest around the nuclei where the potential can be approximated to be spherically symmetric and, thus, one can write

$$\mathbf{E} = -\nabla\Phi(\mathbf{r}) = -\frac{\mathbf{r}}{r}\frac{\mathrm{d}\Phi}{\mathrm{d}r}. \tag{3.40}$$

This leads to the spin-orbit Hamiltonian

$$H_{\text{SO}} = \frac{-e\hbar}{4m^2c^2r}\frac{\mathrm{d}\Phi}{\mathrm{d}r}\sigma(\mathbf{r}\times\mathbf{p}) \tag{3.41}$$

$$= \frac{-e\hbar}{4m^2c^2r}\frac{\mathrm{d}\Phi}{\mathrm{d}r}\mathbf{L}\cdot\mathbf{S} \tag{3.42}$$

$$= \xi(r)\mathbf{L}\cdot\mathbf{S}. \tag{3.43}$$

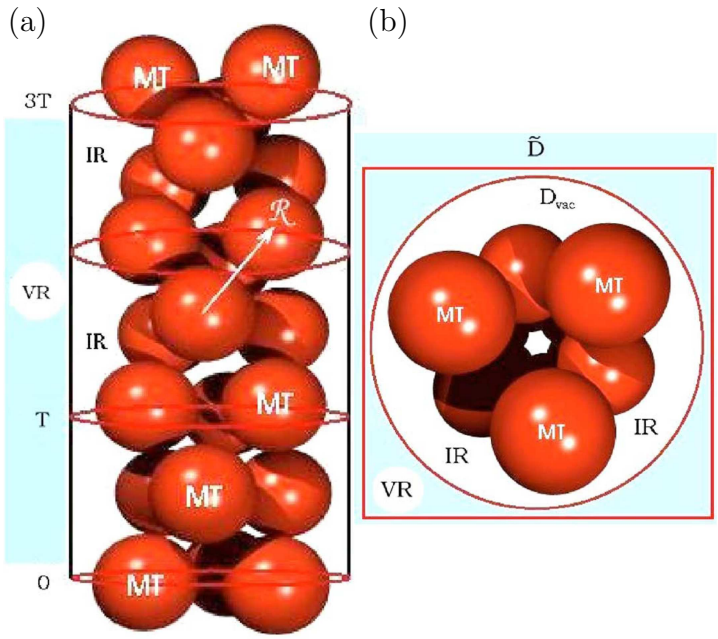

Figure 3.1: (a) Side view of the unit cell of the one-dimensional version of FLEUR and the partitioning into the different regions of space, i.e., the muffin tins (MT), the interstitial region (IR) and the vacuum region (VR) defined by D and $\tilde{D}$. The translational vector T defines the size of the unit cell in z-direction. (b) Top view of the in-plane square unit cell.

In transition metals the magnetism is due to the d electrons. Therefore, one can consider the SOC originating from d electrons and take the radial average of $\xi(r)$ over the d-orbitals:

$$H_{\mathrm{SO}} = \xi \mathbf{L} \cdot \mathbf{S}. \tag{3.44}$$

Assuming $\Phi(r) = -Ze/r$ and using the non-relativistic radial functions $R_{nl}(r) \propto r^l$, one finds

$$\xi_{nl} \propto \langle nl | \frac{1}{r} \frac{Z}{r^2} | nl \rangle \frac{Z^4}{a_{\mathrm{B}}^3} \frac{1}{n^3 l^2}, \tag{3.45}$$

where n and l are the principal and azimuthal quantum numbers, respectively, and a_{B} is the bohr radius. ξ becomes larger for heavier atoms. For $3d$ atoms, ξ is of the order of $50 - 100$ meV and can become as large as about 500 meV for $5d$ elements like Ir.

The term $\mathbf{L} \cdot \mathbf{S}$ describes the angular dependency of the SOC and the matrix elements depend on the quantization axis of the spin $\mathbf{S}$. The dependence of the matrix elements between the various d orbitals for a magnetization direction defined by angles θ and ϕ can be found in Tab. 5.1.

3.2.5 The One-Dimensional Version of the FLEUR Code

The FLEUR code offers a FLAPW implementation with optimized geometries and basis sets for bulk systems, surfaces and 1D structures [20]. Many other codes handle surfaces and 1D structures in a super cell approach:

An isolated monowire running in z-direction is modeled by creating a periodic system of unit cells including one monowire and large spacings in the xy-plane. If the size of the unit cell is large enough, spurious effects due to the interactions of the monowires

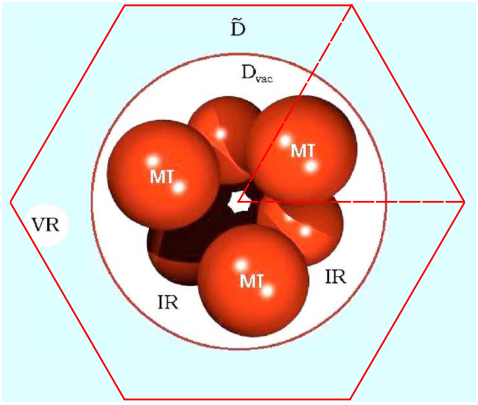

Figure 3.2: Top view of the hexagonal unit cell of the one dimensional version of FLEUR.

are minimized and precise results are achieved. However, the calculations become computationally very demanding due to the large unit cell itself and because a lot of plane waves have to be considered to properly describe the exponential decay of the wave functions between the monowires.

The FLEUR code introduces actual vacuum regions in which the basis sets are exponentially decaying functions and have the optimal cylindrical symmetry:

$$\varphi_{\mathbf{G}}(\mathbf{k},\mathbf{r}) = \begin{cases} \sum_m (A_m^{\mathbf{G}}(k_z) u_m^{G_z}(k_z,r) + B_m^{\mathbf{G}}(k_z)\dot{u}_m^{G_z}(k_z,r)) e^{im\varphi} e^{i(G_z+k_z)z} & \text{vacuum region} \\ \frac{1}{\sqrt{\Omega}} e^{i(\mathbf{G}+\mathbf{k})\mathbf{r}} & \text{interstitial region} \\ \sum_L A_L^{\mu\mathbf{G}}(\mathbf{k}) u_l(r) Y_L(\hat{\mathbf{r}}) + B_L^{\mu\mathbf{G}}(\mathbf{k}) \dot{u}_l(r) Y_L(\hat{\mathbf{r}}) & \text{muffin tin } \mu \end{cases}, \tag{3.46}$$

with $\mathbf{k} = (0, 0, k_z)$. The vacuum region is described in cylindrical coordinates (r, φ, z) and the summation over m goes up to the angular expansion parameter $m_{\max}$, which provides a smooth transition of the wave functions from the interstitial to the vacuum region. Each iteration, for every pair (m, G_z) the vacuum radial basis functions $u_m^{G_z}(k_z, r)$ and their derivatives $\dot{u}_m^{G_z}(k_z, r)$ are obtained by solving the radial Schrödinger equation. The coefficients A_m and B_m for the vacuum regions are determined by the requirement that the basis functions and their derivatives are continuous at the vacuum-interstitial boundary. To determine the potential, the treatment described in subsection 3.2.3 has to be extended to include the new vacuum region. The main idea stays the same and a detailed description can be found in [20]. The vacuum region is defined to be outside a cylinder with radius D_{vac}. In the xy-plane the plane waves of the interstitial region are created in a square lattice with lattice constant $\tilde{D}$, chosen larger than D_{vac} to increase the variational freedom.

Hexagonal vs. Square Unit Cell

The square in-plane unit cell can create problems since the plane wave basis in the interstitial region is created in the square unit cell with length $\tilde{D}$. The square unit cell

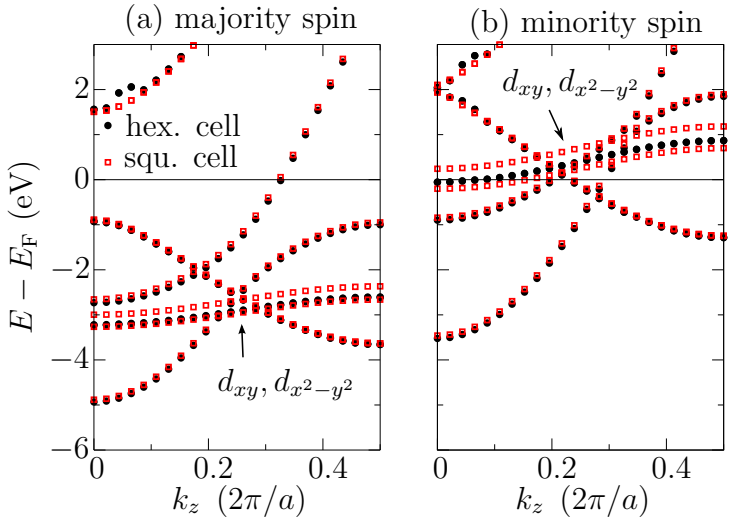

Figure 3.3: (a) and (b) show the bandstructure of a Fe monowire with parameters $D = 4.4$ a.u., $\tilde{D} = 5.5$ a.u., $k_{\max} = 4.8$ a.u., lattice constant $a = 4.18$ a.u., 12 kpoints, and muffin-tin radius 2.0 a.u. using GGA and utilizing the square (red squares) and hexagonal (black filled circles) unit cell for the majority and minority spin channel, respectively.

however does not necessarily have the symmetry of the system under consideration, as in the case of the cylindrical symmetry of monowires. Therefore, depending on the basis, it might happen that the cylindrical symmetry is broken, which leads to an artificial lift of the degeneracy of the d_{xy} and $d_{x^2-y^2}$ states. This can be seen in Fig. 3.3 for a Fe monowire. This problem can be managed by increasing the plane-wave cutoffs. However, this increases the computational time and can also lead to problems in the stability of the method.

Another way to solve this problem for systems with cylindrical symmetry is the use of an hexagonal in-plane unit cell as sketched in Fig. 3.2, which is closer to the cylindrical symmetry. As a part of this thesis, the hexagonal unit cell has been implemented in the 1D-version of `FLEUR`. To do this, the routines considering the symmetry operations had to be adapted. The improvements due to the hexagonal unit cell can be seen in Fig. 3.3. The splitting of $d_{xy}, d_{x^2-y^2}$ states vanishes in the hexagonal cell.

We are now able to obtain a description of the system in terms of delocalized Bloch functions. As a last step, we now need to transform the Bloch functions to localized Wannier functions to be able to set up the Hamilton matrices.

4 Wannier Functions and Construction of the Hamilton Matrices

In the last chapter, we described how we can obtain a description of a solid, surface or monowire in terms of delocalized Bloch functions. In this chapter, we will describe how we can obtain a description in terms of spatially localized Wannier functions. Wannier functions have been introduced by Gregory Wannier in 1937 [44]. For an isolated Bloch state

$$|\psi_{n\mathbf{k}}\rangle = e^{i\mathbf{kr}} u_{n\mathbf{k}} \tag{4.1}$$

with lattice periodic part $u_{n\mathbf{k}}$, wave vector $\mathbf{k}$ and band index n one defines on a discrete $\mathbf{k}$-mesh

$$|\mathbf{R}n\rangle = \frac{1}{\sqrt{N}} \sum_{\mathbf{k}} e^{-i\mathbf{kR}} |\psi_{n\mathbf{k}}\rangle \tag{4.2}$$

$$|\psi_{n\mathbf{k}}\rangle = \frac{1}{\sqrt{N}} \sum_{\mathbf{R}} e^{i\mathbf{kR}} |\mathbf{R}n\rangle \,, \tag{4.3}$$

where $\mathbf{R}$ is a real-space lattice vector and $|\mathbf{R}n\rangle$ is the Wannier function in cell $\mathbf{R}$ with band index n. The equations above constitute a unitary transformation between Bloch and Wannier functions.

Eq. (4.2) leaves a gauge freedom since one can add a $\mathbf{k}$-dependent phase factor $\varphi_n(\mathbf{k})$ to the Bloch functions without changing the physical description of the system:

$$|\tilde{\psi}_{n\mathbf{k}}\rangle = e^{i\varphi_n(\mathbf{k})} |\psi_{n\mathbf{k}}\rangle \,. \tag{4.4}$$

This gauge freedom affects the Wannier functions since different gauges lead to different sets of Wannier functions with different properties, e.g., shapes and spreads. Therefore, this gauge freedom can critically affect the transport properties investigated in this thesis.

Further complications arise in real systems since, in general, one do not have isolated bands but a manifold of J bands. In the most convenient case this manifold of bands is separated from higher bands by a band gap, as, for example, in insulators or semiconductors. In this case, the gauge freedom can be expressed by mixing the bands at wave vector $\mathbf{k}$ via a unitary matrix $U^{(\mathbf{k})}_{mn}$:

$$|\tilde{\psi}_{n\mathbf{k}}\rangle = \sum_{m=1}^{J} U^{(\mathbf{k})}_{mn} |\psi_{n\mathbf{k}}\rangle \,. \tag{4.5}$$

Eq. (4.5) becomes Eq. (4.4) when the $U_{mn}^{(\mathbf{k})}$ are chosen diagonal.

One very successful approach to dissolve the problem of the arbitrariness of the Wannier functions is to demand them to be "maximally localized" [18, 45].

4.1 Maximally Localized Wannier Functions

As a measure of the localization of the Wannier functions, a functional is introduced, which is called the spread of the Wannier functions and which measures the sum of the quadratic spreads of the Wannier functions in the "home" unit cell characterized by the vector $\mathbf{0}$:

$$\Omega = \sum_n \left[\langle \mathbf{0}n|r^2|\mathbf{0}n\rangle - \langle \mathbf{0}n|\mathbf{r}|\mathbf{0}n\rangle^2 \right] = \sum_n \left[\langle r^2\rangle_n - \bar{\mathbf{r}}_n^2 \right]. \tag{4.6}$$

This functional is minimized with respect to the $U_{mn}^{(\mathbf{k})}$, which yields maximally localized Wannier functions (MLWF).

In the case of metals, which are studied extensively in this thesis, further problems arise since the bands of interest are not isolated from other bands. In this case the J bands of interest overlap with other high energy bands reaching into the considered energy window (total number of bands $J_\mathbf{k} \geq J$). Therefore, it is not clear which states to choose at wave vector $\mathbf{k}$ in the Brillouin zone to construct the J Wannier functions. The bands need to be disentangled [46] before the localization procedure introduced above can be applied.

The aim of the disentanglement procedure is to choose the states at each $\mathbf{k}$-point in such a way that the dispersion of the resulting bands is as smooth as possible. The disentanglement procedure is usually done in two steps. The first step is a projection of the wave function on J localized trial orbitals $g_n(\mathbf{r})$:

$$|\phi_{n\mathbf{k}}\rangle = \sum_{m=1}^{J_\mathbf{k}} |\psi_{m\mathbf{k}}\rangle \langle \psi_{m\mathbf{k}}|g_n\rangle =: \sum_{m=1}^{J_\mathbf{k}} |\psi_{m\mathbf{k}}\rangle A_{mn}^{\mathbf{k}}, \tag{4.7}$$

These orbitals are then Löwdin-orthonormalized

$$|\tilde{\psi}_{n\mathbf{k}}\rangle = \sum_{m=1}^{J} |\phi_{m\mathbf{k}}\rangle \left(S_\mathbf{k}^{-1/2}\right)_{mn}, \tag{4.8}$$

where $(S_\mathbf{k})_{mn} = \langle \phi_{m\mathbf{k}}|\phi_{n\mathbf{k}}\rangle$. The projection procedure leads to a smooth subspace since the trial orbitals are localized in real space [18].

The smoothness of the subspace can be further refined by minimizing the gauge invariant part of the spread functional Ω_I:

$$\Omega = \Omega_\mathrm{I} + \tilde{\Omega}, \quad \text{where} \tag{4.9}$$

$$\Omega_\mathrm{I} = \sum_n \left[\langle \mathbf{0}n|r^2|\mathbf{0}n\rangle - \sum_{\mathbf{R}m} |\langle \mathbf{R}m\,|\mathbf{r}|\,\mathbf{0}n\rangle|^2 \right], \tag{4.10}$$

$$\tilde{\Omega} = \sum_n \sum_{\mathbf{R}m\neq\mathbf{0}n} |\langle \mathbf{R}m|\mathbf{r}|\mathbf{0}n\rangle|^2. \tag{4.11}$$

In reciprocal space Ω_{I} can be expressed as

$$\Omega_{\mathrm{I}} = \frac{1}{N} \sum_{\mathbf{k},\mathbf{b}} w_b T_{\mathbf{k},\mathbf{b}}, \tag{4.12}$$

with

$$T_{\mathbf{k},\mathbf{b}} = J - \sum_{m,n} \left| M_{mn}^{(\mathbf{k},\mathbf{b})} \right|^2, \tag{4.13}$$

where N is the number of $\mathbf{k}$-points, $\mathbf{b}$ are vectors connecting $\mathbf{k}$-mesh points with theirs neighbors, w_b are weights arising from discretization procedures, and $M_{mn}^{(\mathbf{k},\mathbf{b})}$ are the overlap matrices:

$$M_{mn}^{(\mathbf{k},\mathbf{b})} = \langle u_{m\mathbf{k}} | u_{n\mathbf{k}+\mathbf{b}} \rangle. \tag{4.14}$$

The subspace is then chosen so that Ω_{I} integrated over the Brillouin zone is minimized.

It is also possible to preserve a chosen set of Bloch states inside the energy window used for the disentanglement. This energy window is called "frozen window" [46].

After the projection and disentanglement process the gauge selection is refined one last time by minimizing $\tilde{\Omega}$, which can be expressed in reciprocal space as:

$$\tilde{\Omega} = \frac{1}{N} \sum_{\mathbf{k},\mathbf{b}} w_b \sum_{m \neq n} \left| M_{mn}^{(\mathbf{k},\mathbf{b})} \right|^2 + \frac{1}{N} \sum_{\mathbf{k},\mathbf{b}} w_b \sum_{n} (-\mathrm{Im} \ln M_{nn}^{(\mathbf{k},\mathbf{b})} - \mathbf{b} \cdot \bar{\mathbf{r}}_n)^2. \tag{4.15}$$

The minimization is done iteratively by variation of $U^{(\mathbf{k})}$. In each iteration the gradient of the spread functional Ω with respect to an infinitesimal gauge transformation is calculated and $U^{(\mathbf{k})}$ is changed accordingly to lead to the minimum of Ω. After the update of $U^{(\mathbf{k})}$ the overlap matrices $M^{(0)(\mathbf{k},\mathbf{b})}$ are updated:

$$M^{(\mathbf{k},\mathbf{b})} = (U^{(\mathbf{k})})^\dagger M^{(0)(\mathbf{k},\mathbf{b})} U^{(\mathbf{k}+\mathbf{b})}, \tag{4.16}$$

and the next iteration begins until the convergence criterion is reached.

The ingredients provided by the FLAPW calculation to calculate the MLWF are the $M^{(\mathbf{k},\mathbf{b})}$ and $A^{(\mathbf{k},\mathbf{b})}$. How these matrices are obtained and how spin-orbit coupling is included within the FLAPW formalism can be found in [47].

The Wannierization, maximal localization, and disentanglement procedure are implemented in the `Wannier90` code [48].

Finally, we now need to formulate the Hamiltonian of the investigated system in terms of the Wannier functions.

4.2 The Wannier Representation of the Hamiltonian

In terms of Bloch functions the Hamiltonian $\hat{H}$ reads:

$$\hat{H} = \frac{1}{N} \sum_{\mathbf{k},n} \epsilon_n(\mathbf{k}) |\psi_{\mathbf{k}n}\rangle \langle \psi_{\mathbf{k}n}|, \tag{4.17}$$

where N is the number of k points and $\epsilon_n(\mathbf{k})$ are the eigenvalues of $\hat{H}$. The Hamiltonian in terms of Wannier functions reads:

$$\hat{H} = \sum_{\mathbf{R}_1 m} \sum_{\mathbf{R}_2 m'} H_{mm'}(\mathbf{R}_1 - \mathbf{R}_2) |\mathbf{R}_1 m\rangle \langle \mathbf{R}_2 m'|, \tag{4.18}$$

where

$$\begin{aligned} H_{mm'}(\mathbf{R}_1 - \mathbf{R}_2) &= \langle \mathbf{R}_1 m | \hat{H} | \mathbf{R}_2 m' \rangle & (4.19)\\ &= \frac{1}{N} \sum_{\mathbf{k}n} \epsilon_n(\mathbf{k}) \langle \mathbf{R}_1 m | \psi_{\mathbf{k}n} \rangle \langle \psi_{\mathbf{k}n} | \mathbf{R}_2 m' \rangle & (4.20)\\ &= \frac{1}{N} \sum_{\mathbf{k}n} \epsilon_n(\mathbf{k}) e^{i\mathbf{k}(\mathbf{R}_1 - \mathbf{R}_2)} \left(U_{mn}^{(\mathbf{k})}\right)^* U_{nm'}^{(\mathbf{k})}. & (4.21) \end{aligned}$$

The hoppings between the Wannier functions can be translated into hoppings between Bloch functions with Eq. (4.2):

$$\begin{aligned} H_{nn'}^{(\mathbf{k})} &= \langle \psi_{\mathbf{k}n} | \hat{H} | \psi_{\mathbf{k}n'} \rangle & (4.22)\\ &= \frac{1}{N} \sum_{\mathbf{R}_1} \sum_{\mathbf{R}_2} e^{i\mathbf{k}(\mathbf{R}_2 - \mathbf{R}_1)} \langle \mathbf{R}_1 n | \hat{H} | \mathbf{R}_2 n' \rangle & (4.23)\\ &= \frac{1}{N} \sum_{\mathbf{R}_1} \sum_{\mathbf{R}_2} H_{nn'}(\mathbf{R}_1 - \mathbf{R}_2) e^{i\mathbf{k}(\mathbf{R}_1 - \mathbf{R}_2)} = \sum_{\mathbf{R}} H_{nn'}(\mathbf{R}) e^{i\mathbf{k}\mathbf{R}}. & (4.24) \end{aligned}$$

An interpolated bandstructure from the Wannier functions can then be calculated by diagonalization of $H_{nn'}^{(\mathbf{k})}$.

4.3 Maximally Localized Wannier Functions, First-Shot Wannier Functions and Others

A major problem with setting up the Hamiltoninan found during the development of this thesis and in Ref. [49] is the assignment of the MLWF to the atoms of the super cell. This especially becomes difficult for systems with many atoms in the super cell and when spin-orbit coupling or non-collinear systems [49] are considered. The problem is that MLWF of orbitals of s character tend to be centered between two atomic sites, which makes it unclear to which atom the Wannier function should be attributed. This further complicates if spin-orbit coupling or non collinearity is present, since this mixes spin-up and spin-down states so that four s-like orbitals can be centered between two atom sites.

In addition, if one wants to compare properties from Hamiltonians utilizing Wannier functions from different FLAPW calculations, one has to be sure that the differences between the results originate from the electronic structure of the FLAPW calculation and not from differences in the gauging of the Wannier functions. For example, if one compares spin-orbit coupling effects in a monowire connecting a molecule between a

magnetization parallel and perpendicular to the monowire axis, one can end up with MLWF with different positions of the centers and different spread sizes although the parameters for the Wannierization are identical. This is caused by the different electronic structures for the two magnetization directions, whereby different states are included during the Wannierization. The properties of the Hamiltonian constructed with these Wannier functions are then not comparable, because they include spurious effects due to the differently gauged Wannier functions. Therefore, one has to choose the setup for both calculations independently, so that the resulting Wannier functions have the same centers and spreads for both setups.

The method introduced in Ref. [49] to solve the problem of attributing s-like orbitals to atom sites are first-shot Wannier functions (FSWF). FSWF are obtained by skipping the minimization of $\tilde{\Omega}$ and only execute the projection and disentanglement procedure. This usually results in Wannier functions centered on atomic sites, but with large spreads ranging from 30 Å to a few hundred Å. This is a convenient method for systems where the dominating hoppings are large. However, as will be shown in Sec. 5.1, for systems where the dominating hoppings are small as in tunnel junctions, the convergence with the included hoppings to neighboring atoms is slow. In these cases MLWF have to be used.

A solution to both problems might be Wannier functions with fixed centers. To fix the centers, a penalty can be added to the spread functional so that the centers are forced to stay at the chosen positions $\mathbf{r}_{0n}$ [50]:

$$\Omega_{\mathrm{FC}} = \Omega + \sum_n \lambda_c(\bar{\mathbf{r}}_n - \mathbf{r}_{0n})^2 = \sum_n \left[\langle r^2\rangle_n - \bar{\mathbf{r}}_n^2 + \lambda_c(\bar{\mathbf{r}}_n - \mathbf{r}_{0n})^2\right]. \tag{4.25}$$

In the case of isolated bands, the implementation is straight-forward and one can force the Wannier functions to be centered at the chosen positions with slightly larger spreads than the maximally localized Wannier functions [50]. However, the formalism does not include the disentangling procedure for entangled bands, which is crucial for the systems investigated in this thesis.

4.4 Construction of the Hamilton Matrices

The Hamilton matrices needed are $\mathbf{H}_{\mathrm{S}}$, $\mathbf{H}_{\mathrm{LS}}$, $\mathbf{H}_{\mathrm{SR}}$, $\mathbf{h}_{\mathrm{L}}$, $\mathbf{h}_{\mathrm{LL}}$, and the analogons for the right lead $\mathbf{h}_{\mathrm{R}}$ and $\mathbf{h}_{\mathrm{RR}}$. As an example we use the Pt system from Chapter 8. A sketch of how the matrices are obtained is displayed in Fig. 4.1.

The starting point are individual `FLEUR` calculations of the perfect lead and the scattering region depicted in Fig. 4.1 (a). The two parts can be connected to one another using the "Locking"-technique [49]. In this example, the primitive cell of the perfect lead contains five atoms and the cell used for the scattering region contains 27 atoms. The Wannierization then yields the hoppings between the atoms.

Depending on the number of hoppings one wants to include in the calculation of the transmission, one has to construct $\mathbf{h}_{\mathrm{L}}$, $\mathbf{h}_{\mathrm{LL}}$, $\mathbf{h}_{\mathrm{R}}$ and $\mathbf{h}_{\mathrm{RR}}$ from the Wannierization of the primitive cell of the perfect leads. Here, the third nearest-neighbor approximation is

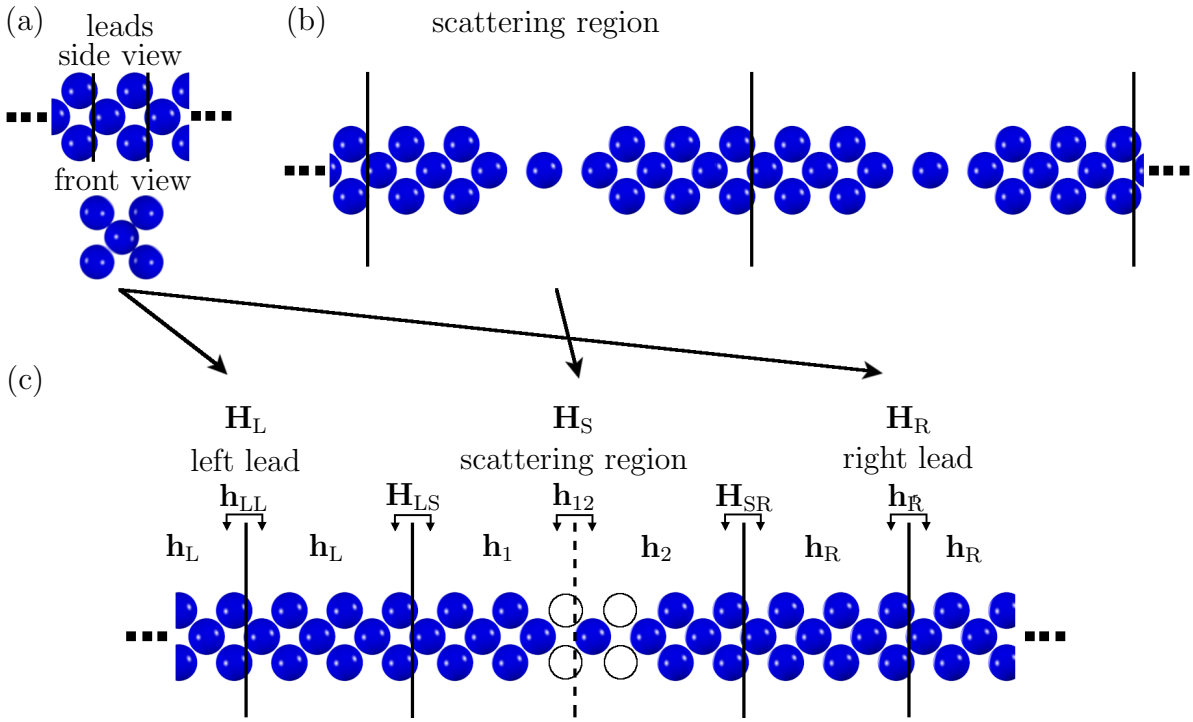

Figure 4.1: (a) Front and side view of the primitive cell used for the calculation of the perfect Pt leads. (b) Side view of the unit cell used to calculate the Pt trimer between two Pt leads. Vertical lines mark the unit cells. (c) Sketch of the geometrical setup of the junction consisting of a Pt trimer connected to Pt leads and of the matrices used to calculate the transmission function. The junction is divided into the scattering region and the left and right lead. The black circles in the scattering region depict "ghost atoms", which are needed to set up the matrices properly.

used. A "neighbor" in this case is considered to be one primitive cell, i.e., five atoms. The super cell of the leads contain 15 atoms as can be seen in Fig 4.1 (b). These matrices are used to calculate the surface green's functions as described in Sec. 2.3.3.

The scattering region is constructed from the FLAPW calculation in the following way. To optimize the numerical treatment, the scattering region is divided into n principal layers as described in Sec. 2.4, which makes $\mathbf{H}_\mathrm{S}$ a tridiagonal matrix

$$\mathbf{H}_\mathrm{S} = \begin{pmatrix} \mathbf{h}_1 & \mathbf{h}_{12} & \mathbf{0} & \mathbf{0} & \mathbf{0} \\ \mathbf{h}_{12}^\dagger & \mathbf{h}_2 & \ddots & \mathbf{0} & \mathbf{0} \\ \mathbf{0} & \ddots & \ddots & \ddots & \mathbf{0} \\ \mathbf{0} & \mathbf{0} & \ddots & \mathbf{h}_{n-1} & \mathbf{h}_{(n-1)n} \\ \mathbf{0} & \mathbf{0} & \mathbf{0} & \mathbf{h}_{(n-1)n}^\dagger & \mathbf{h}_n \end{pmatrix}. \tag{4.26}$$

For the third nearest-neighbor approximation the scattering region is divided into two principal layers labeled 1 and 2 (cf. Fig. 4.1 (c)). Due to the implementation, all matrices need to be quadratic and have the same size. The dimensions of the matrices are $(n_\mathrm{atoms} \cdot n_\mathrm{orb}) \times (n_\mathrm{atoms} \cdot n_\mathrm{orb})$, where n_atoms is the number of atoms in the principal

layer and n_{orb} the number of orbitals per atom. To be able to build matrices with these dimensions for the scattering region, "ghost atoms" are added which are not coupled to any other atoms. In this way the two principal layers of the scattering region sketched in Fig 4.1 (b) now also contain 15 atoms.

The matrices $\mathbf{H}_{\mathrm{LS}}$ and $\mathbf{H}_{\mathrm{SR}}$ can either be taken from the calculation of the scattering region, or can set to be equal to $\mathbf{h}_{\mathrm{LL}}$ and $\mathbf{h}_{\mathrm{RR}}$, respectively.

Hoppings included in the matrices which go beyond the third nearest neighbor have to be set to 0 to avoid spurious effects [49].

5 Tuning the Anisotropic Magnetoresistance in Monowires

The tunneling magnetoresistance and giant magnetoresistance is and has been widely used in hard disk drives, respectively. The TMR and GMR originate from the difference in the conductance for a parallel (G_p) and antiparallel (G_ap) alignment of two ferromagnetic layers. These layers are separated by a tunneling barrier (TMR) or non-magnetic metal (GMR). The first electrode generates a spin-polarized current, while the second electrode acts as a filter on the spin-polarized current allowing to pass through a high current for parallel alignment and a small current for antiparallel alignment. The setup of these two magnetoresistances is sketched in Fig. 5.1 (a). The GMR/TMR can be defined as:

$$\mathrm{GMR/TMR} = 100\% \cdot \frac{G_\mathrm{p} - G_\mathrm{ap}}{G_\mathrm{ap}}. \tag{5.1}$$

Another magnetoresistive effect in bulk transition metals, the AMR, has been experimentally discovered as early as 1857 by Lord Kelvin [2]. A full theoretical description has been provided a century later, where a $\cos^2\Theta$ dependence of the AMR on the angle Θ between magnetization and the current was found. The origin of the AMR was identified to be the anisotropy of the scattering for electrons traveling parallel or perpendicular to the magnetization due to SOC [3]. In bulk materials, the AMR is on the order of a few percents ($\leq 5\,\%$).

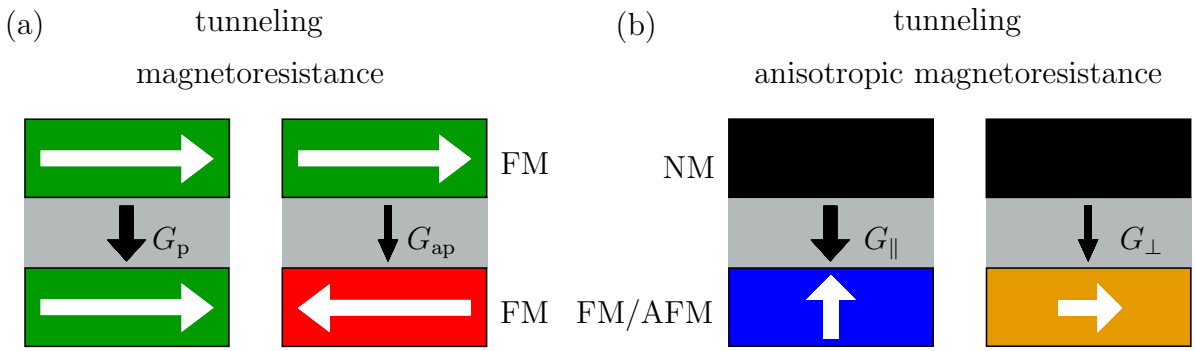

Figure 5.1: (a) Sketch of the tunneling magnetoresistance, which utilizes the difference in the conductance for parallel and antiparallel alignment of two ferromagnetic materials (green and red boxes) separated by a an insulator (gray box), respectively. (b) Sketch of the tunneling anisotropic magnetoresistance, which utilizes the difference in the conductance induced by spin-orbit interaction for the parallel and perpendicular orientation of a magnetic electrode (blue and orange boxes) separated by an insulator from a non-magnetic electrode (black boxes).

In contrast to the GMR/TMR, only one magnetic and one non-magnetic electrode are needed to realize the AMR in a tunneling geometry as sketched in Fig. 5.1 (b), which is advantageous since spin coherence is not needed. Here, the AMR is defined as the difference in the conductance for a parallel ($G_\parallel$) and perpendicular ($G_\perp$) alignment of the magnetization with respect to the current direction

$$\mathrm{AMR} = 100\% \cdot \frac{G_\parallel - G_\perp}{G_\perp}. \tag{5.2}$$

In a tunneling geometry of thin films, the AMR has been first measured in STM experiments probing domains and domain walls of Fe thin films on W(110). It has been explained by spin-orbit induced mixing between minority $d_{xy,xz}$ and minority d_{z^2} states, which can be described by the spin-orbit Hamiltonian introduced in section 3.2.4:

$$\mathbf{H}_{\mathrm{SO}} = \xi \mathbf{L} \cdot \mathbf{S}, \tag{5.3}$$

where ξ is the SOC strength. For the aforementioned orbitals $\langle d_{z^2} | \mathbf{L} \cdot \mathbf{S} | d_{xy,xz} \rangle$ is non-zero for the out-of-plane magnetization in the domains, while it is zero for the in-plane magnetization in the domains. This leads to differences in the local density of states (LDOS) in the vacuum above the two regions, which is detected with the STM [51].

The TAMR has also been found in planar tunnel junctions with ferromagnetic semiconductors [8], and has been explained by SOC induced changes in the LDOS [52, 8]. In both cases, the magnitude of the TAMR is of about 5 %. It was further shown theoretically that resonant surface states may produce sizable TAMR in a Fe(001) surface [53]. Furthermore, one should note that the TAMR in general is sensitive to the applied bias [8, 51, 52, 53].

In the single-atom limit, the TAMR has been measured in Co adatoms on a double-layer Fe film on W(110) by STM finding values of up to 12 % [10]. In break-junction geometries, resonant tip states have been predicted to be the cause of a bias-sensitive TAMR [54]. Further theoretical studies on the TAMR include DFT calculations of an Ir adatom on a double layer of Fe on W(110) [55] and Co, Rh, and Ir adatoms on a non-collinear magnetic surface, namely Mn/W(110) [56].

If the distance between the two electrodes is in the contact regime, the explanation of the AMR via the LDOS breaks down since the orbitals directly overlap and start to hybridize. Therefore, the transmission has to be calculated explicitly. A ballistic anisotropic magnetoresistance (BAMR) has been proposed to occur in the case of an atomic-scale constriction between the electrodes [9]. Monowires show a quantized transmission function, the magnitude of which is determined by the number of modes or bands at a given energy. The BAMR also arises due to SOC induced changes in the electronic structure for a magnetization parallel ($\mathbf{M} \parallel z$) or perpendicular ($\mathbf{M} \perp z$) to the monowire axis (z). In particular, depending on the magnetization direction d-orbitals with different symmetries are allowed to mix (cf. Tab. 5.1). This leads to six bands crossing the Fermi level for $\mathbf{M} \parallel z$, i.e., $G_\parallel = 6\,G_0$ but seven bands for $\mathbf{M} \perp z$, i.e., $G_\perp = 7\,G_0$ and, thus, resulting in a BAMR of about 14 % [9] (cf. Figs. 5.5 (b) and (c)).

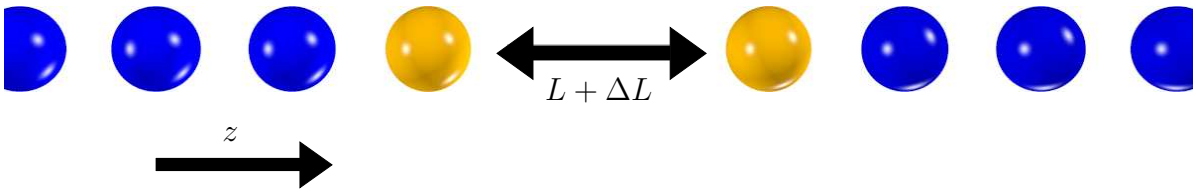

Figure 5.2: Sketch of a symmetric Ni monowire (blue spheres) terminated by Co/Rh/Ir apex atoms (yellow spheres).

Evidence of the BAMR was obtained in break-junction experiments [57]. However, these experiments are difficult to interpret since the exact atomic structure is unknown and ballistic magnetoresistance effects can easily be mimicked by changes of the distances between the atoms due to magnetostriction [58, 59]. In other break-junction experiments, values of BAMR of 25 % to 100 % in the contact regime have been found [60, 61].

Although, it was shown theoretically that it is unlikely that the large magnitude of the BAMR is caused by the quantized transmission since scattering, which is present in each realistic system due to the imperfect geometry or impurities [62, 63, 64, 65], will prevent the transmission function from being ballistic. The scattering especially affects the d-orbitals responsible for the magnetism while the s-orbitals are largely unaffected [62].

Yet, theory predicts that the AMR in single-atom contacts is larger than in bulk systems or on surfaces due to the confined geometry, which limits the number of available conducting modes. The AMR will be the larger the fewer modes are contributing to the transmission function at a given energy since only some of the modes are affected by SOC. The modes not affected by SOC at that energy constitute a background transmission, which limits the size of the AMR.

Further on, it has been shown that the AMR can have a non-trivial and non-monotonic behavior as a function of distance between the apex atoms [65]. However, a localized atomic orbital minimal basis set was used adding SOC in a post-self-consistent approach. No TAMR was found and, therefore, a complete explanation for the different sizes of the AMR in the tunneling and contact regime and its dependence on the bias voltage has not been given yet.

Therefore, in this chapter the AMR in symmetric junctions composed of two Ni monowires terminated by Co, Rh, and Ir apex atoms is investigated. A sketch of the junction can be seen in Fig. 5.2. To study the distance dependence of the AMR, we vary the distance $L + \Delta L$ between the apex atoms from the tunneling to the contact regime and analyze the bias dependence of the AMR at chosen distances ΔL. The chemically different apex atoms compared to the Ni monowire induce scattering, which prevent the transmission from being ballistic in the contact regime. In addition, since the AMR is caused by SOC, the AMR is expected to be the more enhanced the heavier the apex atom. The magnetic moment in the Rh and Ir apex atom is thereby induced by the coupling to the magnetic Ni monowire (MW), while Co is magnetic by itself.

We start by analyzing the AMR of the pure Ni monowire for several spacings and then move on to the Ni monowires terminated by Co, Rh, and Ir apex atoms. We find that the AMR depends sensitively on energy in the tunneling and contact regime. Furthermore,

as a function of distance the AMR at a certain energy can change drastically and even change its sign. This can be understood by the SOC induced mixing and the decay constant of the transition matrix elements between the apex atoms of the d-orbitals, which depend on the orbital symmetry. Finally, we find that the size of the AMR increases for heavier apex atoms reaching values of up to 150 % for Ir. We explain this by analyzing the LDOS, which shows that the increasing SOC constant enhances the mixing of the d-orbitals moving from Co to Rh apex atoms and even induces a spin-mixing for Ir apex atoms at the Fermi level.

The chapter is structured as follows. After introducing the computational details in Sec. 5.1, we discuss the electronic structure and magnetic properties as well as the AMR of Ni monowires in Sec 5.2. Subsequently, in Sec. 5.3 the influence of Co, Rh, and Ir apex atoms on the AMR is analyzed. For a deeper understanding of the origin of the AMR due to SOC induced changes in the electronic structure, we analyze the LDOS in Sec. 5.4. A summary and conclusions are given in the final section.

5.1 Computational Details

Calculations for the Ni monowire leads are preformed in one-atom unit cells with a theoretical lattice constant of 4.18 bohr using 96 k-points in the irreducible Brillouin zone (IBZ) and a value of $k_{\max} = 4.8\,\text{bohr}^{-1}$. The scattering regions are described with symmetric 12-atom unit cells consisting of ten Ni atoms and two apex atoms, which are either Ni, Co, Rh, or Ir. The setup is sketched in Fig. 5.2. Eight k-points in the IBZ and a value of $k_{\max} = 4.6\,\text{bohr}^{-1}$ have been used for the calculation of the scattering region. In all calculations LDA has been used and D and $\tilde{D}$ have been chosen to 8.0 bohr and 9.0 bohr, respectively. The muffin-tin radius has been set to 2.0 bohr for Ni atoms and 2.10, 2.15, and 2.15 bohr for the Co, Rh and Ir atom, respectively. The distance of the Co, Rh, and Ir apex atom to the adjacent Ni atom is fixed to 4.35 bohr.

For the Wannierization of the one-atom unit cell 96 k-points have been used. Five and ten $3d$ orbitals as well as one and two $4s$ orbitals per atom have been used to construct the MLWF out of nine and 20 bands for the SR calculations and calculations with SOC, respectively. For the Wannierization of the 12-atom unit cell eight k-points in the full Brillouin zone have been used. The electronic structure with DFT has been projected on five and ten $3d$ orbitals as well as one and two s orbitals per atom to construct the MLWF out of 90 and 164 bands for the SR and SOC calculations, respectively.

For all calculations a frozen energy window from -5 eV to approximately 2 eV with respect to the Fermi energy has been used, since it was found that this energy window guarantees the desired orbital character of the Wannier functions. The actual value of the upper bound depends on the system.

Hoppings have been taken into account up to the fifth nearest neighbor to obtain converged results for the transmission in the tunneling regime.

During the convergence tests for this system it was found that FSWF converge very slowly in the tunneling regime. In Fig. 5.3 (a, c, e) the transmission obtained with FSWF for a Ni MW with $\Delta L = 2.0$ bohr, 4.0 bohr, and 8.0 bohr, respectively, can be

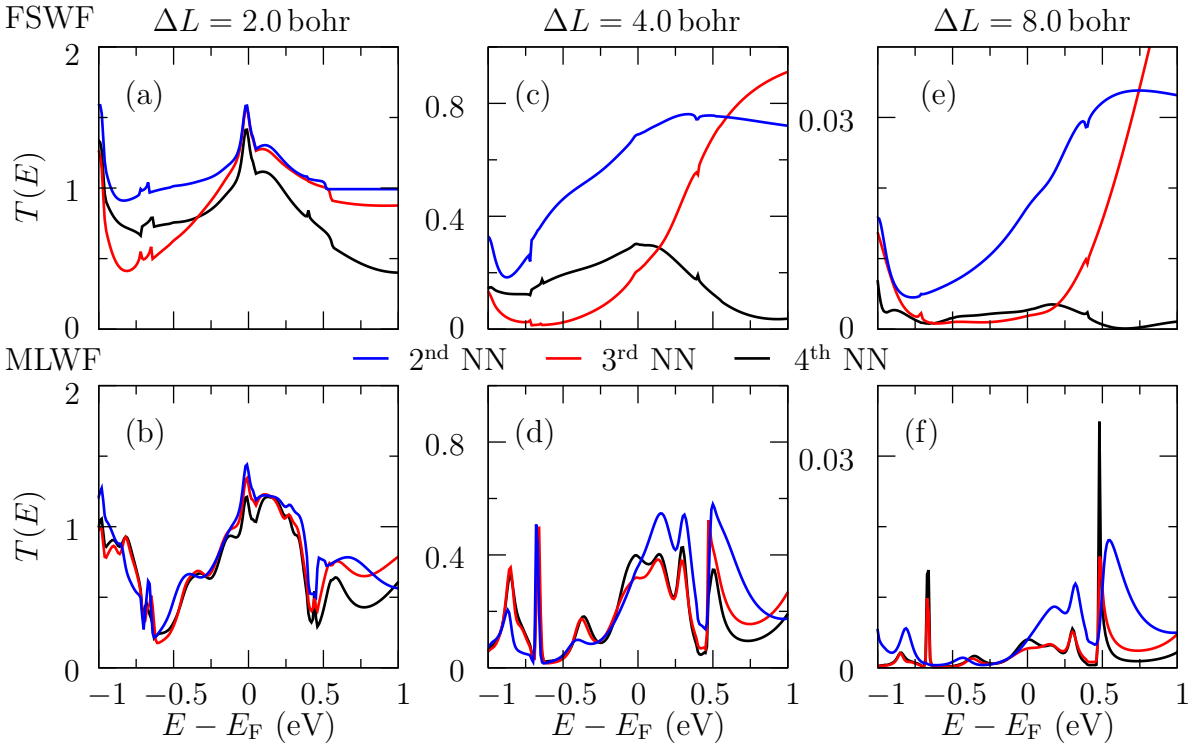

Figure 5.3: (a, c, e) Transmission function of the minority spin channel of a pure Ni monowire in the scalar-relativistic approximation including spacings of $\Delta L = 2.0\,\text{bohr}$, $4.0\,\text{bohr}$, and $8.0\,\text{bohr}$, respectively, obtained by first-shot Wannier functions (FSWF). (b, d, f) shows the same as (a, c, e) obtained with maximally-localized Wannier functions (MLWF). The transmission is obtained in the 2^{nd} (blue line), 3^{rd} (red line), and 4^{th} (black line) nearest-neighbor approximation.

seen. For $\Delta L = 4.0\,\text{bohr}$ and $8.0\,\text{bohr}$ the convergence is very poor, while it is reasonable for $2.0\,\text{bohr}$. The MLWF, on the contrary, converge for all ΔL in Fig. 5.3 (b, d, f).

5.2 Ni Monowire

5.2.1 Electronic Structure and Magnetic Properties

Fig. 5.5 (a) shows the bandstructure of a Ni MW for a SR calculation. The bandstructure calculated utilizing the MLWF taking into account hoppings up to the 5^{th} nearest neighbors shows excellent agreement with the FLAPW calculation. The dispersion of the bands of Δ_1 ($d_{3z^2-r^2}, s$), Δ_3 (d_{zx}, d_{yz}), and Δ_4 (d_{xy}, $d_{x^2-y^2}$) symmetry in Fig. 5.5 (a) can be understood by comparing with the shapes of the orbitals in Fig. 5.4. The overlap of the Δ_1-orbitals in z-direction is large leading to a large dispersion. For the Δ_3-orbitals the dispersion is smaller due to the canted orientation with respect to the z-axis. The Δ_4-orbitals finally are localized mainly perpendicular to the z-axis and, therefore, show a very flat dispersion. The spin-splitting of the bands leads to a magnetic moment of about 1.1 μ_{B} per Ni atom.

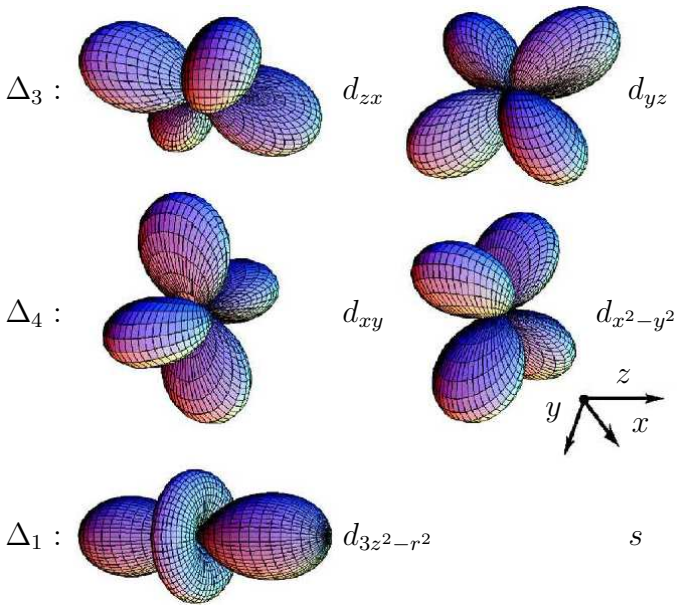

Figure 5.4: Sketches of the d-orbitals of different symmetry. The orbitals are grouped together according to their symmetry: $\Delta_1(d_{3z^2-r^2}, s)$ (s not shown), Δ_3 (d_{zx}, d_{yz}), and Δ_4 (d_{xy}, $d_{x^2-y^2}$). Taken from Ref. [66].

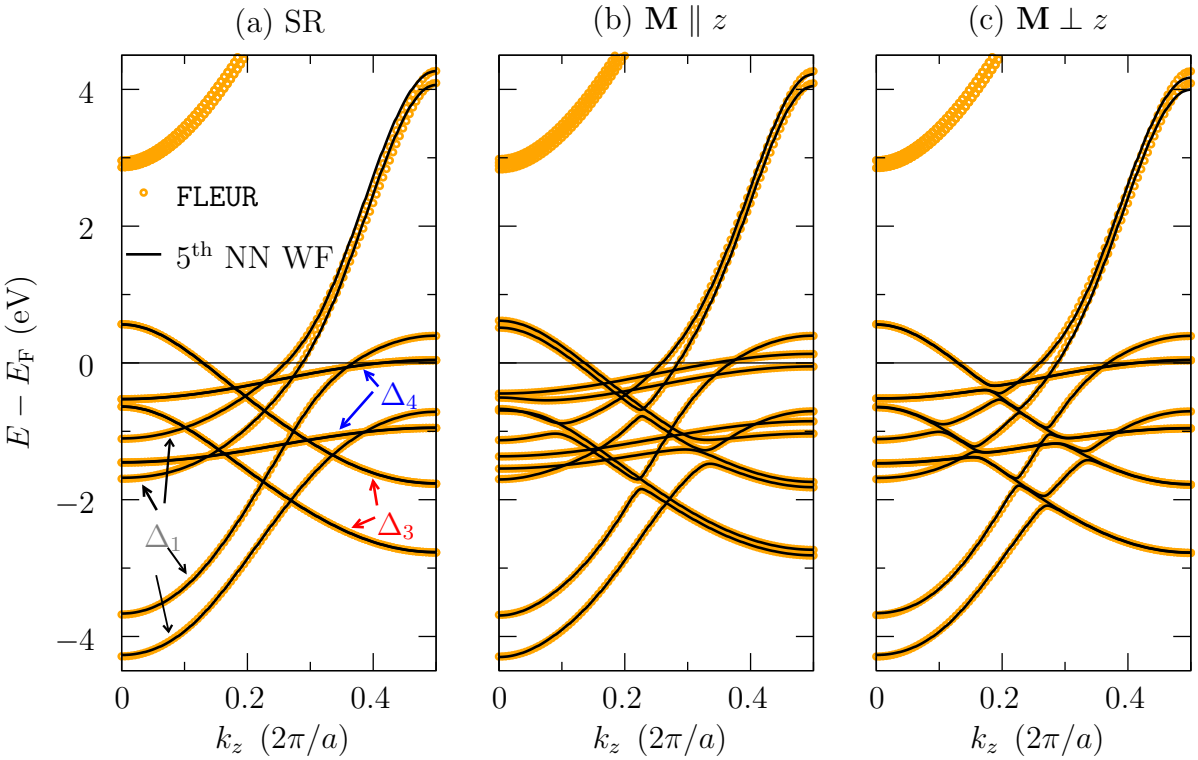

Figure 5.5: Bandstructure of a Ni monowire in (a) a scalar-relativistic calculation, and in calculations including SOC with (b) $\mathbf{M} \parallel z$ and (c) $\mathbf{M} \perp z$. The orange circles show the result of the FLAPW calculation and the black solid line the 5th nearest neighbor (NN) MLWF interpolation.

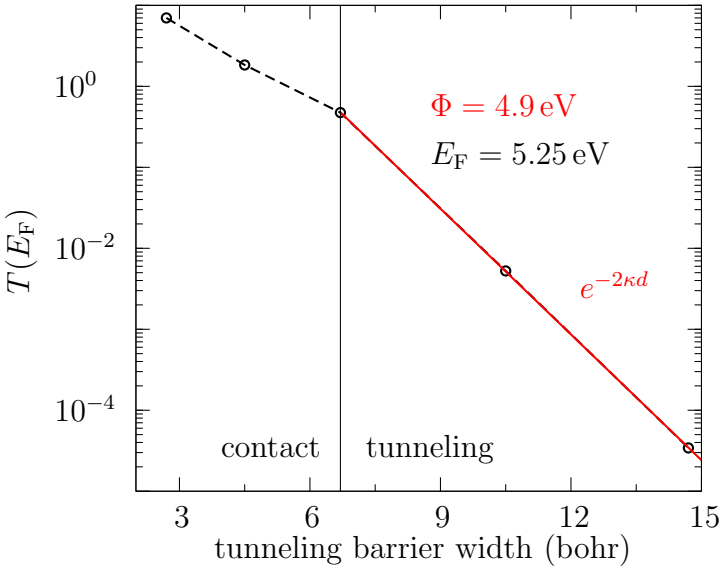

Figure 5.6: Transmission at the Fermi energy with increasing width d of the tunneling barrier between Ni MWs (see text for details) in the SR approximation. The solid line is a fit with an exponentially decaying function. The change of slope at 6.8 bohr marks the transition from the tunneling to the contact regime.

If we now consider SOC and a magnetization parallel ($\mathbf{M} \parallel z$) and perpendicular ($\mathbf{M} \perp z$) to the z-axis in Fig. 5.5 (b, c), several differences between the bandstructures of the two magnetization directions can be seen. SOC causes the matrix elements between the 3d-orbitals to be non-zero depending on the magnetization direction according to Tab. 5.1. In k-space, this hybridization leads to mixing of states with the same k affecting them the stronger the closer the k-states are in energy. For example, the minority Δ_4-bands crossing the Fermi level, which are degenerate in the SR approximation, are degenerate for $\mathbf{M} \perp z$ but not for $\mathbf{M} \parallel z$. The same holds for the Δ_3-bands. Furthermore, several level crossings between Δ_4- and Δ_3-bands, e.g., at $-0.5\,\text{eV}$, $-1\,\text{eV}$, and $-1.5\,\text{eV}$ below the Fermi level, which are present for the SR calculation, become avoided level crossing when SOC is included.

The magnetocrystalline anisotropy energy (MAE) ($E_\parallel - E_\perp$) amounts to 15 meV/atom in favor of the parallel orientation in good agreement with Ref. [67]. For $\mathbf{M} \parallel z$ the spin and orbital moments per Ni atom amount to $1.1\,\mu_B$ and $0.6\,\mu_B$, respectively, and for $\mathbf{M} \perp z$ the values of the spin and orbital moments are $1.1\,\mu_B$ and $0.1\,\mu_B$, respectively.

If now a spacing $\Delta L = 2.0$ bohr is introduced between two Ni atoms of the MW, the spin and orbital moments of the apex atom do not change strongly and amount to $1.1\,\mu_B$ ($1.1\,\mu_B$) and $0.7\,\mu_B$ ($0.3\,\mu_B$), respectively, for $\mathbf{M} \parallel z$ ($\mathbf{M} \perp z$). The MAE increases slightly to 16 meV/atom in favor of the parallel orientation. Further enlargement of ΔL does not change the spin and orbital moments or the MAE considerably.

After having established the general electronic and magnetic properties, we now analyze the transport properties. Figure 5.6 shows the transmission at the Fermi energy (E_F) for increasing width d of the tunneling barrier[1] obtained from SR calculations. One can use the change of the slope around $d = 6.8$ bohr, which corresponds to $\Delta L = 4.0$ bohr,

[1]The width of the tunneling barrier has been determined by evaluating the width of the Coulomb potential determined by the intersection of the Coulomb potential with the Fermi energy. Using this actual width of the tunneling barrier yields a slightly better fit compared to simply using ΔL.

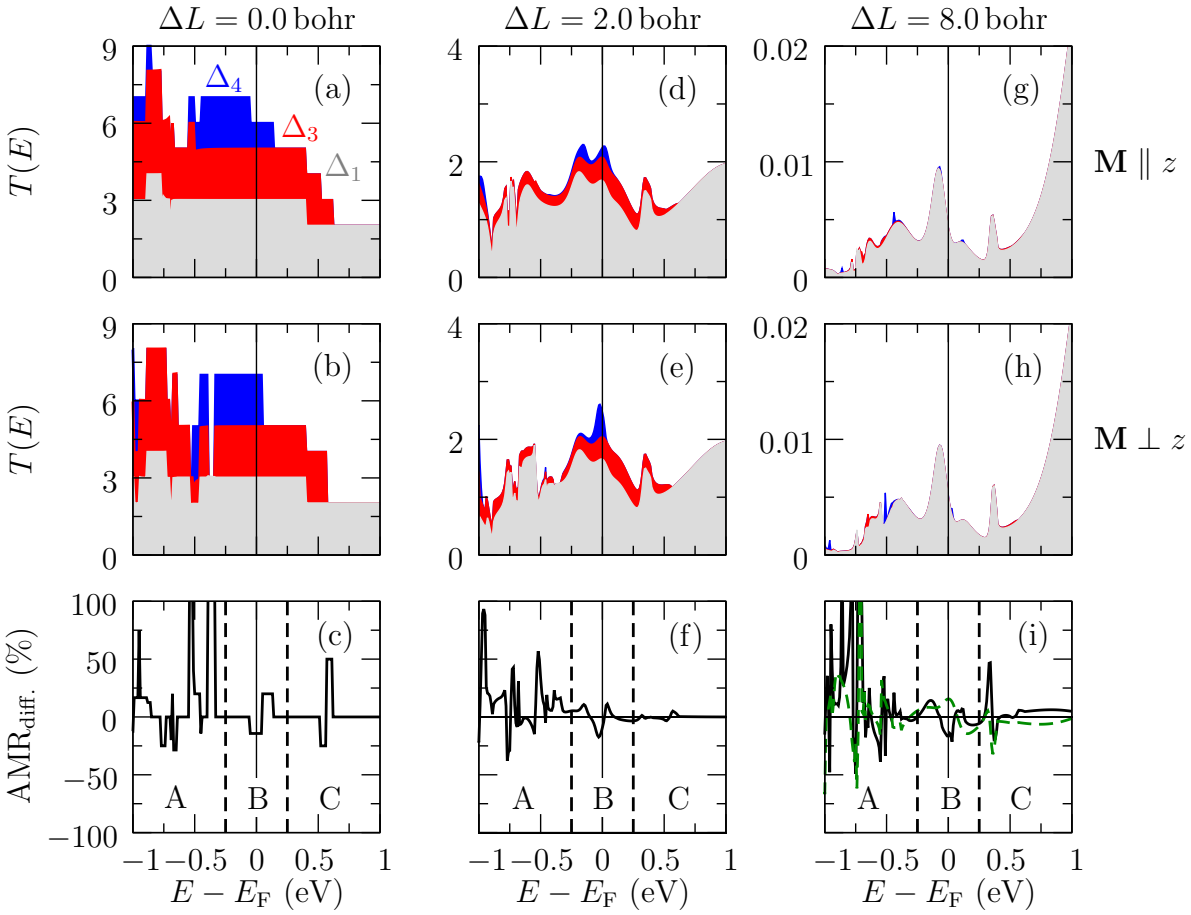

Figure 5.7: (a-c) shows the transmission function for $\mathbf{M} \parallel z$ and $\mathbf{M} \perp z$ as well as the $\mathrm{AMR}_{\mathrm{diff.}}$ of a Ni MW for $\Delta L = 0.0\,\mathrm{bohr}$. (d-f) shows the same for $\Delta L = 2.0\,\mathrm{bohr}$ and (g-i) for $\Delta L = 8.0\,\mathrm{bohr}$. Blue, red and gray color indicate the contribution of orbitals with Δ_1-, Δ_3-, and Δ_4-symmetry to the transmission function, respectively. The dashed line in panel (i) depicts the anisotropy of the Δ_1-LDOS at the apex atom calculated according to Eq. (5.5).

to determine the boundary between the contact and tunneling regime [68]. The transmission in the tunneling regime displays an exponential decay $\propto e^{-2\kappa d}$ with $\kappa = \sqrt{2m\Phi/\hbar^2}$. Fitting the data yields a work function $\Phi = 4.9\,\mathrm{eV}$ in reasonable agreement with the Fermi energy of 5.25 eV of the FLAPW calculation.

5.2.2 Energy Dependence of the AMR

To investigate the energy-dependence of the AMR in the contact regime, we now focus on $\Delta L = 2.0\,\mathrm{bohr}$ and 8.0 bohr.

Figs. 5.7 (a, b) show the orbital-decomposed transmission around the Fermi energy for the perfect Ni MW showing the expected step function of the ballistic regime corresponding to the number of bands at each energy (cf. Fig. 5.5). At the Fermi level in Fig. 5.7 (c) one sees the originally proposed ballistic AMR due to the Δ_4-bands, the degeneracy of which is lifted due to SOC for $\mathbf{M} \parallel z$ but not for $\mathbf{M} \perp z$. The energy-

dependent AMR shown here is defined via the transmission function, which corresponds to the differential conductance, and is defined as

$$\mathrm{AMR}_{\mathrm{diff.}} = 100\% \cdot \frac{T_{\parallel} - T_{\perp}}{T_{\perp}}. \tag{5.4}$$

To simplify further discussions, we divide the energy range in three regions naturally defined by the orbitals which are responsible for the majority of the $\mathrm{AMR}_{\mathrm{diff.}}$ in that energy. Region A extends from $-1\,\mathrm{eV}$ to $-0.25\,\mathrm{eV}$ below E_{F} and contains primarily the $\mathrm{AMR}_{\mathrm{diff.}}$ mainly due to mixing of Δ_1-bands with bands of other symmetries reaching values from 10 % to 100 %. Region B extends from $-0.25\,\mathrm{eV}$ to $0.25\,\mathrm{eV}$ around E_{F} and includes the $\mathrm{AMR}_{\mathrm{diff.}}$ due to mixings involving the Δ_4-bands reaching values of about 20 %. Region C extends from $0.25\,\mathrm{eV}$ to $1\,\mathrm{eV}$ above the Fermi level and comprises the $\mathrm{AMR}_{\mathrm{diff.}}$ originating from mixings of the Δ_3-bands reaching values of about 50 %.

If elastic scattering is introduced by setting $\Delta L = 2.0\,\mathrm{bohr}$, Fig. 5.7 (d-f), the transmission function broadens and especially the contribution from the Δ_3- and Δ_4-orbitals reduces. The $\mathrm{AMR}_{\mathrm{diff.}}$ in regions B and C now only shows magnitudes of about 10 % due to the reduced contribution of the Δ_3- and Δ_4-orbitals. The $\mathrm{AMR}_{\mathrm{diff.}}$ in region A shows a similar shape and the same or slightly decreased magnitude as in the perfect wire. An additional effect in the $\mathrm{AMR}_{\mathrm{diff.}}$ can be seen in region C slightly below $0.5\,\mathrm{eV}$, which originates from the band edge of the Δ_1-band. The results for the perfect MW and a spacing of $\Delta L = 2.0\,\mathrm{bohr}$ are in agreement with Ref. [65].

Eventually, for $\Delta L = 8.0\,\mathrm{bohr}$, Fig. 5.7 (g-i), only the Δ_1-bands contribute to the transmission function. Therefore, the effects in region B and C and at E_{F} originating from the Δ_3- and Δ_4-bands vanish completely and the comparison with the anisotropy of the LDOS of the Δ_1-symmetry bands at the apex atom calculated via

$$\mathrm{AMR}_{\mathrm{LDOS}} = 100\% \cdot \frac{\mathrm{LDOS}_{\parallel} - \mathrm{LDOS}_{\perp}}{\mathrm{LDOS}_{\perp}} \tag{5.5}$$

reproduces the $\mathrm{AMR}_{\mathrm{diff.}}$ quite well, Fig. 5.7 (i). In the tunneling regime, our results differ from the ones obtained in Ref. [65], where no AMR was found at all in the area from $-0.3\,\mathrm{eV}$ below to $0.3\,\mathrm{eV}$ above the Fermi energy. These differences can be attributed to the localized basis set and the post-self-consistent approach to add SOC used in Ref. [65]

5.3 Different Apex Atoms

5.3.1 Magnetic Properties and AMR

We now replace the apex atom of the two Ni monowires with Co, Rh and Ir apex atoms and analyze the electronic, magnetic and transport properties of our symmetric junctions (cf. Fig. 5.2).

Figs. 5.8 (a) and (b) show the spin and orbital moment of the different apex atoms as a function of ΔL for $\mathbf{M} \parallel z$ and $\mathbf{M} \perp z$. The spin moment of the Co apex atom, which is magnetic by itself, stays constant at $2.2\,\mu_B$ for all values of ΔL. The orbital

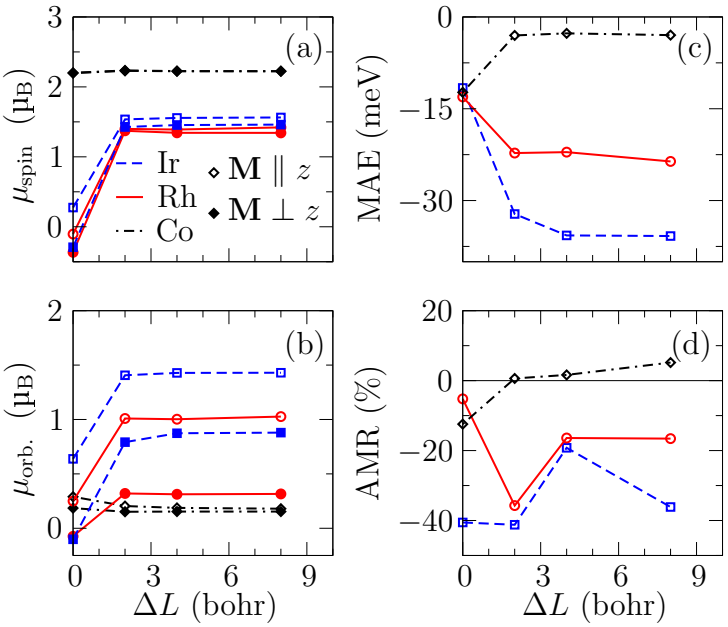

Figure 5.8: (a) Spin (b) and orbital moments of the apex atoms, (c) MAE, and (d) AMR of the conductances for $\mathbf{M} \parallel z$ and $\mathbf{M} \perp z$ obtained by integrating the transmission function from -50 meV below to $+50$ meV above the Fermi level of the symmetric junctions of two Ni monowires terminated by Co (dashed-dotted line), Rh (dashed line), and Ir (solid line) apex atoms as a function of ΔL. The spin and orbital moment for $\mathbf{M} \parallel z$ and $\mathbf{M} \perp z$ are marked with empty and filled symbols, respectively.

moment decreases slightly from $0.29\,\mu_B$ to $0.20\,\mu_B$ when moving from $\Delta L = 0.0$ bohr to 2.0 bohr and stays constant for larger spacings afterwards. For the Rh and Ir apex atoms a qualitatively very similar behavior can be observed. For Rh (Ir) at $\Delta L = 0.0$ bohr the spin moment is $-0.1\,\mu_B$ ($0.27\,\mu_B$) and $-0.36\,\mu_B$ ($-0.29\,\mu_B$) for $\mathbf{M} \parallel z$ and $\mathbf{M} \perp z$, respectively. For $\Delta L = 2.0$ bohr the value for Rh (Ir) rises to $1.39\,\mu_B$ ($1.53\,\mu_B$) and $1.37\,\mu_B$ ($1.42\,\mu_B$) for $\mathbf{M} \parallel z$ and $\mathbf{M} \perp z$, respectively, and after that stays stable with increasing spacing ΔL. A similar trend can be seen for the orbital moments: For Rh (Ir) the orbital moment jumps from $0.24\,\mu_B$ ($0.63\,\mu_B$) to $1.0\,\mu_B$ ($1.4\,\mu_B$) and $-0.07\,\mu_B$ ($-0.1\,\mu_B$) to $0.32\,\mu_B$ ($0.79\,\mu_B$) for $\mathbf{M} \parallel z$ and $\mathbf{M} \perp z$, respectively.

This can be understood in the following way. For large distances between the apex atoms the Rh and Ir apex atoms are polarized by the nearest-neighbor Ni atom. However, for small distances the interaction between the two apex atoms leads to a quenching of their magnetic moments. Quenching of the magnetic moment for small lattice constants in pure Rh and Ir monowires has also been observed in Ref. [69].

The MAE in Fig. 5.8 (c) follows the difference of the orbital moments for the two magnetization directions in accordance with the Bruno model [70]. A value of 15 meV/atom is found for $\Delta L = 0.0$ bohr for all apex atoms, which is very close to the value for the pure Ni MW. For larger spacings, a value of 2.5 meV/atom, 23 meV/atom, and 37 meV/atom is found for Co, Rh and Ir apex atoms, respectively. The large MAE found for the Ir apex atoms is consistent with Ref. [71], where it has been observed that NiIr alloys can exhibit very large anisotropy energies.

Fig. 5.8 (d) shows the AMR of the conductances obtained by integrating the transmission function from -50 meV below to 50 meV above the Fermi level. As for the MAE, the AMR is largest for Ir apex atoms, followed by Rh and then Co apex atoms. The AMR of the Co apex atom shows a change of sign between $\Delta L = 0.0$ bohr and $\Delta L = 2.0$ bohr and stays constant afterwards. The same can be seen for the AMR

of the Rh apex atom, albeit there is an additional large change of the AMR between $\Delta L = 2.0\,\text{bohr}$ and $\Delta L = 4.0\,\text{bohr}$. For Ir, an additional jump of the AMR occurs between $\Delta L = 4.0\,\text{bohr}$ and $\Delta L = 8.0\,\text{bohr}$. This behavior of the AMR for the Co, Rh and Ir apex atom is consistent with the fact, that the $3d$, $4d$, and $5d$ orbitals increase in spread and, therefore, $4d$ and $5d$ orbitals still contribute to the conductance at larger ΔL, while the $3d$ orbitals do not. Since the AMR is mainly created by the d-orbitals, this is reflected by an AMR which is more sensitive to ΔL.

5.3.2 Energy Dependence of the AMR

After having established the magnetic and transport properties for the Ni monowire terminated by different apex atoms, we focus on one point in the contact ($\Delta L = 2.0\,\text{bohr}$) and one in the tunneling ($\Delta L = 8.0\,\text{bohr}$) regime to study the energy dependence of the AMR.

Contact Region

Figs. 5.9 (a, b) shows the transmission function for $\mathbf{M} \parallel z$ and $\mathbf{M} \perp z$ for $\Delta L = 2.0\,\text{bohr}$ of a Ni MW junction with Co apex atoms. The first thing to notice are the missing contributions from Δ_4-bands in the transmission for both magnetization directions. This is due to the weak coupling to the Δ_4-bands of the Ni leads and the small overlap of the Δ_4-orbitals of the two Co apex atoms across the gap. Therefore, in Fig. 5.9 (c) no $\text{AMR}_{\text{diff.}}$ is observed in region B in contrast to the pure Ni MW with $\Delta L = 2.0\,\text{bohr}$ (cf. Fig. 5.7 (f)). Besides that, the $\text{AMR}_{\text{diff.}}$ shows strong similarities in shape and magnitude to the one of the pure Ni monowire with $\Delta L = 2.0\,\text{bohr}$. Similar shapes and magnitudes of the $\text{AMR}_{\text{diff.}}$ as for the Ni MW due to Δ_3-bands can be seen in region C as well as due to the mixing of Δ_1-bands with bands of Δ_3- and Δ_4-symmetry in region A. The enhancement in region C originates from the fact that the contribution of the Δ_3-bands to the transmission function is enhanced in that energy region compared to the pure Ni MW.

For the Rh apex atom, Figs. 5.9 (d-f), the shape of the $\text{AMR}_{\text{diff.}}$ in region A remains similar to the Ni MW, although its magnitude increases and the peaks are broader due to the enhanced SOC. In region B, the $\text{AMR}_{\text{diff.}}$ reaches values of up to $-50\,\%$ due to the Δ_4-contributions and in region C up to $50\,\%$ due to the Δ_3-bands. This is also caused by the aforementioned enhanced SOC and the larger spread of the $4d$-orbitals of Rh compared to the $3d$-orbitals of Co, which leads to larger overlaps of the orbitals of the Rh apex atoms and, therefore, larger contributions to the transmission function reaching values of more than 3 (cf. Figs. 5.9 (d, e)).

This trend continues for Ir apex atoms (Figs. 5.9 (g-i)), where also an $\text{AMR}_{\text{diff.}}$ of up to $-50\,\%$ due to the Δ_4-orbitals is found in region B and even of up to $70\,\%$ caused by the Δ_3-orbitals in region C. Below the Fermi level we observe a very similar shape and magnitude of the $\text{AMR}_{\text{diff.}}$ as for Rh.

In summary, we find that the changes induced by the different apex atoms on the $\text{AMR}_{\text{diff.}}$ originating from Δ_1-bands in region A is relatively small and that it is similar

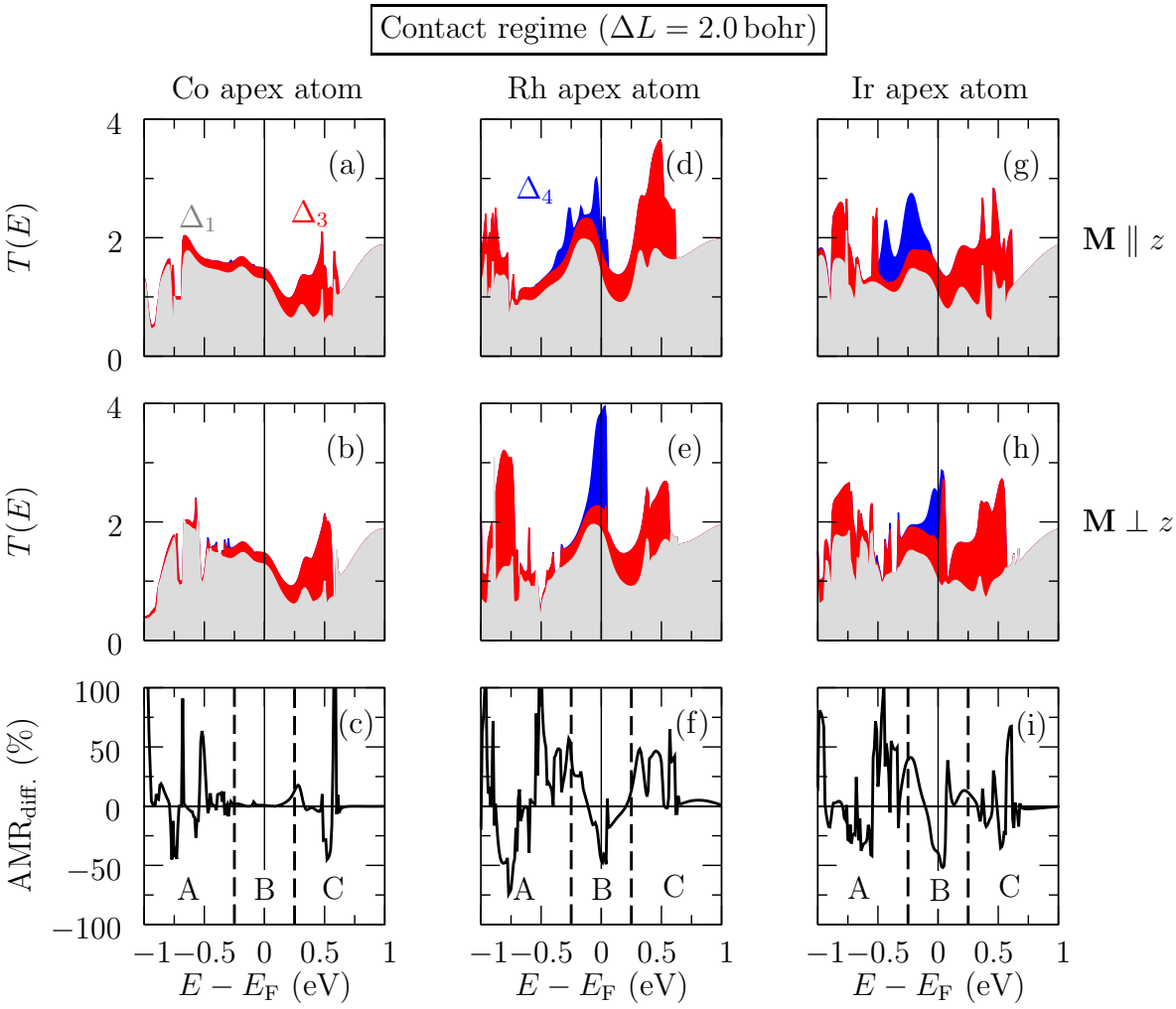

Figure 5.9: (a-c) shows the transmission function for $\mathbf{M} \parallel z$ and $\mathbf{M} \perp z$ and the $\mathrm{AMR}_{\mathrm{diff.}}$ of a Ni MW with Co apex atoms and a spacing of $\Delta L = 2.0$ bohr. (d-f) shows the same of a Ni MW with Rh apex atoms and (g-i) with Ir apex atoms. Blue, red and gray color indicates the contribution of orbitals with Δ_1, Δ_3, and Δ_4-symmetry to the transmission function, respectively.

in shape and magnitude for all apex atoms. The $\mathrm{AMR}_{\mathrm{diff.}}$ due to the more localized Δ_3- and Δ_4-bands in region B and C is much more affected by the apex atom. The fact that the $\mathrm{AMR}_{\mathrm{diff.}}$ caused by the more localized orbitals is stronger affected by the apex atom, which constitutes an impurity to the Ni MW, is consistent with the findings of Ref. [62]. The $\mathrm{AMR}_{\mathrm{diff.}}$ in shows both signs in region A, while it prefers mainly negative values in region B and positive values in region C.

A more detailed discussion of the hybridizations of the Δ_3- and Δ_4-bands can be found in Sec. 5.4.

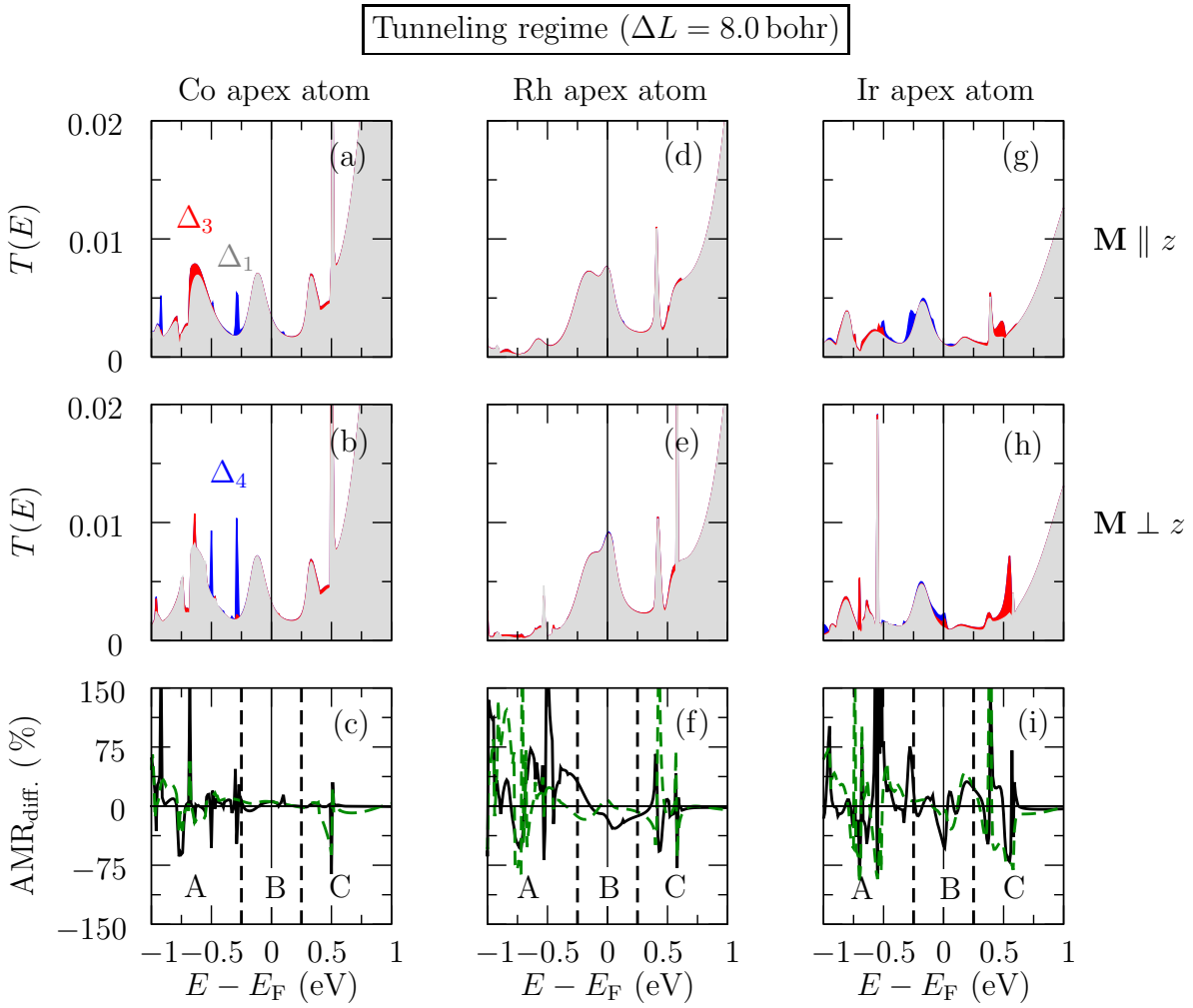

Figure 5.10: (a-c) shows the transmission function for $\mathbf{M} \parallel z$ and $\mathbf{M} \perp z$ as well as the $\mathrm{AMR}_{\mathrm{diff.}}$ of a symmetric junction consisting of two Ni MWs terminated by Co apex atoms and a spacing of $\Delta L = 8.0$ bohr. (d-f) shows the same with Rh apex atoms and (g-i) with Ir apex atoms. Blue, red and gray color indicates the contribution orbitals with Δ_1, Δ_3, and Δ_4-symmetry to the transmission function, respectively. The dashed green line in (c), (f), and (i) depicts the anisotropy of the Δ_1-LDOS at the apex atom calculated analogous to the $\mathrm{AMR}_{\mathrm{diff.}}$.

Tunneling Region

Figs. 5.10 (a, b) show the transmission functions for $\mathbf{M} \parallel z$ and $\mathbf{M} \perp z$ with $\Delta L = 8.0$ bohr for Co apex atoms. Clearly, the Δ_1-states dominate the transmission and only below the Fermi energy one finds sharp features of the Δ_3- and Δ_4-bands reminiscent of the tip resonances found in Ref. [54]. In region A, the $\mathrm{AMR}_{\mathrm{diff.}}$ of the Co apex atoms in Fig. 5.10 (c) has a similar shape as the $\mathrm{AMR}_{\mathrm{diff.}}$ in contact (cf. Fig.5.9 (c)), which can be explained by its primary origin from the Δ_1-bands. In region C, one observes a similar feature as in the $\mathrm{AMR}_{\mathrm{diff.}}$ for $\Delta L = 2.0$ bohr, although much sharper, of smaller magnitude and favoring negative values. The reason for this change is that the

$AMR_{diff.}$ in region C in contact is caused by the Δ_3-bands, which do not contribute to the transmission function in the tunneling regime. Therefore, one sees the $AMR_{diff.}$ caused by the Δ_1-bands at this energy. The $AMR_{diff.}$ is well reproduced by the anisotropy of the LDOS (Eq. (5.5)) of the Δ_1-states at the apex atom. Only the peaks at $-0.25\,\mathrm{eV}$ and $-0.5\,\mathrm{eV}$ below the Fermi level are not reproduced due to their origin from orbitals with Δ_4-symmetry.

In Figs. 5.10 (d, e) the transmission functions for $\mathbf{M} \parallel z$ and $\mathbf{M} \perp z$ for the Rh apex atoms with $\Delta L = 8.0\,\mathrm{bohr}$ also show no contribution of the Δ_3- and Δ_4-bands. The transmission due to the Δ_1-states displays a large double peak around the Fermi energy and generally a very different shape compared to the one of the Co apex atoms. As for Co apex atoms, the $AMR_{diff.}$, Fig. 5.10 (f), in region A is very similar to the $AMR_{diff.}$ in contact (cf. Fig. 5.9 (f)). Region B, where the $AMR_{diff.}$ is caused by the Δ_4-bands in the contact region, now shows a small and broad $AMR_{diff.}$ due to the Δ_1-orbitals. In region C, the $AMR_{diff.}$ in the tunneling region also decreases compared to the contact regime and exhibits sharper peaks favoring a negative sign of the $AMR_{diff.}$. Despite from region B, the $AMR_{diff.}$ can be well reproduced by the anisotropy of the LDOS of the Δ_1-bands at the apex atom.

The transmission functions for $\mathbf{M} \parallel z$ and $\mathbf{M} \perp z$ with $\Delta L = 8.0\,\mathrm{bohr}$ for the Ir apex atoms, Figs. 5.10 (g, h), show more and broader contributions of the Δ_3- and Δ_4-bands compared to the case of Co and Rh apex atoms. This can be understood by the enhanced SOC with leads to stronger mixing of the Δ_3- and Δ_4-bands with the Δ_1-band and the larger spread of the $5d$-orbitals. The shape of the Δ_1-contribution to the transmission function is very different compared to the one of the Co and Rh apex atom. As already seen for the Co and Rh apex atoms, in region A the shape and magnitude of the $AMR_{diff.}$ shown in Fig 5.10 (i) is very similar to the $AMR_{diff.}$ in contact, Fig 5.9 (i), while region B and C show larger differences compared to the contact regime. In region B, the $AMR_{diff.}$ still has the same shape as the $AMR_{diff.}$ for $\Delta L = 2.0\,\mathrm{bohr}$ caused by the Δ_4-bands and only its magnitude decreased. In region C, the $AMR_{diff.}$ has a similar shape as the $AMR_{diff.}$ for $\Delta L = 2.0\,\mathrm{bohr}$, although the sign of most of the peaks changes to negative as seen before for Co and Rh apex atoms. Most of the $AMR_{diff.}$ in the tunneling regime can be well reproduced by the anisotropy of the Δ_1-LDOS at the apex atom.

In summary, we observe a different energy dependence, magnitude, and sign of the $AMR_{diff.}$ in the contact and in the tunneling regime. Since the $AMR_{diff.}$ in region A is dominated by Δ_1-bands, it shows very similar behavior for all apex atoms in the contact and tunneling regime. However, the $AMR_{diff.}$ in region B and region C is dominated by Δ_4- and Δ_3-bands in the contact regime, respectively, but primarily by Δ_1-bands in tunneling regime. This leads to a qualitatively and quantitatively different behavior of the $AMR_{diff.}$ and in region C even to a change of the sign between the $AMR_{diff.}$ in the contact and the tunneling regime. In addition, due to enhanced SOC induced mixings of Δ_1-bands with Δ_3-bands in region C for Rh and Ir, the $AMR_{diff.}$ for these apex atoms is enhanced compared to the Co apex atom or the pure Ni chain.

In the next section, we analyze these effects in more detail based on the local density of states.

Table 5.1: Angular dependency of the SOC matrix elements $\langle d_1|\mathbf{L}\cdot\mathbf{S}|d_2\rangle$ of the d-orbitals (d_1 and d_2 represent d_{xy}, d_{yz}, d_{zx}, $d_{x^2-y^2}$, and $d_{3z^2-r^2}$) for parallel ($\uparrow\uparrow$) and antiparallel ($\uparrow\downarrow$) spin alignment for a magnetization defined by polar angles θ and ϕ with respect to the direction of the current. Taken from [72].

$\uparrow\uparrow$	xy	yz	zx	x^2-y^2	$3z^2-r^2$
xy	0	$\frac{1}{2}i\sin\theta\sin\phi$	$-\frac{1}{2}i\sin\theta\cos\phi$	$i\cos\theta$	0
yz	$-\frac{1}{2}i\sin\theta\sin\phi$	0	$\frac{1}{2}i\cos\theta$	$-\frac{1}{2}i\sin\theta\cos\phi$	$-\frac{1}{2}\sqrt{3}i\sin\theta\cos\phi$
zx	$\frac{1}{2}i\sin\theta\cos\phi$	$-\frac{1}{2}i\cos\theta$	0	$-\frac{1}{2}i\sin\theta\sin\phi$	$\frac{1}{2}\sqrt{3}i\sin\theta\sin\phi$
x^2-y^2	$-i\cos\theta$	$\frac{1}{2}i\sin\theta\cos\phi$	$\frac{1}{2}i\sin\theta\sin\phi$	0	0
$3z^2-r^2$	0	$\frac{1}{2}\sqrt{3}i\sin\theta\cos\phi$	$-\frac{1}{2}\sqrt{3}i\sin\theta\sin\phi$	0	0

$\uparrow\downarrow$	xy	yz	zx	x^2-y^2	$3z^2-r^2$
xy	0	$\frac{1}{2}(\cos\phi + i\cos\theta\sin\phi)$	$\frac{1}{2}(\sin\phi - i\cos\theta\cos\phi)$	$-i\sin\theta$	0
yz	$-\frac{1}{2}(\cos\phi + i\cos\theta\sin\phi)$	0	$-\frac{1}{2}i\sin\theta$	$\frac{1}{2}(\sin\phi - i\cos\theta\cos\phi)$	$\frac{1}{2}\sqrt{3}(\sin\phi - i\cos\theta\cos\phi)$
zx	$\frac{1}{2}(-\sin\phi + i\cos\theta\cos\phi)$	$\frac{1}{2}i\sin\theta$	0	$-\frac{1}{2}(\cos\phi + i\cos\theta\sin\phi)$	$\frac{1}{2}\sqrt{3}(\cos\phi + i\cos\theta\sin\phi)$
x^2-y^2	$i\sin\theta$	$\frac{1}{2}(-\sin\phi + i\cos\theta\cos\phi)$	$\frac{1}{2}(\cos\phi + i\cos\theta\sin\phi)$	0	0
$3z^2-r^2$	0	$\frac{1}{2}\sqrt{3}(-\sin\phi + i\cos\theta\cos\phi)$	$-\frac{1}{2}\sqrt{3}(\cos\phi + i\cos\theta\sin\phi)$	0	0

5.4 Analysis of the LDOS

5.4.1 Contact region

To analyze the origin of the $\mathrm{AMR}_{\mathrm{diff.}}$ in the contact and in the tunneling regime in detail, we study the LDOS of the states at the apex atom and at the adjacent Ni atom of the open quantum system obtained with the transport code described in chapter 2.

For the contact region ($\Delta L = 2.0\,\mathrm{bohr}$), we focus on the more localized Δ_3- and Δ_4-orbitals of the Co apex atom and the Δ_4-orbitals of the adjacent Ni atom. Fig. 5.11 (a) shows the LDOS of the aforementioned orbitals of a SR calculation for the majority and minority spin. In the depicted energy region only minority spin states of Δ_3- and Δ_4-orbitals are present due to the exchange-splitting. The LDOS of the Δ_4-orbitals of the Co apex and adjacent Ni atom show very sharp peaks indicating small hybridization. The weak hybridization leads to the fact that the Δ_4-orbitals do not contribute to the transmission function in the contact regime (cf. Figs. 5.9 (a) and (b)). The LDOS of the Δ_3-orbitals of the Co apex atom shows the expected band-like shape.

SOC leads to several differences in the LDOS for $\mathbf{M} \parallel z$ and $\mathbf{M} \perp z$ shown in Fig. 5.11 (b) and (c). According to Tab. 5.1 for identical spin orientations and $\mathbf{M} \parallel z$

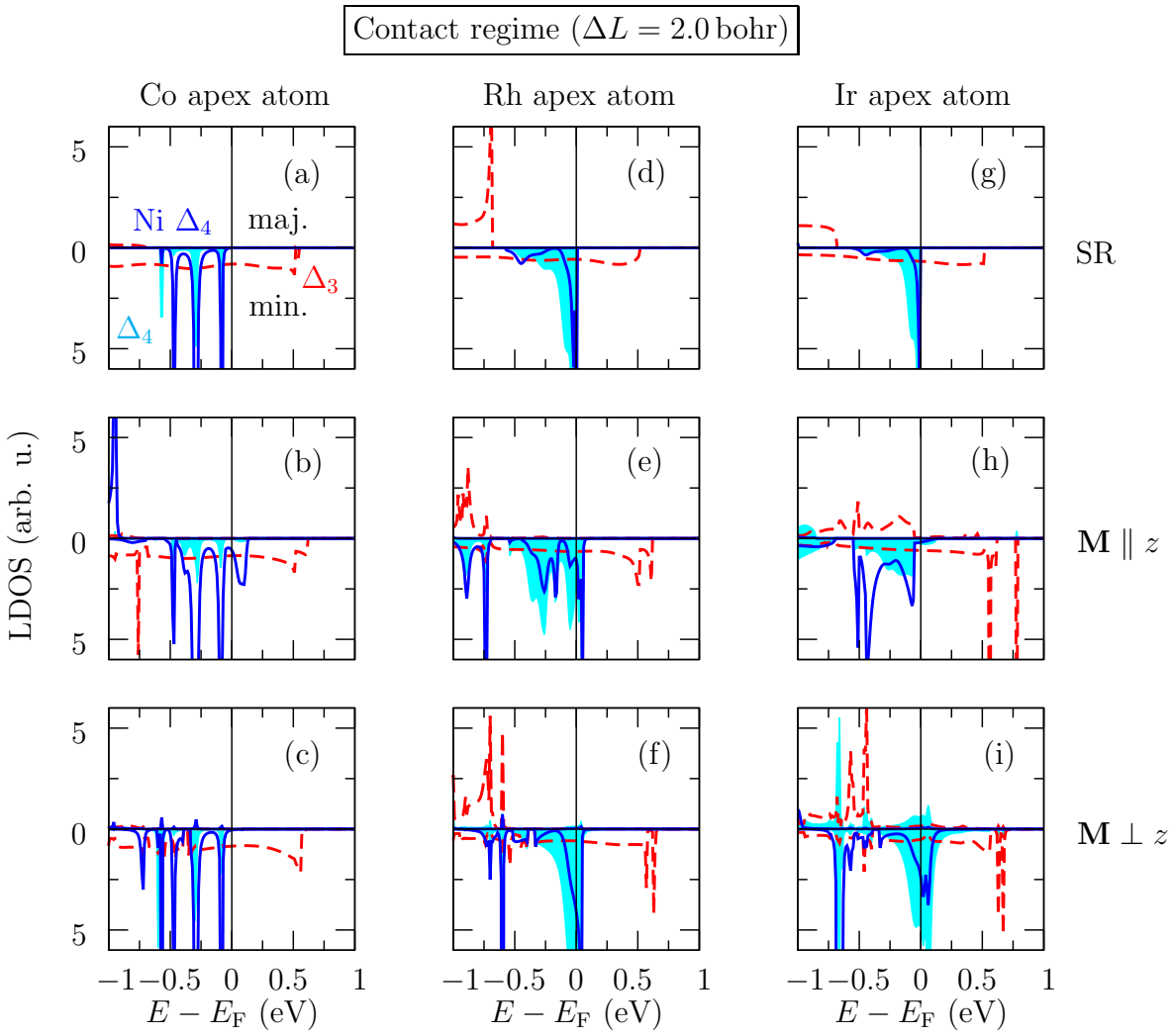

Figure 5.11: LDOS of the Δ_4- (shaded cyan) and Δ_3-orbitals (dashed red line) at the Co apex atom and the Δ_4-orbital (solid blue line) at the nearest-neighbor Ni atom obtained from a SR calculation (a) and calculations including SOC with (b) $\mathbf{M} \parallel z$ and (c) $\mathbf{M} \perp z$ for a spacing of $\Delta L = 2.0$ bohr between the apex atoms terminating the two Ni MWs. (d-f) shows the same for Rh apex atoms and (g-i) for Ir apex atoms.

($\theta = \phi = 0°$) one finds SOC matrix elements (Eq. (5.3)) of $\langle d_{zx}, \uparrow | H_{SO} | d_{yz}, \uparrow \rangle = -\frac{1}{2} i\xi$, while for $\mathbf{M} \perp z$ ($\theta = 90°$, $\phi = 0°$) $\langle d_{zx}, \uparrow | H_{SO} | d_{yz}, \uparrow \rangle = 0$. For $\mathbf{M} \parallel z$ this leads to a lifting of the degeneracy of the Δ_3-states and to a two peak structure around 0.5 eV above E_F. These differences around 0.5 eV above E_F explain the $AMR_{diff.}$ in region C in Fig. 5.9 (c). Analogously, one finds for the Δ_4-states of parallel spin orientation non-vanishing SOC matrix elements for $\mathbf{M} \parallel z$ while they are zero for $\mathbf{M} \perp z$. This leads to the extra peak slightly above E_F present for $\mathbf{M} \parallel z$ but not $\mathbf{M} \perp z$. However, since the Δ_4-states of the Co apex atoms are only weakly coupled to the adjacent Ni atom, no $AMR_{diff.}$ in region B is found around the Fermi level in Fig. 5.9 (c).

The LDOS of the Δ_4-orbitals of the Rh apex atom and the adjacent Ni atom of the SR

calculation in Fig. 5.11 (d) show stronger hybridizations and more band-like structures compared to the Co apex atom. The Δ_3-LDOS of the Rh apex atom is very similar to the one of the Co apex atom. The LDOS obtained from calculations including SOC for $\mathbf{M} \parallel z$ and $\mathbf{M} \perp z$ are shown in Figs. 5.11 (e, f). One sees the same splitting at the Δ_3 band edge (0.5 eV above the E_F) as found for the Co apex atom and around the Fermi level for the Δ_4-states. However, due to the larger hybridization of the Δ_4-states of the Rh apex atom with the adjacent Ni atom, the SOC induced mixing of the Δ_4-states now creates an $\mathrm{AMR}_{\mathrm{diff.}}$ in region B around the Fermi level in Fig. 5.9 (f). In addition to the SOC induced mixing found already for Co, hybridization between minority and majority spin states of Δ_3- and Δ_4-character can be found in the energy region from -1.0 eV to -0.5 eV below the Fermi level for both magnetization directions. Comparing with Tab. 5.1 yields non-vanishing SOC matrix elements for $\langle d_{xy},\uparrow | H_\mathrm{SO} | d_{zx},\downarrow\rangle$ and $\langle d_{x^2-y^2},\uparrow | H_\mathrm{SO} | d_{yz},\downarrow\rangle$ for $\mathbf{M} \parallel z$ as well as for $\langle d_{yz},\uparrow | H_\mathrm{SO} | d_{zx},\downarrow\rangle$ for $\mathbf{M} \perp z$. The reasons why these hybridizations are visible for Rh but not for Co lie in the larger SOC constant for Rh and in the smaller spin-splitting of the states at the Rh apex atom compared to the Co apex atom (cf. Fig.5.8 (a)). These additional mixings are the reason for the increased $\mathrm{AMR}_{\mathrm{diff.}}$ for Rh apex atoms compared to Co apex atoms in region A in Fig. 5.9 (f).

The LDOS of the Δ_4-state of the Ir apex atom and the adjacent Ni atom of the SR calculation in Fig. 5.11 (g) is very similar to the one of the Rh apex atom. Considering SOC for $\mathbf{M} \parallel z$ and $\mathbf{M} \perp z$ the mixings described for Co and Rh apex atoms can also be found for the Ir apex atom in Fig. 5.11 (h, i). The mixing of minority and majority Δ_3- and Δ_4-states moves closer to the Fermi level due to the reduced spin-splitting for Ir apex atoms. The reduced spin-splitting also leads to additional hybridizations of the Δ_4-states of majority and minority spin for $\mathbf{M} \perp z$ originating from the matrix elements $\langle d_{xy},\uparrow | H_\mathrm{SO} | d_{x^2-y^2},\downarrow\rangle = -i$, which is only weakly visible for Rh and not at all for Co apex atoms.

5.4.2 Tunneling region

For a deeper understanding of the effects of the different apex atoms on the $\mathrm{AMR}_{\mathrm{diff.}}$ in the tunneling regime ($\Delta L = 8.0$ bohr), the LDOS of the delocalized Δ_1- and Δ_3-orbitals of the apex atom as well as the Δ_1-orbital of the adjacent Ni atom is analyzed for the three different apex atoms.

The LDOS of the Δ_3-states obtained with a SR calculation at the Co apex atom, Fig. 5.12 (a), shows the same shape as in the contact region, Fig. 5.11 (a). The LDOS of the Δ_1-states shows the expected broad features due to the strong overlap of the orbitals of the apex atom with the adjacent Ni atom in the majority and minority spin channel. Including SOC for $\mathbf{M} \parallel z$ lifts the degeneracy of the Δ_3-states is lifted, as already observed in the contact regime, leading to the emergence of a shoulder in the LDOS at 0.5 eV above E_F. In addition, at -0.7 eV a kink can be seen in the minority Δ_3-LDOS and the majority Δ_1-LDOS, which can be attributed to the non-vanishing SOC matrix elements $\langle zx,\uparrow | H_\mathrm{SO} | 3z^2 - r^2,\downarrow\rangle$ and $\langle yz,\uparrow | H_\mathrm{SO} | 3z^2 - r^2,\downarrow\rangle$ (cf. Tab. 5.1). The same kinks can also be seen for $\mathbf{M} \perp z$ since also here $\langle zx,\uparrow | H_\mathrm{SO} | 3z^2 - r^2,\downarrow\rangle$ is

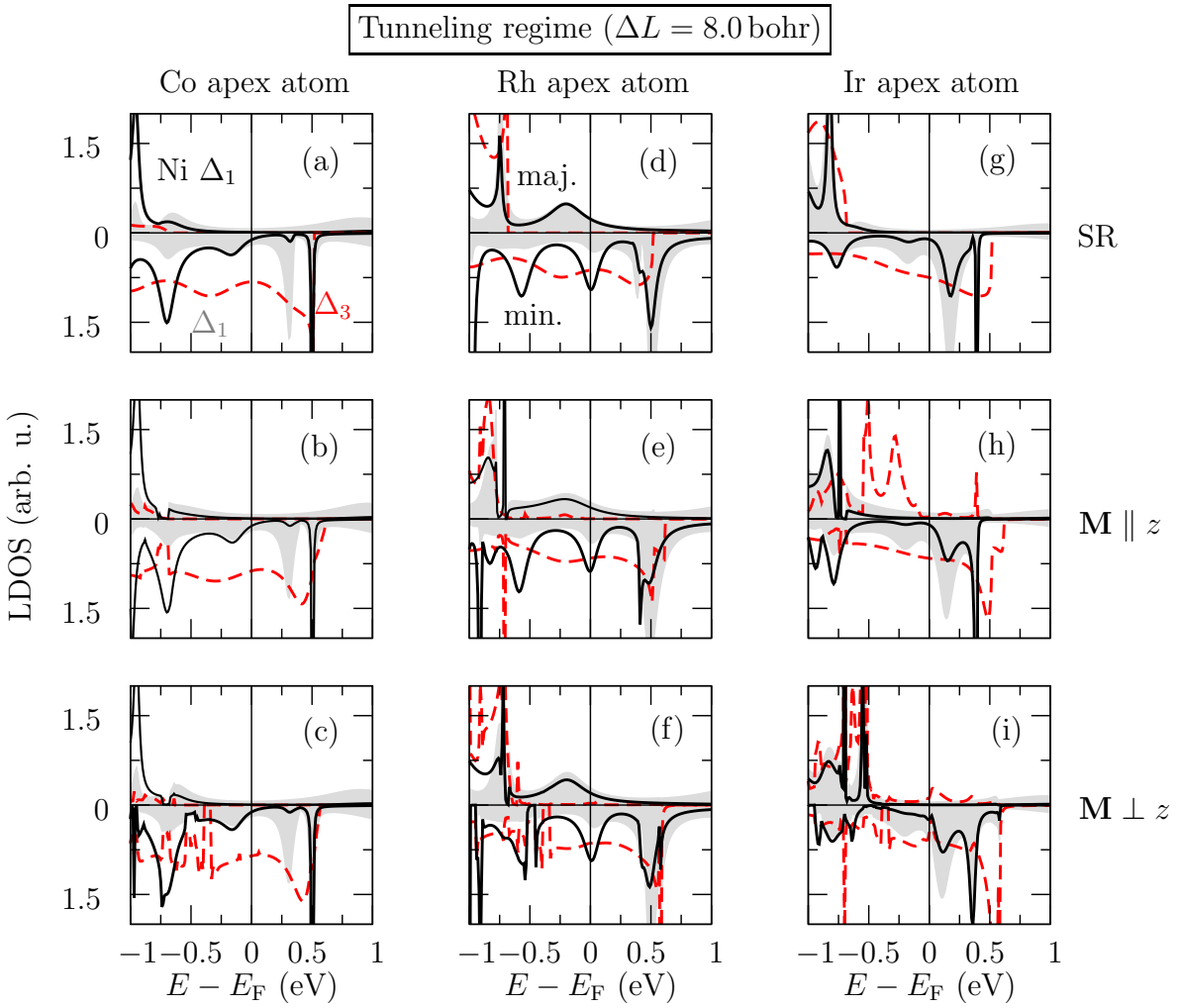

Figure 5.12: LDOS of the Δ_1- (shaded gray) and Δ_3- (dashed red line) orbitals at the apex atom and the Δ_1-orbital (solid black line) at the nearest-neighbor Ni atom for the SR calculation (a) and the calculations including SOC (b) $\mathbf{M} \parallel z$ and (c) $\mathbf{M} \perp z$ for a spacing of $\Delta L = 8.0$ bohr between the apex atoms terminating the two Ni MWs. (d-f) shows the same for Rh apex atoms and (g-i) for Ir apex atoms.

non-zero. In addition, Δ_3- and Δ_1-orbitals of parallel spin are allowed to mix, creating the kink at -0.7 eV. These two kinks in the LDOS of the Δ_3- and Δ_1-orbitals are the origin of the $\mathrm{AMR}_{\mathrm{diff.}}$ in region A in Fig. 5.10 (c). The sharp peak at -0.5 eV in the $\mathrm{AMR}_{\mathrm{diff.}}$ in region B can be explained by the mixing of Δ_3- and Δ_1-orbitals of minority spin character. Although, it is barely visible for the Co apex atom and can be seen much clearer for the Rh and Ir apex atom.

The LDOS of the Δ_3- and Δ_1-states at the Rh apex atom obtained with a SR calculation, Fig. 5.12 (d), show additional and more pronounced peaks compared to one at the Co apex atom. However, the general shape is similar. Including SOC similar mixing between the orbitals are found for $\mathbf{M} \parallel z$ and $\mathbf{M} \perp z$ as for the Co apex atom. For the Rh apex atom one now clearly sees the mixing of minority Δ_1- and Δ_3-states

slightly above $E_F + 0.5\,\text{eV}$ leading to the $\text{AMR}_{\text{diff.}}$ in region C (cf. Fig. 5.10 (f)).

The LDOS obtained in the SR approximation at the Ir apex atom in Fig. 5.12 (g) shows a very similar shape as the one at the Co apex atom. When SOC is included the same mixings as before occur for the two magnetization direction. However, due to the larger SOC constant for the Ir apex atom, the mixings are more pronounced and occur on larger energy scales, e.g., the mixing of minority Δ_1- and Δ_3-states slightly above $E_F + 0.5\,\text{eV}$ for $\mathbf{M} \perp z$. For $\mathbf{M} \parallel z$ one now sees mixing of minority and majority Δ_1- and Δ_3-states slightly below $E_F + 0.5\,\text{eV}$ and near the Fermi level. Due to the larger mixings for the Ir apex atoms in Fig. 5.10 (i), the $\text{AMR}_{\text{diff.}}$ is larger and broader in all regions.

5.5 Summary

In summary, the AMR was studied in symmetric junctions consisting of Ni MWs terminated by Co, Rh and Ir apex atoms as a function of the spacing ΔL introduced between the apex atoms of the monowire. We have focused on the $\text{AMR}_{\text{diff.}}$ of the transmission function, which corresponds to the AMR of the differential conductance. We have found that the $\text{AMR}_{\text{diff.}}$ depends sensitively on energy and can be enhanced by replacing the Ni or Co apex atoms using isoelectronic but heavier $4d$ and $5d$ transition metals Rh and Ir, respectively, reaching values of up to 150 %. As a function of ΔL we have found a non-trivial and non-monotonic evolution of the AMR, which can even change its sign when moving from the contact to the tunneling regime. The findings can be explained by the different symmetry of the orbitals constituting the transmission in the two regimes. The decay constants of the transition matrix elements between the orbitals at the apex atoms on each side of the gap and the SOC induced mixing depend on the orbital symmetry. The AMR is dominated by spatially delocalized and localized orbital types in the tunneling and contact regime, respectively, and, therefore, the AMR can differ strongly between the two regimes.

6 From Tunneling to Ballistic AMR in Single-Atom Junctions

In the last chapter, we have analyzed the $\mathrm{AMR}_{\mathrm{diff.}}$ of the transmission function, which corresponds to the AMR of the differential conductance as a function of energy and distance of Ni monowires terminated by Co, Rh and Ir apex atoms. In this chapter, we will focus on the distance dependence of the AMR of the conductance, i.e., the integrated transmission function, defined by

$$\mathrm{AMR}(\Delta z) = 100\% \cdot \frac{G_{\parallel}(\Delta z) - G_{\perp}(\Delta z)}{G_{\perp}(\Delta z)}. \tag{6.1}$$

This is motivated by STM experiments performed by Johannes Schöneberg and Nicolas Néel in the group of Prof. Richard Berndt at the Christian-Albrechts-Universität zu Kiel. In these experiments, Co and Ir adatoms on a double layer of Fe on W(110) have been probed by a non-magnetic W tip. The experimental setup is sketched in Fig. 6.1. The Fe double layer on W(110) is known to exhibit ferromagnetic domains with an out-of-plane magnetization that rotates into the film plane in domain walls (Néel walls) [51]. DFT calculations have shown that due to exchange coupling the magnetic moments of Co and Ir adatoms, whereby Ir is polarized by the substrate, on the domain and domain wall point in the same direction as the moments of the underlying Fe atoms [10, 55]. Therefore, the distance dependent current (or conductance) of adatoms deposited on domains and domain walls can be used to calculate the AMR as a function of the vertical tip displacement. A great advantage of this approach is that an external magnetic field is not needed and, thus, magnetostriction is not an issue.

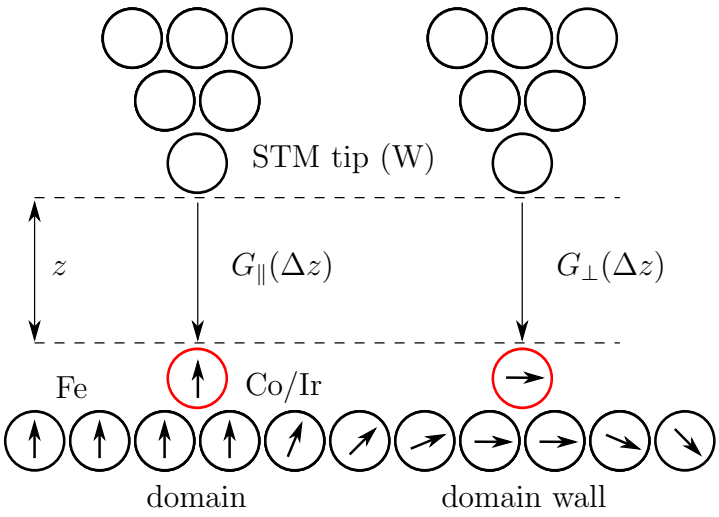

Figure 6.1: Sketch of the experimental setup of Co and Ir adatoms on the domain and domain wall of a double layer of Fe on W(110) probed by a W STM tip. The conductances for the two magnetization directions $G_{\parallel}$ and $G_{\perp}$ are measured as a function of the tip displacement Δz and are used to calculate the distance dependence of the AMR.

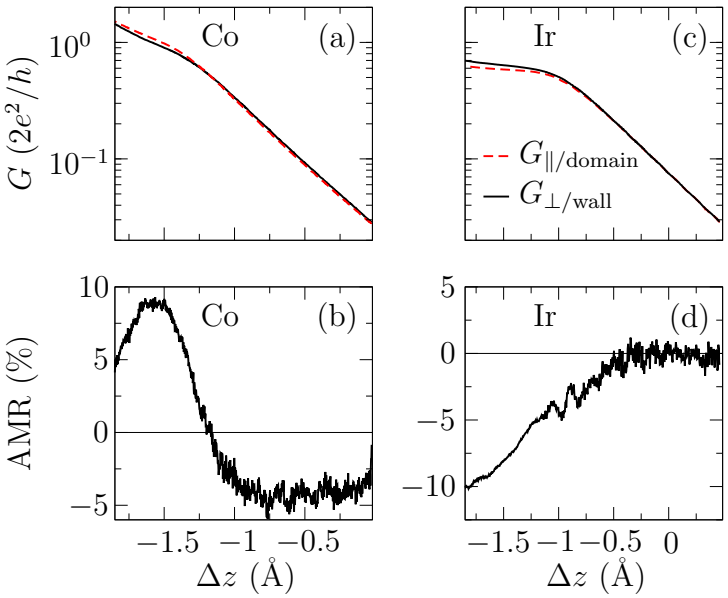

Figure 6.2: Conductance G versus vertical tip displacement Δz for (a) Co and (c) Ir adatoms on an Fe double layer on W(110). Bias voltages were set to 50 mV (Co) and 100 mV (Ir). Negative Δz corresponds to reduction of the tip-adatom distance. The dashed and solid curves show the conductances for an adatom on a domain ($G_{\parallel/\text{domain}}$) and on a domain wall ($G_{\perp/\text{wall}}$), respectively. The AMR was calculated from the data in (a) and (c) using Eq. (6.1). (b) and (d) display the results for Co and Ir, respectively. Experimental data taken from Ref. [73].

The experimental AMR is shown in Figs. 6.2 (b) and (d) for Co and Ir adatoms, respectively. As a function of the tip displacement Δz the AMR of Ir adatoms changes from 0 % for $\Delta z = 0.0$ Å to −10 % for $\Delta z = -1.5$ Å as the tip approaches the adatom. The AMR of Co adatoms shows a non-monotonic behavior and a change of sign whereby the values range from −5 % to 5 %. From the conductance curves in Figs. 6.2 (a) and (c) it can be seen that the AMR starts to change at the transition from the tunneling to the contact region (cf. with definition of tunneling and contact region in Sec. 5.2).

We have seen in the previous chapter that depending on the spacing between the apex atoms of the Ni monowires orbitals of different symmetry dominate the shape of the transmission function. Further it has been demonstrated that this influences the AMR and can even change its sign. Here, we show that albeit the more complex geometry of the experimental STM junction, the same mechanism is responsible for the distance dependence of the AMR in the STM experiments. With the help of DFT calculations we show that a similar behavior of the conductance as seen in the experimental data can be found for Fe monowires terminated by Co or Ir apex atoms. Thereby, the geometrical setup is the same as in chapter 5 (cf. Fig. 5.2).

To account for the more complex geometry in the experiment, we generalize our findings by devising a TB model similar to the one of the tunneling AMR on surfaces presented in Ref. [10] but take into account the contact region and calculate the conductance. The TB model consists of two orbital types of different symmetry characterized by the decay of the transition matrix elements of these orbitals across the gap in between the adatom and the STM apex atom. SOC is introduced as an off-diagonal matrix element to account for the magnetization-direction dependent mixing between the orbitals. This generic TB model is capable to explain the experimentally observed conductances and AMR.

Additionally, we present an analytical model of the distance dependence of the conductance which can be used to fit the experimental data. From these fits, the decay constants characterizing the orbitals of different symmetries can be obtained for adatoms on domains and domain walls. In a further step of interpretation the differences of the decay constants of adatoms on domains and domain walls can be attributed to a change in the effective mass of the electrons populating the orbitals. Since the effective mass can be calculated from the electronic structure this interpretation directly links the fitted values to the SOC induced changes in the electronic structure.

6.1 DFT Calculations of Distance-Dependent AMR

We consider symmetric atomic junctions as in chapter 5 (cf. Fig. 5.2). Instead of Ni we use Fe monowires and consider Co and Ir apex atoms and perform calculations for several distances L between the apex atoms. We integrate the transmission function in an energy interval corresponding to the width of the voltage window of the experiment, i.e., in an energy range of 50 meV and 100 meV for Co and Ir, respectively. The energy dependence of the AMR has been discussed in detail in the last chapter. Here, the focus is on a small energy region around the Fermi level where a behavior as in the experiment is obtained. The larger coordination number of the apex atom of the STM tip and the adatom in the full STM geometry will lead to an energy shift and broadening of the electronic states located at the adatom and the apex atom. In addition, further changes will arise since the junction considered in the experiment is asymmetric, while in the DFT calculations it is symmetric. Therefore, the energy interval need to be chosen differently compared to the experiment. However, in the next sections we will show using a TB and an analytical model that these complications do not change the underlying physical mechanism.

For the Co apex atom we focus on the energy region from -100 meV to -50 meV marked by the gray shaded area in the transmission function for $L = 5.5$ Å in the tunneling region and $L = 2.56$ Å in the contact region depicted in Fig. 6.3 (a) and (c), respectively. In the tunneling region the transmission function is dominated by sd_{z^2} states. A sharp peak in the shaded area for $\mathbf{M} \perp z$ can be seen, which is due to weak SOC induced mixings of the d_{yz} state with $d_{x^2-y^2}$ and d_{z^2} states (cf. Tab. 5.1). This peak can also be seen in the LDOS at the Co apex atom for $L = 5.5$ Å in Fig. 6.3 (b). For $\mathbf{M} \parallel z$ the corresponding matrix elements vanish due to symmetry.

On the other hand, in the contact region the transmission is dominated by the d_{xy,x^2-y^2} states. Due to SOC the degeneracy of the d_{xy} and $d_{x^2-y^2}$ states is lifted for $\mathbf{M} \parallel z$ (cf. Tab. 5.1), which can also be seen in the LDOS of the d_{xy,x^2-y^2} states in Fig. 6.3 (d). This leads to a larger transmission function for $\mathbf{M} \parallel z$ in the energy region marked by the gray shading, Fig. 6.3 (c), in contrast to the tunneling regime, where the transmission function for $\mathbf{M} \perp z$ is larger. One can already estimate that this will lead to a change of sign in the AMR between tunneling and contact regime.

The conductances for the two magnetization directions $G_\parallel$ and $G_\perp$ of the Co apex atoms obtained by integrating the transmission function from -100 meV to -50 meV

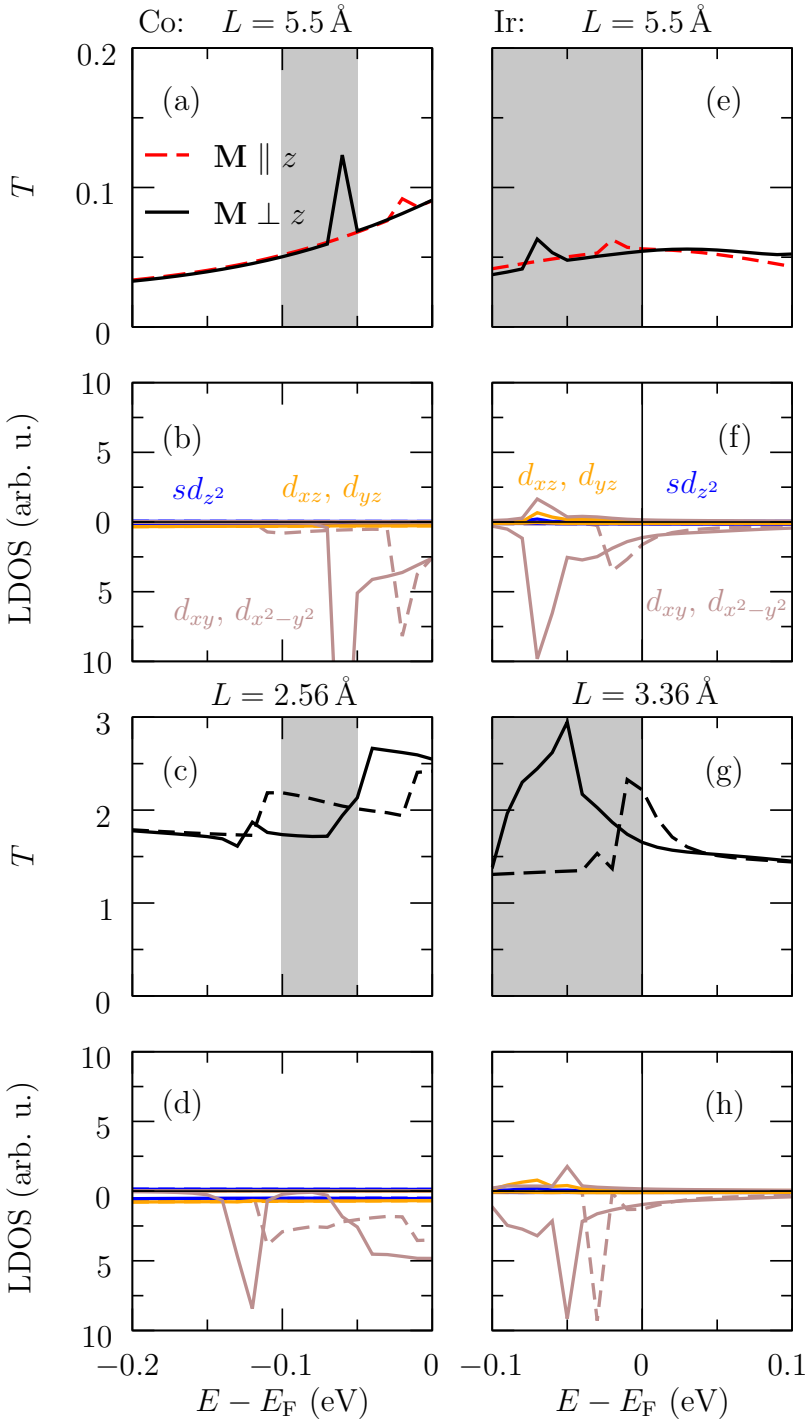

Figure 6.3: Transmission from DFT for a junction of two Fe MWs terminated with Co apex atoms in (a) the tunneling region ($L = 5.5$ Å) and (c) at contact ($L = 2.56$ Å) for $\mathbf{M} \parallel z$ (dashed line) and $\mathbf{M} \perp z$ (solid line). (e, g) the same for Ir apex atoms at separations $L = 5.5$ Å and $L = 3.36$ Å. The shaded areas in (a, e, c, g) mark the integration ranges chosen to obtain the conductances. (b, d) LDOS corresponding to (a, c) of the sd_z (blue lines), $d_{x^2-y^2,xy}$ (brown lines) and $d_{xz,yz}$ (orange lines) states at the apex atom for $\mathbf{M} \parallel z$ (dashed lines) and $\mathbf{M} \perp z$ (solid lines). (f, h) the same for Ir apex atoms at separations $L = 5.5$ Å and $L = 3.36$ Å.

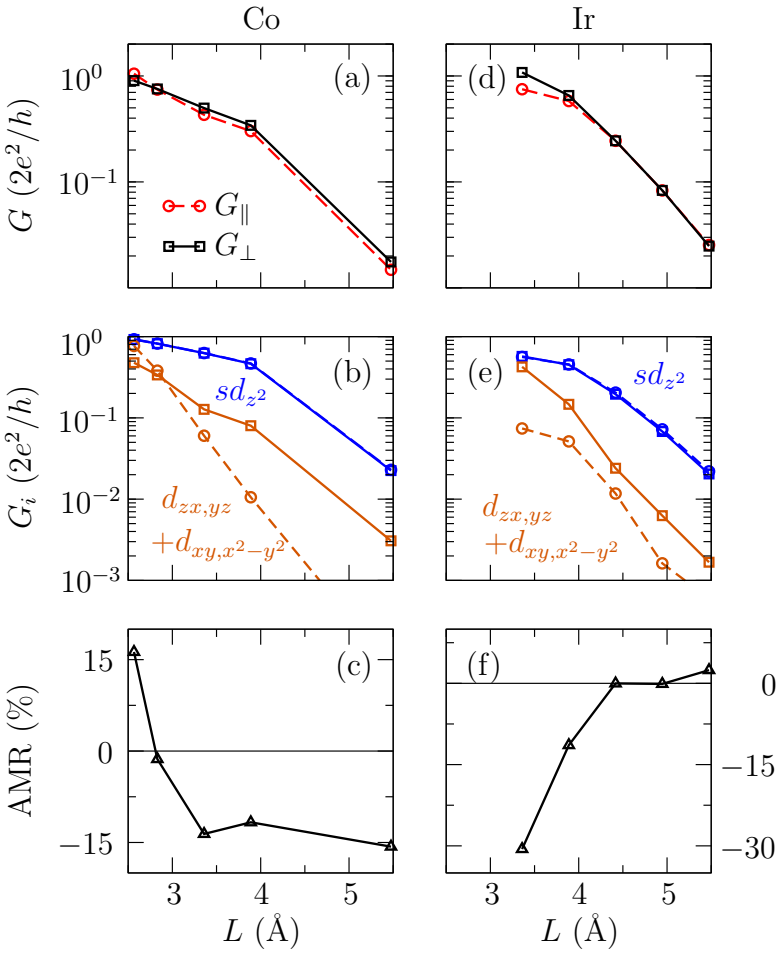

Figure 6.4: (a, d) Calculated distance dependence of the conductances $G_\parallel$ (circles, dashed line) and $G_\perp$ (squares, solid line) for a symmetric junction of two Fe monowires terminated by Co (Ir) apex atoms separated by a spacing L. The conductance has been obtained by an energy integration of the transmission function between $E_\mathrm{F} - 100\,\mathrm{meV}$ and $E_\mathrm{F} - 50\,\mathrm{meV}$ for Co apex ataoms and between E_F and $E_\mathrm{F} - 100\,\mathrm{meV}$ for Ir apex atoms. (b, e) Decomposition of the conductances for $\mathbf{M} \parallel z$ (dashed line) and $\mathbf{M} \perp z$ (solid line) shown in (a) and (d) into delocalized orbitals (sd_{z^2}) (blue lines) and localized orbitals ($d_{xz,yz} + d_{x^2-y^2,xy}$) (orange lines). (c, f) Corresponding AMR defined in Eq. (6.1).

are depicted in Fig. 6.4 (a). In the tunneling region $G_\perp > G_\parallel$ holds leading to an AMR of $-15\,\%$ as seen in Fig. 6.4 (c). As the contact region is entered the AMR changes to a positive value of $+15\,\%$. This behavior of the AMR qualitatively agrees with the experimental data. The conductances are also in good agreement quantitatively, while the values of the AMR are slightly too large. The smaller values of the AMR in the experiment can be attributed to the more complex geometry in the experimental setup leading to more scattering and, therefore, a broadening of the electronic states and the conductances associated with these states that leads to a smaller AMR [62].

The decomposition of the conductance in the delocalized orbitals (sd_{z^2}) and localized orbitals ($d_{xz,yz}+d_{x^2-y^2,xy}$) in Fig. 6.4 (b) yields further insight into the origin of the AMR. While the conductance in the tunneling regime is dominated by the delocalized orbitals, the contribution of the localized orbitals starts to quickly increase as the contact regime is approached. This leads to the sign change of the AMR.

For the Ir apex atom the energy region from $-100\,\mathrm{meV}$ to the Fermi level is chosen as the integration range. The transmission function of the tunneling region ($L = 5.5\,\text{Å}$) in Fig. 6.3 (e) is again dominated by sd_{z^2} states showing a similar shape as for Co, i.e., a small peak at $-0.07\,\mathrm{eV}$ for $\mathbf{M} \perp z$ due to the same SOC induced mixing of d-orbitals

as described above for the Co adatom and additional spin-mixing as can be seen in LDOS in Fig. 6.3 (f). In contrast to the Co apex atom, for the Ir apex atom the peak at $-0.01\,\mathrm{eV}$ in the transmission function for $\mathbf{M} \parallel z$ originating from the band edge of the d_{xy,x^2-y^2} states is included (cf. with tip resonances [54]) in the integration range. Therefore, the AMR calculated according to Eq. (6.1) using the conductances obtained by integrating the transmission functions from $-100\,\mathrm{meV}$ to the Fermi level vanishes.

The transmission in the contact region ($L = 3.36\,\text{Å}$) depicted in Fig. 6.3 (g) is dominated by the d_{xy,x^2-y^2} states. For $\mathbf{M} \perp z$ the d_{xy,x^2-y^2} states hybridize strongly with the $d_{zx,yz}$ states with the same and opposite spin character (cf. Tab. 5.1). This is also clearly visible in the LDOS in Fig. 6.3 (h). This hybridizations lead to a broad peak in the transmission function for $\mathbf{M} \perp z$ below the Fermi level and, therefore, to $G_\perp > G_\parallel$.

The resulting conductances $G_\parallel$ and $G_\perp$ obtained by integrating the transmission function from $-100\,\mathrm{meV}$ to the Fermi level are depicted in Fig. 6.4 (d). As in the experiment the curves for $G_\parallel$ and $G_\perp$ lie on top of each other in the tunneling region but start to deviate as the contact region is entered. The resulting AMR depicted in Fig. 6.4 (e) vanishes in the tunneling region and starts to become negative as the contact region is entered reaching a value of $-30\,\%$. As for the Co apex atoms the qualitative agreement between the AMR obtained from the DFT calculations and the experiment is good as well as the quantitative agreement of the conductances. The AMR obtained from the DFT calculations is larger than the one measured in the experiment as has been found for Co apex atoms. Again the decomposition into the delocalized orbitals (sd_{z^2}) and localized orbitals ($d_{xz,yz} + d_{x^2-y^2,xy}$) shown in Fig. 6.4 (f) reveals the origin of the distance dependence of the AMR, which is due to the The character of the orbitals dominating the conductances changes from mainly sd_{z^2} to a mixture of sd_{z^2} and $d_{xz,yz} + d_{x^2-y^2,xy}$.

6.2 Tight-Binding Model

In the DFT calculations described in the last section a idealized monowire geometry was assumed. The agreement between theoretically and experimentally obtained AMR was already good (cf. Fig.6.2 and Fig. 6.4). The more complex geometry of the experimental setup will lead to several differences in the electronic structure, which are stronger scattering due to the contact geometry [62], lifting of the degeneracy of the $d_{zx,yz}$ and d_{xy,x^2-y^2} states by the crystal field of the (110) surface, and energy offsets of the states located at the adatom and apex atom of the STM tip caused by the asymmetry of the junction.

To further support our interpretation of the experimental data we devise a generic minimal TB model similar to the TB model of the tunneling AMR on surfaces [10, 55], which takes the aforementioned complications into account and which yields the transmission function numerically. A schematic drawing of the TB model is sketched in Figs. 6.5 (a) and (b). We consider the adatom and the apex atom of the STM tip of the actual geometrical setup of the junction depicted in Fig. 6.5 (a). The coupling of the

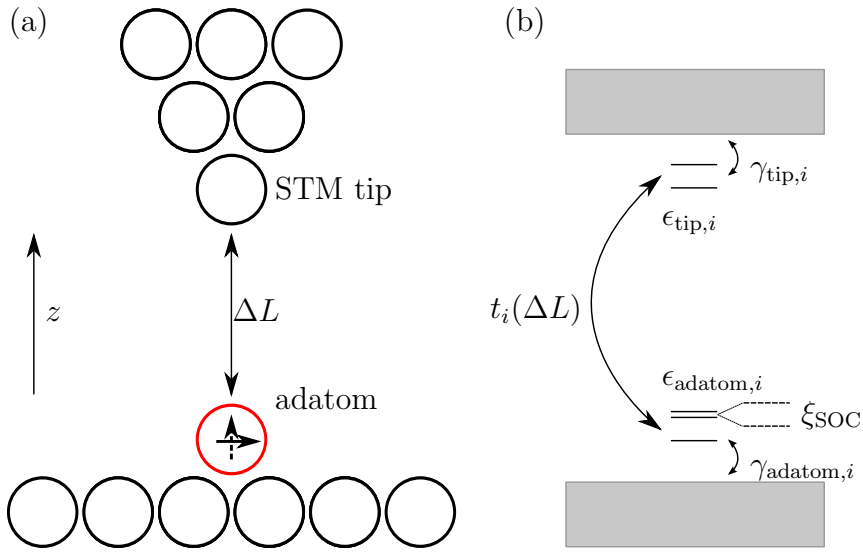

Figure 6.5: (a) Sketch of an adatom with $\mathbf{M} \parallel z$ or $\mathbf{M} \perp z$ probed by an STM tip. (b) Schematic drawing of the TB model used to model the junction sketched in (a).

adatom and the apex atom for each orbital i to the surface and the rest of the STM tip is modeled by the energy independent self-energy $\gamma_{\mathrm{adatom},i}$ and $\gamma_{\mathrm{tip},i}$, respectively. Three orbitals are considered located at the adatom and the apex atom. At the apex atom two of the orbitals are energetically degenerate while these orbitals are not degenerate at the adatom to account for the crystal-field splitting. SOC is introduced as an off-diagonal matrix element ξ_{SOC} between the two orbitals at the adatom, which is only nonzero for $\mathbf{M} \parallel z$. The orbitals of the adatom are connected to the apex atom via a hopping term depending exponentially on the displacement ΔL between the apex atom and the adatom:

$$t_i(\Delta L) = t_{0,i} \exp(-\kappa_i \Delta L). \tag{6.2}$$

The chosen values are shown in Tab. 6.1. The reference hoppings are chosen as $t_{0,1} = 1.5\,\mathrm{eV}$ and $t_{0,2} = t_{0,3} = 0.2\,\mathrm{eV}$ and the decay constants are chosen to $\kappa_1 = 1.1\,\mathrm{Å}^{-1}$ and $\kappa_2 = \kappa_3 = 1.7\,\mathrm{Å}^{-1}$.

The choice of these values is motivated by the analysis of the decay of the transition matrix elements of the orbitals across the spacing between the apex atoms of the Fe monowires obtained from the DFT calculations presented in the previous section.

Figs. 6.6 (a) and (b) show the hoppings of the maximally-localized Wannier functions of $d_{xz,yz}$, $d_{x^2-y^2,xy}$, d_{z^2}, and s character located at the apex atoms as a function of distance between the apex atoms for $\mathbf{M} \perp z$ for Co and Ir apex atoms. The transition matrix elments of each orbital type i can be fitted with

$$t_i(L) = t_{0,i} \exp(-\kappa_i L). \tag{6.3}$$

	ϵ_1 (eV)	ϵ_2 (eV)	ϵ_3 (eV)	γ_1 (eV)	$\gamma_2 = \gamma_3$ (eV)	ξ_{SOC} (eV)
adatom	−0.2	0.15	0.05	−1.0	−0.15	0.3
tip atom	0.3	−0.15	−0.15	−1.0	−0.15	0.0

Table 6.1: Parameters chosen for the TB model sketched in Fig. 6.5.

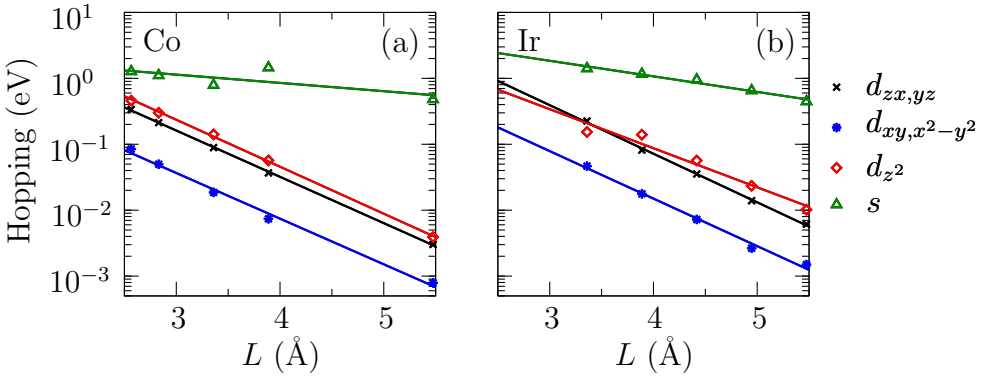

Figure 6.6: Hoppings of the maximally-localized Wannier functions of $d_{xz,yz}$ (black crosses), $d_{x^2-y^2,xy}$ (blue stars), d_{z^2} (red diamonds), and s (green triangles) character located at the apex atoms as a function of the distance L between the (a) Co and (b) Ir apex atoms. Solid lines depict the fits obtained with Eq. (6.3) for each listed orbital-type for $\mathbf{M} \perp z$ from which the decay constants in Tab. 6.2 are obtained.

The values of the decay constants κ_i obtained by fitting the data are shown in Tab. 6.2. While the decay constants for the localized orbitals ($d_{xz,yz}$ and $d_{x^2-y^2,xy}$) are in the range of $1.7\,\text{Å}^{-1}$, the average value of the s and d_{z^2} state, which are strongly hybridized, is about $1.0\,\text{Å}^{-1}$. The matrix elements due to SOC obtained from the MLWF between the states of $d_{xz,yz}$ and $d_{x^2-y^2,xy}$ character yields values of $\xi_{\text{SOC}}^{\text{Ir}} \approx 400\,\text{meV}$ and $\xi_{\text{SOC}}^{\text{Co}} \approx 80\,\text{meV}$ for Co and Ir apex atoms, respectively.

Returning to the TB model according to the chosen values, orbital 1 can be interpreted as an sd_{z^2} orbital and orbital 2 and 3 as d_{zx} and d_{yz} or d_{xy} and $d_{x^2-y^2}$ orbitals. The orbital symmetry is reflected by the values of the broadening γ_i, which leads to broad (sd_{z^2}) or sharper (d_{zx}, d_{yz} or d_{xy}, $d_{x^2-y^2}$) LDOS at the adatom depicted in Fig. 6.7 (a). Furthermore, it is reflected by the values of the decay constant κ_i, which is small for the s orbital and large for the d_{zx} and d_{yz} orbitals leading to a slow and fast decay of the transmission function attributed to these orbitals as the distance between the apex atom and the adatom is increased, respectively, as is found in the DFT calculations (cf. Fig. 6.4) and in the literature [74]. The crystal-field splitting of the d_{zx} and d_{yz} orbitals of the adatom is represented by the small offset between the on-site energies ϵ_2 and ϵ_3. For $\mathbf{M} \parallel z$ the SOC induced hybridization between these orbitals increases this offset as seen in Fig. 6.7 (a).

adatom	κ_{Δ_3} (Å^{-1})	κ_{Δ_4} (Å^{-1})	$\kappa_{d_{z^2}}$ (Å^{-1})	κ_s (Å^{-1})
Co, $\mathbf{M} \parallel z$	1.61	1.59	1.63	0.29
Co, $\mathbf{M} \perp z$	1.61	1.59	1.64	0.29
Ir, $\mathbf{M} \parallel z$	1.41	1.69	1.51	0.51
Ir, $\mathbf{M} \perp z$	1.70	1.66	1.36	0.54

Table 6.2: Decay constants for the different orbital types obtained by fitting the data shown in Figs. 6.6 (a, b) with Eq. (6.3).

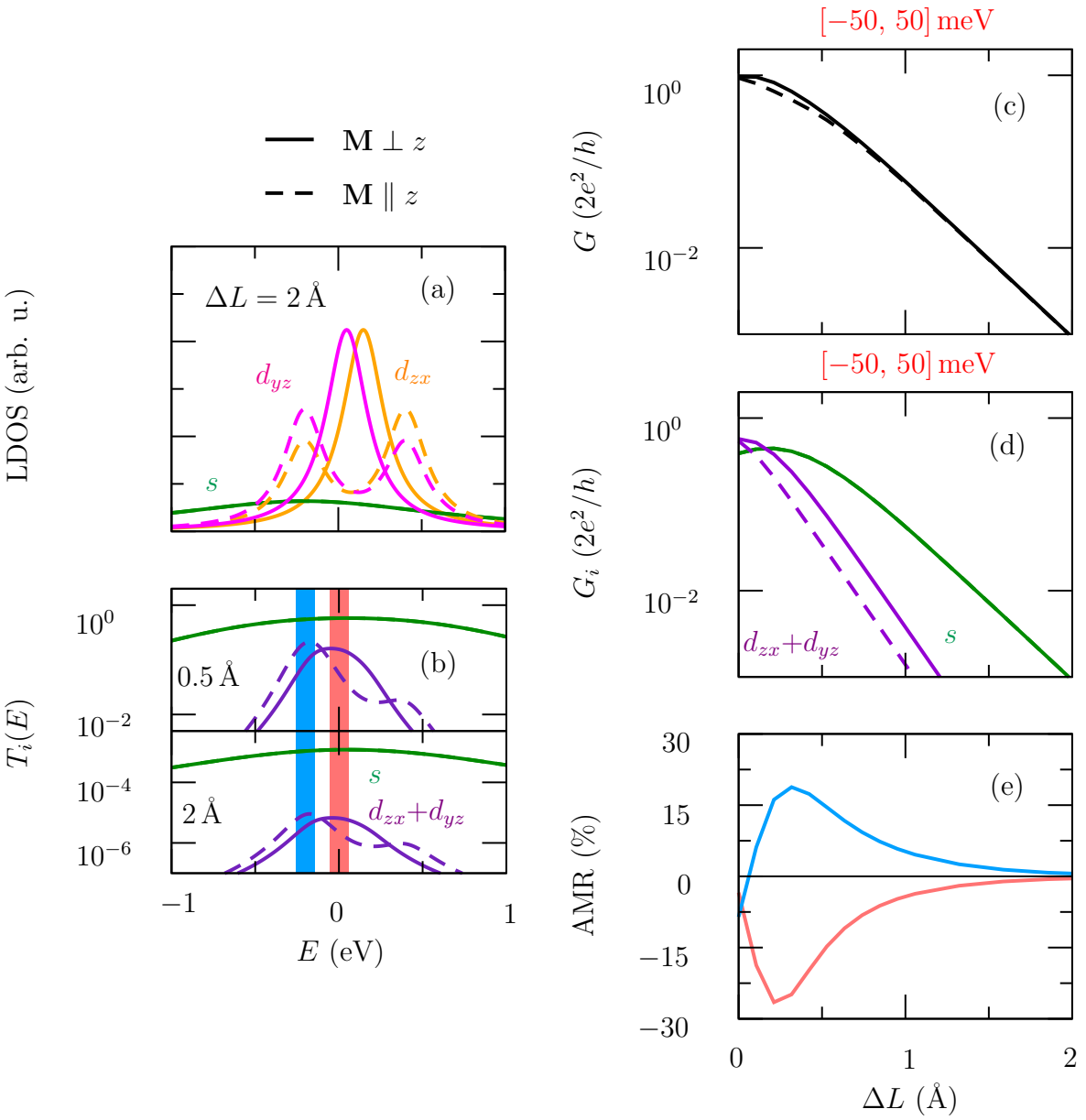

Figure 6.7: (a) LDOS at the adatom in the tunneling region ($\Delta L = 2.0$ Å) obtained from the TB model sketched in Fig. 6.5 for parameters representing s (green line) and d_{zx} and d_{yz} orbitals (magenta and orange line) for $\mathbf{M} \parallel z$ (dashed lines) and $\mathbf{M} \perp z$ (solid lines). (b) Energy-dependent and orbital-decomposed transmission functions of the s (green line) and $d_{zx} + d_{yz}$ (violet line) orbitals in the contact ($\Delta L = 0.5$ Å, upper panel) and tunneling ($\Delta L = 2.0$ Å, lower panel) region. (c) Total conductance obtained by integrating the transmission functions from −50 meV to +50 meV. (d) Orbital-decomposed conductance obtained by integrating the transmission functions from −50 meV to +50 meV. (e) AMR of the conductances obtained by integrating the transmission functions from −50 meV to +50 meV (red line) and from −150 meV to −50 meV (blue line) corresponding to the red and blue shaded areas in (c).

This also reflects itself in the energy-dependent transmission function of the individual orbitals T_i in Fig. 6.7 (b). However, in the tunneling region ($\Delta L = 2\,\text{Å}$) this does not affect the transmission properties since the contributions from the d_{zx} and d_{yz} orbitals are orders of magnitudes smaller than the one from the s orbital due to the larger decay constant. On the other hand, in the contact region the transmission function from the d_{zx} and d_{yz} orbitals and s orbitals are on the same order of magnitude.

The resulting conductances obtained from integrating the transmission function from $-50\,\text{meV}$ to $+50\,\text{meV}$ can be seen in Fig. 6.7 (c). They show the same distance dependence as the DFT calculations for the Ir adatom (cf. Fig. 6.4 (c)) and the experimental data of the Ir adatom (cf. Fig. 6.2 (c)). The origin of the distance dependence can be easily understood by the decomposition of the conductance into the two orbitals types G_i depicted in Fig. 6.7 (d). Far in the tunneling region only the s orbital contributes considerably to the conductance, while at smaller values of ΔL the d_{zx} and d_{yz} orbitals start to contribute. Since the contribution of the d_{zx} and d_{yz} orbitals is different for $\mathbf{M} \parallel z$ and $\mathbf{M} \perp z$ due to SOC induced hybridizations, the characteristic distance dependence of the AMR in Fig. 6.7 (e) is found. The decrease of the conductance of the s orbital close to $0\,\text{Å}$ is caused by the strong mixing at these distances between the s orbital located at the adatom and apex atom, which leads to a splitting of the peak in the LDOS of the s orbital and, therefore, a reduction of the LDOS in the integration interval. This effect has also been found in DFT calculations in Ref. [74].

From Fig. 6.7 (b) it can be seen that if the integration range is chosen differently (or the states are located at a different energy with respect to the Fermi level), a different behavior of the AMR will be obtained. For example, if the integration range is chosen from $-150\,\text{meV}$ to $-50\,\text{meV}$, the inverse behavior of the AMR can be seen, i.e., qualitatively the one of the Co adatom (cf. Fig. 6.4 (b) and Fig. 6.2 (b)). This shows the bias sensitivity of the AMR, which has been mentioned in the literature [51, 8, 52, 53] and which has been described for the $\text{AMR}_{\text{diff.}}$ of the transmission functions in the previous chapter.

The sign change of the slope of the AMR at $0.25\,\text{Å}$ for both integration ranges can be attributed to the fact that the conductance of the $d_{zx} + d_{yz}$ orbitals reaches saturation earlier for $\mathbf{M} \perp z$ than for $\mathbf{M} \parallel z$ due to the SOC induced mixing. A similar behavior of the experimentally obtained AMR can be seen in Fig. 6.2 (b) for the Co adatom.

In principle, the non-zero AMR in the tunneling regime could be modeled by adding another off-diagonal element between one of the localized and the delocalized orbital. However, to keep the model minimal we refrain from doing so but show in the next section that the distance dependence of the conductance within this TB model can be derived analytically using the Green's function formalism. The analytical model can be used to fit the experimental data yielding very good agreement.

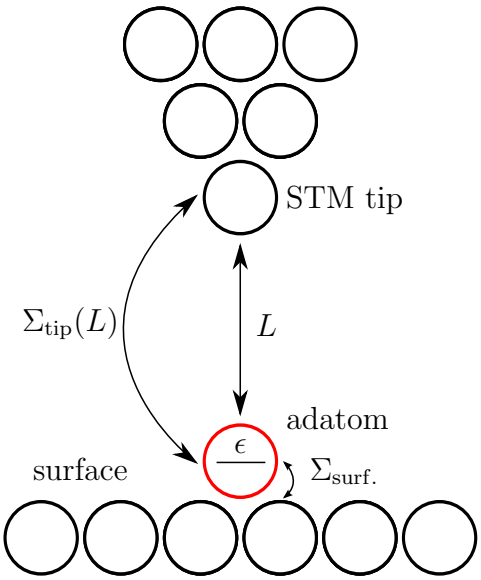

Figure 6.8: Sketch of the setup of the Green's function model mimicking an adatom on a surface probed by an STM tip.

6.3 Analytical Model

The distance dependence of the conductance obtained with TB model used in the last section can be derived analytically utilizing the Green's function formalism introduced in chapter 2.

We consider one energy level on an adatom coupled to a surface and an STM tip as sketched in Fig. 6.8. The electronic structure of the adatom can be described with the help of the Green's function G_{adatom}. The influence of the surface and the STM tip is taken into account via the self-energies $\Sigma_{\text{surf.}}$ and $\Sigma_{\text{tip}}(L)$, respectively. We thereby assume that the self-energies $\Sigma_{\text{surf.}}$ and $\Sigma_{\text{tip}}(L)$ describing these couplings are constant in energy. The latter depends on the separation L of the adatom to the STM tip. The self-energy $\Sigma_{\text{tip}}(L)$ can be calculated with the help of the Green's function of the isolated STM tip G_{tip} and the coupling of the adatom to the tip, which is assumed to be exponential as in the TB model in the previous section, $V_{\text{tip}}(L) = te^{-\kappa L}$ via:

$$\Sigma_{\text{tip}}(L) = V_{\text{tip}}(L)^{\dagger} G_{\text{tip}} V_{\text{tip}}(L) = V_{\text{tip}}(L)^2 G_{\text{tip}}. \tag{6.4}$$

The Green's function of the adatom then states:

$$G_{\text{adatom}}(L) = [E - \epsilon - \Sigma_{\text{tip}}(L) - \Sigma_{\text{surf.}}]^{-1}. \tag{6.5}$$

Using Eq. (2.88) this results in a distance dependence of the transmission function

$$T_E(L) = T_{0,E} \frac{e^{-2\kappa L}}{1 - a_E e^{-2\kappa L} + b_E e^{-4\kappa L}} \tag{6.6}$$

at energy E. For large L one regains the well-known exponential behavior of the tunneling current $\propto e^{-2\kappa L}$ (cf. Fig. 5.6). In the linear response regime [28] one obtains for the conductance

$$G(L) = \frac{e^2}{h} T_{E_{\text{F}}}(L). \tag{6.7}$$

adatom	κ_1 (Å^{-1})	κ_2 (Å^{-1})	$L_{0,1}$ (Å)	$L_{0,2}$ (Å)
Ir, $\mathbf{M} \parallel z$	1.02	2.87	−1.17	−2.18
Ir, $\mathbf{M} \perp z$	1.00	2.67	−1.15	−2.27
Co, $\mathbf{M} \parallel z$	1.03	1.39	−1.47	−2.16
Co, $\mathbf{M} \perp z$	1.07	1.76	−1.44	−2.37

Table 6.3: Decay constants κ_i and distance $L_{0,i}$ at which the conductance associated with orbital type i reaches its maximum obtained by fitting the analytical model to the experimental data using Eq. (6.8) for Co and Ir adatoms on domains ($\mathbf{M} \parallel z$) and domain walls ($\mathbf{M} \perp z$).

If one assumes that the modes on the adatom are independent from each other, one can add up the contributions from all the individual modes:

$$G_{\mathrm{tot}}(L) = \sum_i G_{0,i} T_{E_\mathrm{F},i}(L). \tag{6.8}$$

In practice, it has been found that one should use

$$T_{E_\mathrm{F},i}(L) = \frac{(1 - \tilde{a}_i + \tilde{b}_i) e^{-2\kappa_i (L - L_{0,i})}}{1 - \tilde{a}_i e^{-2\kappa_i (L - L_{0,i})} + \tilde{b}_i e^{-4\kappa_i (L - L_{0,i})}} \tag{6.9}$$

for the fitting.

With Eq. (6.8) we can fit the experimental data and obtain effective decay constants κ_i. To do that in our particular case, we assume two orbital types with differing decay constants κ_i as in the TB model presented in the previous section. This is motivated by the DFT calculations and the results from Ref. [74], which show that at the beginning of the contact region only two types of orbitals are contributing considerably to the transmission, e.g., sdz^2, d_{zx} and d_{yz} orbitals. In addition, we do not consider the effect of the crystal-field on the d_{zx} and d_{yz} orbitals effective, averaged orbitals which are degenerate.

Good fits are obtained by choosing $G_{0,1} = 0.5\,G_0$ and $G_{0,2} = 1.5\,G_0$ shown in Figs. 6.9 (a) and (b) for $\mathbf{M} \perp z$ for Co and Ir adatoms, respectively, and in Figs. 6.9 (c) and (d) for $\mathbf{M} \parallel z$, respectively. The values $G_{0,i}$ define the maximum value of conductance associated with orbital type i that is reached when $L = L_{0,i}$. Therefore,

adatom	$\tilde{a}_1$	$\tilde{a}_2$	$\tilde{b}_1$	$\tilde{b}_2$
Ir, $\mathbf{M} \parallel z$	0.43	−39.46	1.00	−28.78
Ir, $\mathbf{M} \perp z$	0.62	−59.16	1.02	−38.42
Co, $\mathbf{M} \parallel z$	1.24	0.83	1.00	1.65
Co, $\mathbf{M} \perp z$	0.95	−1.11	1.01	4.09

Table 6.4: Dimensionless fitting constants $\tilde{a}_i$ and $\tilde{b}_i$ obtained by fitting the analytical model to the experimental data using Eq. (6.8) for Co and Ir adatoms on domains ($\mathbf{M} \parallel z$) and domain walls ($\mathbf{M} \perp z$).

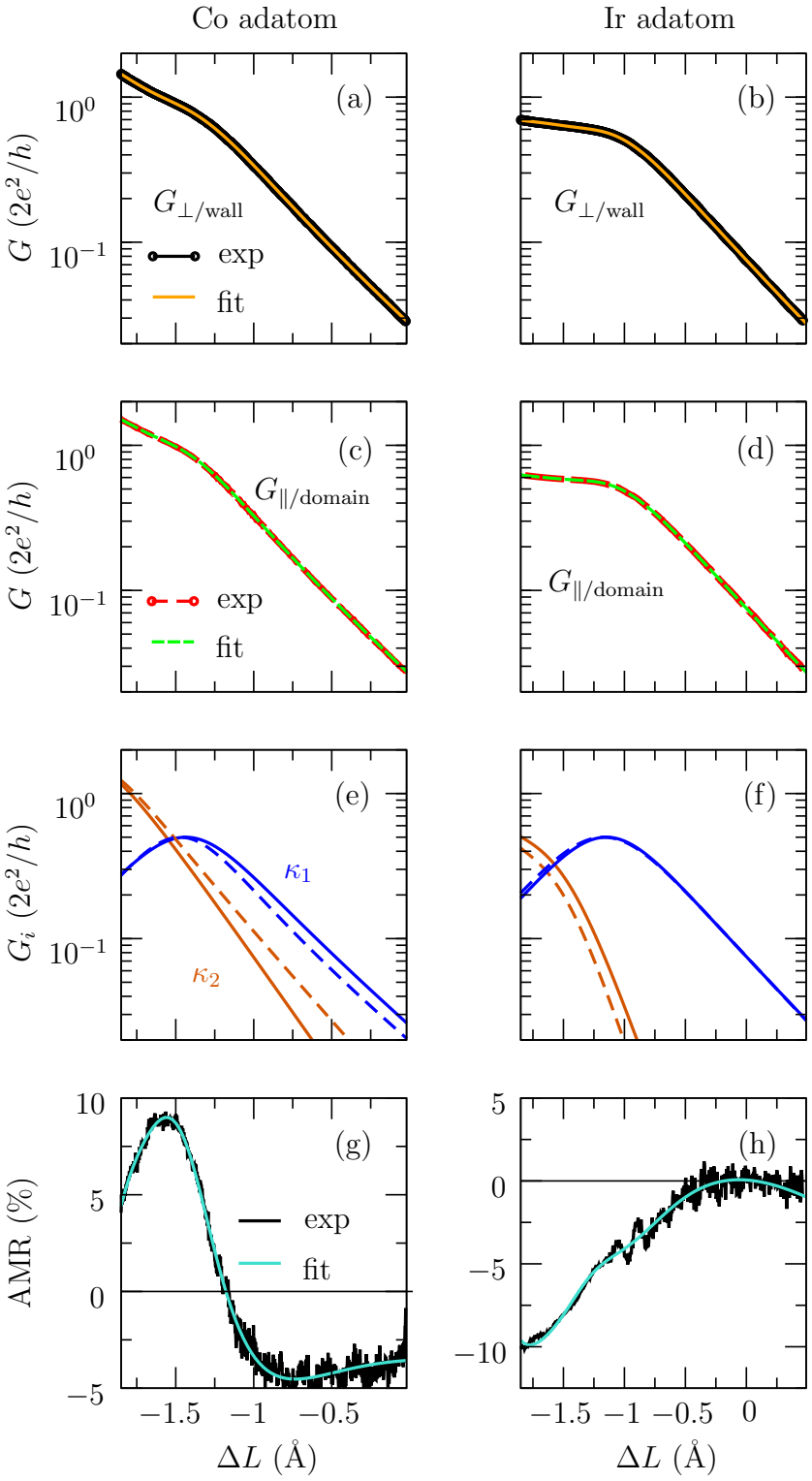

Figure 6.9: (a) Conductance obtained experimentally (solid black line) for a Co adatom located on a domain wall ($\mathbf{M} \perp z$) of a double layer Fe on W(110) and the fit (solid orange line) obtained with Eq. (6.8) assuming two orbital types. (b) shows the same as (a) for Ir adatoms. (c) shows the same as (a) for Co adatoms located on a domain ($\mathbf{M} \parallel z$): Experimental data (dashed red line) and Fit (dashed green line). (d) shows the same as (c) for Ir adatoms. (e) and (f) show the decomposition of the fitted conductance into the two assumed orbital types with decay constants κ_1 (blue lines) and κ_2 (red lines) for $\mathbf{M} \parallel z$ (dashed lines) and $\mathbf{M} \perp z$ (solid lines) for Co and Ir adatoms, respectively. (g) and (h) AMR calculated according to Eq. (6.1) from the experimental data (black line) and the fits (turquoise line) for Co and Ir adatoms, respectively. Experimental data taken from Ref. [73].

orbital type 1 effectively consists of one orbital and orbital type 2 of three orbitals[1]. The decay constants and the distance $L_{0,i}$ at which the maximum conductance associated with orbital type i is reached are given in Tab. 6.3. The decay constant κ_1 for the Ir adatom is very similar for $\mathbf{M} \parallel z$ and $\mathbf{M} \perp z$, which can also be seen in the very similar shape of the orbital-decomposed conductances shown in Fig. 6.9 (f). This is consistent with the vanishing AMR in the tunneling region found for Ir adatoms. The decay constant κ_2 shows stronger deviations for $\mathbf{M} \parallel z$ and $\mathbf{M} \perp z$. The orbital-decomposed conductances show the same qualitative behavior as the ones obtained from the TB model in Fig. 6.7 (d).

For the Co adatom the difference between the decay constant κ_1 for the two magnetization directions is twice as large as for the Ir adatom resulting in a clear difference between the orbital-decomposed conductances in Fig. 6.9 (e). This is consistent with the AMR in the tunneling region found for Co adatoms. Also κ_2 differs a lot for the two magnetization directions leading to the AMR found in the contact region.

The values for $L_{0,i}$ show the same behavior as the values for κ_i, i.e., $L_{0,1}$ is very similar for both magnetization directions, while $L_{0,2}$ changes considerably. This also holds for the dimensionless fitting parameters $\tilde{a}_i$ and $\tilde{b}_i$ in Tab. 6.4, which contain the information of the self-energies and are not easy to interpret. The parameters $\tilde{a}_1$ and $\tilde{b}_1$ for orbital type 1 are similar for Co and Ir adatoms, while $\tilde{a}_2$ and $\tilde{b}_2$ differ strongly. This can be understood by the stronger SOC induced mixing for the localized orbitals of Ir adatoms compared to Co adatoms found in the DFT calculations in Sec. 6.1. The stronger SOC induced mixing for Ir adatoms, which even leads to spin-mixing, changes the orbital character of the localized orbitals compared to the Co adatoms.

For both adatoms a decrease of the conductance of delocalized orbital-type (κ_1) that has also been seen in the TB model for the orbital of s character is found in Figs. 6.9 (e) and (f). As mentioned above this decrease can be attributed to the strong hybridization of the orbitals of the apex atom of the tip and the adatom for small separations leading to a peak splitting in the LDOS as described in Ref. [74].

The AMR calculated via Eq. (6.1) using the experimental data and the fits shown in Figs. 6.9 (g) and (h) for Co and Ir adatoms, respectively, is in very good agreement.

Although the decay constants are not the only changing parameter obtained from the fitting for the two magnetization directions, they are easiest to interpret. The decay constant can be analyzed with the well-known formula from the tunneling effect

$$\kappa_i = \sqrt{\frac{2m_i^*}{\hbar^2}\Phi}, \tag{6.10}$$

where Φ is the work function and m_i^* is the effective mass of the electron in mode i accounting for the mobility of the d-electrons, which has to be considered for the conductivity [3]. The effective mass can then be calculated according to

$$m_i^* = 3.8096\frac{\kappa_i[\text{Å}^{-1}]}{\Phi[eV]} \cdot m_e, \tag{6.11}$$

[1] If the spin is taken into account, each mode carries a conductance quantum $G_0/2 = e^2/h$.

adatom	m_1^* (m_e)	m_2^* (m_e)
Ir, $\mathbf{M} \parallel z$	0.97	2.73
Ir, $\mathbf{M} \perp z$	0.95	2.54
Co, $\mathbf{M} \parallel z$	0.98	1.32
Co, $\mathbf{M} \perp z$	1.02	1.68

Table 6.5: Effective masses in electron masses m_e obtained from the fitted decay constants κ_i calculated using Eq. (6.11) with $\Phi = 4\,\mathrm{eV}$ for the Co and Ir adatom for $\mathbf{M} \parallel z$ and $\mathbf{M} \perp z$.

where m_e is the electron mass. For a typical value of $\Phi = 4\,\mathrm{eV}$, we obtain the effective masses shown in Tab. 6.5. The orbitals with small values of κ_1 corresponding to sd_{z^2} orbitals show values close to m_e, i.e., of electrons with a free-electron like dispersion. The effective masses of more strongly bound electrons corresponding to decay constant κ_2 (d_{zx} and d_{yz} or d_{xy} and $d_{x^2-y^2}$ orbitals) are in the range of 1.3 to 2.7 electron masses.

The effective mass is connected to the electronic structure via its definition:

$$m_i^* = \hbar^2 \left[\frac{\mathrm{d}^2 \epsilon_i(k)}{\mathrm{d}k^2} \right]^{-1} . \tag{6.12}$$

As we have seen in the previous chapter (cf. Fig. 5.5) and as has been shown in [9] the SOC induced hybridizations lead to changes in the electronic structure, which in periodic systems can be seen as changes of the dispersion relation in the bandstructure or alternatively in the LDOS. Therefore, one can attribute the effective masses obtained via the fitting of the experimental data for the two magnetization directions directly to the SOC induced differences in the electronic structure.

6.4 Summary

We have shown how the distance dependence of the AMR measured on Co and Ir adatoms on a double layer of Fe on W(110) can be explained by DFT calculations of Fe monowires terminated by Co and Ir adatoms. Furthermore, to account for the more complex geometry of the experiment we developed a generic TB model to obtain the conductances and the AMR of adatoms on surfaces. This model captures the essential physics of the distance dependence of the AMR observed in the experiment and in the DFT calculations. Finally, we presented an analytical model based on the Green's function formalism presented in chapter 2 of the distance dependence of the conductance. With the model one is able to explain the measured conductance curves and extract effective decay constants of the involved orbitals. These decay constants differ for adatoms on domain ($\mathbf{M} \parallel z$) and domain walls ($\mathbf{M} \perp z$) due to SOC induced changes in the electronic structure. The analytical distance dependence found for the conductance can be interpreted as an extension regime of the known exponential behavior of the tunneling current to the contact.

7 Molecular Anisotropic Magnetoresistance

In the previous chapters, we have seen that the AMR reaches values of more than 100 % in monowires but only about 10 % for adatoms on surfaces due to the strong interaction of the adatoms with the surface. In this chapter, we will show how the AMR can be enhanced by the orbital-symmetry filtering properties on the transmission function of metal-benzene complexes.

As we have seen in the previous chapter, the AMR is caused by the SOC induced mixing of specific orbitals at a certain energy which depend on the magnetization direction. However, the magnitude is limited by orbitals which are not affected by SOC at that certain energy but provide a background to the transmission function. This limits the size of the AMR. Therefore, isolating the contribution to the transmission function of the orbitals which are affected by SOC at a certain energy would lead to a large enhancement of the AMR.

A possibility to realize this are molecules. The interactions between organic materials and metals can lead to a very different behavior compared to what is expected from the isolated entities. In combination with spin application the field has been coined "spinterface" science [75]. Apart from interfaces of metals with organic semiconductors, it is also possible to investigate the interface of single molecules with metals theoretically and experimentally [75]. Effects that occur in these spinterface systems are for example spin filtering [75], spin injection [76], and magnetoresistance [77]. In the organic semiconductor/metal interface magnetoresistances of up to 300 % have been found experimentally [77].

For interfaces of metals with single molecules magnetoresistances up to 100 % have been predicted theoretically [78, 79, 80]. Experimentally, values ranging from 16 % to 80 % have been found in break-junction experiments [81, 82], in experiments using the nanopore technique [83], and in STM experiments [84].

Regarding the anisotropic magnetoresistance, values of 3 % in metal/organic semiconductor interfaces have been found [85] and up to 53 % in single molecules utilizing the jump-to-contact STM break-junction technique [86]. The AMR in single molecules observed in Ref. [86] is explained with the help of DFT calculations by the electronic coupling at the interface of the molecule and the leads. However, the calculated transmission coefficients are much larger than the measured conductance [86].

Furthermore, STM experiments have been found to offer sophisticated control of the experimental geometry. For example, it has been shown that the electrodes for single-molecule contacts can be engineered on the atomic-scale [87]. In addition, it is possible to probe the spin-polarization of Co-Phthalocyanine (Co-Pc) molecules absorbed on surfaces with intramolecular spatial resolution [88] and that it should be possible to

map the spatial distributions of the different orbitals of a pyridine-2,5-dicarboxylic acid molecule [76]. Further on, for the Co-Pc molecule it has been shown that the energetically localized molecular orbitals can lead to a negative differential resistance [89] or can have a rectifying effect on the current [90]. It is interesting to note that in Ref. [90] a graphene spacer layer is used to keep the Co-Pc from hybridizing too much with the Ru(0001) substrate, conserving the molecular orbital character, which is critical for the observed effect. Recently, it has been shown that magnetism can be induced in pure organic molecules by doping with single magnetic atoms, where the magnetic atom prefers hybridization with the organic ligands over hybridization with the surface resulting in energetically very localized metal-ligand spin states [91].

We here show that the molecule's energetically localized molecular orbital (MO) can act as a orbital-symmetry filter on the transmission function, which can enhance the AMR created in the contacting monowires by orders of magnitudes. We use sandwich molecules of the VBz_2-type as a model system, which have been studied experimentally [92] and theoretically [93] as isolated entities. The VBz_2-type molecules are contacted by monowires as sketched in Fig. 7.1.

In the following, we will first discuss the computational details of the DFT calculations. Then, we present the scalar-relativistic results for a VBz_2 molecule connected by Ni monowires. We thereby vary the distance between the apex atom of the Ni monowire and the molecule to analyze the general characteristics of the hybridization between the leads and the molecule, which determines the quality of the orbital-symmetry filtering. After that SOC is taken into account for a perpendicular ($\mathbf{M} \perp z$) and a parallel ($\mathbf{M} \parallel z$) orientation of the magnetization with respect to the monowire axis (z-axis). Since molecules are the decisive component in the junction to achieve huge AMRs, we define the molecular AMR via the transmission function as

$$\mathrm{MAMR} = 100\% \cdot \frac{T_{\parallel} - T_{\perp}}{T_{\perp}}. \tag{7.1}$$

To analyze the influence of the contacted molecule on the orbital-symmetry filtering, the VBz_2 molecule is replaced by $NbBz_2$, $TaBz_2$, Bz, and V_2Bz_3, respectively. The influence of the contacting leads is analyzed by replacing the Ni monowires by Co monowires. Finally, a generic TB model is presented, which reproduces the orbital-

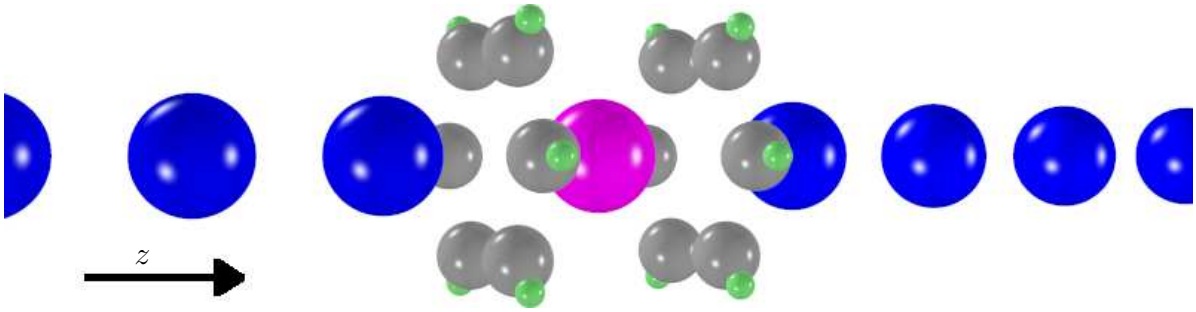

Figure 7.1: Schematic drawing of the Ni-VBz_2-Ni junction. Blue, violet, gray, and green spheres mark Ni, V, C, and H atoms, respectively.

symmetry filtering and shows that the MAMR might also be found in STM experiments of molecules on surfaces.

7.1 Computational Details

To obtain the Hamiltonian of the leads a unit cell containing one Ni (or Co) atom with the theoretical lattice constant of 4.18 bohr using 96 kpts in the IBZ and a value of $k_{\max} = 4.8\,\text{bohr}^{-1}$ has been calculated with the 1D-version of `FLEUR`. The MLWF are obtained from the self-consistent calculations by using 96 k-points in the full Brillouin zone and projecting on five d orbitals and one s orbital per atom out of ten bands for calculations without SOC. For calculations with SOC the numbers of orbitals and bands were doubled.

The unit cell of the scattering region consists of six Ni (or Co) atoms and the molecule. For the VBz_2 (or $NbBz_2$ or $TaBz_2$) molecule the distance of the central metal atom of the molecule to the center of the benzene (Bz) ring is 3.431 bohr. For the benzene the radius of the C ring is 2.675 bohr and the distance between C and H atoms is 2.047 bohr. These are the relaxed distances obtained for the isolated VBz_2 molecule in Ref. [66]. The same distances were also chosen for the V_2Bz_3 molecule. Since this is a concept study and not a study of a realistic system, we did not relax every system individually. In addition, it has been found the the relaxed values do not change a lot for $NbBz_2$, $TaBz_2$ or V_2Bz_3 [93]. For the scattering region eight k-points in the IBZ and a value of $k_{\max} = 4.0\,\text{bohr}^{-1}$ have been used. The MLWF are then obtained using eight k-points in the full Brillouin zone and by projecting on five d orbitals and one s orbital per Ni (Co) atom and V (Nb, Ta) atom and one p_z orbitals per C atom out of 159 bands for the calculations without SOC. For calculations with SOC the number of orbitals and bands were doubled. The energy window has to be chosen such that the relevant states of the molecule are included [94]. In all calculations the local density approximation [95] has been used. The vacuum parameters D and $\tilde{D}$ were chosen 12.0 and 13.0 bohr. The muffin tin radii have been chosen to 1.25, 0.65, 2.4, and 2.0 bohr for the C, H, V (Nb, Ta), and Ni (Co) atom, respectively.

The influence of the number of included nearest neighbors in the Hamiltonian is analyzed in Fig. 7.2 (a) for the Ni−VBz_2−Ni junction with $L_{\text{Ni-V}} = 5.6$ bohr. The unit cell of the scattering region includes five Ni atoms on each side of the molecule. It is found that the transmission function does not change critically if more hoppings than the third nearest neighbor hopping are included.

Fig. 7.2 (b) compares the transmission function of the Ni−VBz_2−Ni junction with $L_{\text{Ni-V}} = 8.0$ bohr including SOC for the third nearest neighbor approximation obtained from a unit cell of the scattering region including three or five Ni atoms on each side of the molecule. It is found that three Ni atoms on each side of the molecule are sufficient to obtain reliable results.

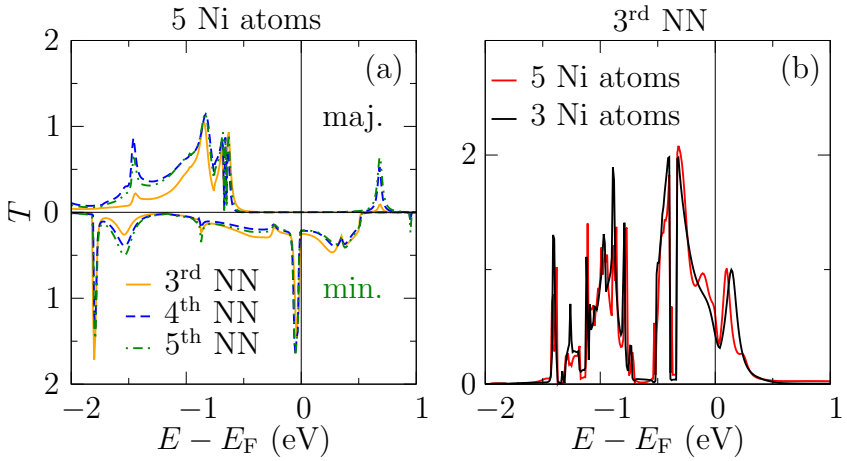

Figure 7.2: (a) Transmission function of the Ni−VBz_2−Ni junction with $L_{\mathrm{Ni-V}} = 5.6\,\mathrm{bohr}$ neglecting SOC and using five Ni atoms on each side of the molecule in the third (orange solid line), fourth (blue dashed line) and fifth (green dashed-dotted line) nearest-neighbor approximation. (b) Transmission function of the Ni−VBz_2−Ni junction with $L_{\mathrm{Ni-V}} = 8.0\,\mathrm{bohr}$ including SOC for $\mathbf{M} \perp z$ taking into accounts hoppings up to the third nearest neighbor obtained using a unit cell for the scattering region containing three (black line) or five (red line) Ni atoms on each side of the molecule.

7.2 Orbital-Symmetry Filtering of the Transmission using VBz_2

The bandstructure of the infinite Ni MW and the local density of states of the isolated VBz_2 molecule neglecting spin-orbit coupling are shown in Fig. 7.3 (a) and (b). The spin splitting of the minority and majority states in the Ni MW leads to a magnetic moment of the Ni atoms of about $1.1\,\mu_{\mathrm{B}}$. For the transmission function the critical bands are the largely dispersive bands of Δ_1-symmetry (s, d_{z^2}) and of the very localized states of Δ_4-symmetry $(d_{xy}, d_{x^2-y^2})$. The bands of Δ_3-symmetry (d_{xz}, d_{yz}) are of minor importance due to the fact that the MOs of the VBz_2 molecule of Δ_3-symmetry are lying energetically very low. In contrast, the molecular orbitals of Δ_1- and Δ_4-symmetry lie very close to the Fermi level and overlap energetically with the corresponding bands in the Ni MW. In the V atom the splitting of minority and majority states leads to a magnetic moment of $1.0\,\mu_{\mathrm{B}}$.

Fig. 7.3 (c) shows the resulting transmission of a VBz_2 molecule contacted by Ni MWs with $L_{\mathrm{Ni-V}} = 8.0\,\mathrm{bohr}$, which means that the distance between the Ni apex atom and the Bz ring is 4.6 bohr. The transmission shows localized contributions of Δ_1-symmetry in the minority and majority channel at $+0.13\,\mathrm{eV}$ and $-0.93\,\mathrm{eV}$ with respect to the Fermi level, respectively, conserving roughly the energy difference between the majority and minority MOs of Δ_1-symmetry of $+1.4\,\mathrm{eV}$. The states of Δ_4-symmetry contribute broad, band-like features from -0.5 to $\pm 0.0\,\mathrm{eV}$ and -1.4 to $-1.0\,\mathrm{eV}$ with respect to the Fermi energy in the minority and majority channel, respectively, coinciding energetically precisely with the Δ_4-bands in the isolated Ni MW.

The strong and weak hybridization of the Δ_4- and Δ_1-orbitals of the Ni apex atoms and the molecule, respectively, can be understood by the insets in Fig. 7.3 (b), which

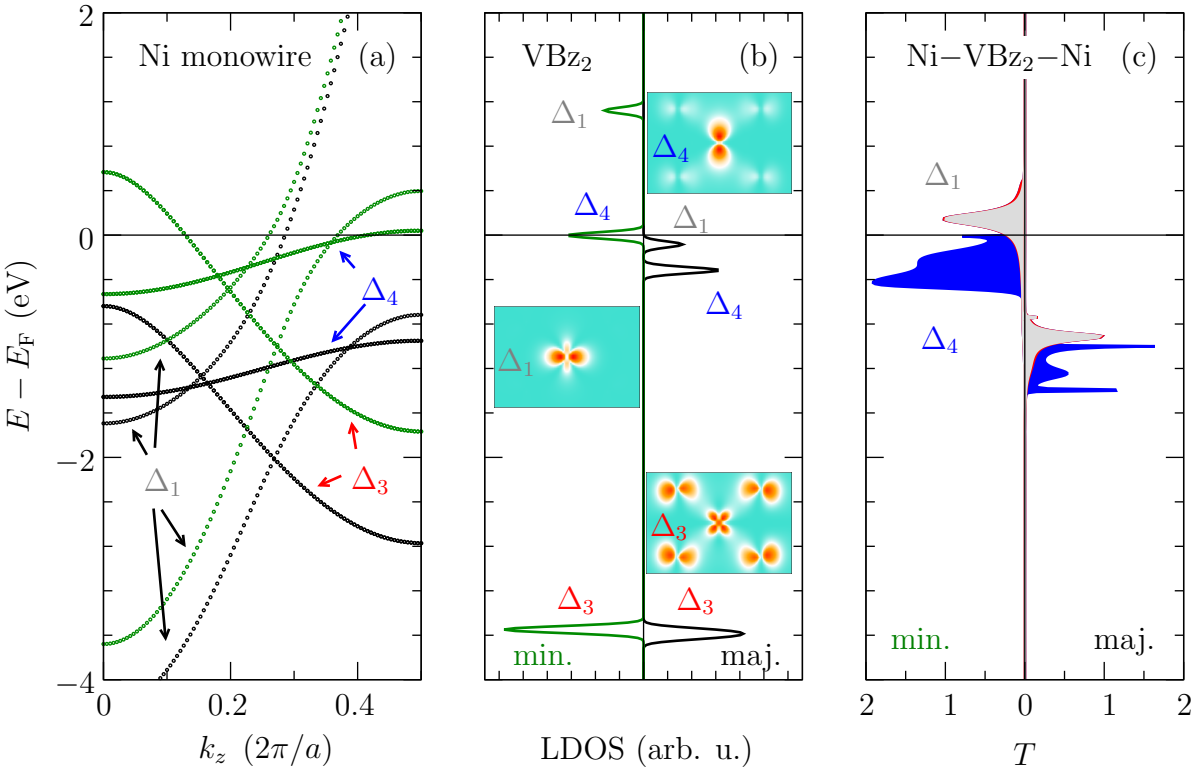

Figure 7.3: (a) Bandstructure of a Ni monowire neglecting spin-orbit interaction. Majority and minority states are marked with black and green circles, respectively. (b) Spin-decomposed local density of states of an isolated VBz_2 molecule neglecting spin-orbit interaction. The insets show plots of the charge density of the orbitals of Δ_1-, Δ_3- and Δ_4-symmetry in the xz-plane. (c) Spin-decomposed transmission of a VBz_2 molecule contacted by Ni monowires neglecting spin-orbit interaction with a distance $L_{\mathrm{Ni-V}} = 8.0\,\mathrm{bohr}$ between the Ni apex atoms and the V atom. The contributions of orbitals of Δ_1-, Δ_3- and Δ_4-symmetry are colored in gray, red and blue, respectively.

show the charge density distribution in the xz-plane of the molecular orbitals. The charge of the molecular orbital of Δ_1-symmetry is concentrated strongly around the V atom and not at all in the C rings. On the other hand, the charge of the Δ_4 molecular orbital is more delocalized covering also the C rings. This leads to an effective bonding distance of the Δ_1-orbitals that is larger than the one of the Δ_4-orbitals.

As one can see in Fig. 7.3 (c) the molecule acts as an orbital-symmetry filter on the transmission function (cf. Fig. 5.7). The quality of the filtering depends on the details of the hybridization between the Ni apex atom and the molecule. To analyze this we vary the distance $L_{\mathrm{Ni-V}}$.

Fig. 7.4 (a) shows the transmission function for a distance $L_{\mathrm{Ni-V}} = 5.6\,\mathrm{bohr}$. The transmission function shows mainly band-like contributions from the Δ_1-orbitals, while sharp peaks from the Δ_3- and Δ_4-orbitals can be seen in the minority channel. The transmission function for $L_{\mathrm{Ni-V}} = 12.0\,\mathrm{bohr}$ in Fig. 7.4 (b) shows only sharp Δ_1-peaks at $-1\,\mathrm{eV}$ below and directly at the Fermi level in the majority and minority spin channel,

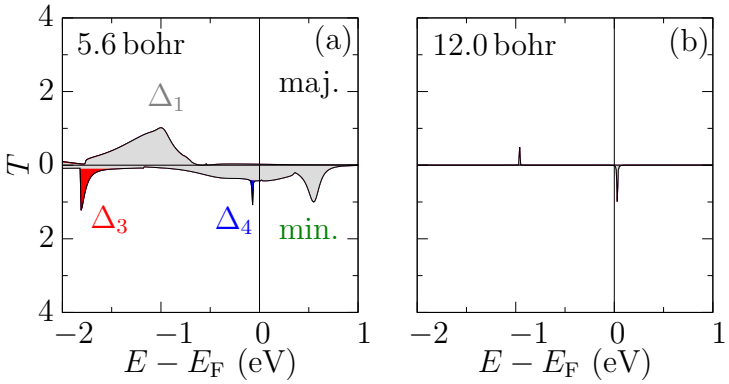

Figure 7.4: Spin-decomposed transmission of a VBz_2 molecule contacted by Ni monowires neglecting spin-orbit interaction for (a) $L_{Ni-V} = 5.6$ bohr and (b) $L_{Ni-V} = 12.0$ bohr, respectively. The contributions of orbitals of Δ_1-, Δ_3- and Δ_4-symmetry are colored in gray, red and blue, respectively.

respectively. The shape of the transmission function for the different L_{Ni-V} can be understood by the local density of states of the VBz_2 molecule and the nearest-neighbor Ni atom for the three values of L_{Ni-V} in Fig. 7.5.

A glance at the LDOS of the nearest neighbor Ni atom and the VBz_2 molecule in Fig. 7.5 (a, b) for $L_{Ni-V} = 12.0$ bohr reveals that the interaction between the lead and the molecule is very small. The LDOS of the VBz_2 shows two peaks in each spin-channel: one composed of the Δ_1-orbitals of the V atom hybridized with p_z orbitals of the C atoms and the other one composed of Δ_4-orbitals of the V and C p_z orbitals. The LDOS is very similar to the one of the completely isolated VBz_2, although the levels of the molecular orbitals are slightly shifted with respect to each other as well as to the Fermi level. The small hybridization between the Δ_1-orbitals of the V atom and the Ni leads explains the two very sharp peaks in the transmission function. The Δ_4-states of the V atom do not hybridize at all with the Δ_4-orbitals of the Ni atom due to the large distance and, therefore, do not contribute to the transmission function.

While the LDOS of the Ni apex atom in Fig. 7.5 (c) for $L_{Ni-V} = 8.0$ bohr does not differ much compared to the case of $L_{Ni-V} = 12.0$ bohr, the Δ_1-peaks in the VBz_2 LDOS, Fig. 7.5 (d), broadens significantly due to the enhanced hybridization with the Ni atom, which also explains the broader transmission peaks of Δ_1-character in Fig. 7.3 (c). The Δ_4-states now show a band-like LDOS similar to the Ni atom and, so to say, continue the Δ_4-band of the Ni leads, which leads to a large transmission contribution of the Δ_4-states.

Further decreasing the distance to $L_{Ni-V} = 5.6$ bohr leads to further broadening of the Δ_1-states of the V atom and the Ni apex atom in Fig.7.5 (e, f), where one sees a very broad LDOS of the Δ_1-orbitals for the Ni atom and the molecule. The Δ_4-orbitals of the Ni atom are now strongly hybridized with the ones of the V atom and the C p_z orbitals. One sees two very sharp features at the Fermi level and -0.7 eV in the LDOS of the molecule and the Ni atom. The reason for this is that the distance of the apex Ni atom to the Bz ring is now smaller than to the next Ni atom in the lead. The Δ_4-states of the adjacent Ni atom decouple from the rest of the lead and the hybridization with the Δ_4-orbitals of the V atom and the C p_z orbitals becomes very strong. The small distance also causes the hybridization of the Δ_3-orbitals with the C p_z orbitals, which explains the Δ_3-contribution to the transmission function.

As we have seen, the orbital-filtering properties are sensitive to the distance L_{Ni-V}.

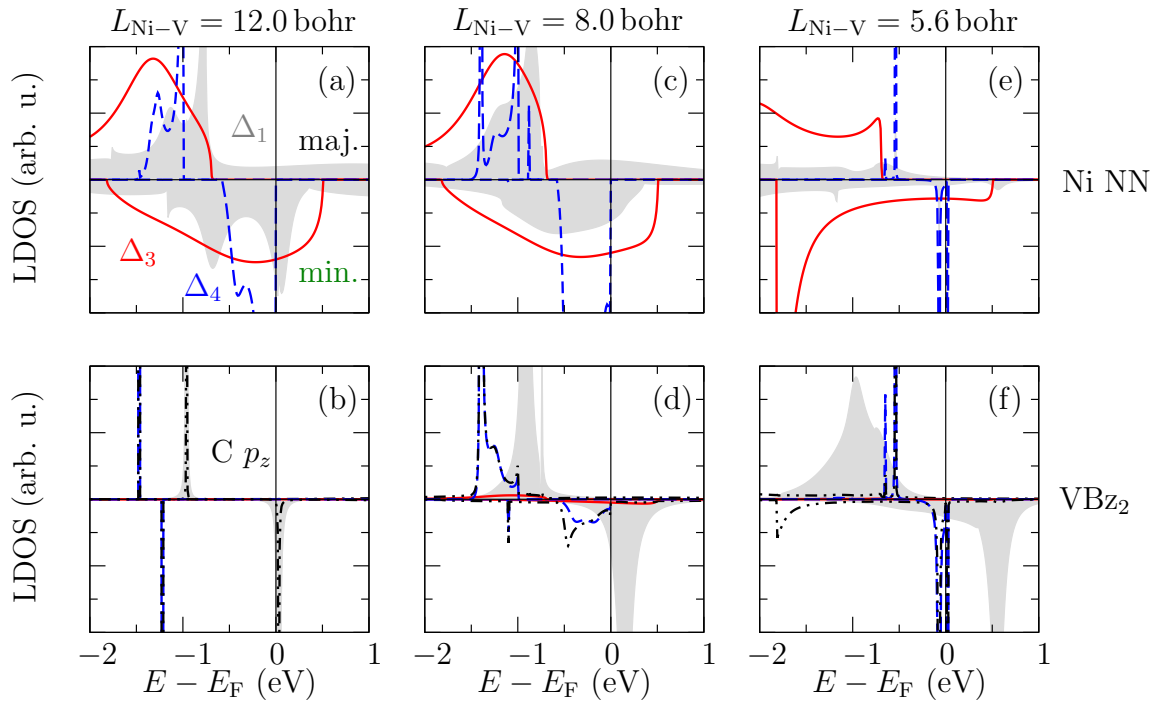

Figure 7.5: LDOS of the Δ_1- (shaded gray), Δ_3- (solid red line) and Δ_4-orbitals (dashed blue lines) of the nearest-neighbor Ni atom (upper panels) and the VBz_2 molecule (lower panels) of a Ni-VBz_2-Ni junction with (a, b) $L_{\mathrm{Ni-V}} = 12.0\,\mathrm{bohr}$, (c, d) 8.0 bohr, and (e, f) 5.6 bohr, respectively. C p_z orbitals are marked by dashed-dotted black lines. SOC is neglected.

If the hybridization between the apex atom and the molecule is too strong ($L_{\mathrm{Ni-V}} = 5.6\,\mathrm{bohr}$), the quality of the filtering decreases since the states of the molecule broaden and contribute to the transmission over a larger energy region. On the other hand, if the hybridization between the apex atom and the molecule is too weak ($L_{\mathrm{Ni-V}} = 12.0\,\mathrm{bohr}$) only the very delocalized orbitals of Δ_1-character remain and nothing else is left to filter. Since the largest SOC effects are occurring for the localized d orbitals an intermediate distance of $L_{\mathrm{Ni-V}} = 8.0\,\mathrm{bohr}$ is the optimal case to combine the orbital-symmetry filtering with the AMR.

7.3 Combining AMR with Orbital-Symmetry Filtering

After establishing the orbital-symmetry filtering effect of the VBz_2 molecule on the transmission function, we now analyze the impact of SOC for the two magnetization directions with respect to the wire axis ($\mathbf{M} \perp z$ and $\mathbf{M} \parallel z$).

Fig. 7.6 (a) shows the bandstructure of a perfect Ni MW for the two directions of magnetization. We focus here on the three marked splittings labeled 1, 2 and 3. 1 is the crossing of the Δ_4- and Δ_3-bands at $E_\mathrm{F} - 0.38\,\mathrm{eV}$, which becomes an avoided level crossing due to SOC induced hybridization for $\mathbf{M} \perp z$. As a result there are only states of Δ_1-symmetry available from $E_\mathrm{F} - 0.4\,\mathrm{eV}$ to $E_\mathrm{F} - 0.33\,\mathrm{eV}$. The changes

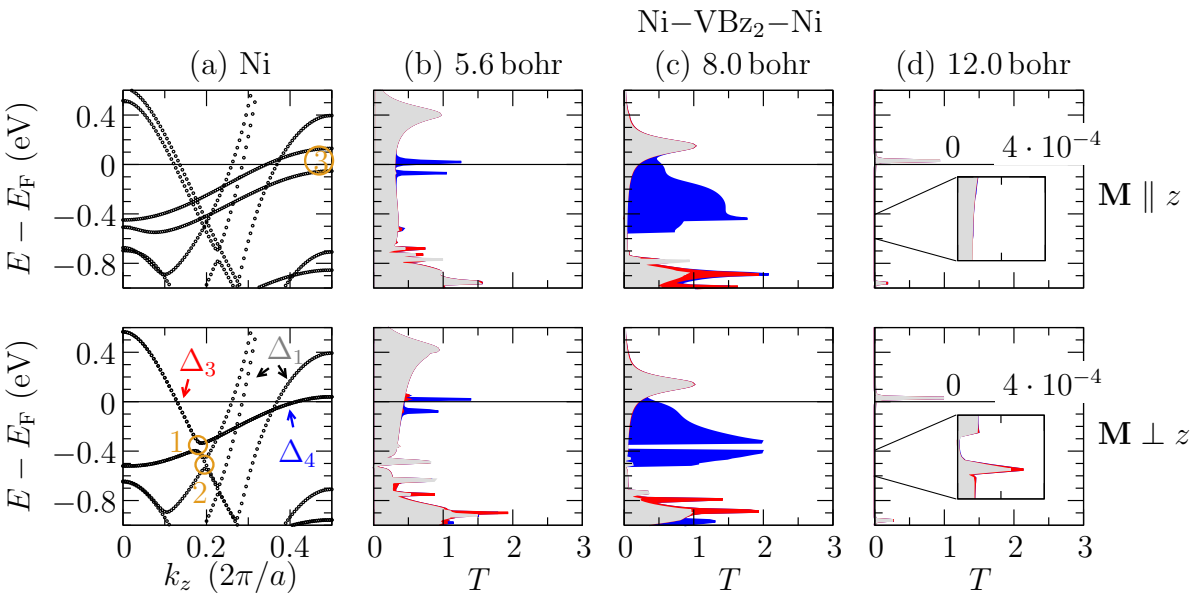

Figure 7.6: (a) Ni bandstructure with spin-orbit coupling for $\mathbf{M} \perp z$ (top) and $\mathbf{M} \parallel z$ (bottom). (b) Transmission function of the Ni-VBz$_2$-NI junction with $L_{\mathrm{Ni-V}} = 5.6\,\mathrm{bohr}$ for $\mathbf{M} \parallel z$ (top) and $\mathbf{M} \perp z$ (bottom). The contributions of orbitals of Δ_1-, Δ_3- and Δ_4-symmetry are colored in gray, red and blue, respectively. (c) shows the same as (b) for $L_{\mathrm{Ni-V}} = 8.0\,\mathrm{bohr}$. (d) shows the same as (c) for $L_{\mathrm{Ni-V}} = 12.0\,\mathrm{bohr}$.

in the bandstructure due to SOC are directly passed on to the transmission function of the Ni−VBz$_2$−Ni junction with $L_{\mathrm{Ni-V}} = 8.0\,\mathrm{bohr}$ in Fig. 7.6 (c). For $\mathbf{M} \perp z$ the Δ_4-contribution to the transmission function is quenched between $E_\mathrm{F} - 0.4\,\mathrm{eV}$ to $E_\mathrm{F} - 0.33\,\mathrm{eV}$ and the magnitude of the remaining transmission function is on the order of 0.05 is due to the tail of the localized Δ_1-peaks at $E_\mathrm{F} + 0.1\,\mathrm{eV}$ and $E_\mathrm{F} - 0.9\,\mathrm{eV}$. However, for $\mathbf{M} \parallel z$ the transmission function has a value of about 1.5 originating mainly from the Δ_4-states. This leads to a MAMR on the order of 1000 %. The BAMR at the Fermi level described by Velev *et al.* [9] originating from the lifted degeneracy of the Δ_4-states (cf. Fig. 7.6 (a)) marked by 3, is enhanced to a value of −30 % compared to the −18 % of the pure Ni monowire (cf. chapter 5). The reason for this smaller enhancement is that the Δ_1-peak in the transmission function is also close to the Fermi level yielding a large background.

For the case of $L_{\mathrm{Ni-V}} = 5.6\,\mathrm{bohr}$, Fig. 7.6 (b), one does not find a large MAMR due to the very strong hybridization between the Ni apex atom and the molecule described in the previous section. The differences in the transmission for the two magnetization directions here only lead to values of the MAMR of similar magnitude as for the infinite Ni MW.

Fig. 7.6 (d) shows the case of $L_{\mathrm{Ni-V}} = 12.0\,\mathrm{bohr}$. Here, the MAMR in the energy region from $-0.4\,\mathrm{eV}$ to $-0.33\,\mathrm{eV}$ vanishes, since the contribution from the Δ_4-states to the transmission vanishes. However, one now sees an effect from the avoided level crossing at $-0.5\,\mathrm{eV}$ of the Δ_1- and Δ_3-band in Fig. 7.6 (a) for $\mathbf{M} \perp z$ marked by 2. Since only Δ_1-states contribute to the transmission at $L_{\mathrm{Ni-V}} = 12.0\,\mathrm{bohr}$ this leads to an MAMR of about 1000 %.

7.3.1 Influence of the Electronic Structure of the Molecule and the Leads

Size of the Molecule

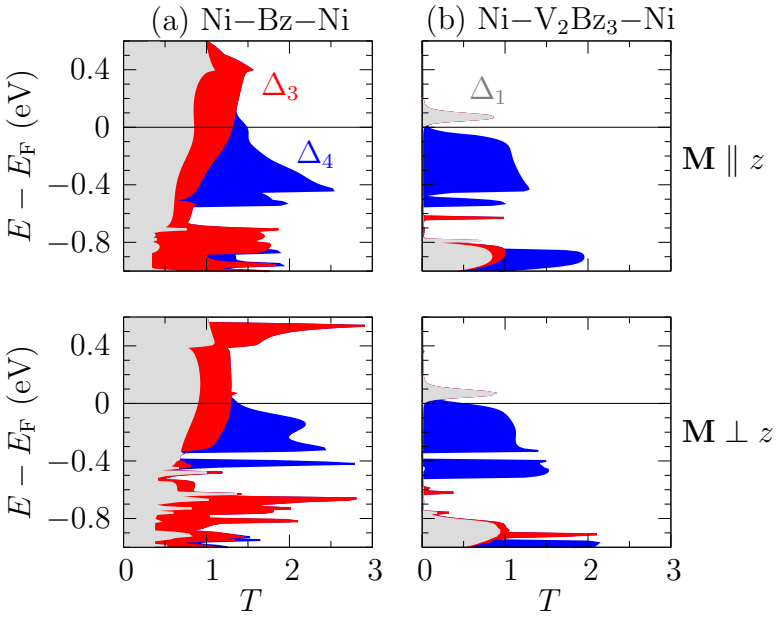

Figure 7.7: (a) Transmission function of a Bz molecule contacted by Ni monowires with $L_{\mathrm{Ni-Bz}} = 4.59\,\mathrm{bohr}$ for $\mathbf{M} \parallel z$ (top) and $\mathbf{M} \perp z$ (bottom). The contributions of orbitals of Δ_1-, Δ_3- and Δ_4-symmetry are colored in gray, red and blue, respectively. (b) shows the same as (a) of a V_2Bz_3 molecule for $L_{\mathrm{Ni-V}} = 8.0\,\mathrm{bohr}$.

The strength of the orbital-symmetry filtering does not only depend on the distance $L_{\mathrm{Ni-V}}$ but can also be "engineered" by the size of the contacted molecule.

For a Bz molecule contacted by a Ni MW, Fig. 7.7 (a), with a distance of $L_{\mathrm{Ni-Bz}} = 4.59\,\mathrm{bohr}$ between the Ni apex atom and the Bz ring[1] the contribution of the states of Δ_1- and Δ_3-symmetry to the transmission function show band-like features due to the strong hybridization of the Ni apex atoms with the Bz ring and each other through the Bz ring. This leads to poor orbital-symmetry filtering leaving a value of the transmission function of about 0.7 for $\mathbf{M} \perp z$ in the energy range from $-0.4\,\mathrm{eV}$ to $-0.33\,\mathrm{eV}$ below the Fermi level. The transmission function for $\mathbf{M} \parallel z$ shows a value of about 2.2 leading to a MAMR of about 200 % one magnitude smaller compared to the VBz_2 junction.

If V_2Bz_3 is contacted by the Ni leads with $L_{\mathrm{Ni-V}} = 8.0\,\mathrm{bohr}$, the MAMR is enhanced even more compared to the case of VBz_2. For this system the Δ_1-transmission peak at 0.05 eV in Fig. 7.7 (b) becomes very sharp and also the tails of the peaks at 0.05 eV and $-0.9\,\mathrm{eV}$ are strongly suppressed. Therefore, the transmission function between $-0.4\,\mathrm{eV}$ to $-0.33\,\mathrm{eV}$ is nearly solely constituted by states of Δ_4-symmetry. The remaining transmission function in this energy region for $\mathbf{M} \perp z$ is only of the order of 10^{-3}, while for a parallel magnetization it is 1.2. This results in an MAMR of about 100000 %, which is two magnitudes larger compared to the VBz_2 junction.

The AMR at the Fermi level due to the lifted degeneracy of the Δ_4-states at the Fermi level is enhanced to −85 %.

[1] This is the same distance between the Ni apex atom and the Bz ring as in the VBz_2 junction contacted by Ni MWs with $L_{\mathrm{Ni-V}} = 8.0\,\mathrm{bohr}$.

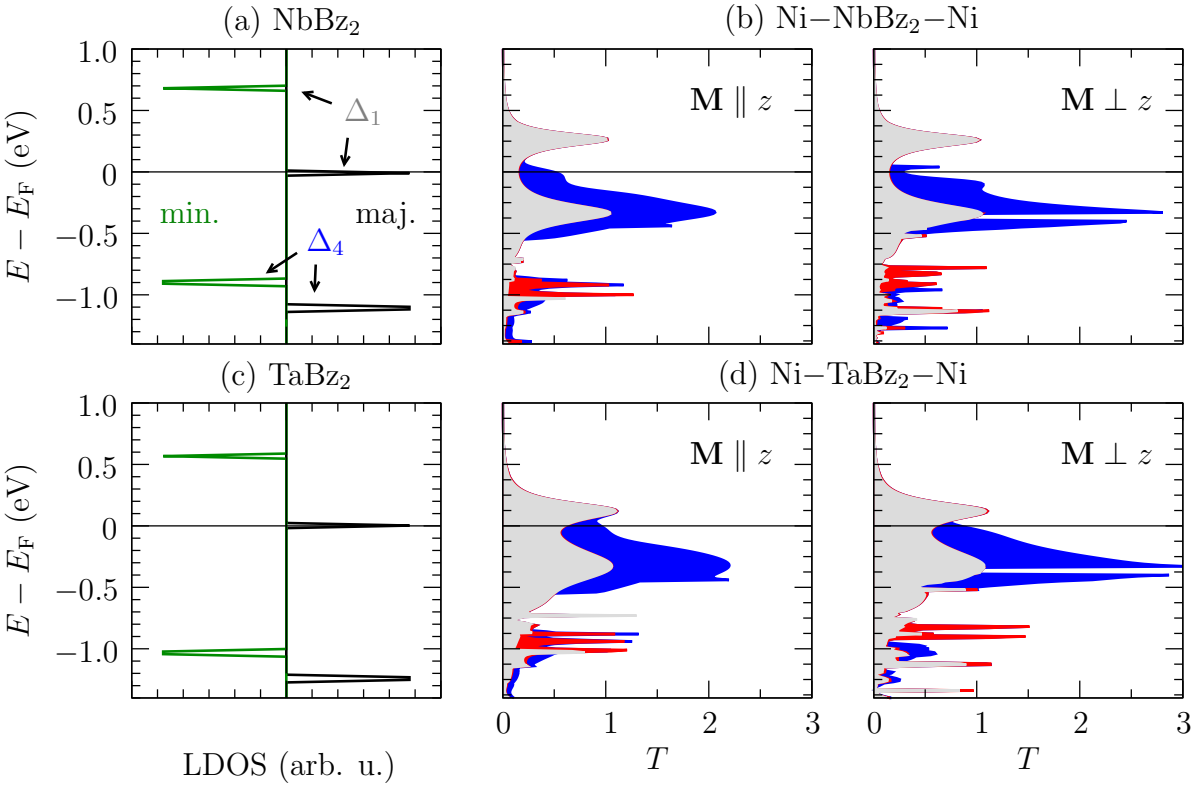

Figure 7.8: (a) Spin-decomposed local density of states of an isolated $NbBz_2$ molecule neglecting spin-orbit interaction. (b) Transmission function of a $NbBz_2$ molecule contacted by Ni monowires with SOC for $\mathbf{M} \parallel z$ (left) and $\mathbf{M} \perp z$ (right). The contributions of orbitals of Δ_1-, Δ_3- and Δ_4-symmetry are colored in gray, red and blue, respectively. (c) Spin-decomposed local density of states of an isolated $TaBz_2$ molecule neglecting SOC. (d) Transmission function of a $TaBz_2$ molecule contacted by Ni monowires with SOC for $\mathbf{M} \parallel z$ (left) and $\mathbf{M} \perp z$ (right).

Electronic Structure of the Molecule

The quality of the orbital-symmetry filtering of the junctions strongly depends on the energetic position of the MOs of the contacted molecule. Fig. 7.8 (a) shows the LDOS of $NbBz_2$, which is very similar to VBz_2. However, the spin splitting of the MOs of Δ_1-symmetry amounts only to 0.7 eV, half as large as for VBz_2, which is also mirrored in the magnetic moment of 0.67 μ_B. As we have seen before for VBz_2, the spin splitting between the states of Δ_1-symmetry is nearly conserved when the molecule is contacted by the Ni MW, which in the case of $NbBz_2$ is about 0.6 eV, Fig. 7.8 (b). This leads to the fact that in the transmission the peak due to the majority state of Δ_1-symmetry lies at −0.36 eV, which is directly in the energy region of the avoided level crossing in the bandstructure of the Ni MW for $\mathbf{M} \perp z$. Therefore, the transmission function for $\mathbf{M} \perp z$ still shows a value of about 1 in the energy region from −0.4 eV to −0.33 eV and a value of 1.7 for $\mathbf{M} \parallel z$. The resulting MAMR then amounts only to 90 %. The MAMR at the Fermi level amounts to 67 %, approximately four times as large as the originally proposed BAMR [9].

Table 7.1: Top: MAMR at $E_F - 0.36\,\text{eV}$ of a VBz_2 molecule contacted by Ni leads with distances L_{Ni-V} ranging from 5.6 to 12.0 bohr and of different molecules contacted by Ni leads with $L_{Ni-V} = 8.0$ bohr. Bottom: MAMR at $E_F - 0.36\,\text{eV}$ for different molecules contacted by Ni MWs whereby the distance from the nearest neighbor Ni atom to the metal atom of the molecule is 8.0 bohr or 4.59 bohr to the benzene ring. The AMR of the Ni MW is shown for comparison.

	L_{Ni-V} (bohr)					
	5.6	7.0	8.0	9.0	12.0	Ni MW
MAMR (%)	0	2500	3500	74	3	130
	molecule at $L_{Ni-V} = 8.0$ bohr					
	Bz	VBz_2	V_2Bz_3	$TaBz_2$	$NbBz_2$	Ni MW
MAMR (%)	230	3500	130000	100	90	130

For Ta in Fig. 7.8 (c) and (d) the spin splitting of the MOs has a very similar size as for Nb and the MAMR in the energy region from $-0.4\,\text{eV}$ to $-0.33\,\text{eV}$ only amounts to about 100 %. At the Fermi level the MAMR only reaches a value of -8 %.

This behavior is counter-intuitive because Nb and Ta are heavier than V and, therefore, one would expect a larger MAMR due to the enhanced SOC. However, the size of the SOC in the molecule is not decisive here since the size of the avoided level crossing is determined by the Ni MW and the molecule only acts as a filter.

Tab. 7.1 summarizes the values of the MAMR at $-0.36\,\text{eV}$ of a VBz_2 molecule contacted by Ni MWs with distances L_{Ni-V} ranging from 5.6 to 12.0 bohr. The MAMR starts with a value of 0 % at a distance of 5.6 bohr, rises to its maximum at 7.0 bohr and 8.0 bohr of a few thousands of percent and then decays again to 3 % at 12.0 bohr. This behavior is due to the different strengths of the hybridization of orbitals between the Ni apex atom and the VBz_2 molecule. At small distances L_{Ni-V} the hybridizations are very strong leading to a large background to the transmission function which quenches the MAMR created by the states of Δ_4-symmetry. The hybridization reduces strongly for the states of Δ_1- and Δ_3-symmetry at intermediate distances of 7.0 bohr and 8.0 bohr, while it stays strong for the states of Δ_4-symmetry as has been discussed for Fig. 7.5. Therefore, the orbital-symmetry filtering is at its best at these distances. Eventually, at very large distances the overlap of the states of Δ_4-symmetry vanishes and with it the MAMR and only tunneling through the delocalized states of Δ_1-symmetry remains. Tab. 7.1 also summarizes the MAMR for the different contacted molecules.

Electronic Structure of the Leads

To demonstrate the influence of the leads, we replace the Ni MWs in the Ni−VBz_2−Ni junction with Co MWs where $L_{Co-V} = 8.0$ bohr. In the bandstructure of an infinite Co MW calculated neglecting SOC, Fig. 7.9 (a), the bands of Δ_3- and Δ_4-symmetry cross at $-0.13\,\text{eV}$ marked with 1. Therefore, also the avoided level-crossing for $\mathbf{M} \perp z$ due to SOC is created at that energy as can be seen in Fig. 7.9 (b) for $\mathbf{M} \perp z$. Since Co is

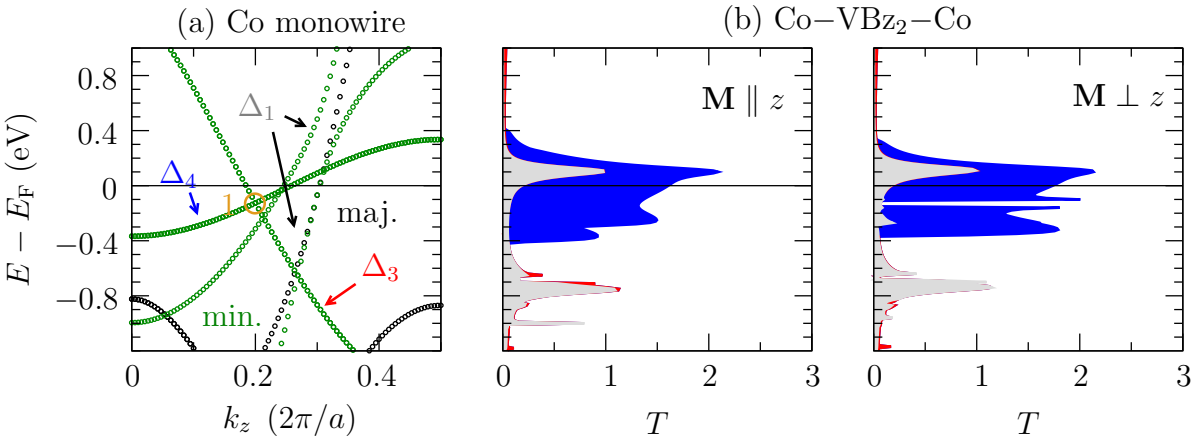

Figure 7.9: (a) Bandstructure of an infinite Co monowire neglecting SOC. Majority and minority states are marked with black and green circles, respectively. (b) Transmission function of a VBz_2 molecule contacted by Co monowires with SOC for $L_{Co-V} = 8.0\,\text{bohr}$ for $\mathbf{M} \parallel z$ (left) and $\mathbf{M} \perp z$ (right). The contributions of orbitals of Δ_1-, Δ_3- and Δ_4-symmetry are colored in gray, red and blue, respectively.

slightly lighter than Ni, the SOC effects are reduced compared to the Ni leads and the energy range devoid of states of Δ_3- and Δ_4-symmetry for $\mathbf{M} \perp z$ goes from $-0.1\,\text{eV}$ to $-0.15\,\text{eV}$, i.e., over a range of 50 meV compared to 67 meV for the Ni MW. The MAMR in this energy region is about 1800 % of a similar magnitude as for the molecule contacted by Ni.

7.4 Tight-Binding Model of the Orbital-Symmetry Filtering

In Fig. 7.10 we present a TB model of the orbital-symmetry filtering. It consists of the apex atom of an STM tip and a molecule coupled to a surface. The STM tip is assumed to be in contact with the molecule so the couplings to the molecule are rather large. The molecule is only weakly coupled to the surface assuming that it keeps its molecular orbitals. As found in the results from DFT we assume the effective bonding distance of the localized d_{xy} state of the molecules to the surface to be smaller than for the s state. Therefore, the transition matrix element from the apex atom to the molecule is larger for the xy state than for the s state. The electronic states of the substrate and the molecule are assumed to be spin split so we only have to consider three orbitals of minority spin character, which are of s, d_{xy}, and d_{yz} type. The parameters of the TB model are displayed in Tab. 7.2.

The LDOS at the apex atom of the STM tip in Fig. 7.11 (a) of the s orbital is rather broad while the one for d_{xy} and d_{yz} orbital is sharp. The d_{xy} orbital shows a two peak structure due to the hybridization with the molecule, which is not possible for the d_{yz} orbital since the on-site energies of the molecule and the adatom of this orbital are assumed to differ strongly (cf. Tab. 7.2). The LDOS at the molecule in Fig. 7.11 (b) shows a rather sharp peak of the s orbital and a two peak structure of the d_{xy} orbital

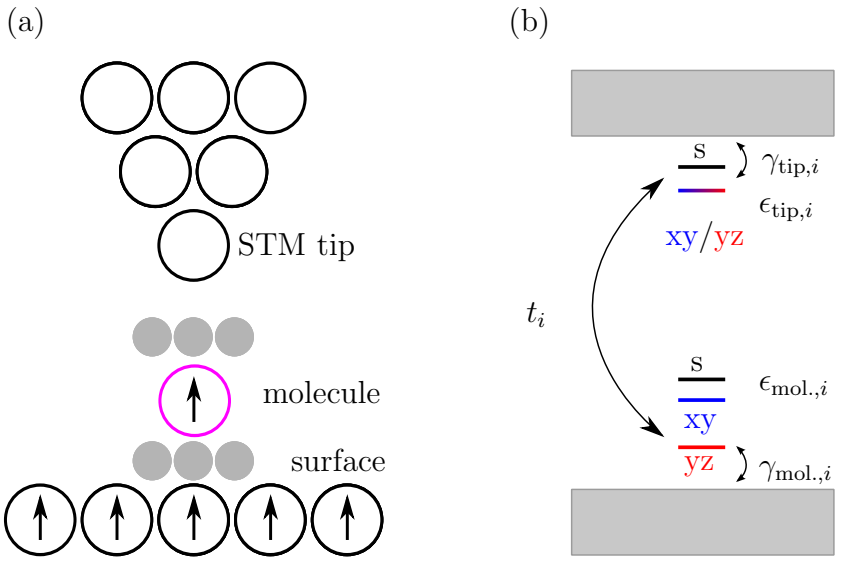

Figure 7.10: (a) Sketch of the geometry assumed in the TB model used to simulate the orbital-symmetry filtering for molecules on surfaces. (b) Energy levels and couplings of the TB model of the orbital-symmetry filtering.

with the same width as on the apex atom.

The transmission function in Fig. 7.11 (c) also shows a sharp peak of the s orbital and a broad band-like feature of the d_{xy} orbital. The result is very similar to the one obtained for the VBz_2 molecule contacted by Ni monowires in Fig. 7.3 and suggests that the orbital-symmetry filtering can also be found for molecules on surfaces.

Experimentally, it has been shown that ferrocene molecules, which are structurally very similar to the metal-benzene molecules considered here, form physisorbed molecular layers on metal surfaces [96, 97]. Since they are mainly bound by van der Waals forces, the states of the molecules keep their MO character. As shown in the previous sections and in Ref. [10] the AMR can also be found on surfaces. Therefore, it should be possible to combine the AMR of a magnetic surface with the orbital-symmetry filtering of the metal-benzene molecules.

7.5 Summary

We have shown that the interface of 3d-metal MWs with metal-benzene molecules leads to an orbital-symmetry filtered transmission function. Furthermore, we have shown how the quality of the orbital-symmetry filtering depends on the details of the hybridization of the apex atom of the MW with the molecule and on the chemical composition of

	ϵ_s (eV)	ϵ_{xy} (eV)	ϵ_{yz} (eV)	γ_s (eV)	γ_{xy} (eV)	γ_{yz} (eV)
tip atom	0.0	−0.2	−0.2	0.5	0.075	0.1
molecule	0.1	−0.2	−3.5	0.05	0.1	0.1
$t_{\mathrm{tip-mol.}}$	t_s	t_{xy}	t_{yz}			
	0.1	0.15	0.1			

Table 7.2: Parameters chosen for the TB model sketched in Fig. 7.11.

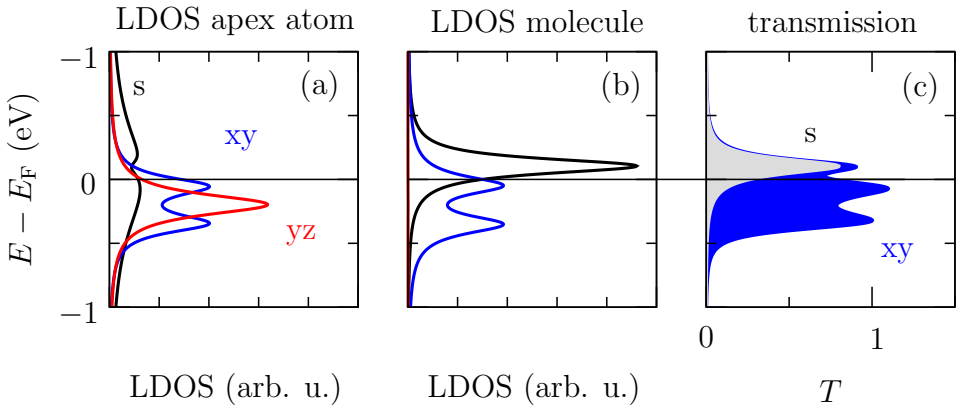

Figure 7.11: LDOS at (a) the apex atom of the STM tip and (b) the molecule. The LDOS of the s, d_{xy}, and d_{yz} state are depicted by black, blue, and red lines, respectively. (c) shows the transmission function. The s, d_{xy}, and d_{yz} contributions are colored gray, blue, and red, respectively.

the molecule. In addition, the AMR caused by SOC in the contacting leads, which is limited to about 100 % in the infinite MW, can be enhanced with the help of the orbital-symmetry filtering by orders of magnitudes reaching values of more than 1000 %. Since molecules are the pivotal part in these junctions, we dubbed the combination of the orbital-symmetry filtering with the anisotropic magnetoresistance MAMR. Finally, we have shown with a generic TB model that the orbital-symmetry filtering might also be found in molecules on surfaces and, thus, also the MAMR.

8 Anisotropic Magnetoresistance of Pt Break Junctions

In the previous chapters we analyzed the general features of the anisotropic magnetoresistance in the contact and tunneling regime of single-atom and -molecule contacts utilizing idealized monowire geometries for the leads. Here, we go beyond the idealized monowire geometry and take into account a more realistic geometry for the leads and structural relaxations of a Pt trimer connected to bulk-like bcc-(001) contacts in a break-junction geometry.

Bulk Pt is close to fulfilling the Stoner criterion for ferromagnetism. In break junctions, it is known to form atomic wires [98, 99]. According to several theoretical studies Pt becomes magnetic for systems with reduced dimensions [100, 101, 102, 103], because the reduced coordination number leads to a smaller bandwidth of the LDOS fulfilling the Stoner criterion. However, direct experimental verification of this emergent magnetism is very challenging. A workaround to detect this magnetism directly is to measure the AMR, which requires the existence of a spontaneous magnetization. Therefore, the detection of the AMR would be an indirect proof an emergent magnetization.

It has already been mentioned that the detection of the AMR in break-junction experiments itself is challenging. Several papers report the AMR in a contact and tunneling geometry of intrinsically magnetic break junctions consisting of $3d$-elements Co [57, 63], Fe [61, 63] and Ni [63]. However, other interpretations in terms of magnetostriction [58, 59] or quantum interference [60] remain possible.

Recently, results of Pt break-junction experiments have been presented [22] strongly indicating an emergent magnetism of Pt in reduced dimensions. However, due to the unknown geometry of the break junction speculation about the interpretation of the results is unavoidable and theoretical calculations of the transport properties are necessary. In Ref. [22] values of around 1.0 to $1.25\,G_0$ attributed to monoatomic chains of two to four Pt atoms are found. Theoretical calculations indicate that the easy magnetization direction lies along the monowire axis [104, 105, 106]. Therefore, the measured magnetoconductance ratio (MCR) in Ref. [22] defined as the difference between the conductance with an applied magnetic field perpendicular to the current direction and without an applied magnetic field divided by the latter value is a first indicator of the anisotropic magnetoresistance in these systems[1]. The obtained MCR is on the order of 10 % to 30 % with changing sign during elongation. A hysteresis of the MCR has been found and has been proposed to be connected to the anisotropy energy

[1]The MCR is the anisotropic magnetoresistance if the magnetic field is large enough to align all magnetic moments and if the magnetization without an applied magnetic field really lies parallel to the current.

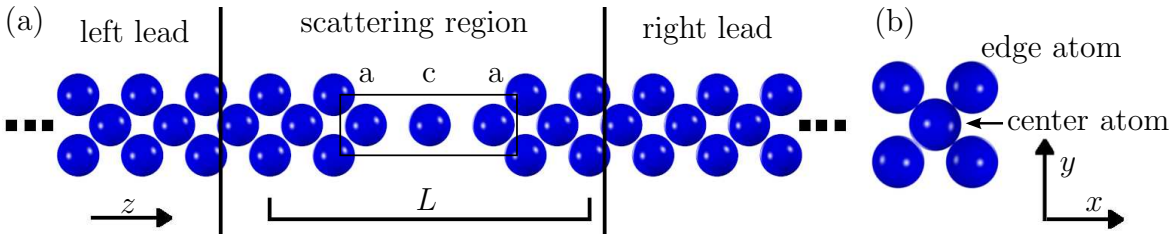

Figure 8.1: (a) Sketch of the junction used to calculate the transmission function of the Pt trimer marked by the rectangular box attached to bulk-like bcc-(001) electrodes. The trimer consists of two apex atoms and a central atom marked by letters a and c, respectively. (b) Front view of the bulk-like bcc-(001) Pt electrodes.

of the electrodes. The AMR as a function of the angle of the applied magnetic fields with respect to the direction of the current θ is in the range of 6 %, changes sign during elongation, and follows approximately a $\cos^2\Theta$-dependence [22]. The different values of the MCR and AMR can be attributed to the applied magnetic field, which ranges from -8 to $+8$ T for the MCR but only has a magnitude of 2.5 T for the AMR.

The transmission function of Pt chains contacted by bulk electrodes has been studied in Ref. [106] considering three to five atoms. However, the distances between the atoms were fixed and the effect of the continuous elongation of the break junction was not considered.

Here, we provide a complementary theoretical study to the experiments presented in Ref. [22] of the anisotropy of the transmission function of a Pt trimer suspended between bulk-like bcc-(001) contacts elongated to several distances, the magnetic and geometrical properties of which are presented in detail in Ref. [104].

The geometrical setup can be seen in Fig. 8.1. The distance between the layers of the leads L is elongated by ΔL ranging from 0.0 to 3.0 bohr. The values for the relaxed structure are taken from Ref. [104] and the transmission function for a magnetization parallel to the trimer axis $\mathbf{M} \parallel z$ and parallel to the x-axis $\mathbf{M} \parallel x$ denoted as $\mathbf{M} \perp z$, is calculated.

The analysis starts with details on the setup of the calculation and cutoff tests regarding the choice of the Wannier functions. Due to the high complexity in this system, which is only a little more complicated than the monowire, we first analyze the transmission function in the scalar-relativistic approximation. Then SOC is considered for $\mathbf{M} \parallel z$ and $\mathbf{M} \perp z$.

We find slightly smaller values of the conductance compared to the experimental results ranging from 0.75 to $0.9\,G_0$ which change slightly during elongation. The AMR goes up to about 20 % in magnitude and changes sign during elongation. During the elongation of the trimer a sign change and an increase in magnitude near the Fermi level can be found for the differential $\mathrm{AMR}_{\mathrm{diff.}}$ of the transmission function. These effects originate from changes in the electronic structure due to the emergent magnetism and the bonding characteristics in the trimer for the different elongations ΔL. We furthermore find that SOC changes the transport properties dramatically compared to the SR approximation, which is attributed to the SOC induced spin- and orbital-mixing.

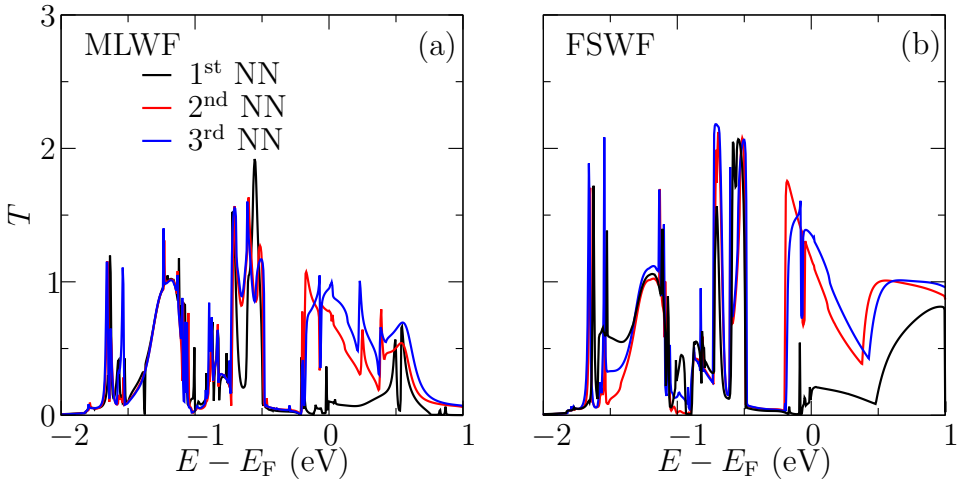

Figure 8.2: Transmission function of the majority spin channel of the Pt trimer attached to bulk-like bcc-(001) electrodes with $\Delta L = 1.2$ bohr using (a) maximally-localized Wannier functions and (b) first-shot Wannier functions in the first (black), second (red), and third (blue) nearest-neighbor approximation without SOC.

8.1 Computational Details

Fig. 8.1 shows the geometrical setup of the junction investigated in this chapter. In the DFT study of these junctions [104] the contact separation $L = 30.1$ bohr is enlarged by ΔL ranging from 0.0 bohr to 3.0 bohr. All atoms except the three atoms of the trimer are kept fix. The central atom of the trimer is fixed by symmetry and, therefore, the relaxation is defined by the movement of the two apex atoms of the trimer. We here take the relaxed values obtained in Ref. [104].

The scattering region is calculated using the 1D-version of `FLEUR` in a unit cell with a length of 44.2 bohr including 27 atoms. $k_{\max}$ is set to 3.6 bohr^{-1} and eight k-points are used in the IBZ. SOC is taken into account self-consistently. GGA is used and the muffin tin radii are set to 2.6 bohr. The vacuum parameters D and $\tilde{D}$ are chosen 13.0 and 14.0 bohr, respectively.

First-shot Wannier functions are used since it was not possible to obtain MLWF for the systems including SOC in adequate quality. In Figs. 8.2 (a, b) it can be seen that the qualitative difference between the transmission function from FSWF and MLWF is not large. Only the localization of the s-like orbitals of the FSWF leads to a slightly enhanced transmission function around the Fermi level compared to the MLWF, while the transmission of the d-orbitals shows very similar shapes and magnitudes. The FSWF were obtained by projecting on five d and one s orbitals per Pt atom out of 243 bands. For calculations with SOC these numbers were doubled.

The leads are calculated in a unit cell with a length of 7.04 bohr including five Pt atoms, using 16 k-points and $k_{\max} = 3.6$ bohr^{-1}. The FSWF were obtained by projecting on five d and one s orbitals per Pt atom out of 45 bands. For calculations with SOC the numbers were doubled.

The scattering region consisting of the trimer and two base layers of four atoms

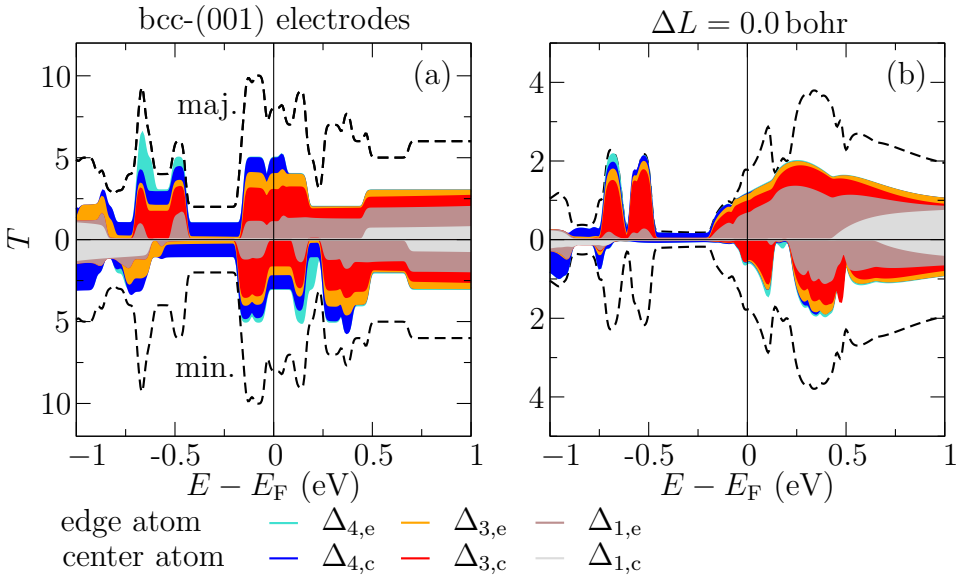

Figure 8.3: Spin-decomposed transmission function of (a) the bulk-like bcc-(001) electrodes and (b) the Pt trimer with $\Delta L = 0.0\,\text{bohr}$ attached to bulk-like bcc-(001) electrodes. The contributions of orbitals of different character and their localization at the edge or center atom are marked in the colors as stated in the legend. The dashed lines show the total transmission summed over both spin channels for comparison.

on each side is attached to semi-infinite leads as sketched in Fig. 8.1. Regarding the hoppings, the 3rd nearest-neighbor approximation with respect to layers is used to calculate the transmission function, where one nearest-neighbor layer consists of five atoms. Ghost atoms are added to the trimer to fill the matrices properly. As can be seen in Figs. 8.2 (a) and (b) for both, the MLWF and the FSWF, the third and second nearest-neighbor approximation yield very similar results indicating an already well converged transmission function using three nearest-neighboring layers.

To simplify the interpretation of the data we use a moderate Gaussian broadening with standard deviation $\sigma = 0.01\,\text{eV}$ to calculate the transmission function and local density of states, which can be interpreted as a temperature broadening.

8.2 Magnetic and Transport Properties neglecting SOC

We start by analyzing the transmission function of the bulk-like bcc-(001) electrodes contacting the junction in Fig. 8.3 (a) for the majority and minority spin channel. The transmission function is spin-polarized due to the formation of magnetic moments of the Pt atoms caused by the reduced coordination number. The magnetic moments of the bulk-like bcc-(001) electrodes amounts to $0.18\,\mu_\text{B}$ and $0.44\,\mu_\text{B}$ for the center and edge atoms, respectively. The decomposition into the different orbital types and atoms surprisingly shows that around the Fermi level from -0.5 to $0.5\,\text{eV}$ no Δ_1 (s, d_{z2})-states from the center atom are contributing to the transmission of the majority or minority spin channel. However, Δ_3 (d_{xz}, d_{yz})- and Δ_4 $(d_{xy}, d_{x^2-y^2})$-states of the center atom

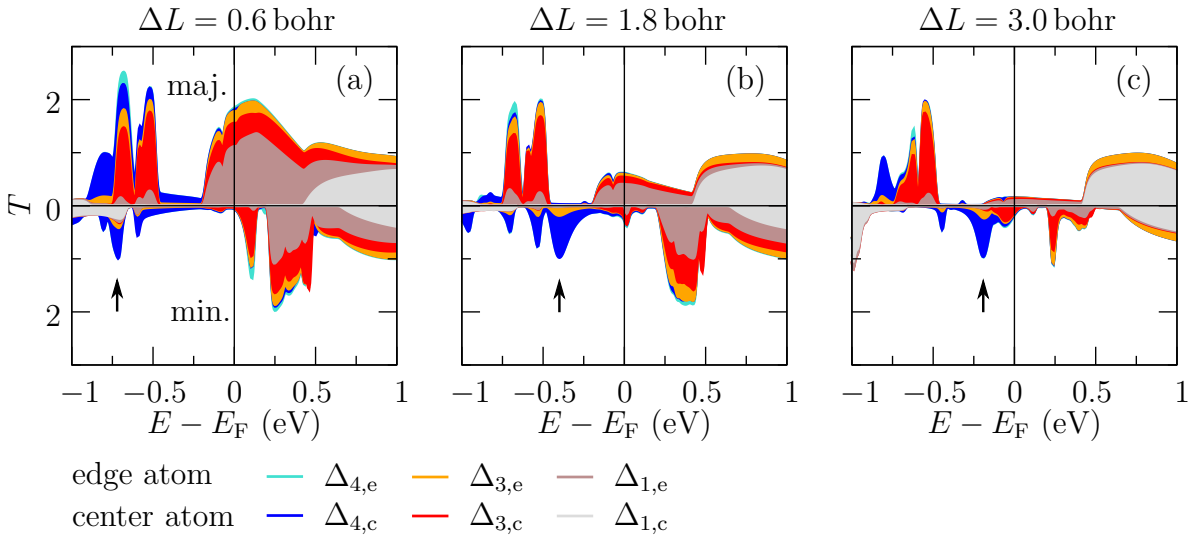

Figure 8.4: Spin-decomposed transmission function of the Pt trimer with (a) $\Delta L = 0.6\,\text{bohr}$, (b) $\Delta L = 1.8\,\text{bohr}$, and (c) $\Delta L = 3.0\,\text{bohr}$ attached to bulk-like bcc-(001) electrodes. The contributions of orbitals of different character and localized at the edge or center atom are marked in the colors as stated in the legend.

are contributing as well as Δ_1-, Δ_3-, and Δ_4-states of the four edge atoms. Note, that although the degeneracy of the d_{xy} and $d_{x^2-y^2}$ is lifted by the geometry of the electrodes, we here keep the Δ_4 notation for simplicity until otherwise noted.

Moving to the trimer with $\Delta L = 0.0\,\text{bohr}$ in Fig. 8.3 (b) the transmission function reduces by approximately a factor of three. In particular, the contribution of the Δ_4-states of the center and edge atom nearly vanishes completely around the Fermi level, while Δ_3- and Δ_1-contributions from the center and edge atoms remain. The energetic positions of the contributions to the transmission function from the different states coincides with the ones of the perfect lead, i.e., the shape of the transmission is determined by the leads and the trimer mainly leads to a decrease in magnitude.

If the trimer is now pulled apart, Fig. 8.4, for several distances ΔL, one first notices that the contributions of the edge atoms strongly decrease while the contributions of the central atom remain. This is consistent with the fact that the distance of the edge atoms on each side of the trimer is about 16.0 bohr for $\Delta L = 0.0\,\text{bohr}$, which indicates that the transmission function between these atoms is in the tunneling regime. However, for the center atom the transmission function is not in the tunneling regime. The bonds between the atoms of the trimer are not broken and the changes in the transmission function are caused by rearrangements of the electronic states due to the geometrical relaxation and the different bond lengths. A very prominent feature is the Δ_4-peak in the minority channel marked with an arrow, which moves from $E_\text{F} - 0.7\,\text{eV}$ for $\Delta L = 0.6\,\text{bohr}$ to $E_\text{F} - 0.25\,\text{eV}$ for $\Delta L = 3.0\,\text{bohr}$.

This peak is directly connected to the build-up of the magnetic moment and can also be seen in the LDOS, Fig. 8.5, of the d_{xz} and d_{yz} states (Δ_3-symmetry[2]) as well as

[2]Note, that the small differences in the LDOS of the two orbitals are artifacts from

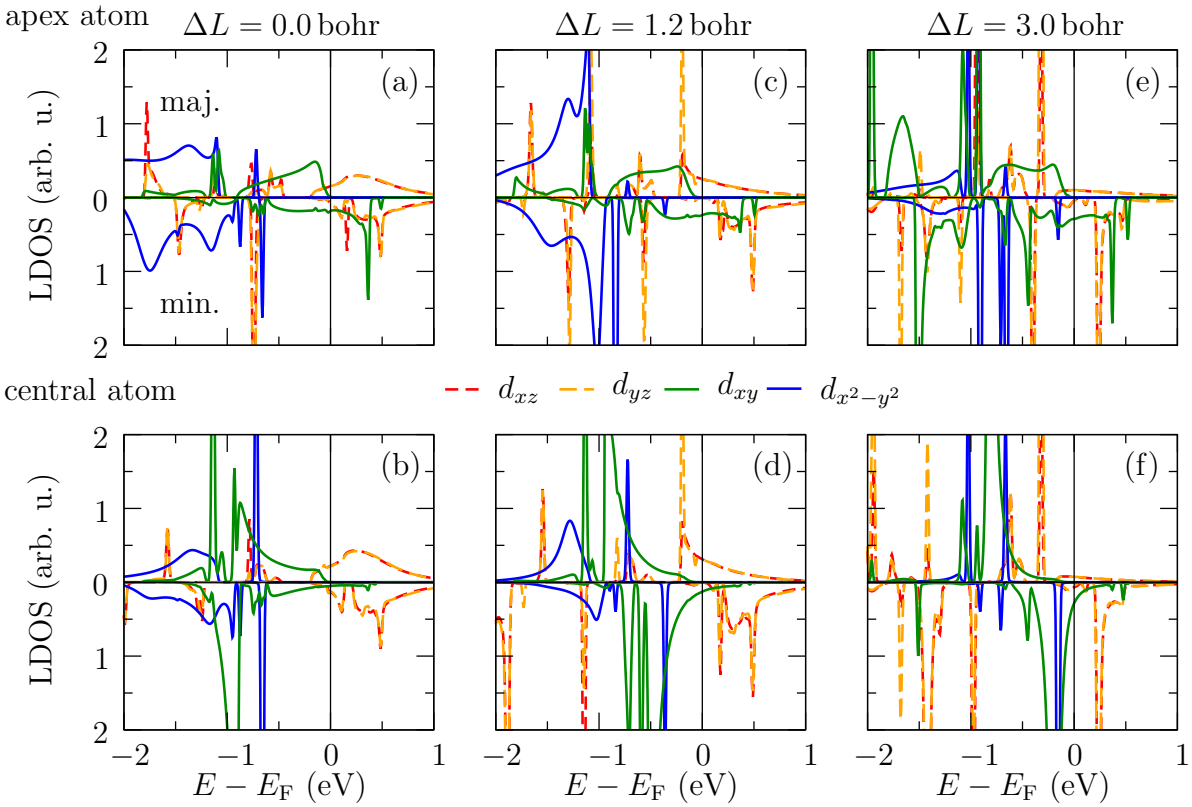

Figure 8.5: Spin- and orbital-decomposed local density of states calculated without SOC of the d_{xz}, d_{yz}, $d_{x^2-y^2}$, and d_{xy} orbitals located at the apex (upper panels) and central (lower panels) atom of the Pt trimer with (a, b) $\Delta L = 0.0\,\text{bohr}$, (c, d) $\Delta L = 1.2\,\text{bohr}$, and (e, f) $\Delta L = 3.0\,\text{bohr}$ attached to bulk-like bcc-(001) electrodes.

the d_{xy} and $d_{x^2-y^2}$ states (Δ_4-symmetry in the monowire geometry) for different ΔL at the apex and central atom of the trimer. While the symmetry of the Δ_3-orbitals is conserved, the symmetry of the Δ_4-states is broken due to the quadratic leads. The shifting Δ_4-peak in the transmission function for increasing ΔL in the minority channel discussed above can be clearly attributed to the LDOS of the d_{xy} and $d_{x^2-y^2}$ orbitals in the minority channel at the central atom (cf. Figs. 8.5 (b, d, f)), which continuously move towards higher energies for increasing ΔL. This also changes the magnetic moment of the central atom from around $0\,\mu_\text{B}$ to around $1\,\mu_\text{B}$ for $\Delta L = 0.0\,\text{bohr}$ and $3.0\,\text{bohr}$, respectively. The energetic positions of the Δ_3-states stays constant for increasing ΔL but the LDOS becomes sharper as expected for decreasing hybridization due to the larger distance between the atoms.

At the apex atom the magnetic moment is created by the d_{xy} states which slightly shift to lower energies in the majority channel and to higher energies in the minority channel.

The build-up of the magnetic moment of the central and the apex atom of the trimer can be seen in Fig. 8.6 (a). A sharp jump from a magnetic moment close to zero at

the Wannierization.

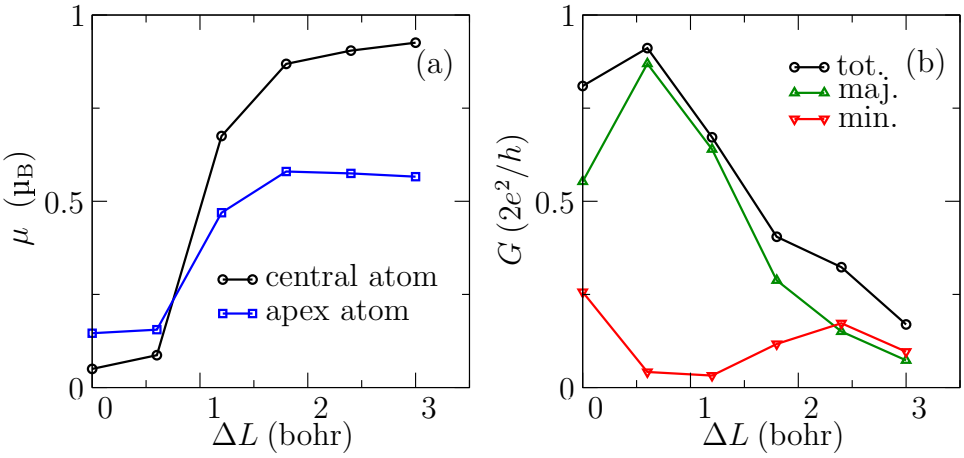

Figure 8.6: (a) Spin moment at the central (black circles) and at the apex atom (blue squares) of the Pt trimer as a function of ΔL calculated without SOC. (b) Conductance (black line) and spin-decomposed conductance (green up-triangle and red down-triangles mark majority and minority states, respectively) obtained by integrating the transmission function from -0.05 below to 0.05 eV above the Fermi level.

$\Delta L = 0$ bohr to a value of about $0.5\,\mu_B$ and $0.8\,\mu_B$ around $\Delta L = 1.2$ bohr for the apex and central atom, respectively, can be seen, consistent with the movement of the d_{xy} LDOS discussed above.

The conductance obtained by integrating the transmission function from -0.05 eV below to 0.05 eV above the Fermi level as a function of ΔL is shown in Fig. 8.6 (b). The total conductance continuously decreases with increasing ΔL. Furthermore, for small ΔL the conductance is strongly spin-polarized. For large ΔL the spin-polarization is reversed. This might seem contradictory to the behavior of the magnetic moment, however, the conductance around the Fermi level is dominated by the Δ_1- and Δ_3-orbitals and their contribution to the magnetic moment is limited.

As we will see in the next chapter, the behavior of the transmission function and conductance is profoundly changed by SOC.

8.3 Magnetic and Transport Properties including SOC

If SOC is included the spin and orbital moment of the central and apex Pt atom in Fig. 8.7 (a, b) also rise as a function of increasing ΔL for both magnetization directions. However, the rise is more continuous compared to the SR calculations. The spin and orbital moments for $\mathbf{M} \parallel z$ are larger than for $\mathbf{M} \perp z$. This also leads to a MAE favoring a magnetization parallel to the z-axis with about -4 meV which jumps to -4.5 meV at $\Delta L = 1.2$ bohr. The MAE follows approximately the difference in magnitude of the orbital moments for the two magnetization directions in accordance with the Bruno model [70].

The different magnitude of the magnetic moment at the central atom for the two magnetization directions can be understood by the induced hybridizations between the

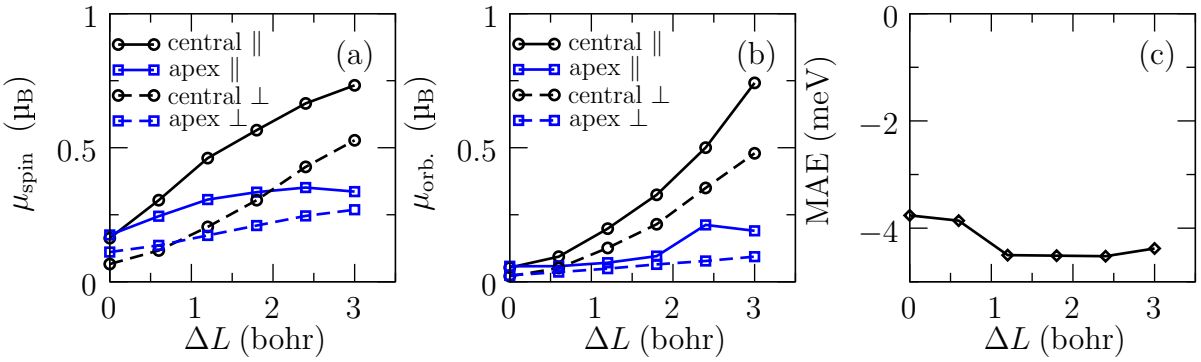

Figure 8.7: (a) Spin and (b) orbital moment at the central (black circles) and apex (blue squares) atom of the Pt trimer attached to bulk-like bcc-(001) electrodes for $\mathbf{M} \parallel z$ (solid lines) and $\mathbf{M} \perp z$ (dashed lines) as a function of ΔL. (c) Magnetocrystalline anisotropy energy ($E_{M\parallel z} - E_{M\perp z}$) per atom as a function of ΔL.

orbitals, which can be seen in the local density of states in Fig. 8.8. As for the SR case one sees that the $d_{x^2-y^2}$ and d_{xy} orbitals in the minority spin channel shift to higher energies with increasing ΔL. This leads to the increasing magnetic moment. However, for the case of $\mathbf{M} \perp z$ the d_{xy} orbitals are allowed to mix with the $d_{x^2-y^2}$ orbitals of

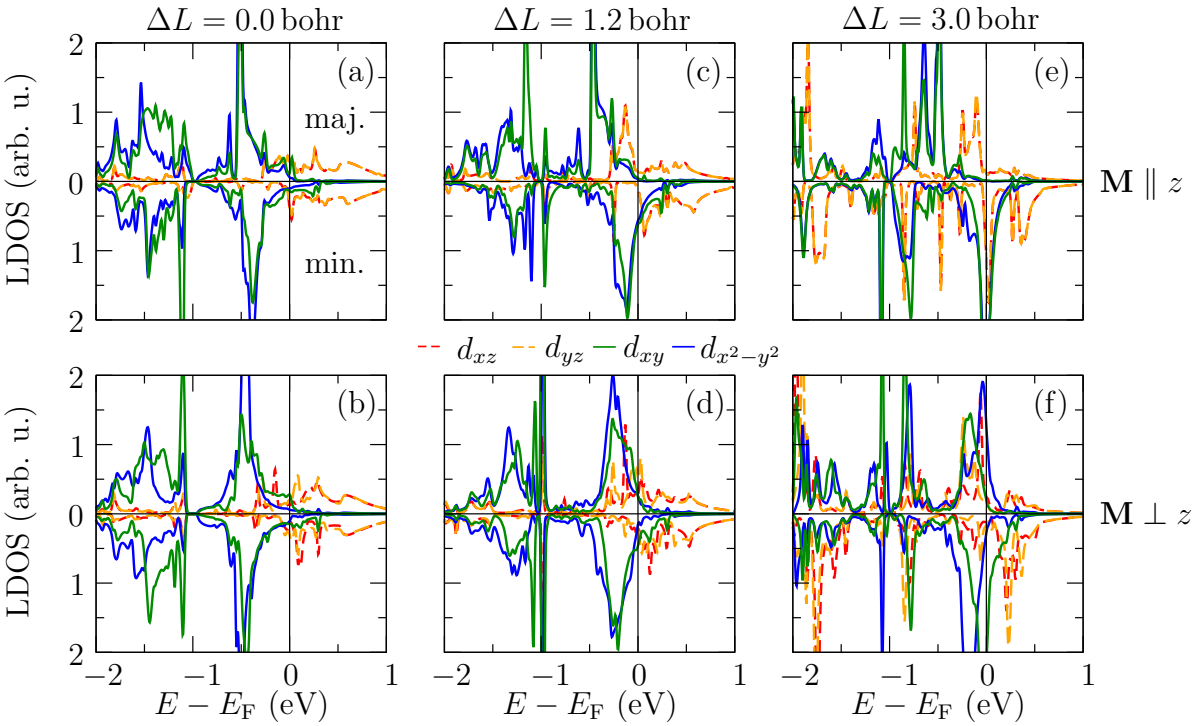

Figure 8.8: Spin- and orbital-decomposed local density of states of the d_{xz}, d_{yz}, $d_{x^2-y^2}$, and d_{xy} orbitals at the central atom of the Pt trimer calculated with SOC for (a, b) $\Delta L = 0.0$ bohr, (c, d) $\Delta L = 1.2$ bohr, and (e, f) $\Delta L = 3.0$ bohr attached to bulk-like bcc-(001) electrodes for $\mathbf{M} \parallel z$ (upper panels) and $\mathbf{M} \perp z$ (lower panels).

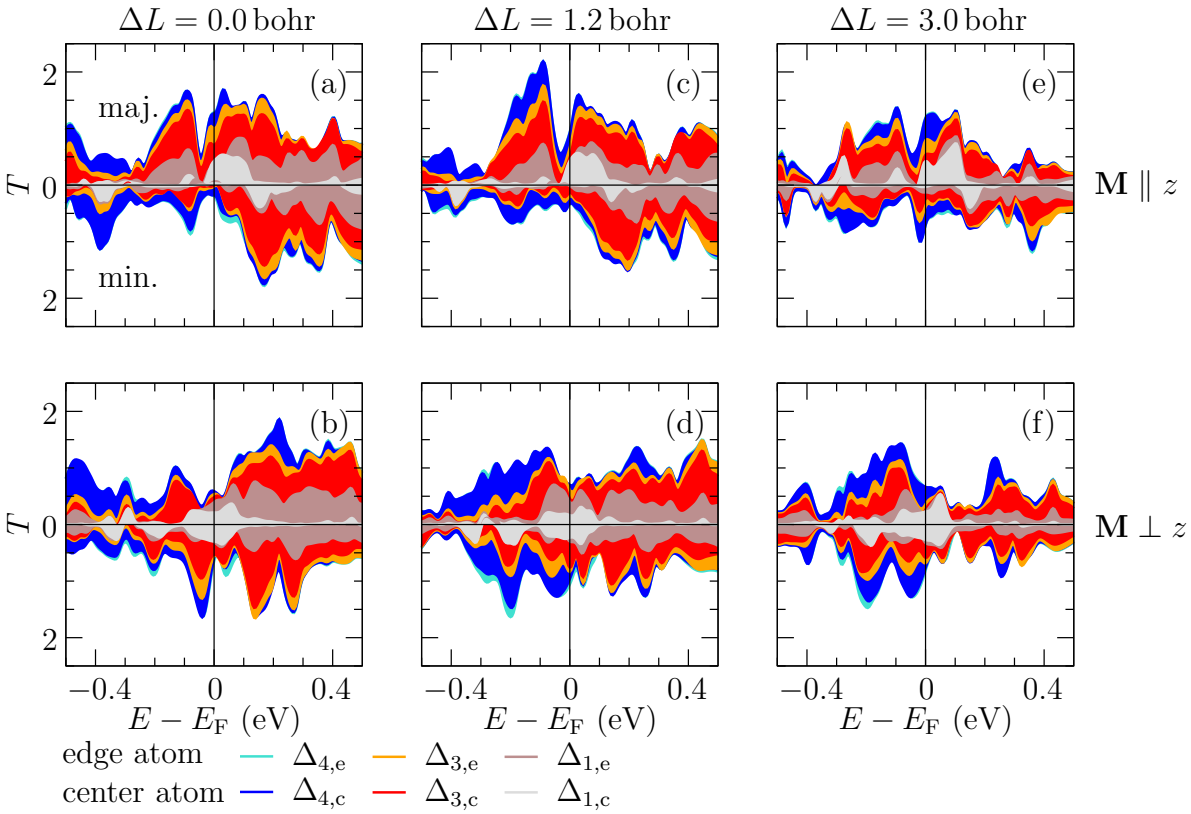

Figure 8.9: Spin- and symmetry-decomposed transmission function of the Pt trimer with (a, b) $\Delta L = 0.0\,\text{bohr}$, (c, d) $\Delta L = 1.2\,\text{bohr}$, and (e, f) $\Delta L = 3.0\,\text{bohr}$ attached to bulk-like bcc-(001) electrodes calculated with SOC for $\mathbf{M} \parallel z$ (upper panels) and $\mathbf{M} \perp z$ (lower panels). The contributions of orbitals of different character and localized at the edge or central atom are marked in the colors as stated in the legend.

opposite spin character (cf. Tab. 5.1). Because of that also the $d_{x^2-y^2}$ and d_{xy} orbitals of majority spin character move to higher energies for increasing ΔL, which reduces the magnetic moment for $\mathbf{M} \perp z$ considerably.

For $\mathbf{M} \perp z$ also the degeneracy of the d_{xz} and d_{yz} orbitals is lifted since the d_{yz} state is allowed to hybridize with the d_{z^2} state while the d_{xz} orbital is not (cf. Tab. 5.1 in chapter 5). For both magnetization directions the LDOS of the d_{xz} and d_{yz} orbitals becomes more spiky with increasing ΔL, which can be understood by the increased distance and, therefore, reduced hybridization between the atoms of the Pt trimer.

The two effects described above, the movement of the Δ_4-orbitals and the sharpening of the Δ_3-orbitals with increasing ΔL, lead to differences in the transmission function for the two magnetization directions as shown in Fig. 8.9. For $\mathbf{M} \perp z$ one can clearly see how the Δ_4-contributions move closer to the Fermi level in the majority and the minority spin channel with increasing ΔL (cf. Fig. 8.9 (b, d, f)). The contribution from the Δ_3-orbitals decreases and especially at 0.1 eV a kink forms in the Δ_3-contribution of minority spin character starting at $\Delta L = 0.0\,\text{bohr}$ until no contribution from these states is present at that energy at $\Delta L = 3.0\,\text{bohr}$. The kink is due to the sharpening of

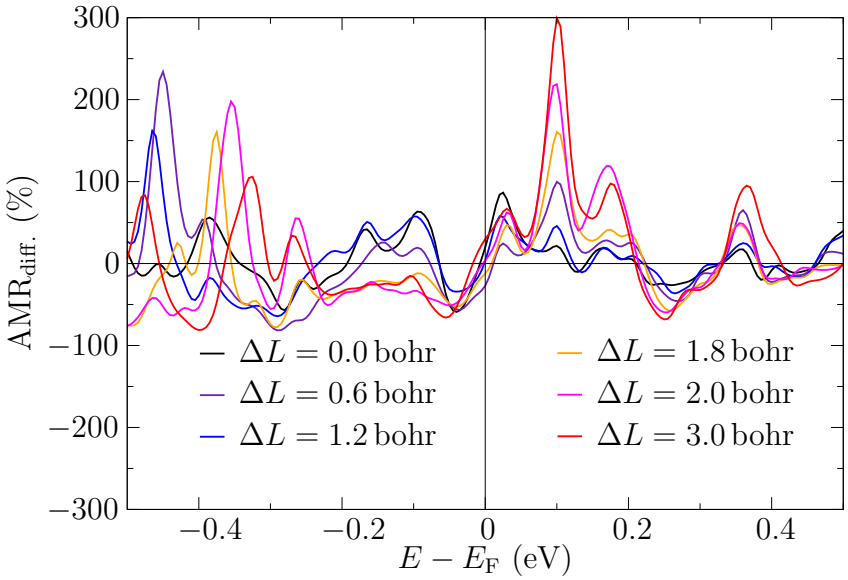

Figure 8.10: AMR$_{\text{diff.}}$ of the transmission function around the Fermi level calculated according to Eq. (5.4) for $\Delta L = 0.0$ bohr to $\Delta L = 3.0$ bohr of the Pt trimer contacted by bulk-like bcc-(001) electrodes.

the LDOS and the hybridization of the d_{yz} with the d_{z^2} orbitals, which is not allowed for $\mathbf{M} \parallel z$ as described in the discussion of the LDOS.

For $\mathbf{M} \parallel z$ the movement of the main Δ_4-peak in the LDOS of the minority spin channel around the Fermi level is not seen as clearly in the transmission function (cf. Fig. 8.9 (a, c, e)). In general, one sees a decrease of the transmission function for the Δ_3-states as well as the Δ_4-states.

The two features in the transmission function for $\mathbf{M} \perp z$, i.e., the kink from the Δ_3-states at 0.1 eV and the movement of the Δ_4-states, lead to an AMR$_{\text{diff.}}$ (cf. Eq. (5.4)) dependent on ΔL. As can be seen in Fig. 8.10 the peak at 0.1 eV grows monotonically with ΔL. In the region below the Fermi level the sign of the AMR$_{\text{diff.}}$ changes gradually from positive values for small ΔL to negative ones for ΔL larger than 1.2 bohr. These two effects are both directly connected to SOC and the build-up of the magnetic moment.

We now compare the results from this work with the experimental results from Ref. [22]. The conductance integrated from -0.05 eV to 0.05 eV around the Fermi level as a function of ΔL presented in Fig. 8.11 shows a very different behavior compared to the case without SOC. It stays rather constant around values of $0.75\,G_0$. This behavior is consistent with the data presented in Ref. [22], although they obtain values on the order of $1.0\,G_0$.

The AMR of the integrated conductance shows a sign change as a function of ΔL. This was also found in Ref. [22] for the MCR on a similar scale of distance and also for the experimental AMR. The magnitude of the AMR found here is three times larger than found for the experimental angular dependent AMR in Ref. [22]. However, the theoretical values compare well with the MCR, which shows values in the range of 30 % and an oscillating behavior.

What is also interesting to note is that for $\mathbf{M} \parallel z$ the spin-polarization has the opposite sign compared to $\mathbf{M} \perp z$. This can be attributed to the missing contribution of the Δ_1-minority states to the transmission function at the Fermi level for $\mathbf{M} \parallel z$, while for

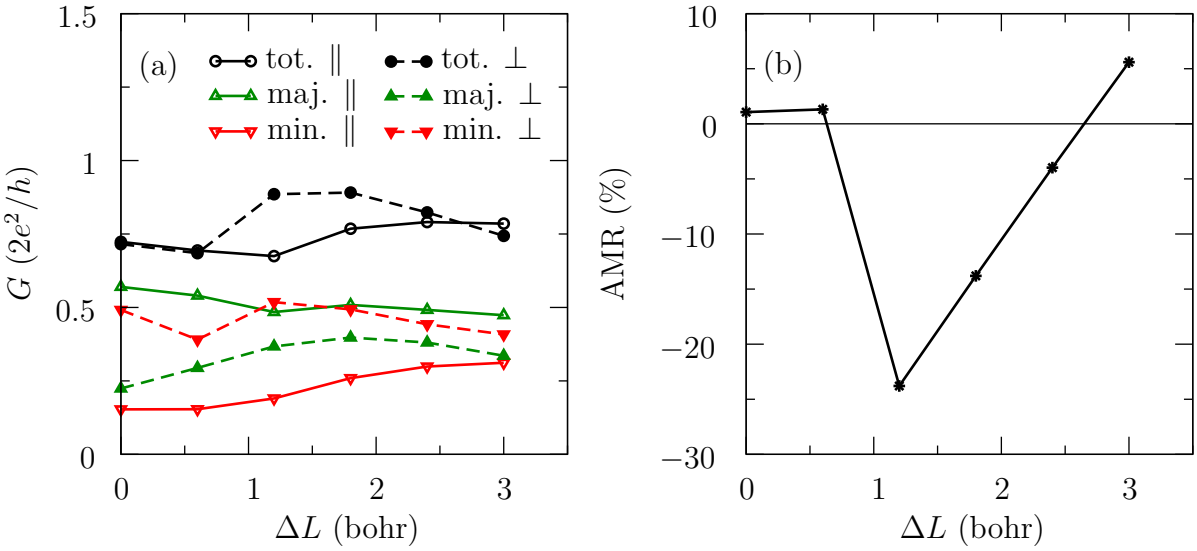

Figure 8.11: (a) Conductance (black circles) and spin-decomposed conductance (green up-triangle and red down-triangles mark majority and minority states, respectively) of the Pt trimer connected to bulk-like bcc-(001) electrodes obtained by integrating the transmission function from −50 below to +50 eV above the Fermi level for $\mathbf{M} \parallel z$ (empty symbols and solid lines) and $\mathbf{M} \perp z$ (filled symbols and dashed lines) as a function of ΔL. (b) AMR of the integrated conductance as a function of ΔL.

$\mathbf{M} \perp z$ the Δ_1-states of both spin channels contribute. In addition, as described during the discussion of Fig. 8.8 due to the SOC induced mixing the LDOS for $\mathbf{M} \perp z$ is very similar for both spin channels while larger differences can be seen for $\mathbf{M} \parallel z$. Therefore, the spin-polarization of the conductance is also larger for $\mathbf{M} \parallel z$ than for $\mathbf{M} \perp z$.

Fig. 8.12 (a) shows the conductances obtained by integrating over energy intervals with a size of 200 meV around the Fermi level. The obtained conductances for all integration ranges are slightly larger than for the integration range of 100 meV. This can be understood by comparing with Fig. 8.9, which shows that there is a local minimum of the transmission function around the Fermi level. At higher and lower energies with respect to the Fermi level the transmission function shows larger values.

The AMR for the conductances obtained by integrating the transmission function from $E_\mathrm{F} - 100\,\mathrm{meV}$ to $E_\mathrm{F} + 100\,\mathrm{meV}$ depicted in Fig. 8.12 (b) shows a similar behavior to the AMR for an integration range from $E_\mathrm{F} - 50\,\mathrm{meV}$ to $_\mathrm{F} + 50\,\mathrm{meV}$, Fig. 8.11 (b). If the integration range is set to negative values, i.e., $E_\mathrm{F} - 200\,\mathrm{meV}$ to $E_\mathrm{F}\,\mathrm{meV}$, the shape of the AMR is similar to the two integration ranges already discussed: The AMR changes from positive to negative sign when ΔL is enlarged. However, the magnitude of the AMR reached for large ΔL is increased. This can be understood by the $\mathrm{AMR}_\mathrm{diff.}$, Fig. 8.10, which changes from being positive to negative in this energy for increasing ΔL. If the integration range is chosen positive (E_F to $E_\mathrm{F} + 200\,\mathrm{meV}$), the AMR stays positive and increases in magnitude when the junction is elongated reaching values of 80 %. This also can be attributed to the increasing $\mathrm{AMR}_\mathrm{diff.}$ in this energy region discussed above.

It is intersting to note that for all integration ranges the AMR stays relatively stable

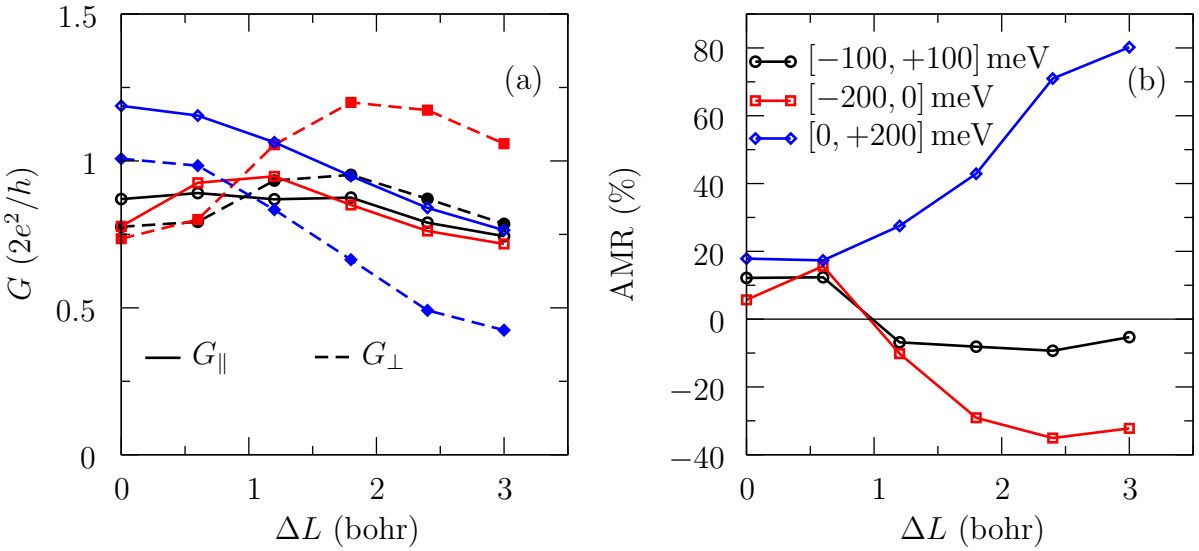

Figure 8.12: (a) Conductance of the Pt trimer connected to bulk-like bcc-(001) electrodes obtained by integrating the transmission function from $E_\mathrm{F} - 100\,\mathrm{meV}$ to $E_\mathrm{F} + 100\,\mathrm{meV}$ (black circles), $E_\mathrm{F} - 200\,\mathrm{meV}$ to $E_\mathrm{F}\,\mathrm{meV}$ (red squares), and E_F to $E_\mathrm{F} + 200\,\mathrm{meV}$ (blue diamonds) for $\mathbf{M} \parallel z$ (empty symbols and solid lines) and $\mathbf{M} \perp z$ (filled symbols and dashed lines) as a function of ΔL. (b) AMR of the integrated conductance as a function of ΔL for the three integration ranges.

for $\Delta L = 0.0\,\mathrm{bohr}$ and $\Delta L = 0.6\,\mathrm{bohr}$ and then jumps to higher or lower values. This jump can also be seen in the MAE in Fig. 8.7 (c) and the orbital moment in Fig. 8.7 (b). Therefore, one can attribute this jump to the emergent magnetism in the Pt trimer.

8.4 Summary

We calculated the transport properties of a Pt trimer contacted by bulk-like bcc-(001) electrodes as a function of the elongation of the trimer ΔL going beyond the monowire geometry used in the previous chapters. We used the structural parameters found by relaxing the atoms of the trimer from Ref. [104]. We find that SOC has large effects on the magnetic properties of the Pt trimer, which is reflected in the conductance. For calculations including SOC we find values of the conductance ranging from 0.75 to $0.9\,G_0$, which change slightly during elongation of the trimer. The AMR goes up to about 20 % in absolute value and changes sign during elongation. During the chain elongation a sign change and an increase in magnitude near the Fermi level can be found of the $\mathrm{AMR}_{\mathrm{diff.}}$ of the transmission function. These effects can be attributed to changes in the electronic structure due to the emergent magnetism and the bonding characteristics in the trimer for the different elongations ΔL. Furthermore, we found that it is critical to include SOC in the calculations since it changes the magnetic and transport properties dramatically.

Qualitatively the results compare well with the experimental results from Ref. [22].

Quantitatively, the values found for the conductance experimentally are slightly larger (1.0 to 1.25 G_0). The MCR is of a similar magnitude as the theoretically obtained AMR and also changes sign during elongation of the break junction. The experimentally obtained AMR as a function of the angle of the applied magnetic field also changes sign as a function of elongation but shows smaller values of only about 6 %. The fact that the theoretical AMR compares better with the experimental MCR than the AMR can be understood by the applied magnetic field, which is lower for the AMR measurements than for the MCR measurements. Therefore, it might be the case that during the measurement of the AMR not all magnetic moments are aligned.

Summarizing, the experimental and theoretical findings are in reasonable agreement. This supports the interpretation of emergent magnetism in Pt break junctions. However, some uncertainties remain due to the unknown exact atomic structure of the break junction and the idealization of the calculations.

9 Tunneling Non-Collinear Magnetoresistance

In this chapter, we propose a novel type of magnetoresistance to explain STM experiments with non spin-polarized tips on non-collinear (NC) spin structures. It is known that in a non-collinear spin structure a mixing between the spin channels occurs resulting in changes of the band structure and the local density of states compared to the ferromagnetic (FM) case [25, 107]. We here argue that this hybridization between bands of different spin character in non-collinear spin structures can lead to large changes in the local density of states in the vacuum and, therefore, also in the $\mathrm{d}I/\mathrm{d}U$ spectrum obtained in STM experiments. We propose that this effect can be used to detect non-collinear spin structures in a setup as sketched in Fig. 9.1. In analogy to the anisotropic magnetoresistance one only needs one magnetic electrode. The TNCMR is then defined by

$$\mathrm{TNCMR} = 100\% \cdot \frac{(\mathrm{d}I/\mathrm{d}U)_{\mathrm{NC}} - (\mathrm{d}I/\mathrm{d}U)_{\mathrm{FM}}}{(\mathrm{d}I/\mathrm{d}U)_{\mathrm{FM}}} \tag{9.1}$$

to measure the strength of the effect. We show that the magnitude of the TNCMR can be correlated with the size of the angles between adjacent atoms. Thus, the TNCMR is ideally suited to detect localized NC structures in FM environments.

In particular, this theoretical analysis was motivated by experiments performed by Christian Hanneken in the group of Prof. Roland Wiesendanger at the University of Hamburg. In these experiments W tips have been used to probe the bilayer PdFe/Ir(111) system in the skyrmion phase.

Skyrmions are particle-like spin structures which are topologically-protected, which means that they cannot be annihilated in a continuous manner. They can be found

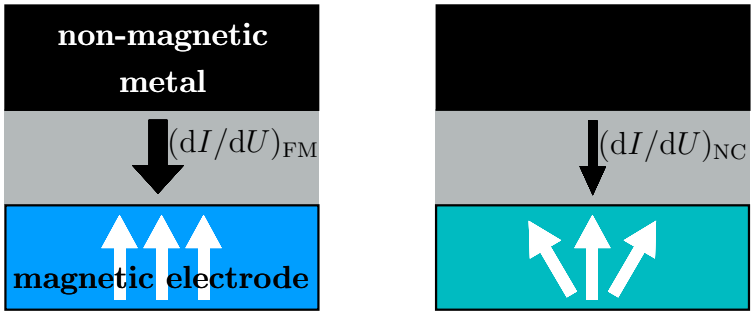

Figure 9.1: Sketch of the tunneling non-collinear magnetoresistance, which measures the difference in the differential conductance $\mathrm{d}I/\mathrm{d}U$ of a junction consisting of a non-magnetic metal and a magnetic electrode separated by a tunneling barrier between the ferromagnetic (FM) state and a non-collinear spin state of the magnetic electrode. Adapted from Ref. [1].

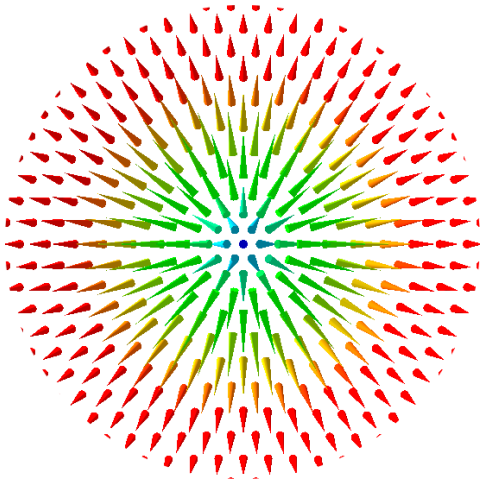

Figure 9.2: Perspective view of a two-dimensional skyrmion from above the center of the skyrmion. The cones represent the magnetization direction of individual atoms and the colorscale ranging from dark blue (magnetization pointing away from the reader) to red (magnetization pointing towards the reader) scales with the z-component of the magnetization. In the center the magnetization points away from the reader and then rotates into the opposite direction. Povray script courtesy of B. Dupé.

in bulk materials [108, 109] and at interfaces and surfaces [110]. Here, we focus on skyrmions on surfaces. A sketch of a skyrmion can be seen in Fig. 9.2. In the skyrmion center the magnetization points antiparallel to the magnetization in the surrounding and rotates continuously in a unique sense in between. Due to this spin arrangement one cannot simply unwind a skyrmion continuously. The unique rotational sense is imposed by the Dzyaloshinskii-Moriya interaction [111, 112], which arises due to spin-orbit interaction in systems with broken inversion symmetry such as a surface. A skyrmion can be characterized by its topological charge

$$S = \frac{1}{4\pi} \int \mathbf{n} \cdot \left(\frac{\partial \mathbf{n}}{\partial x} \times \frac{\partial \mathbf{n}}{\partial y} \right) \mathrm{d}x\mathrm{d}y, \tag{9.2}$$

where $\mathbf{n}$ is the unit vector of the local magnetization and the term $\mathbf{n} \cdot \left(\frac{\partial \mathbf{n}}{\partial x} \times \frac{\partial \mathbf{n}}{\partial y} \right)$ is called skyrmion density. The topological charge of a skyrmion is 1.

The bilayer PdFe/Ir(111) has been found to be an ideal playground for experiments with skyrmions. The ground state of PdFe/Ir(111) is a spin spiral. However, when a magnetic field is applied the skyrmion phase becomes energetically favorable until at large enough fields the FM state occurs [23, 24]. Furthermore, it has been demonstrated in this system that it is possible to write and delete skyrmions with spin-polarized currents [23]. Recently, from spin-polarized STM measurements it has been shown that the field-dependent magnetization profile of a skyrmion can be described by superimposing the profiles known for domain walls [113]. This allows to characterize a skyrmion by two field-dependent parameters $c(B)$ and $w(B)$. For the polar angle of the magnetization one can write

$$\theta(r) = \pi - \arcsin\left(\tanh\left(\frac{2(r-c)}{w} \right) \right) - \arcsin\left(\tanh\left(\frac{2(r+c)}{w} \right) \right), \tag{9.3}$$

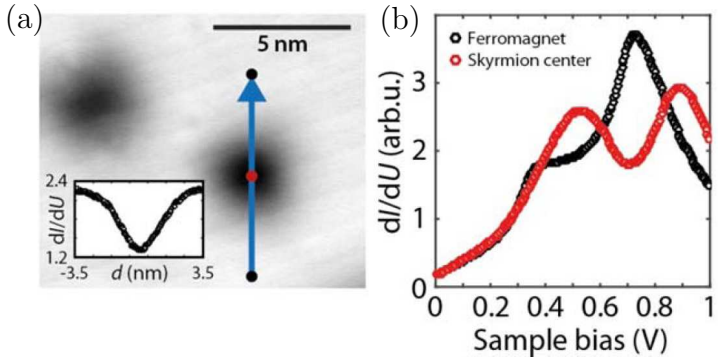

Figure 9.3: (a) Close view of two skyrmions, $\mathrm{d}I/\mathrm{d}U$ map, the inset presents a profile along the blue arrow (experimental parameters: $B = -2.5\,\mathrm{T}$, $U = +0.7\,\mathrm{V}$, $I = 1\,\mathrm{nA}$, $T = 4\,\mathrm{K}$). (b) $\mathrm{d}I/\mathrm{d}U$ tunnel spectra in the center of a skyrmion (red) and outside the skyrmion in the FM background (black); (experimental parameters: $B = -2.5\,\mathrm{T}$, $T = 4\,\mathrm{K}$, stabilization parameters $U = -1\,\mathrm{V}$, $I = 1\,\mathrm{nA}$). Figures taken from [1].

and for the azimuth angle

$$\tan\phi(r) = \frac{y}{x}. \tag{9.4}$$

Surprisingly, it was recently discovered that skyrmions can also be observed with non-magnetic STM tips.

Fig. 9.3 (a) shows a map of the the differential conductance of two skyrmions measured at a voltage of 0.7 V and with a non-magnetic STM tip. When the tip is moved along the blue arrow from the FM edge of the skymrion to its center, one obtains the profile shown in the inset of Fig. 9.3 (a). Values of about 1.2 and 2.4 are found at the center of the skyrmion and in the FM area at the edge of the skyrmion, respectively. According to Eq. (9.1) this would result in a TNCMR of 50 %. Fig. 9.3 (b) shows the bias dependence of the $\mathrm{d}I/\mathrm{d}U$ signal at the center of the skyrmion and in the FM surrounding. In the FM region a peak at 0.7 eV and a shoulder at 0.35 eV can be seen. At the center of the skyrmion the peak at 0.7 eV splits into two located at 0.9 eV and 0.5 eV leaving a local minimum at 0.7 eV. The $\mathrm{d}I/\mathrm{d}U$ spectra for smaller magnetic field strengths can be seen in Fig. 9.14 (c). They reveal that the shift of the high energy peak increases continuously with the magnetic field strength. From the $\theta(r)$ profiles obtained from the experimental $c(B)$ and $w(B)$ values for different magnetic fields shown in Fig. 9.15 (a) it can be seen that also the slope of $\theta(r)$ at the center of the skyrmion increases continuously with increasing magnetic field strength. Since the slope of $\theta(r)$ determines the angle α between the central atom of the skyrmion and its neighbors, one can assume that shift of the high-energy peak correlates with α. The same correlation can be found when the lateral dependence shown in Fig. 9.3 (a) is considered.

Understanding this correlation is the goal of this chapter. Since DFT calculations of skyrmions with the size found in this experiment are currently out of reach, we explain the observed peak-splitting by using a two-orbital TB model on a hexagonal lattice, which is adapted to the results of DFT calculations of spin spirals. The orbitals are assumed to be of minority and majority spin character and only hoppings to the nearest neighbors are taken into account. The non-collinearity is accounted for by introducing matrix elements between the two orbitals, which magnitude depends on

the angle between the magnetization direction of adjacent atoms calculated with the spin-rotation matrix. The "periodic TB model" is solved in reciprocal space and, thus, is ideally suited to describe periodic structures like spin spirals. It can also be used to locally describe non-periodic structures. The "full TB model" is solved in real space and able to describe large NC spin structures, i.e., skyrmions. We first introduce these two TB models and compare with results obtained from density functional theory calculations. Good agreement is found, which proves that the assumed simplifications are justified. We then show that the TB model explains the experimental data, which is available for skyrmions at several magnetic field strengths, very well and that the shift of the high-energy peak can be correlated with the mean angle between adjacent atoms. Furthermore, we find that the lateral dependence of the height of the high-energy peak can be used to determine the shape of the emergent magnetic field or skyrmion density. We then analyze the TNCMR as a function of bias voltage for different field strengths and compare the TNCMR to the TMR and TAMR. Finally, we shortly investigate the ballistic transport properties of spin spirals and skyrmions.

Parts of this chapter have been published in Ref. [1][1].

9.1 Periodic TB Model

In the following, we introduce the so-called "periodic TB model". It consists of two orbitals of majority or minority spin character in a one-atom unit cell taking into account hoppings to the nearest neighbors. Non-collinearity is introduced by off-diagonal matrix elements, the magnitudes of which depend on the angle between neighboring atoms. It is solved in reciprocal-space and, thus, ideally suited to describe periodic structures. However, also non-periodic structures can be described if the obtained results are regarded as local quantities.

Bandstructure, Density of States, and Vacuum Density of States

The energy of an isolated Bloch state can be calculated via the Schrödinger equation:

$$H\left|\Psi_{n\mathbf{k}}\right\rangle = E_n(\mathbf{k})\left|\Psi_{n\mathbf{k}}\right\rangle . \tag{9.5}$$

Recalling the definition of the Wannier functions from Sec. 4.1

$$\left|\Psi_{n\mathbf{k}}\right\rangle = \frac{1}{\sqrt{N}}\sum_{\mathbf{R}} e^{i\mathbf{k}\mathbf{R}}\left|\mathbf{R}n\right\rangle , \tag{9.6}$$

and plugging it into the Schrödinger equation yields:

$$\frac{1}{\sqrt{N}}\sum_{\mathbf{R}} e^{i\mathbf{k}\mathbf{R}} H\left|\mathbf{R}n\right\rangle = E(\mathbf{k})\frac{1}{\sqrt{N}}\sum_{\mathbf{R}} e^{i\mathbf{k}\mathbf{R}}\left|\mathbf{R}n\right\rangle . \tag{9.7}$$

[1]Note, that here we use different parameters to model the local density of states in the vacuum.

Multiplying with $\langle \mathbf{R}'n|$ from the left and using the orthonormality of Wannier functions $\langle \mathbf{R}'n|\mathbf{R}n\rangle = \delta_{\mathbf{R}\mathbf{R}'}$ leads to:

$$\sum_{\mathbf{R}} e^{i\mathbf{k}\mathbf{R}} \langle \mathbf{R}'n| H |\mathbf{R}n\rangle = E(\mathbf{k}) e^{i\mathbf{k}\mathbf{R}'} \tag{9.8}$$

$$\Leftrightarrow \sum_{\mathbf{R}} e^{i\mathbf{k}(\mathbf{R}-\mathbf{R}')} \langle \mathbf{R}'n| H |\mathbf{R}n\rangle = E(\mathbf{k}). \tag{9.9}$$

This eventually yields the band energy at each $\mathbf{k}$ point:

$$E(\mathbf{k}) = \sum_{\Delta\mathbf{R}} e^{i\mathbf{k}\Delta\mathbf{R}} \langle \mathbf{0}n| H |\Delta\mathbf{R}n\rangle . \tag{9.10}$$

For a NN approximation this simplifies to

$$E(\mathbf{k}) = \epsilon_0 + \sum_{i=1}^{N_{NN}} t e^{i\mathbf{k}\mathbf{T}_i}, \tag{9.11}$$

where $\mathbf{T}_i$ are the vectors from a site to its nearest neighbors, $\epsilon_0 = \langle \mathbf{0}n| H |\mathbf{0}n\rangle$ is the on-site energy of the sites and $t = \langle \mathbf{0}n| H |\mathbf{T}_i n\rangle$ the hopping to the nearest neighbors, which is assumed identical for all nearest neighbors.

For the case of a hexagonal lattice ($\mathbf{T}_i = -\mathbf{T}_{i+3}, i \in [1,3]$) the energy dispersion simplifies to

$$E(\mathbf{k}) = \epsilon_0 + 2t[\cos(\mathbf{k}\mathbf{T}_1) + \cos(\mathbf{k}\mathbf{T}_2) + \cos(\mathbf{k}\mathbf{T}_3)]. \tag{9.12}$$

To calculate the density of states at energy E one needs to count the number of states at that certain energy

$$D(E) = \frac{1}{N_{\mathbf{k}}} \sum_{\mathbf{k}} \delta(E - E(\mathbf{k})), \tag{9.13}$$

where $N_{\mathbf{k}}$ is the total number of $\mathbf{k}$-points. Computationally, it is convenient to approximate the δ function by a Gaussian distribution with standard deviation σ to count the states:

$$\delta(E - E(\mathbf{k})) = \frac{1}{\sqrt{2\pi\sigma^2}} \exp\left(-\frac{(E - E(\mathbf{k}))^2}{2\sigma^2}\right). \tag{9.14}$$

σ can be interpreted as a broadening due to the coupling to an underlying surface.

Within the Tersoff-Hamann model, the $\mathrm{d}I/\mathrm{d}U$ signal in an STM experiment is proportional to the LDOS at the tip position, i.e., in the vacuum a few Å above the surface [114, 115]. Therefore, it is of great interest to be able to calculate this quantity. The LDOS in the vacuum can be interpreted as the result of a tunneling process of electrons localized at the surface into a vacuum plane with a distance d to the surface plane. The tunneling barrier is approximated to be rectangular and the height is defined by the work function Φ. In the vacuum plane the electron can move freely and, thus,

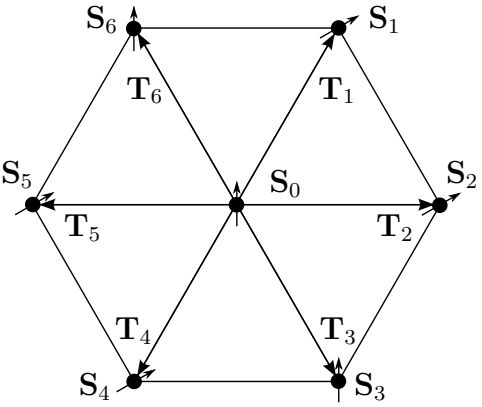

Figure 9.4: Sketch of the hexagonal unit cell. The spin quantization axis on the neighboring sites $\mathbf{T}_j$ are labeled by $\mathbf{S}_j$. Here, the spin quantization axis are chosen exemplary according to a spin spiral.

has a free-electron dispersion which scales with $\mathbf{k}^2$. The vacuum density of states can then be calculated by:

$$\mathrm{VDOS}(E) = \frac{1}{N_\mathbf{k}} \sum_\mathbf{k} \frac{1}{\sqrt{2\pi\sigma^2}} \exp\left(-\frac{(E - E(\mathbf{k}))^2}{2\sigma^2}\right) \exp\left(-2d\sqrt{\frac{2m_\mathrm{el}\Phi}{\hbar^2} + \mathbf{k}^2}\right). \quad (9.15)$$

Due to the $\mathbf{k}$ dependence of the local density of states in the vacuum (VDOS) the magnitude of the VDOS around the $\bar{\Gamma}$ point is amplified compared to the LDOS at the atom.

One needs to set the work function Φ and the distance d to calculate the VDOS.

Non-collinearity

Non-collinearity is now introduced in the model by allowing the two orbitals to mix according to the angle α_{0j} between the spin quantization axes at one site and its neighboring sites j characterized by the vector $\mathbf{T}_j$.

For the collinear case the on-site Hamiltonian states

$$\mathbf{H}_0 = \begin{pmatrix} \epsilon_\uparrow & 0 \\ 0 & \epsilon_\downarrow \end{pmatrix}, \quad (9.16)$$

where $\epsilon_\uparrow$ and $\epsilon_\downarrow$ are the on-site energies of the two orbitals for majority and minority spin states, respectively. The site is connected to neighboring site $\mathbf{T}_j$ via the transition matrix elements $t_\uparrow$ and $t_\downarrow$:

$$\mathbf{V}_{0,j} = \begin{pmatrix} t_\uparrow & 0 \\ 0 & t_\downarrow \end{pmatrix}. \quad (9.17)$$

The non-collinearity leads to a mixing of majority- and minority-spin orbitals on neighboring sites. The hopping from one site to the adjacent atomic site $\mathbf{T}_j$ is obtained by rotating the wave function from the local spin quantization axis $\mathbf{S}_j$ from site j characterized by angles Θ and Φ into the local spin quantization axis $\mathbf{S}_0$, which is assumed to lie in z-direction, with the spin-rotation matrix

$$\mathbf{U}(\Theta, \Phi) = \begin{pmatrix} e^{-i\frac{\Phi}{2}} \cdot \cos(\frac{\Theta}{2}) & -e^{-i\frac{\Phi}{2}} \cdot \sin(\frac{\Theta}{2}) \\ e^{-i\frac{\Phi}{2}} \cdot \sin(\frac{\Theta}{2}) & e^{i\frac{\Phi}{2}} \cdot \cos(\frac{\Theta}{2}) \end{pmatrix}. \quad (9.18)$$

Since we are only regarding the hopping between two atomic sites pairwise, one can assume that the spin quantization axes are lying in a plane and, thus, the rotation matrix can be described by the absolute angle between the spin quantization axes $\alpha_{0j} = \arccos(\mathbf{S}_j \cdot \mathbf{S}_0)$:

$$\mathbf{U}(\alpha_{0j}) = \begin{pmatrix} \cos(\frac{\alpha_{0j}}{2}) & -\sin(\frac{\alpha_{0j}}{2}) \\ \sin(\frac{\alpha_{0j}}{2}) & \cos(\frac{\alpha_{0j}}{2}) \end{pmatrix}. \tag{9.19}$$

The matrix $\mathbf{V}_{0j}$ then becomes [116]:

$$\mathbf{V}_{0j} = \begin{pmatrix} t_{\uparrow} \cos(\alpha_{0j}/2) & -t_{\downarrow\uparrow} \sin(\alpha_{0j}/2) \\ t_{\uparrow\downarrow} \sin(\alpha_{0j}/2) & t_{\downarrow} \cos(\alpha_{0j}/2) \end{pmatrix}, \tag{9.20}$$

where $t_{\uparrow\downarrow}$ and $t_{\downarrow\uparrow}$ are the hopping integrals between the orbitals of majority and minority spin character on neighboring sites, the values of which depend on the assumed orbital character of the majority and minority spin states.

In reciprocal-space this translates to a mixing between **k**-states of the majority and minority band according to the Hamiltonian

$$\mathbf{H}_{\mathbf{k}} = \begin{pmatrix} E_{\uparrow}(\mathbf{k}) & t_{\downarrow\uparrow,\mathbf{k}} \\ t_{\uparrow\downarrow,\mathbf{k}} & E_{\downarrow}(\mathbf{k}) \end{pmatrix}. \tag{9.21}$$

$E_{\uparrow/\downarrow}(\mathbf{k})$ is calculated via Eq. (9.11) and the mixing between the orbitals translates to a mixing between states at the same **k**-point, which can be obtained from the Wannier formalism as described in Sec. 4.2 via Eq. (4.24):

$$t_{\uparrow\downarrow/\downarrow\uparrow,\mathbf{k}} = \sum_{i=1}^{6} \pm t_{\uparrow\downarrow/\downarrow\uparrow} \sin(\alpha_{0j}/2) e^{i\mathbf{k}\mathbf{T}_i}. \tag{9.22}$$

Diagonalizing Eq. (9.21) leads to the eigenvalues:

$$\lambda_{1/2} = \frac{E_{\uparrow}(\mathbf{k}) + E_{\downarrow}(\mathbf{k})}{2} \pm \sqrt{\left(\frac{E_{\uparrow}(\mathbf{k}) - E_{\downarrow}(\mathbf{k})}{2}\right)^2 + t_{\uparrow\downarrow,\mathbf{k}} t_{\downarrow\uparrow,\mathbf{k}}}. \tag{9.23}$$

The angles α_{0j} can in principle be chosen arbitrarily so that also non-periodic structures, for example, the center of a skyrmion, can be described approximately by interpreting the bandstructure as a "local bandstructure".

9.2 Full TB Model

The periodic TB model cannot account for the full spin-structure of a skyrmion since the unit cell only consists of one atom. In principle, a multi-atom basis which includes the spin-structure of the skrmion could be incorporated and which would then be repeated periodically in the periodic TB model. However, this would increase the computational effort tremendously. Therefore, we here introduce the so-called "full

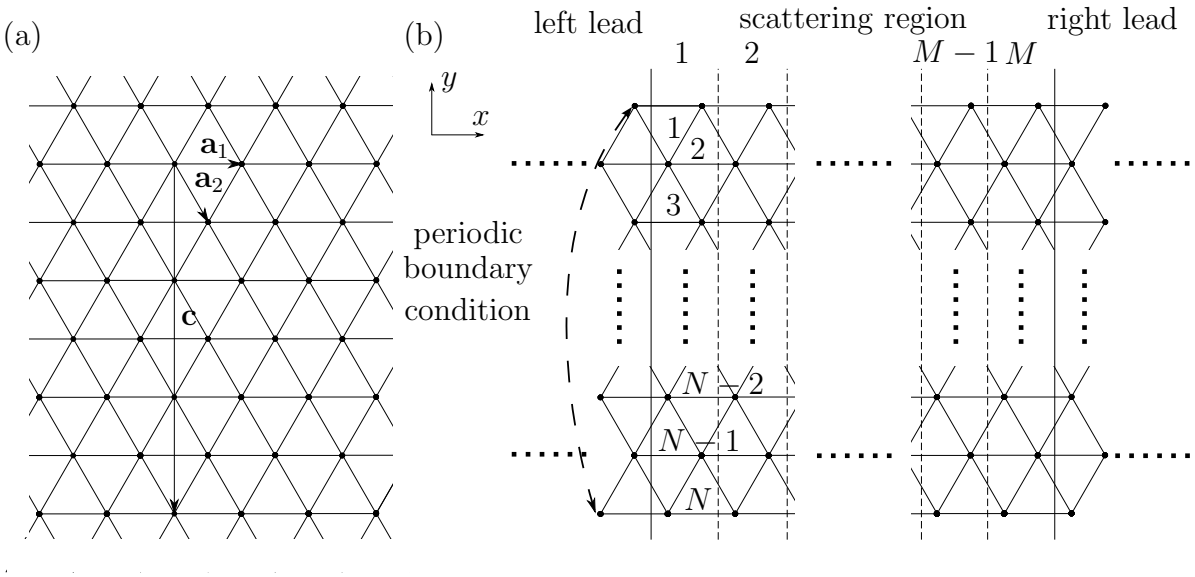

Figure 9.5: Sketch of the geometrical setup used for the full TB model in real space.

TB model" based on the Green's function code described in chapter 2. The full TB model is solved in real space which is computationally more convenient for intrinsically non-periodic structures such as isolated skyrmions. In addition, the Green's function method allows for connecting the skyrmion to semi-infinite environments abolishing the need for periodic repetition of the unit cell. As in the periodic TB model hoppings to the nearest neighbors are taken into account.

Starting from the infinite hexagonal lattice in Fig. 9.5 (a) characterized by the basis vectors

$$\mathbf{a}_1 = (1, 0)^{\mathrm{T}} \qquad \mathbf{a}_2 = (0.5, -\sqrt{3/4})^{\mathrm{T}}, \tag{9.24}$$

one chooses a vector $\mathbf{c}$ defined by

$$\mathbf{c} = \frac{N}{2}\mathbf{a}_1 - N\mathbf{a}_2, \tag{9.25}$$

with $N \in \mathbb{N}$. Atoms connected by vector $\mathbf{c}$ are assumed to be identical. This cuts out a stripe containing N atoms as sketched in Fig. 9.5 (b). N is always an even number by construction. The scattering region is created by repeating this stripe M times. The scattering region is connected to the leads as described in chapter 2.

Two orbitals per atom are assumed and, therefore, the Hamiltonian for stripe m of

the scattering region takes the form:

$$\mathbf{H}^m = \begin{pmatrix} \mathbf{H}^m_{1,1} & \mathbf{V}^m_{1,2} & \mathbf{0} & \cdots & \mathbf{0} & \mathbf{V}^m_{1,N} \\ \mathbf{V}^m_{2,1} & \mathbf{H}^m_{2,2} & \mathbf{V}^m_{2,3} & \ddots & \mathbf{0} & \mathbf{0} \\ \mathbf{0} & \ddots & \ddots & \ddots & \ddots & \vdots \\ \vdots & \ddots & \ddots & \ddots & \ddots & \mathbf{0} \\ \mathbf{0} & \mathbf{0} & \ddots & \ddots & \mathbf{H}^m_{N-1,N-1} & \mathbf{V}^m_{N-1,N} \\ \mathbf{V}^m_{N,1} & \mathbf{0} & \cdots & \mathbf{0} & \mathbf{V}^m_{N,N-1} & \mathbf{H}^m_{N,N} \end{pmatrix}, \tag{9.26}$$

with $\mathbf{H}^m_{n,n}$ and $\mathbf{V}^m_{n,n+1}$ being 2×2 matrices. As one can see from Eq. (9.26) periodic boundary conditions are assumed in y-direction. The on-site energies are given by

$$\mathbf{H}^m_{n,n} = \begin{pmatrix} \epsilon_\uparrow & 0 \\ 0 & \epsilon_\downarrow \end{pmatrix}. \tag{9.27}$$

The neighboring stripes m and m' are connected to each other via

$$\mathbf{V}^{m,m'} = \begin{pmatrix} \mathbf{V}^{mm'}_{1,1} & \mathbf{V}^{mm'}_{1,2} & \mathbf{0} & \cdots & \mathbf{0} & \mathbf{V}^{mm'}_{1,N} \\ \mathbf{V}^{mm'}_{2,1} & \mathbf{V}^{mm'}_{2,2} & \mathbf{V}^{mm'}_{2,3} & \ddots & \mathbf{0} & \mathbf{0} \\ \mathbf{0} & \ddots & \ddots & \ddots & \ddots & \vdots \\ \vdots & \ddots & \ddots & \ddots & \ddots & \mathbf{0} \\ \mathbf{0} & \mathbf{0} & \ddots & \ddots & \mathbf{V}^{mm'}_{N-1,N-1} & \mathbf{V}^{mm'}_{N-1,N} \\ \mathbf{V}^{mm'}_{N,1} & \mathbf{0} & \cdots & \mathbf{0} & \mathbf{V}^{mm'}_{N,N-1} & \mathbf{V}^{mm'}_{N,N} \end{pmatrix}. \tag{9.28}$$

Matrices connecting sites in neighboring rows, i.e., $n \neq n'$, differ due to the zigzag structure of each stripe for the cases $m' = m+1$ and $m' = m-1$, i.e., going from left to right or right to left. For $m' = m+1$ and n odd: $\mathbf{V}^{mm'}_{n,n'} \neq \mathbf{0}$, but for n even: $\mathbf{V}^{mm'}_{n,n'} = \mathbf{0}$. For $m' = m-1$ it is the other way around.

The matrices for the leads and the matrices connecting the leads to the scattering region are created analogously. The Green's function formalism gives access to the local density of states at each site as well as to the lateral transmission function in x-direction.

Incorporation of the Spin Structure

For each site characterized by indices m and n the direction of the spin quantization axis can be written as:

$$\mathbf{S}(m,n) = \begin{pmatrix} \sin\theta(m,n)\cos\phi(m,n) \\ \sin\theta(m,n)\sin\phi(m,n) \\ \cos\theta(m,n) \end{pmatrix}. \tag{9.29}$$

To calculate the hoppings between neighboring sites we pairwise rotate the spin quantization axes of neighboring sites into each other. As in the periodic TB model

we can assume that the spin quantization axes pairwise lie in a plane and, thus, the rotation matrix can be described by the absolute angle between the spin quantization axes $\alpha_{mn,m'n'} = \arccos\left(\mathbf{S}(m,n)\cdot\mathbf{S}(m',n')\right)$:

$$\mathbf{U}(\alpha_{mn,m'n'}) = \begin{pmatrix} \cos(\frac{\alpha_{mn,m'n'}}{2}) & -\sin(\frac{\alpha_{mn,m'n'}}{2}) \\ \sin(\frac{\alpha_{mn,m'n'}}{2}) & \cos(\frac{\alpha_{mn,m'n'}}{2}) \end{pmatrix}. \tag{9.30}$$

The matrices $\mathbf{V}_{nn'}^{mm'}$ then state

$$\mathbf{V}_{nn'}^{mm'} = \begin{pmatrix} t_{\uparrow}\cos(\frac{\alpha_{mn,m'n'}}{2}) & -t_{\downarrow\uparrow}\sin(\frac{\alpha_{mn,m'n'}}{2}) \\ t_{\uparrow\downarrow}\sin(\frac{\alpha_{mn,m'n'}}{2}) & t_{\downarrow}\cos(\frac{\alpha_{mn,m'n'}}{2}) \end{pmatrix}. \tag{9.31}$$

The skyrmion spin structure is incorporated using Eq. (9.3) and Eq. (9.4) for the determination of $\mathbf{S}(m,n)$ in the scattering region. For the case of skyrmions the scattering region is attached to FM leads (cf. Fig. 9.13).

Spin spirals propagating along the x-direction are implemented by choosing the number of stripes $M = 1$ and the angle between adjacent sites

$$\alpha_{mn,m'n'} = \begin{cases} \frac{2\pi}{2N_{\mathrm{S}}} & \text{for} \quad m = m' \\ \frac{2\pi}{N_{\mathrm{S}}} & \text{for} \quad m \neq m' \end{cases} \tag{9.32}$$

in the scattering region as well as in the leads. The wavelength of the spin spiral then is $\lambda = N_{\mathrm{S}}a$.

Periodic Boundary Conditions and Effective Coupling to an Underlying Crystal

The periodic boundary conditions allow only certain $\mathbf{k}$-vectors. They are defined by the vector $\mathbf{c}$ forcing atoms connected by that vector to be identical as sketched in Fig. 9.5 (a). Graphically speaking, the hexagonal lattice is rolled up and becomes a tube analogous to carbon nanotubes. The allowed $\mathbf{k}$ vectors are defined by

$$\mathbf{k}\cdot\mathbf{c} = 2\pi\nu. \tag{9.33}$$

According to the choice of $\mathbf{c}$ in Eq. (9.25), this leads to a quantization of k_y while k_x is not affected:

$$k_y = \frac{2\pi\nu}{N\sqrt{3/4}}. \tag{9.34}$$

To get rid of these artificial quantization effects due to the periodic boundary conditions and to account for the hybridization of the surface atoms with the underlying layers in real surfaces, we add an effective self-energy Σ to the diagonal elements of Eq. (9.27) which then reads

$$\mathbf{H}_{n,n}^{m} = \begin{pmatrix} \epsilon_{\uparrow} - i\Sigma & 0 \\ 0 & \epsilon_{\downarrow} - i\Sigma \end{pmatrix}. \tag{9.35}$$

The effects due to the periodic boundary conditions and the broadening due to the self-energy are discussed in Sec. 9.2.1.

Modeling the Vacuum Local Density of States

As stated in Sec. 9.1 the decay of the states from the surface into the vacuum leads to a filtering effect on the VDOS depending on $\mathbf{k}$. Since the full TB model is solved in real space, one cannot model the vacuum decay as for the periodic TB model directly as a function of $\mathbf{k}$. To access the VDOS we here introduce a second layer of sites, the vacuum sites, as sketched in Fig. 9.6. At each vacuum site two orbitals are located as for the atomic sites. Eqs. (9.26) and (9.28) then have the form

$$\mathbf{H}^m = \begin{pmatrix} \mathbf{H}^m_{\mathrm{at}} & \mathbf{V}^m_{\mathrm{at,V}} \\ \mathbf{V}^m_{\mathrm{V,at}} & \mathbf{H}^m_{\mathrm{V}} \end{pmatrix} \tag{9.36}$$

and

$$\mathbf{V}^{m,m'} = \begin{pmatrix} \mathbf{V}^{m,m'}_{\mathrm{at}} & \mathbf{V}^{m,m'}_{\mathrm{at,V}} \\ \mathbf{V}^{m,m'}_{\mathrm{V,at}} & \mathbf{V}^{m,m'}_{\mathrm{V}} \end{pmatrix}, \tag{9.37}$$

where the subscript "at" and "V" stands for the atomic and vacuum sites, respectively.

The structure of $\mathbf{H}^m_{\mathrm{V}}$ and $\mathbf{V}^{m,m'}_{\mathrm{V}}$ is the same as for to the atomic sites, i.e., only interactions up to the nearest neighbor are taken into account. The version of Eqs. (9.27) and (9.31) for the vacuum sites state:

$$\left(\mathbf{H}^m_{n,n}\right)_{\mathrm{V}} = \begin{pmatrix} \epsilon_{\mathrm{V}} & 0 \\ 0 & \epsilon_{\mathrm{V}} \end{pmatrix} \tag{9.38}$$

and

$$\left(\mathbf{V}^{mm'}_{nn'}\right)_{\mathrm{V}} = \begin{pmatrix} t_{\mathrm{V}} & 0 \\ 0 & t_{\mathrm{V}} \end{pmatrix}. \tag{9.39}$$

The structure of the matrices connecting atomic to vacuum sites $\mathbf{V}^{m,m'}_{\mathrm{at,V}}$ is the same as in Eq. (9.28). The individual matrices contained in $\mathbf{V}^{m,m'}_{\mathrm{at,V}}$ state:

$$\left(\mathbf{V}^{mm'}_{nn'}\right)_{\mathrm{at,V}} = \begin{pmatrix} \left(t^{mm'}_{\uparrow,nn'}\right)_{\mathrm{at,V}} & 0 \\ 0 & \left(t^{mm'}_{\downarrow,nn'}\right)_{\mathrm{at,V}} \end{pmatrix}. \tag{9.40}$$

Thereby

$$\left(t^{mm'}_{\uparrow,nn'}\right)_{\mathrm{at,V}} = \begin{cases} t^{\mathrm{at,V}}_{\uparrow} & \text{for} \quad m = m' \quad \text{and} \quad n = n' \\ t^{\mathrm{at,V}}_{\uparrow} e^{-\kappa \Delta b} & \text{for} \quad m \neq m' \quad \text{or} \quad n \neq n' \end{cases} \tag{9.41}$$

and analogously for $\left(t^{mm'}_{\downarrow,nn'}\right)_{\mathrm{at,V}}$. The values $\kappa = \sqrt{2\frac{m\Phi}{\hbar^2}}$ and $\Delta b = b - d = \sqrt{d^2 + a^2} - d$ account for the decreased magnitude of the hoppings from atomic sites to vacuum sites, which are not located directly above each other as sketched in Fig. 9.6. Here, a is the lattice constant, Φ the work function and d the distance from the vacuum plane to the atomic plane.

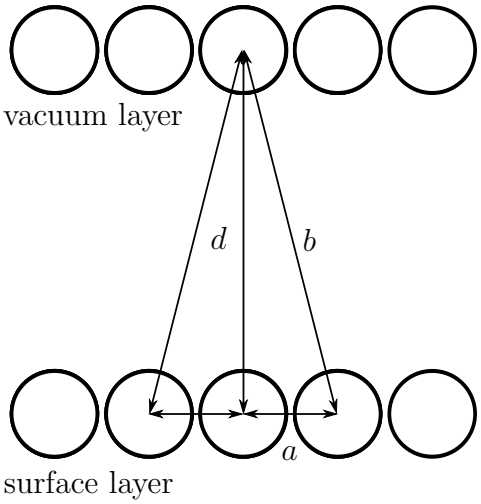

Figure 9.6: Sketch of the geometry used to calculate the vacuum density of states.

t_V should now be chosen to yield the dispersion of the free electron gas. The work function Φ is connected to the on-site energy of the vacuum sites ϵ_V by Eq. (9.12) for $\mathbf{k} = \mathbf{0}$:

$$\Phi = \epsilon_\mathrm{V} + 6t_\mathrm{V}. \tag{9.42}$$

9.2.1 Computational Details of the Full TB Model

Quantization Effects and Effective Broadening

Fig. 9.7 (a) shows the local density of states of an orbital at an atomic site of the hexagonal lattice for the FM state obtained from the full TB model for parameters $\epsilon = 0\,\mathrm{eV}$, $t = -0.25\,\mathrm{eV}$ and $\Sigma = 0\,\mathrm{eV}$. For $N = 1$ and $N = 2$ a monowire and zigzag wire is modeled, respectively. For $N = 4$ the full bandwidth of $11 \cdot t = 2.75\,\mathrm{eV}$ is reached as expected for the full hexagonal lattice. The peaks originate from the quantization of k_y. As N increases the number of quantization peaks increases.

Fig. 9.7 (b) shows the effect of the Lorentzian broadening on the LDOS caused by the self-energy Σ for the same parameters as above and $N = 30$. As Σ increases the quantization peaks broaden and eventually vanish for $\Sigma = 0.1\,\mathrm{eV}$. The results compare well with the ones obtained from the periodic TB model for a Gaussian broadening of $\sigma = 0.1\,\mathrm{eV}$.

Quality of Vacuum Local Density of States

To model the vacuum decay at least four new parameters have to be introduced: ϵ_V, t_V, $t_\uparrow^{\mathrm{at,V}} = t_\downarrow^{\mathrm{at,V}}$ and d. Although ϵ_V and t_V are in principle defined by the desired work function Φ and by demanding a free electron like dispersion of the vacuum states, it has been found that the quality of the VDOS sensitively depends on these parameters and that it must not necessarily be the best choice to demand t_V to result in a free-electron like dispersion. This has multiple reasons.

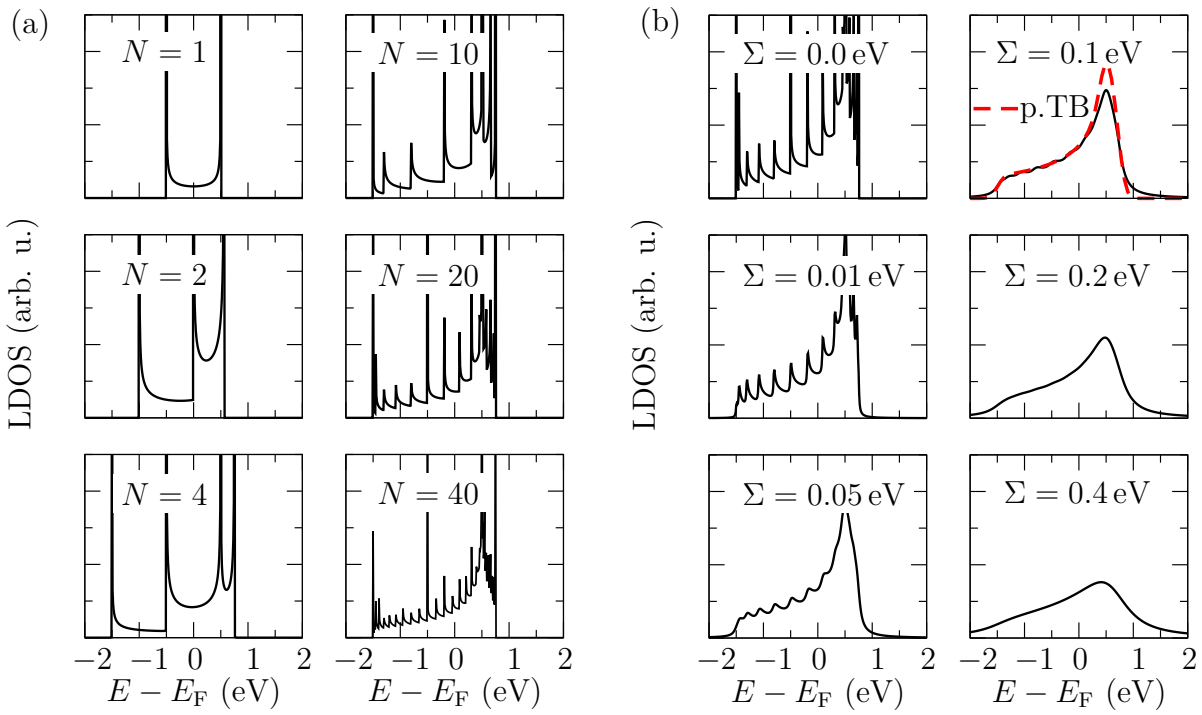

Figure 9.7: (a) Local density of states of one orbital at the atom of an unsupported hexagonal monolayer obtained from the full TB Model for increasing number of atoms N in the stripe to illustrate the quantization effects. (b) Local density of states at the atom of obtained from the full TB model of an hexagonal monolayer with $N = 30$ atoms in the stripes with different effective broadenings Σ, which mimic the hybridization with an underlying crystal. The dashed red line is obtained from the periodic TB model with $\sigma = 0.1\,\mathrm{eV}$.

First, as can be seen in Fig. 9.8 (a) one cannot achieve a perfect free electron dispersion within the nearest-neighbor approximation. The second reason can be seen when the VDOS is regarded in a perturbation theory approach. The VDOS in **k**-space can be regarded as a perturbation of the free electron state $\left|\frac{\hbar^2\mathbf{k}^2}{2m_e}\right\rangle$ in the vacuum by a state in the solid $|\mathbf{k}, n\rangle$, where n is the band index. The states interact via the perturbation $V_{\mathrm{at,V}}$. This yields a first correction to the vacuum state of:

$$\widetilde{\left|\frac{\hbar^2\mathbf{k}^2}{2m_e}\right\rangle} = |\mathbf{k}, n\rangle \frac{\langle \mathbf{k}, n|V_{\mathrm{at,V}}|\frac{\hbar^2\mathbf{k}^2}{2m_e}\rangle}{\frac{\hbar^2\mathbf{k}^2}{2m_e} - E_{\mathbf{k},n}}. \tag{9.43}$$

Using the Wannier transformation (Eq. (4.3)) for the state in the solid and in the vacuum, as well as $\Delta E(\mathbf{k}) = \frac{\hbar^2\mathbf{k}^2}{2m_e} - E_{\mathbf{k},n}$ yields:

$$\widetilde{\left|\frac{\hbar^2\mathbf{k}^2}{2m_e}\right\rangle} = \frac{1}{N\Delta E(\mathbf{k})} |\mathbf{k}, n\rangle \sum_{\mathbf{R}} \sum_{\mathbf{R}_V} e^{i\mathbf{k}(\mathbf{R}-\mathbf{R}_V)} \langle \mathbf{R}, n|H_1|\mathbf{R}_V\rangle, \tag{9.44}$$

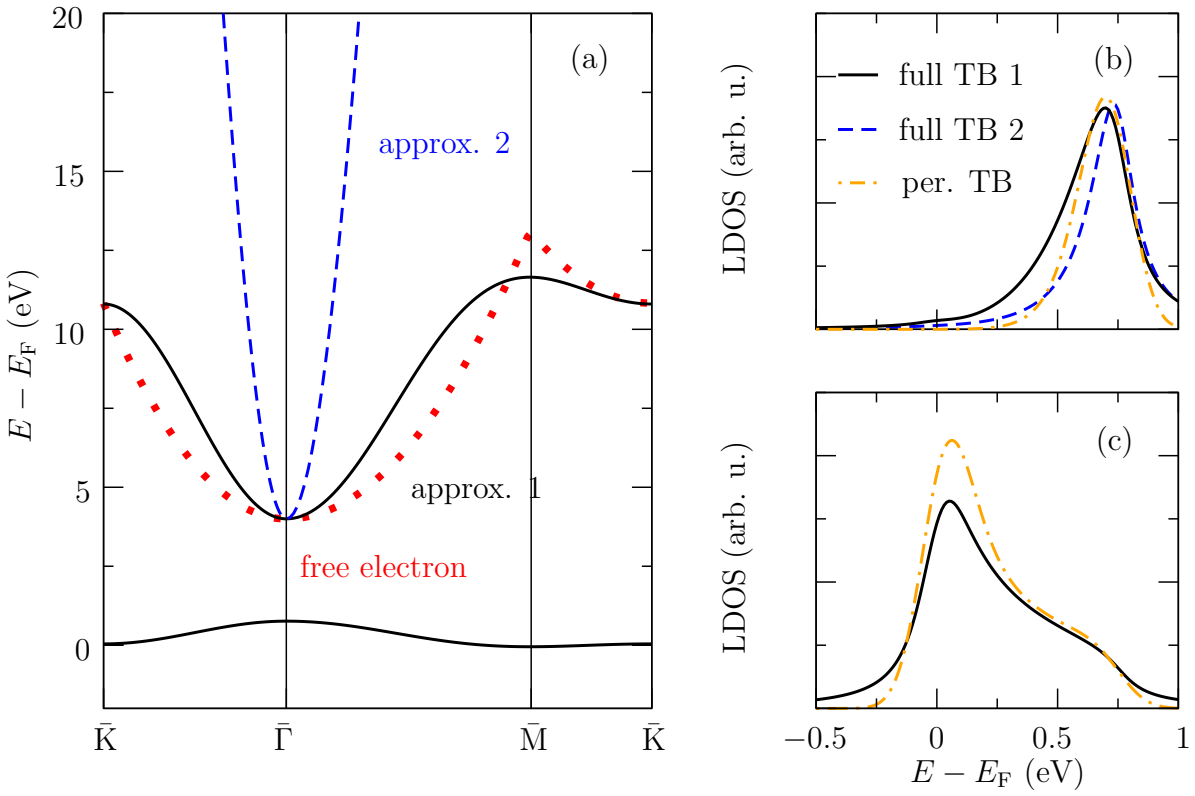

Figure 9.8: (a) Bandstructures of a band localized at the surface (solid black line at 0 eV) and of two approximations (solid black line and dashed blue line) of the free electron dispersion (dotted red line) obtained from the periodic TB model. (b) Local density of states in the vacuum at a distance of 12 Å obtained from the full TB model for the two approximations (solid black and dashed blue lines) of the free electron dispersion and with the periodic TB model (orange dashed-dotted line). (c) Local density of states at the atom used in the full TB model (solid black line) and periodic TB model (orange dashed-dotted line).

where $\mathbf{R}_V$ are the lattice sites in the vacuum. We now choose

$$\langle \mathbf{R}, n | V_{\mathrm{at,V}} | \mathbf{R}_V \rangle = \begin{cases} t_{\mathrm{at,V}} & \text{if } \mathbf{R} \text{ and } \mathbf{R}_V \text{ are on top of each other} \\ t_{\mathrm{at,V}} e^{-\kappa \Delta b} & \text{if } \mathbf{R} \text{ and } \mathbf{R}_V \text{ are in-plane nearest-neighbors} \\ 0 & \text{otherwise} \end{cases} , \quad (9.45)$$

as in Eq. (9.41), which leads to

$$\left| \widetilde{\frac{\hbar^2 \mathbf{k}^2}{2m_e}} \right\rangle = \frac{1}{N \Delta E(\mathbf{k})} |\mathbf{k}, n\rangle \, N \sum_{\mathbf{R}_V} e^{i\mathbf{k}(\mathbf{0}-\mathbf{R}_V)} \langle \mathbf{0}, n | H_1 | \mathbf{R}_V \rangle \quad (9.46)$$

$$= \frac{t_{\mathrm{av}}}{\Delta E(\mathbf{k})} |\mathbf{k}, n\rangle \left(1 + e^{-\kappa \Delta b} \sum_{\Delta \mathbf{R} \in \mathbf{NN}} e^{i\mathbf{k}\Delta\mathbf{R}} \right) \quad (9.47)$$

Eq. (9.47) shows that in the nearest neighbor approximation there are two origins of the $\mathbf{k}$-filtering effects of the vacuum decay. The term $\frac{t_{\mathrm{av}}}{\Delta E(\mathbf{k})}$ leads to a pronunciation of

$\Delta b_{1^{\text{st}}\text{NN}}$ (Å)	$\Delta b_{2^{\text{nd}}\text{NN}}$ (Å)	$\Delta b_{3^{\text{rd}}\text{NN}}$ (Å)
0.30	0.88	1.16

Table 9.1: Values of Δb for a hexagonal lattice with vacuum distance $d = 12\,\text{Å}$ and lattice constant $a = 2.71\,\text{Å}$.

states close to the $\bar{\Gamma}$ point but is independent of the distance of the vacuum layer to the surface layer. The origin of the distance dependence of the VDOS is the hopping from the vacuum sites to the atomic sites, which are not directly below the vacuum site. Since

$$\Delta b = d\left(\sqrt{1+\left(\frac{a}{d}\right)^2}-1\right) \to 0 \quad \text{for} \quad d \to \infty, \tag{9.48}$$

it can be seen that these terms become especially important for larger distances.

Exemplary values of Δb for the 1st, 2nd and 3rd in-plane nearest neighbor are shown in Tab. 9.1 for a vacuum distance of $d = 12\,\text{Å}$ and a lattice constant of $a = 2.71\,\text{Å}$. The small values suggests that to achieve a good description of the VDOS the 2nd in-plane nearest neighbor should be considered since they will lead to an enhancement of the **k**-point filtering. Therefore, one can try to improve the quality of the obtained VDOS by abolishing the demand that t_V yields a free electron like dispersion but to choose t_V larger so that the filtering effect is enhanced due to the $\frac{t_\text{av}}{\Delta E(\mathbf{k})}$ term.

Fig. 9.8 (a) shows the perfect free electron dispersion and two approximation obtained from the periodic TB model with parameters $\epsilon_\text{V}^1 = 9.1\,\text{eV}$ and $t_\text{V}^1 = -0.85\,\text{eV}$ in the first and $\epsilon_\text{V}^2 = 49\,\text{eV}$ and $t_\text{V}^2 = -7.5\,\text{eV}$ in the second approximation. This results in $\Phi = 4\,\text{eV}$ in both cases. The other parameters are chosen identical: $d = 12\,\text{Å}$ and $t_{\text{at,V}} = 0.005\,\text{eV}$. The surface band for which the vacuum density of states is calculated is also shown. The parameters for this band are $\epsilon = 0.22\,\text{eV}$ and $t = -0.09\,\text{eV}$.

Fig. 9.8 (c) shows the LDOS at the atom of this band obtained from the periodic and the full TB model for $\sigma = \Sigma = 0.09\,\text{eV}$ and $N = 30$ showing good agreement. In Fig. 9.8 (b) the VDOS obtained from the periodic TB model for $\Phi = 4\,\text{eV}$ and $d = 12\,\text{Å}$ is used as a reference, too, and is compared to the VDOS obtained from the full TB model for the two approximations of the free electron dispersion. One can see that both approximations result in the correct shape of the peak. However, the peak width of approximation 2 is in better agreement with the periodic TB model. Therefore, in the following we will use the vacuum parameters from approximation 2 in the following.

9.3 TNCMR in Spin Spirals and Skyrmions

In this section we model specific bands of the PdFe/Ir(111) system with the periodic and the full TB model. The parameters used in the models are motivated from density functional theory calculations and the experimental results.

We first motivate the choice of the parameters used for the periodic TB model by DFT calculations of the FM state of PdFe/Ir(111) and then compare the results obtained for

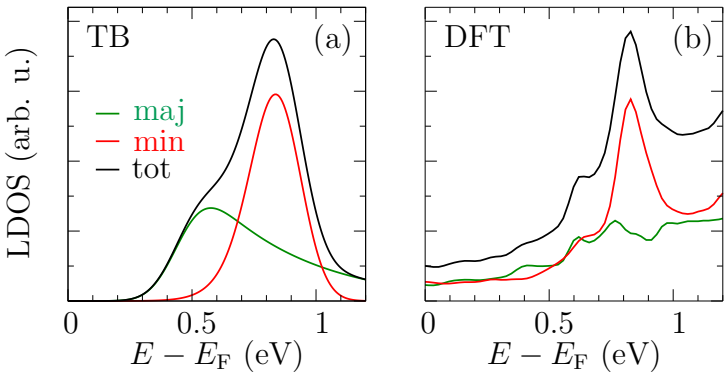

Figure 9.9: (a) Local density of states in the vacuum obtained from the periodic TB model. The TB parameters are chosen such that the shape of the density of states resembles the local density of states in the vacuum obtained from DFT calculations which is displayed in (b).

spin spirals with the corresponding DFT calculations and the experimental data. Finally, we use the same parameters for the full TB model to calculate the TNCMR in the full skyrmion structure and compare with the experimental results.

FM state

In Fig. 9.3 (b) a large peak in the experimental $\mathrm{d}I/\mathrm{d}U$ spectrum around 0.7 V can be seen. DFT calculations using the FLAPW method as implemented in the `FLEUR` code [24] indicate that the peak is due to minority d states at the Fe atom hybridizing with Pd p states as depicted in Fig. 9.9 (b)[2]. The shoulder in the $\mathrm{d}I/\mathrm{d}U$ spectrum around 0.5 V can be attributed to majority states of s and p character at the Fe and Pd atoms. The sharpness of the majority peak in the LDOS indicates a flat band and the broader features of the shoulder created by minority states indicate a band of larger dispersion.

This is considered in the periodic TB model by choosing the values $\epsilon_{\mathrm{min.}} = 0.50\,\mathrm{eV}$ and $t_{\mathrm{min}} = 0.09\,\mathrm{eV}$ for the minority band and $\epsilon_{\mathrm{maj.}} = 3.50\,\mathrm{eV}$ and $t_{\mathrm{min}} = -0.5\,\mathrm{eV}$ for the majority band. The parameters used to obtain the VDOS shown in Fig. 9.9 (a) are chosen as $d = 12\,\text{Å}$ and $\Phi = 4\,\mathrm{eV}$. The broadening is set to $\sigma = 0.09\,\mathrm{eV}$. The VDOS of the DFT calculations and the periodic TB model show good agreement.

Furthermore, the electronic structure can be represented by the bandstructure shown in Fig 9.10 (a). In the TB model the chosen values lead to a band with a small dispersion of minority spin character and a band with large dispersion of majority spin character. Due to the aforementioned **k**-point filtering caused by the vacuum decay, the VDOS singles out the band edges of the majority and minority band near $\bar{\Gamma}$. Since the minority band is flat, many states near $\bar{\Gamma}$ are localized at energies around 0.9 eV leading to a large peak in the VDOS, while the larger dispersion of the majority band only leads to a shoulder at 0.5 eV. This is also found in the marked regions in the bandstructure for the FM state obtained from DFT in Fig. 9.10 (b), albeit the number of bands is much larger since more orbitals are involved. However, qualitatively one sees largely dispersive bands of majority spin character with a pronounced band edge at 0.5 eV and flatter bands of minority spin character with a band edge at 0.9 eV.

[2] In the DFT calculations the peak is found at a slightly higher energy of 0.9 eV

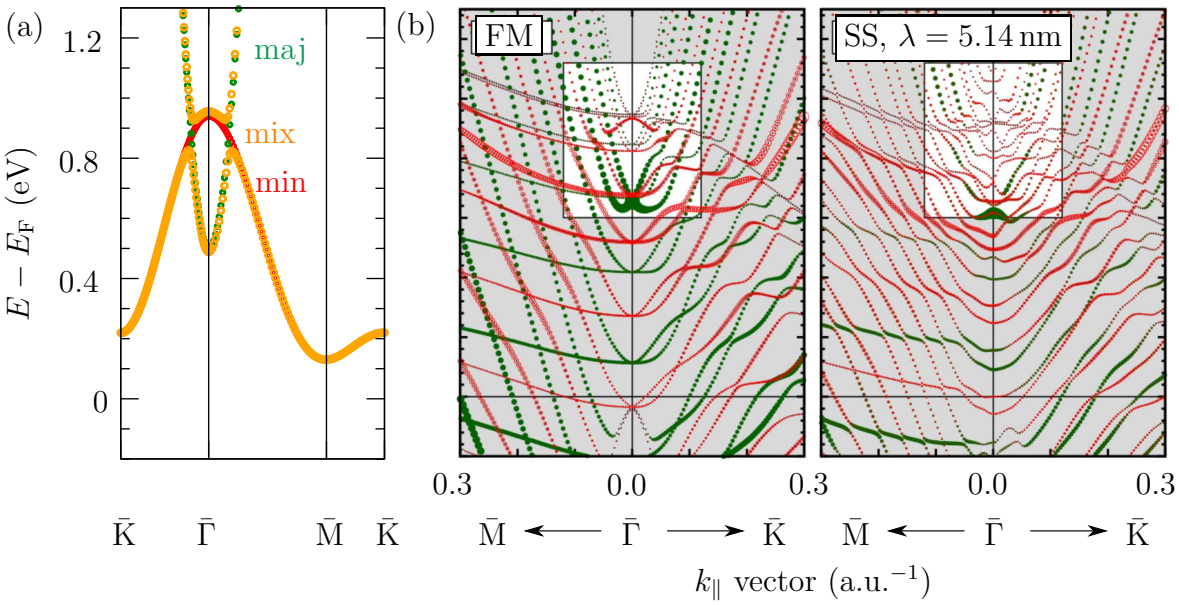

Figure 9.10: (a) Bandstructure of the FM state and a spin spiral in closed-packed direction with $\lambda = 5.14\,\text{nm}$ obtained from the periodic TB model. Bandstructure of PdFe/Ir(111) obtained from DFT calculations in (b) the FM state and (c) the same spin-spiral state, i.e., $\lambda = 5.14\,\text{nm}$, as calculated with the periodic TB model. (b) and (c) are taken from Ref. [1]. States with majority and minority spin character are represented by green and red circles, respectively. Orange circles represent mixed states.

Spin Spirals

If one now considers a spin spiral, the majority and minority states are allowed to mix. In the DFT calculations[3] this leads to a shift to lower and higher energies of the majority and minority band edge, respectively, in Fig. 9.10 (b) for a spin spiral in the $\bar{\Gamma} - \bar{M}$ direction with $\lambda = 5.14\,\text{nm}$. In addition to these shifts in energy, one also sees transitions from bands of minority character to bands of majority character leading to avoided level crossing where former crossings took place. The same behavior for the two bands of the periodic TB model can be seen in Fig. 9.10 (a) when the same spin spiral is considered. The parameter for the spin mixing is set to $t_{\downarrow\uparrow} = -t_{\uparrow\downarrow} = 0.17\,\text{eV}$[4].

If one increases the angle α between the atoms by choosing a smaller wavelength of the spin spiral, the mixing between minority and majority states enhances and the gap between the bands enlarges. This can be seen in Fig. 9.11 (a) where the VDOS obtained from the periodic TB model is shown for decreasing wavelength. While for the largest wavelength ($\lambda = 5.14\,\text{nm}$) the peak at 0.9 eV becomes only a little smaller and moves slightly to higher energies one can see a two peak structure for $\lambda = 2.57\,\text{nm}$. One should mention that the high-energy peak is caused solely by the shifting band edge of the minority states, while the low-energy peak is a superposition of the majority band edge

[3] for details see supplementary information of Ref. [1]
[4] The choice of the value is motivated by the experimental results.

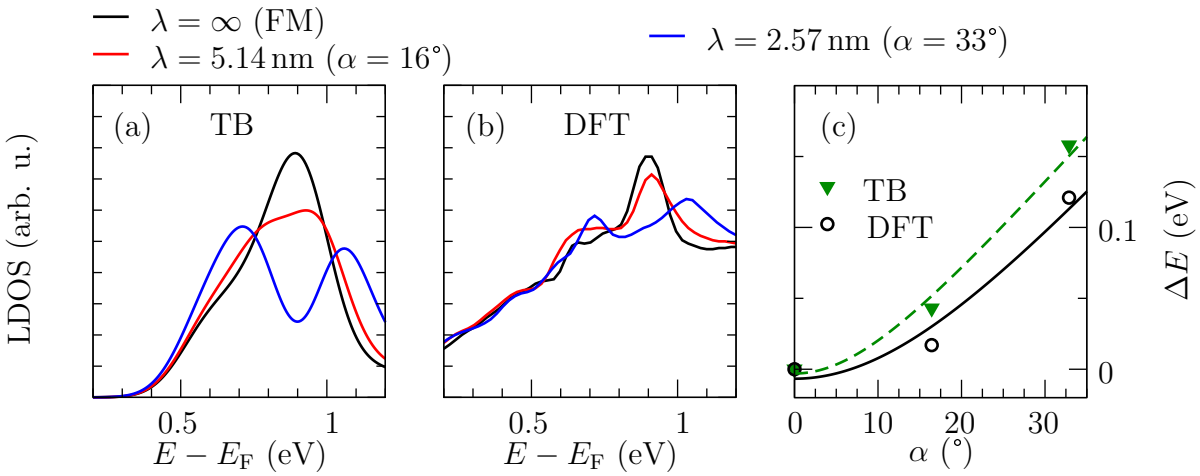

Figure 9.11: (a) Local density of states in the vacuum obtained from the periodic TB model for spin spirals in the closed-packed direction with different wavelengths. (b) Local density of states in the vacuum of the same spin spirals obtained from DFT calculations. (c) Shift of the high-energy peak as a function of the angle α between neighboring atomic rows corresponding to different wavelengths of the spin spiral obtained from the TB model (green triangles) and DFT (black circles). Lines are a fit with Eq. (9.49).

and the extra band edge created by the avoided level crossing. The broadening prevents one from identifying each peak individually. The broadening also prevents one to see a two peak structure for large wavelengths, i.e., small splittings. In the following we focus on the high-energy peak.

The same qualitative behavior of the VDOS as a function of the wavelength of the spin spiral can also be seen in the DFT calculations in Fig. 9.11 (b).

A quantitative comparison of the shift of the high-energy peak ΔE obtained from the periodic TB model and the DFT calculations is shown in Fig. 9.11 (c) and shows good agreement. The data can be fitted with a version of Eq. (9.23):

$$f(\alpha) = a_0 + \sqrt{a_1^2 + (a_2 \cdot \sin(\alpha/2))^2}. \tag{9.49}$$

In the considered range of α the sine is approximately linear, which leads to

$$f(\alpha) = a_0 + \sqrt{a_1^2 + (a_2 \cdot (\alpha/2))^2} = a_0 + a_1\sqrt{1 + \left(\frac{a_2}{2a_1}\right)^2 \alpha^2}. \tag{9.50}$$

The strongest hybridization takes place at $\mathbf{k}$-states which are close in energy. Therefore, comparison with Eq. (9.23) implies $a_2 \gg a_1$. For large α one can assume $\left(\frac{a_2}{2a_1}\right)^2 \alpha^2 \gg 1$ so that one obtains a linear dependence on α:

$$f(\alpha) \approx a_0 + \left(\frac{a_2}{2}\right)\alpha. \tag{9.51}$$

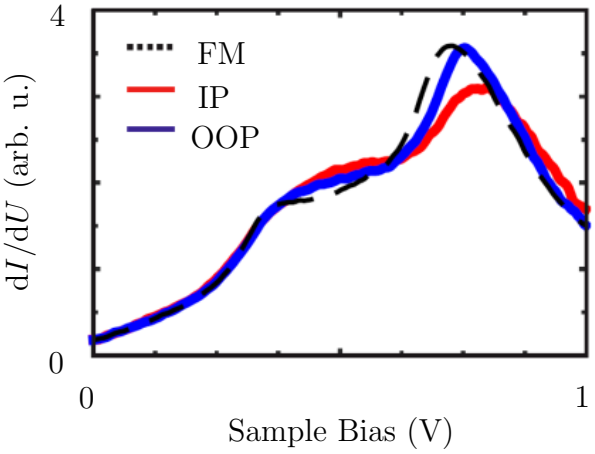

Figure 9.12: Experimental tunnel spectra at a maximal (blue, out-of-plane magnetization) and minimal (red, in-plane magnetization) $\mathrm{d}I/\mathrm{d}U$ signal of a spin spiral in PdFe/Ir(111), in comparison to the FM spectrum taken at $B = -2.5\,\mathrm{T}$ (black) ($T = 4\,\mathrm{K}$, stabilization parameters $U = -1\,\mathrm{V}$, $I = 1\,\mathrm{nA}$). Figure taken from Ref. [1].

For small angles the square root can be expanded as a Taylor series and one obtains a quadratic dependence on α:

$$f(\alpha) \approx a_0 + a_1 + \frac{a_2^2}{8a_1}\alpha^2. \tag{9.52}$$

This means that for small angles α a quadratic dependence of the peak shift of the high-energy peak is expected, while it is expected to be linear for large values of α. This is consistent with the data depicted in Fig. 9.11 (c).

The experimental $\mathrm{d}I/\mathrm{d}U$ spectrum of a spin spiral with a wavelength close to 5.14 nm of PdFe/Ir is shown in Fig. 9.12. The same behavior as observed in the TB model and the DFT calculations can be seen, i.e., compared to the FM state the peak at 0.7 eV shifts to higher energies, and decreases in height when the spin spiral is probed. The difference for the spin spiral probed at sites with in-plane and out-of-plane magnetization can be attributed to the magnetocrystalline anisotropy, which favors the magnetization to be out-of-plane [24, 113]. This leads to a faster rotation and, thus, larger angles between the atoms for a large in-plane component and smaller angles when they have a large out-of-plane components, i.e., the spin spiral is inhomogeneous.

Skyrmions: Field-Dependence at the Center

To describe the skyrmions we choose the same parameters as for the spin spirals in the previous chapter with the only difference that the on-site energies are shifted by 0.18 eV to lower energies to account for the fact that the experimental $d\mathrm{I}/d\mathrm{U}$ spectra of the FM state are shifted by this energy compared to the DFT calculations. The parameters are: $\epsilon_{\mathrm{min}} = 0.22\,\mathrm{eV}$, $\epsilon_{\mathrm{maj}} = 3.22\,\mathrm{eV}$, $t_{\mathrm{min}} = 0.09\,\mathrm{eV}$, $t_{\mathrm{maj}} = -0.5\,\mathrm{eV}$, $\Sigma = 0.09\,\mathrm{eV}$. The parameters to obtain the VDOS are $\epsilon_{\mathrm{V}} = 49\,\mathrm{eV}$, $t_{\mathrm{V}} = -7.5\,\mathrm{eV}$, $d = 12\,\text{Å}$ and $t_{\mathrm{at,V}} = 0.005\,\mathrm{eV}$. 30×30 sites are used in the scattering region, which is then attached to FM leads. The spin structure of the skyrmion is obtained from Eq. (9.3) and Eq. (9.4) using the magnetic field dependent parameters $c(B)$ and $w(B)$ obtained experimentally [113]. The geometrical setup of the calculation in the full TB model can be seen in Fig. 9.13 for a skyrmion at $B = 2.5\,\mathrm{T}$.

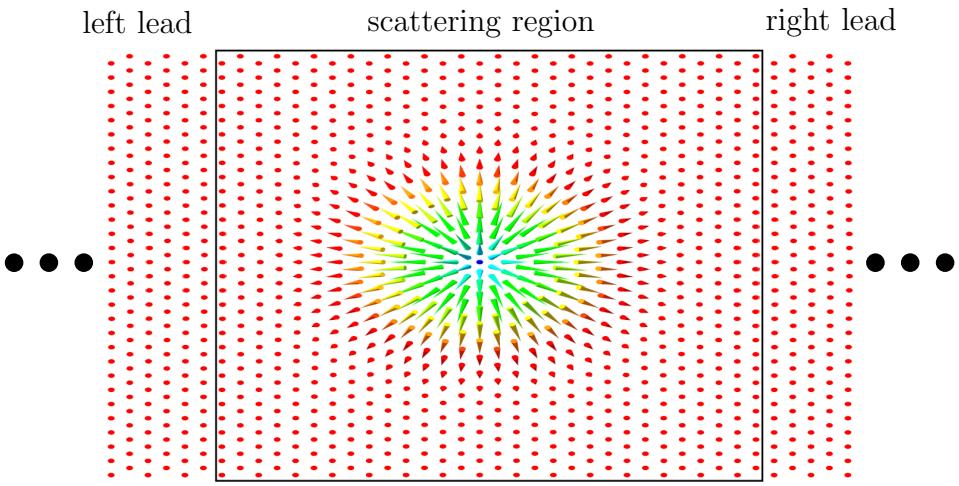

Figure 9.13: Sketch of the geometry used in the full TB model. The skyrmion in the scattering region is attached to two ferromagnetic leads.

Figs. 9.14 (a-c) show the VDOS for the FM case and at the center of the skyrmion for increasing magnetic field strengths obtained from the periodic and full TB model and the experimental $\mathrm{d}I/\mathrm{d}U$ spectra. All three plots show the same qualitative behavior that has been observed for the spin spiral, i.e., a shift of the high-energy peak at 0.7 eV and an emergent second peak around 0.5 eV. These features become the stronger the larger the field strength. As shown in Sec. 9.2.1 the exact position and the height of the peak is very sensitive to the vacuum parameters in the full TB model. This is also the main reason for the differences between the VDOS obtained from the periodic

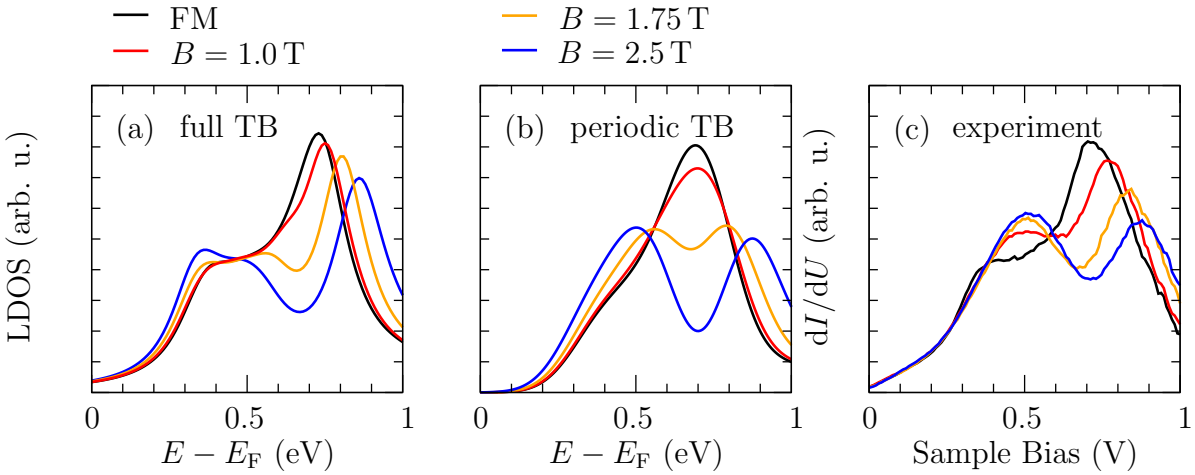

Figure 9.14: Local density of states in the vacuum above the center of skyrmions at magnetic fields of 1.0 T (red line), 1.75 T (orange line), and 2.5 T (blue line) and the FM state (black line) obtained from the (a) periodic and (b) full TB model. (c) Experimentally obtained $\mathrm{d}I/\mathrm{d}U$ spectra obtained at the center of skyrmions with the same applied magnetic fields. Experimental data taken from Ref. [117].

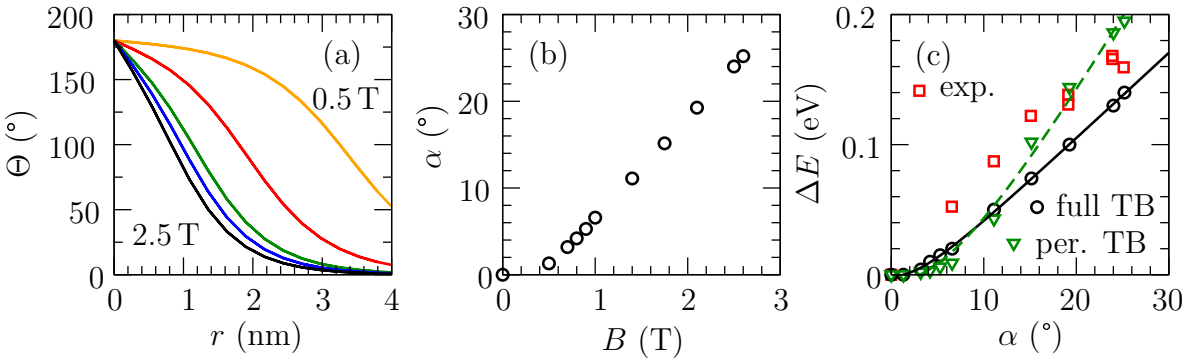

Figure 9.15: (a) $\Theta(r)$ profile for magnetic fields of 0.5 T, 1.0 T, 1.75 T, 2.1 T, and 2.5 T from top to bottom obtained via Eq. (9.3) with experimentally obtained $c(B)$ and $w(B)$ values [113]. (b) Angle α between the atom at the center of the skyrmion and its nearest neighbors as a function of the magnetic field. (c) Shift of the high-energy peak ΔE obtained from the experimental data (red squares), periodic TB model (green triangles), and full TB model (black circles) as a function of α. Experimental data taken from Ref. [117].

and full TB model in Figs. 9.14 (a) and (b) since the LDOS at the atom is very similar (cf. Fig. 9.8 (c)). The same plot for different vacuum parameters can be found in Ref. [1].

We now again analyze the peak shift of the high-energy peak ΔE quantitatively. We first correlate the angle between the atoms at the center of the skyrmion with the magnetic field. The shape of $\Theta(r)$ for different magnetic fields obtained from the spin-polarized STM experiments [113] used in the simulations can be seen in Fig. 9.15 (a). It is found that the angle α between the central atom of the skyrmion and its neighbors of the skyrmion scales linearly with the applied magnetic field as depicted in Fig. 9.15 (b). The experimentally found peak shift ΔE is also linear as a function of the angle as seen in Fig. 9.15 (c). For large angles a linear dependence is also found in the periodic and full TB model. For smaller angles one sees a quadratic behavior. The data obtained from the TB models follows Eq. (9.49) as the data obtained for the spin spiral. The steeper slope of the periodic TB model can be attributed to the fact that not the full spin structure is taken into account in the periodic TB model.

Skyrmions: Lateral Dependence

We now turn to the lateral dependence of the experimental $\mathrm{d}I/\mathrm{d}U$ data and VDOS obtained from the full TB model when moving from the FM surrounding of the skyrmion to its center. In Fig. 9.16 (a) and (b) this is shown for $B = 1.0\,\mathrm{T}$ for the theoretical and experimental data, respectively. Both data sets show the same behavior, i.e., the high-energy peak moves to higher energy as the lateral position is moved from the outskirts to the center of the skyrmion, reaching the maximum ΔE at about 1.62 nm and 1.2 nm distance from the center for the theoretical and experimental data, respectively. ΔE then decreases as the skyrmion center is approached.

The same plots of the theoretical and experimental data for a magnetic field of $B = 2.5\,\mathrm{T}$ are depicted in Fig. 9.16 (c) and (d), respectively. There, the peak shift ΔE

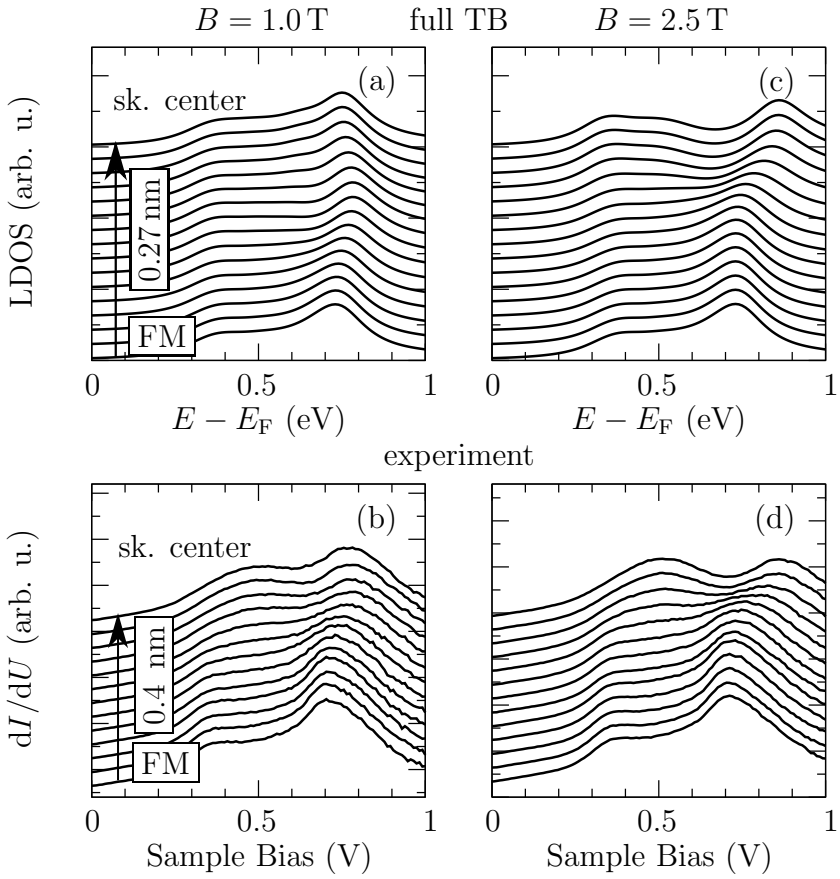

Figure 9.16: VDOS obtained from the full TB model at a distance r from the center of a skyrmion at a magnetic field of (a) $B = 1.0\,\mathrm{T}$ and (c) $B = 2.5\,\mathrm{T}$; the FM spectrum at the bottom and spectra towards the skyrmion center (top) have a vertical offset for clarity. (b, d) Corresponding plot of the experimental $\mathrm{d}I/\mathrm{d}U$ tunnel spectra measured with a W tip. Experimental data taken from Ref. [117].

increases monotonically as the center of the skyrmion is approached. Compared to the case of 1 T the peak shift starts at smaller distances from the center of about 1.89 nm and 2 nm for the theoretical and experimental data, respectively.

A quantitative analysis of the peak shift ΔE reveals that it can be correlated with the mean angle of the neighboring atoms at the lateral position defined as:

$$\bar{\alpha}(r) = \frac{1}{6}\sum_{i=1}^{6}\alpha_i(r), \tag{9.53}$$

where i sums over the angles α_i to the nearest neighbors of the atom at position r. The comparison between the experimental and theoretical data of the peak shift as a function of the distance r to the skyrmion center for $B = 1.0\,\mathrm{T}$ and 2.5 T is depicted in Figs. 9.17 (a) and (b), respectively. For $B = 1.0\,\mathrm{T}$ the theoretical data reaches a maximum of 0.05 eV at 2 nm and the experimental data a maximum of 0.06 eV at 1.5 nm. For 2.5 T the agreement between theoretical and experimental data is slightly better showing a maximum of 0.13 eV and 0.15 eV at the center of the skyrmion, respectively.

Comparing with $\bar{\alpha}(r)$ in Fig. 9.17 (c) and (d) shows that the largest peak shift ΔE is found at distances r where also $\bar{\alpha}(r)$ shows a maximum of 15° and 25° at about 2 nm and about 0.0 nm for 1.0 T and 2.5 T, respectively. The relation between $\bar{\alpha}$ and ΔE is very close to the one found in Fig. 9.15 (c) for the skyrmion center, e.g., for the maximum

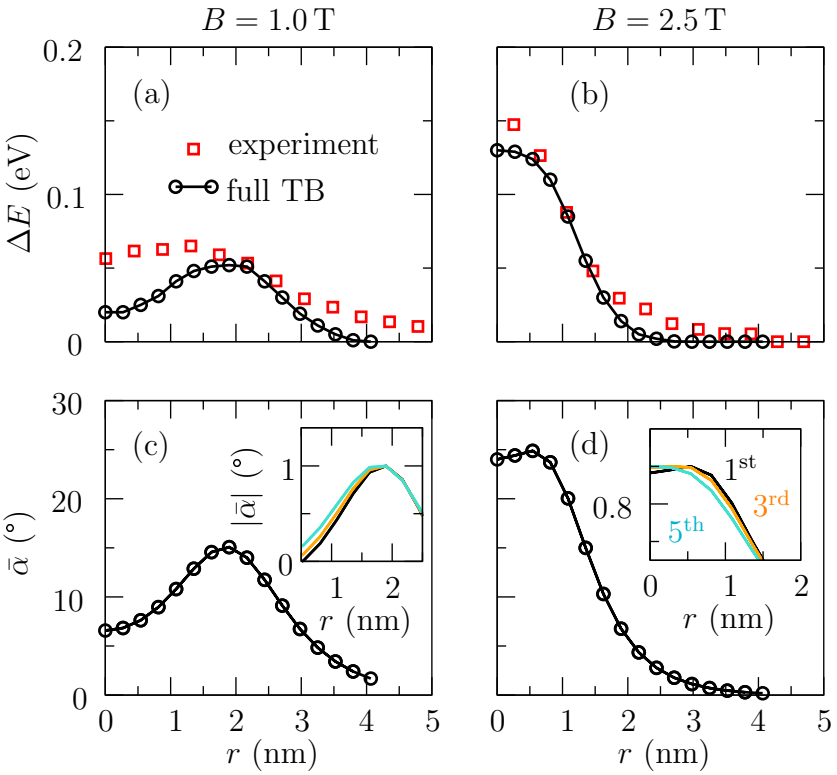

Figure 9.17: Peak shift ΔE obtained from the experimental and theoretical data as a function of the distance r from the center of a skyrmion at a magnetic field of (a) $B = 1.0\,\mathrm{T}$ and (b) $B = 2.5\,\mathrm{T}$. Mean angle $\bar{\alpha}$ between the atom at distance r from the center of the skyrmion and its neighboring defined in Eq. (9.53) for (c) $B = 1.0\,\mathrm{T}$ and (d) $B = 2.5\,\mathrm{T}$. The insets show the normalized value $|\bar{\alpha}|$ summing over the 1^{st}, 3^{rd}, and 5^{th} nearest neighbors. Experimental data taken from Ref. [117].

value of $\bar{\alpha} = 25°$ for skyrmions at $B = 2.5\,\mathrm{T}$ the peak shift is $\Delta E = 0.14$ eV and for the maximum value of $\bar{\alpha} = 15°$ for skyrmions at $B = 1.0\,\mathrm{T}$ the peak shift amounts to $\Delta E = 0.5$ eV (cf. Fig. 9.15 (c)).

The insets in Fig. 9.15 (c) and (d) show the normalized value of $\bar{\alpha}$ summing over the 1^{st}, 3^{rd}, and 5^{th} nearest neighbor. As one can see the qualitative agreement becomes the better the more neighbors are included, i.e., for 1.0 T the maximum of $|\bar{\alpha}|$ becomes more asymmetric and for 2.5 T the maximum of $|\bar{\alpha}|$ moves from slightly off-center to at-center in better agreement with the maximum of ΔE. This shows that the electronic structure is also indirectly affected by the non-local magnetic structure and that not only the nearest neighbors are important. This has already been seen when the peak-shift at the center of the skyrmion obtained from the periodic and the full TB model in Fig. 9.15 (c) was compared.

To complete the analysis we now compare the lateral variation of the relative change of the intensity of the high-energy peak ΔI_{peak} obtained from the theoretical and experimental data shown in Figs. 9.18 (a) and (b) for 1.0 T and 2.5 T, respectively. The experimental and theoretical data are in good agreement. For 1.0 T ΔI_{peak} obtained from the theoretical and experimental data shows a maximum at 2 nm and 1.3 nm distance from the center reaching values of 10 % and 20 %, respectively. For 2.5 T the maximum is found closer to the center at 1 nm and 0.9 nm reaching a value of 24 % and 26 % considering the theoretical and experimental data, respectively.

The intensity change of the high-energy peak ΔI_{peak} approximately follows the radial

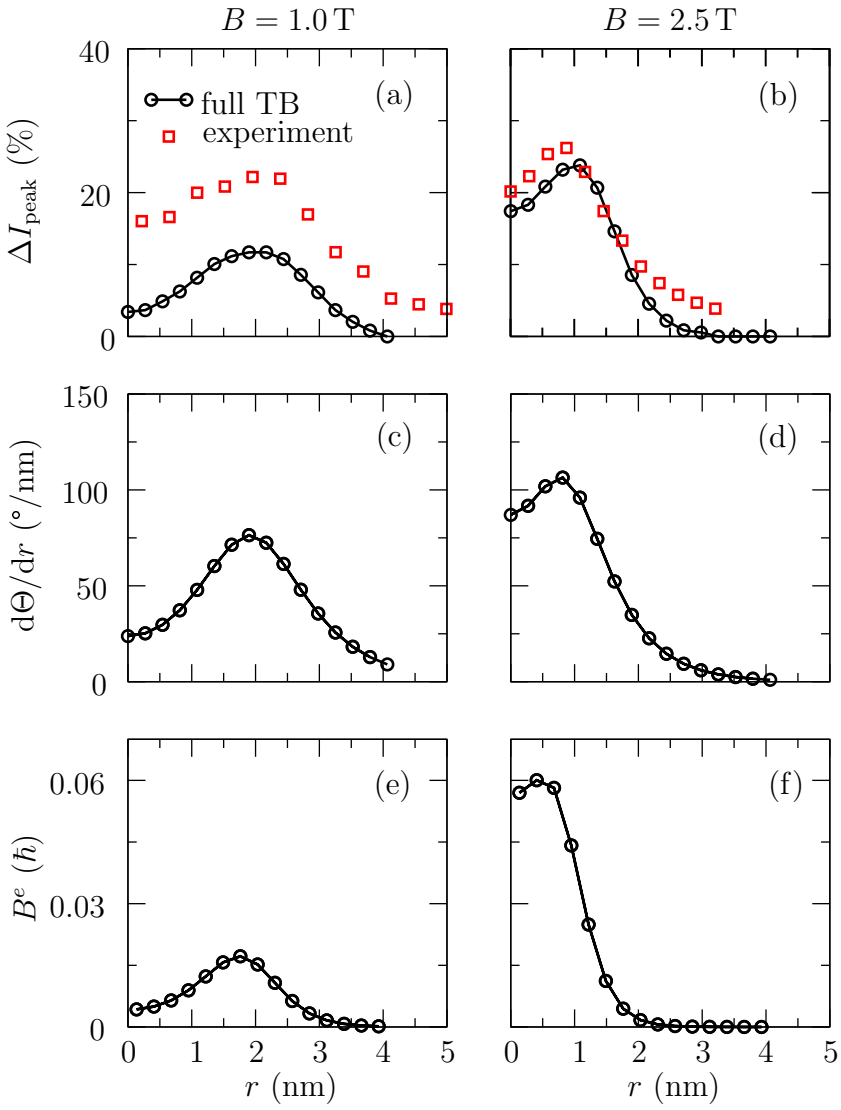

Figure 9.18: (a) and (b) show the relative change of the intensity of the high-energy peak ΔI_{peak} with respect to the height of the FM peak at 0.7 eV as a function of the distance r from the center of the skyrmion for $B = 1.0\,\text{T}$ and $B = 2.5\,\text{T}$, respectively. Experimental data taken from Ref. [117]. (c) and (d) show $\text{d}\Theta/\text{d}r$ for $B = 1.0\,\text{T}$ and $B = 2.5\,\text{T}$, respectively. (e) and (f) show the emergent magnetic field B^e or skyrmion density as a function of r for the two magnetic field strengths.

derivation of the polar angle of the skyrmion profile $\frac{\text{d}\theta}{\text{d}r}$ as can be seen by comparing with Figs. 9.18 (c) and (d). This is a nice feature since the norm of the emergent magnetic field or skyrmion density defined as [118, 119]:

$$B^e(x,y) = \frac{h}{2}\mathbf{S}\cdot\left(\frac{\partial\mathbf{S}}{\partial x}\times\frac{\partial\mathbf{S}}{\partial y}\right) \tag{9.54}$$

can be conveniently expressed in polar coordinates as

$$B^e(r,\varphi) = \frac{h}{2}\frac{\sin\theta(r)}{r}\frac{\partial\theta}{\partial r}. \tag{9.55}$$

The emergent magnetic field is the effective field an electron feels when it travels across a magnetic structure [119]. In Fig. 9.18 (e) and (f) B^e is shown for a magnetic field of 1.0 T and 2.5 T. The emergent magnetic field is proportional to $\frac{\text{d}\theta}{\text{d}r}$ just as ΔI_{peak}. For $B = 1.0$ T the modification due to the $\frac{\sin\theta(r)}{r}$ term leads to a steeper slope of

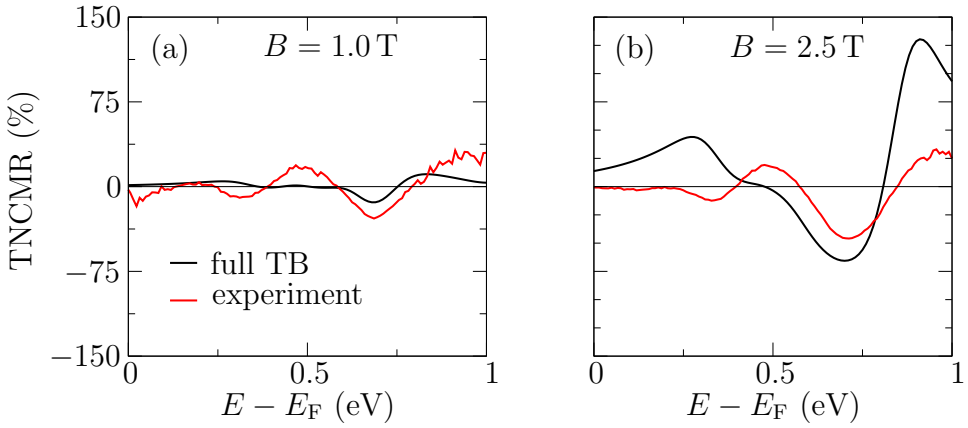

Figure 9.19: (a) TNCMR calculated using Eq. (9.1) utilizing the experimental $\mathrm{d}I/\mathrm{d}U$ value (red line) and the VDOS (black line) obtained theoretically for $B = 1.0\,\mathrm{T}$ (see text for details). (b) shows the same for $B = 2.5\,\mathrm{T}$. Experimental data taken from Ref. [117].

the emergent magnetic field compared to the slope of $\frac{\mathrm{d}\theta}{\mathrm{d}r}$ for radii r larger than 1.9 nm. However, the maximum of the emergent magnetic field coincides with the maximum of $\frac{\mathrm{d}\theta}{\mathrm{d}r}$. For $B = 2.5$ T the maximum of B^e is reached at $r = 0.4\,\mathrm{nm}$ a slightly smaller value compared to $r = 0.9$, where the maximum of $\frac{\mathrm{d}\theta}{\mathrm{d}r}$ is reached. Nevertheless, the general shape of B_e is very similar to $\frac{\mathrm{d}\theta}{\mathrm{d}r}$. Therefore, one can roughly estimate the shape of the emergent magnetic field by analyzing the height of the high-energy peak.

Comparison of TNCMR with TMR and TAMR

Figs. 9.19 (a) and (b) shows the energy-dependent TNCMR calculated using Eq. (9.1) utilizing the experimental $\mathrm{d}I/\mathrm{d}U$ value and the VDOS obtained within the TB model for $B = 1.0\,\mathrm{T}$ and $B = 2.5\,\mathrm{T}$, respectively. At the position of the high-energy peak in the FM state at 0.7 eV the TNCMR reaches values of 14 % and 66 % considering the theoretical data for 1.0 T and 2.5 T, respectively. The experimental values yield a slightly lower TNCMR for $B = 2.5\,\mathrm{T}$ and a slightly higher one for 1 T. The TNCMR as a function of energy is larger for high magnetic fields than for low magnetic fields.

However, if the TNCMR is exploited in devices, it is very unlikely that an STM tip is used as the probing electrode. Therefore, we mimic a disk-like electrode by integrating the vacuum density of states ($\propto \mathrm{d}I/\mathrm{d}U$) obtained theoretically over an area of a disk with radius r located above the skyrmion center:

$$\Xi_{\mathrm{skyrm}}(r) = 2\pi \int_0^r \mathrm{VDOS}_{\mathrm{Skyrm}}(\tilde{r})\tilde{r}\mathrm{d}\tilde{r} \tag{9.56}$$

and compare it to the FM case

$$\Xi_{\mathrm{FM}}(r) = \pi r^2 \mathrm{VDOS}_{\mathrm{FM}}. \tag{9.57}$$

The $\mathrm{TNCMR}_{\bigcirc}$ is then defined as:

$$\mathrm{TNCMR}_{\bigcirc}(r) = 100\% \cdot \frac{\Xi_{\mathrm{skyrm}}(r) - \Xi_{\mathrm{FM}}(r)}{\Xi_{\mathrm{FM}}(r)}. \tag{9.58}$$

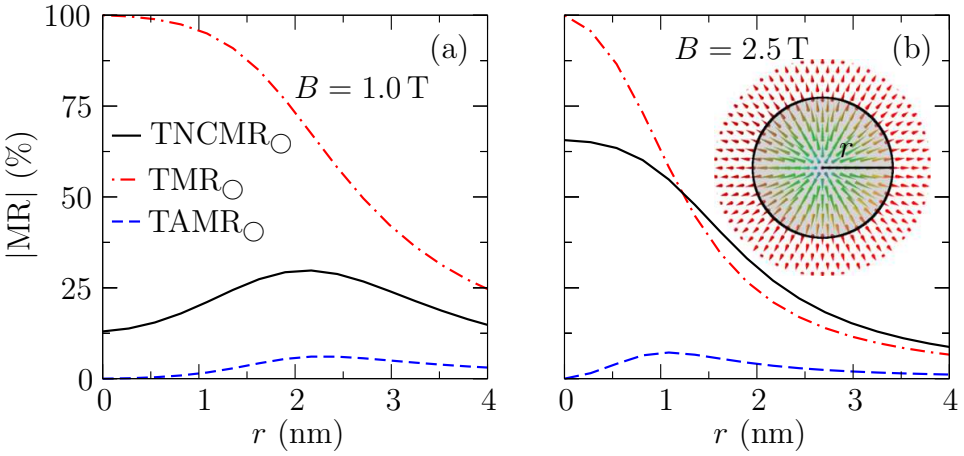

Figure 9.20: (a) $\mathrm{TNCMR}_{\bigcirc}$ (solid black line) obtained from Eq. (9.58) considering the integrated VDOS for $B = 1.0\,\mathrm{T}$. $\mathrm{TMR}_{\bigcirc}$ (dashed-dotted red line) and $\mathrm{TAMR}_{\bigcirc}$ (dashed blue line) calculated analogously to the TNCMR assuming a dependency on the magnetization direction of the skyrmion profile $\theta(r)$ according to Eqs. (9.59) and (9.60) for $B = 1.0\,\mathrm{T}$. (b) shows the same for $B = 2.5\,\mathrm{T}$.

As one can see in Fig. 9.20 (a) and (b), the $\mathrm{TNCMR}_{\bigcirc}$ reaches its maximum value of about 25 % at $r = 2\,\mathrm{nm}$ and 1 nm for $B = 1.0\,\mathrm{T}$ and 2.5 T, respectively. For disk sizes covering the whole skyrmion of about $r = 4\,\mathrm{nm}$ the value of the $\mathrm{TNCMR}_{\bigcirc}$ for 1.0 T is about 10 %, while the one for 2.5 T is only half as large. This is due to the larger area of non-collinear magnetization for skyrmions at $B = 1.0\,\mathrm{T}$ compared to skyrmions at $B = 2.5\,\mathrm{T}$, albeit the TNCMR(E) is significantly larger for $B = 2.5\,\mathrm{T}$ than for $B = 1.0\,\mathrm{T}$.

To compare the TNCMR with the TMR and TAMR, we assume that the VDOS changes with the direction of the magnetization $\theta(r)$ of the skyrmion according to

$$\mathrm{VDOS}_{\mathrm{TMR}}(r) = \mathrm{VDOS}_0(1 + P_{\mathrm{eff}} \cos\theta(r)) \tag{9.59}$$

$$\mathrm{VDOS}_{\mathrm{TAMR}}(r) = \mathrm{VDOS}_0(1 + \gamma_{\mathrm{TAMR}} \cos^2\theta(r)) \tag{9.60}$$

with $P_{\mathrm{eff}} = P_{\mathrm{S}} P_{\mathrm{T}}$, where P_{S} and P_{T} are the spin-polarization of the two electrodes, respectively. We then integrate as described above for the $\mathrm{TNCMR}_{\bigcirc}$. The value of $\gamma_{\mathrm{TAMR}} = 0.1$ determines the strength of the TAMR. $\theta(r)$ is the profile of the polar angle of the spin structure, i.e., the skyrmion profile for skyrmions and $\theta(r) \equiv 0$ for the FM case. The above Eqs. (9.59) and (9.60) ignore contributions to the VDOS originating from neighboring atomic sites (cf. with complete formulas in Refs. [55, 110, 120]), which is sufficient for the assessment done here. The vacuum density of states is integrated in the same way as has been described for the $\mathrm{TNCMR}_{\bigcirc}$. The variation due to the TAMR given by γ_{TAMR} is chosen to be 10 %, relying on values from previous publications [110]. For the TMR $P_{\mathrm{eff}} = 100\,\%$ is chosen assuming perfect spin-polarization of the electrodes.

The $\mathrm{TAMR}_{\bigcirc}$ for skyrmions at both field strengths, Figs. 9.20 (a) and (b), does not reach values larger than 7 %, although the value of γ_{TAMR} is chosen quite large. At the center of the skyrmion the $\mathrm{TAMR}_{\bigcirc}$ vanishes due to the $\cos^2\theta(r)$ dependence. For the

$\mathrm{TMR}_{\bigcirc}$ the $\cos\theta(r)$ dependence leads to a maximum value of 100 % at the center and then decreases to a value of 25 % and 6 % for disk radii of $r = 4\,\mathrm{nm}$ for $B = 1.0\,\mathrm{T}$ and $B = 2.5\,\mathrm{T}$, respectively. The decline is faster for $B = 2.5\,\mathrm{T}$ than for $B = 1.0\,\mathrm{T}$, which can be attributed to the $\Theta(r)$ profile, the rotation of which is faster for skyrmions at larger magnetic fields. The $\mathrm{TNCMR}_{\bigcirc}$ starts with values of 12 % and 65 % for skyrmions at $B = 1.0\,\mathrm{T}$ and $B = 2.5\,\mathrm{T}$ and disk radius $r = 0\,\mathrm{nm}$, respectively. For skyrmions at $B = 2.5\,\mathrm{T}$ the $\mathrm{TNCMR}_{\bigcirc}$ decreases continuously to 8.5 % at $r = 4\,\mathrm{nm}$, slightly larger than the $\mathrm{TMR}_{\bigcirc}$. For skyrmions at $B = 1.0\,\mathrm{T}$ the $\mathrm{TNCMR}_{\bigcirc}$ reaches its maximum value of 30 % at $r = 2.2\,\mathrm{nm}$ and then declines to 15 % for $r = 4\,\mathrm{nm}$, only 10 % smaller than the $\mathrm{TMR}_{\bigcirc}$. The $\mathrm{TNCMR}_{\bigcirc}$ for disk radii more than $r = 2.2\,\mathrm{nm}$ is larger for skyrmions at $B = 1.0\,\mathrm{T}$ than $B = 2.5\,\mathrm{T}$ since the area of non-collinear spin arrangement is larger for slower rotating skyrmions.

For larger disk radii the $\mathrm{TNCMR}_{\bigcirc}$ is of similar magnitude as the $\mathrm{TMR}_{\bigcirc}$ and can even be larger depending on the spin structure. For all disk radii the magnitude of the $\mathrm{TNCMR}_{\bigcirc}$ is more than five times larger than the $\mathrm{TAMR}_{\bigcirc}$. Since spin-coherence is not need for the $\mathrm{TNCMR}_{\bigcirc}$, it provides an easy possibility to detect skyrmions in future devices.

9.4 Ballistic Transport through Spin Spirals and Skyrmions

So far we considered the vertical transport properties of skyrmions and spin spirals in a tunneling geometry. However, lateral transport measurements may be another possibility to detect non-collinear spin structures. The full TB model gives access to the lateral transport properties in the x-direction. Here, we compare ballistic transport properties through spin spirals along the x-direction direction with the ones of skyrmions. Thereby, the parameters for the bands are chosen as in the previous section.

Figs. 9.21 (a) and (b) show the local density of states at the atom for spin spirals with different wavelength ranging from $\lambda = \infty\,\mathrm{nm}$ (FM case) to $\lambda = 1.63\,\mathrm{nm}$ and the corresponding transmission function, respectively. The emerging two peak structures in the LDOS around 0.7 eV discussed in detail in the previous sections for shorter wavelengths leads to a large decrease of the transmission function around 0.7 eV. This effect increases with decreasing wavelength.

Fig. 9.21 (c) and (d) show the local density of states of atoms at different distances ranging from $d = 0.0\,\mathrm{nm}$ to $d = 3.25\,\mathrm{nm}$ from the center of a skyrmion at $B = 2.5\,\mathrm{T}$ and the transmission function through this skyrmion, respectively. Since the two peak structure is only present in the LDOS in a small area around the center of the skyrmion, the transmission function shows no difference compared to the one for the FM structure. The large nearly FM surrounding of the skyrmion prevents the decrease of the lateral transmission that is seen for spin spirals. This also holds for larger skyrmions at a magnetic field of $B = 1.0\,\mathrm{T}$ (not shown).

We now compare the change in the transmission function at 0.7 eV due to the non-collinearity of the spin spirals, which corresponds to a change in the resistance and compare with the results of Ref. [121] obtained for domain wall profiles of $L1_0$-ordered

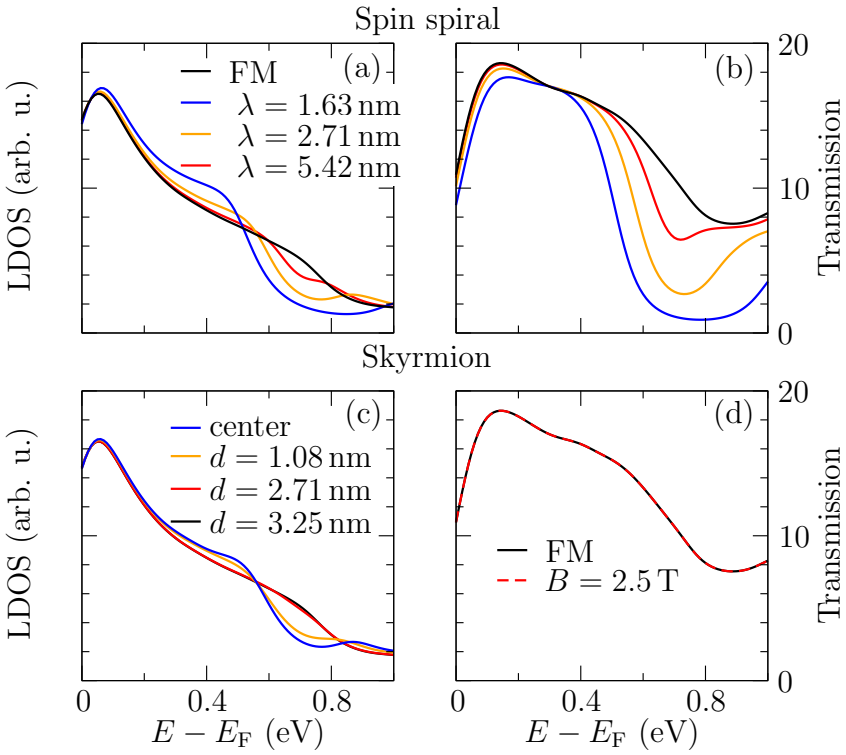

Figure 9.21: (a) LDOS at the atom obtained from the full TB model for spin spirals along the x-direction direction with different wavelengths λ. (b) Corresponding transmission function to the LDOS shown in (a). (c) LDOS at the atom obtained from the full TB model at different positions d in a skyrmion for $B = 2.5\,\mathrm{T}$. (d) Corresponding transmission function through a skyrmion at $B = 2.5\,\mathrm{T}$ and the FM structure for comparison.

FePd and FePt alloys with a thickness of 30 nm. The $L1_0$ ordering indicates an fcc structure with alternating layers consisting of Fe and Pt/Pd. In Ref. [121] by first-principles calculations based on micromagnetic simulations of domain walls in $L1_0$-FePd and $L1_0$-FePt the contribution due to the rotating magnetization

$$\rho_\mathrm{SSP}/\rho_0 = \frac{\rho(\lambda) - \rho_0}{\rho_0} \tag{9.61}$$

is calculated, whereby $\rho_0 = 1/G_\mathrm{FM}$ is the resistance for FM structures and $\rho(\lambda)$ the

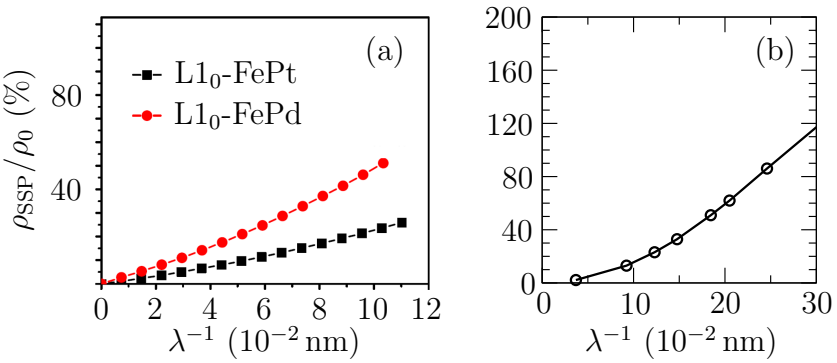

Figure 9.22: (a) Resistance of a domain wall of $L1_0$-FePd and $L1_0$-FePt as a function of the reciprocal wavelength of the domain wall. Taken from Ref. [121]. (b) Resistance of a spin spiral as a function of the reciprocal wavelength at $E_\mathrm{F} = 0.7\,\mathrm{eV}$ obtained from the full TB model with the parameters from Sec. 9.3.

resistance for a spin spiral with wavelength λ. In Ref. [121] a resistance of ρ_{SSP} mainly proportional to λ^{-1} (cf. Fig. 9.22 (a)) is found. Our results shown in Fig. 9.22 (b) for infinite spin spirals obtained from the fullTB model with the same parameters that were used in the previous section qualitatively agree with these finding in the wavelength range investigated in Ref. [121] but show a quadratic behavior for large λ^{-1}.

9.5 Summary

We have explained the origin of a novel magnetoresistance effect first observed in STM experiments probing non-collinear spin structure using nonmagnetic tips. The TNCMR originates from spin mixing of majority and minority bands in non-collinear spin structures. We have shown this by introducing a two-band TB model motivated from DFT. The TB model was solved for periodic spin structures and the full skyrmion profile. We have shown that the variation of the experimental $\mathrm{d}I/\mathrm{d}U$ signal at the center of a skyrmion for different applied magnetic fields can be attributed to the angle between the magnetic moment of the center and its neighbors. Furthermore, the lateral variation of the $\mathrm{d}I/\mathrm{d}U$ signal as the tip is moved across the skyrmion can be correlated with the mean angle between the neighboring atomic sites at each position in the skyrmion. The difference in the $\mathrm{d}I/\mathrm{d}U$ signal between non-collinear structures and the FM state constitutes the tunneling non-collinear magnetoresistance, which could be used to detect non-collinear structures in devices, e.g., skyrmions in a race-track geometry [122], without the need of a magnetic read-out electrode.

10 Summary

In this thesis the tunneling and ballistic anisotropic magnetoresistance of single-atom and single-molecule junctions have been studied based on first-principles electronic structure theory using density functional theory (DFT). In addition, a new magnetoresistance effect, coined the tunneling non-collinear magnetoresistance (TNCMR), has been investigated based on electronic structure theory combining DFT and tight-binding (TB) calculations.

In atomically wide constrictions, the AMR is expected to be enhanced due to the large reduction of conducting modes. Here, we have used an approach to obtain the transmission function of such atomic-scale junctions which is based on DFT calculations utilizing the full-potential linearized augmented plane wave (FLAPW) method as implemented in the `FLEUR` code. The electronic structure obtained by the FLAPW method is projected on Wannier functions preserving all the information, e.g., spin-orbit coupling (SOC) effects, contained in the FLAPW results. With the help of the Wannier functions, Hamiltonian matrices for the open quantum system are constructed, which are then used in a Green's function formalism to yield the transmission function. The method has been described in chapters 2 to 4.

In chapter 5, the calculated AMR of symmetric Ni monowires terminated with Co, Rh and Ir apex atoms has been presented. Here, the distance between the apex atoms is varied, which yields the distance dependence of the AMR in atomic-scale junctions from the tunneling to the contact regime. It has been found that the AMR increases for heavier apex atoms reaching values of up to 150 %. The distance dependence of the AMR has been found to be non-trivial and even sign changes were observed. These findings can be explained by the different symmetry of the orbitals dominating the transmission function in the contact and tunneling regime.

The insights gained from the DFT results on single-atom junctions from chapter 5 allowed to explain scanning tunneling microscopy (STM) experiments of Co and Ir adatoms on a double layer of Fe on W(110) as discussed in chapter 6. The double layer of Fe on W(110) exhibits domains and domain walls with a magnetization pointing parallel and perpendicular to the surface, respectively. The magnetic moments of the adatoms on domains and domain walls are coupled by the exchange interaction to the magnetic moments of the underlying Fe atoms. Thereby, the two configurations needed to probe the AMR are realized without the requirement of an external magnetic field. The adatoms have been approached with a W tip yielding the distance dependence of the AMR with a magnitude of about 10 %. A TB model, the key ingredients of which are the orbital mixing due to SOC at the adatom and the orbital-dependent decay of the transmission function across the gap between adatom and STM tip, is used to explain

the experimental results. Furthermore, an analytical form of the distance dependence of the conductance for each contributing mode has been derived based on the Green's function formalism. This analytical result leads to a very good fit of the experimental data.

In chapter 7, a new concept to enhance the AMR in atomic-scale junctions is presented. In particular, molecules have been used to provide a symmetry filter for the conducting channels. To demonstrate this effect the AMR has been calculated for model junctions of Ni and Co monowires contacting the molecules Bz, VBz_2, $TaBz_2$, $NbBz_2$, and V_2Bz_3. It has been found that the interface of the metal monowires with the molecules filters the transmission function according to the orbital symmetry. The quality of the orbital-symmetry filtering depends strongly on the electronic structure of the molecule and the interactions with the contacting leads. The AMR in monowires can be enhanced to gigantic values due to the orbital-symmetry filtering. A generic TB model has been presented, which suggests that this molecular AMR can also be found in molecules on surfaces that may be studied using STM.

In Chapter 8, we have gone beyond the idealized monowire geometry and considered a more realistic break junction geometry of Pt trimers. Pt is expected to become magnetic in low-dimensional systems. However, direct experimental verification is currently out of reach and therefore one has tried to use the AMR to indirectly verify the theoretical predictions. Motivated by recent experimental magnetoresistance measurements on Pt break junctions, we have investigated these systems and found conductances in the range of 0.75 to 0.9 $2e^2/h$ and an AMR of up to 20 %. During elongation these values vary, which can be attributed to changes in the electronic structure caused by the emergent magnetism and the bonding characteristics for the different elongations. Qualitatively, our findings agree well with the experimental data.

In chapter 9, a new magnetotransport effect has been presented. The TNCMR was recently discovered in STM experiments with non-magnetic tips probing large non-collinear spin structures, i.e., skyrmions. Here, we provided the first understanding by a two-orbital TB model incorporating the full spin structure adapted to results from DFT calculations of spin-spiral states. A pronounced peak shift in the experimental $\mathrm{d}I/\mathrm{d}U$ signal when the STM tip is moved from the ferromagnetic environment to the center of the skyrmion can be attributed to the mixing between states of majority and minority spin due to the non-collinearity of the spin structure. The TNCMR provides a possibility for an all-electrical detection of skyrmions in ferromagnetic environments and could be used to detect skyrmions in future devices.

Bibliography

[1] C. Hanneken, F. Otte, A. Kubetzka, B. Dupé, N. Romming, K. von Bergmann, R. Wiesendager and S. Heinze, *Electrical detection of magnetic skyrmions by tunnelling non-collinear magnetoresistance*, Nature Nanotechnology **10**, 1039 (2015).

[2] W. Thomson, *On the electro-dynamic qualities of metals:–effects of magnetization on the electric conductivity of nickel and of iron*, Proc. R. Soc. **8**, 546 (1856).

[3] T. R. McGuire and R. I. Potter, *Anisotropic magnetoresistance in ferromagnetic 3d alloys*, IEEE Trans. Magn. **11**, 1018 (1975).

[4] G. Binasch, P. Grünberg, F. Saurenbach and W. Zinn, *Enhanced magnetoresistance in layered magnetic structures with antiferromagnetic interlayer exchange*, Phys. Rev. B **39**, 4828 (1989).

[5] M. N. Baibich, J. M. Broto, A. Fert, F. N. Van Dau, F. Petroff, P. Etienne, G. Creuzet, A. Friederich and J. Chazelas, *Giant magnetoresistance of (001)fe/(001)cr magnetic superlattices*, Phys. Rev. Lett. **61**, 2472 (1988).

[6] C. Chappert, A. Fert and F. N. Van Dau, *The emergence of spin electronics in data storage*, Nature Materials **6**, 813 (2007).

[7] M. Julliere, *Tunneling between ferromagnetic films*, Phys. Lett. A **54**, 225 (1975).

[8] C. Gould, C. Rüster, T. Jungwirth, E. Girgis, G. M. Schott, R. Giraud, K. Brunner, G. Schmidt and L. W. Molenkamp, *Tunneling anisotropic magnetoresistance: A spin-valve-like tunnel magnetoresistance using a single magnetic layer*, Phys. Rev. Lett. **93**, 117203 (2004).

[9] J. Velev, R. F. Sabirianov, S. S. Jaswal and E. Y. Tsymbal, *Ballistic anisotropic magnetoresistance*, Phys. Rev. Lett. **94**, 127203 (2005).

[10] N. Néel, S. Schröder, N. Ruppelt, P. Ferriani, J. Kröger, R. Berndt and S. Heinze, *Tunneling anisotropic magnetoresistance at the single-atom limit*, Phys. Rev. Lett. **110**, 037202 (2013).

[11] G. Binnig, H. Rohrer, C. Gerber and E. Weibel, *Tunneling through a controllable vacuum gap*, Appl. Phys. Lett. **40** (1982).

[12] R. Wiesendanger, H.-J. Güntherodt, G. Güntherodt, R. J. Gambino and R. Ruf, *Observation of vacuum tunneling of spin-polarized electrons with the scanning tunneling microscope*, Phys. Rev. Lett. **65**, 247 (1990).

[13] P. Hohenberg and W. Kohn, *Inhomogeneous electron gas*, Phys. Rev. **136**, B864 (1964).

[14] W. Kohn and L. J. Sham, *Self-consistent equations including exchange and correlation effects*, Phys. Rev. **140**, A1133 (1965).

[15] D. R. Hamann, *Semiconductor charge densities with hard-core and soft-core pseudopotentials*, Phys. Rev. Lett. **42**, 662 (1979).

[16] E. Wimmer, H. Krakauer, M. Weinert and A. J. Freeman, *Full-potential self-consistent linearized-augmented-plane-wave method for calculating the electronic structure of molecules and surfaces:* o_2 *molecule*, Phys. Rev. B **24**, 864 (1981).

[17] L. Keldysh, *Diagram technique for nonequilibrium processes*, Sov. Phys. JETP **20**, 1018 (1965).

[18] N. Marzari, A. A. Mostofi, J. R. Yates, I. Souza and D. Vanderbilt, *Maximally localized wannier functions: Theory and applications*, Rev. Mod. Phys. **84**, 1419 (2012).

[19] www.flapw.de .

[20] Y. Mokrousov, G. Bihlmayer and S. Blügel, *Full-potential linearized augmented plane-wave method for one-dimensional systems: Gold nanowire and iron monowires in a gold tube*, Phys. Rev. B **72**, 045402 (2005).

[21] R. Landauer, *Spatial variation of currents and fields due to localized scatterers in metallic conduction*, IBM J. Res. Dev. **1**, 223 (1957).

[22] F. Strigl, C. Espy, M. Bückle, E. Scheer and T. Pietsch, *Emerging magnetic order in platinum atomic contacts and chains*, Nature Communications **6**, 6172 (2015).

[23] N. Romming, C. Hanneken, M. Menzel, J. E. Bickel, B. Wolter, K. von Bergmann, A. Kubetzka and R. Wiesendanger, *Writing and deleting single magnetic skyrmions*, Science **341**, 636 (2013).

[24] B. Dupé, M. Hoffmann, C. Paillard and S. Heinze, *Tailoring magnetic skyrmions in ultra-thin transition metal films*, Nature Communications **5**, 4030 (2014).

[25] L. M. Sandratskii, *Energy band structure calculations for crystals with spiral magnetic structure*, Phys. Status Solidi B **136**, 167 (1986).

[26] S. Sanvito, *Ab-initio methods for spin-transport at the nanoscale level*, arXiv:cond-mat/0503445v2 [cond-mat.mes-hall] (2005).

[27] D. Bozec, M. A. Howson, B. J. Hickey, S. Shatz, N. Wiser, E. Y. Tsymbal and D. G. Pettifor, *Mean free path effects on the current perpendicular to the plane magnetoresistance of magnetic multilayers*, Phys. Rev. Lett. **85**, 1314 (2000).

[28] S. Datta, *Electronic Transport in Mesoscopic Systems*, Cambridge Studies in Semiconductor Physics and Microelectronic Engineering, Cambridge University Press (1997).

[29] M. Büttiker, Y. Imry, R. Landauer and S. Pinhas, *Generalized many-channel conductance formula with application to small rings*, Phys. Rev. B **31**, 6207 (1985).

[30] M. Büttiker, *Symmetry of electrical conduction*, IBM J. Res. Dev. **32**, 317 (1988).

[31] D. S. Fisher and P. A. Lee, *Relation between conductivity and transmission matrix*, Phys. Rev. B **23**, 6851 (1981).

[32] F. Guinea, C. Tejedor, F. Flores and E. Louis, *Effective two-dimensional hamiltonian at surfaces*, Phys. Rev. B **28**, 4397 (1983).

[33] M. Wimmer, *Quantum transport in nanostructures: From computational concepts to spintronics in graphene and magnetic tunnel junctions*, Ph.D. thesis, University of Regensburg (2008).

[34] Y. Meir and N. S. Wingreen, *Landauer formula for the current through an interacting electron region*, Phys. Rev. Lett. **68**, 2512 (1992).

[35] R. Lake, G. Klimeck, R. C. Bowen and D. Jovanovic, *Single and multiband modeling of quantum electron transport through layered semiconductor devices*, J. Appl. Phys. **81**, 7845 (1997).

[36] C. Caroli, R. Combescot, P. Nozieres and D. Saint-James, *Direct calculation of the tunneling current*, J. Phys. C: Solid State **4**, 916 (1971).

[37] A. Svizhenko, M. P. Anantram, T. R. Govindan, B. Biegel and R. Venugopal, *Two-dimensional quantum mechanical modeling of nanotransistors*, J. Appl. Phys. **91**, 2343 (2002).

[38] M. Levy, *Universal variational functionals of electron densities, first-order density matrices, and natural spin-orbitals and solution of the v-representability problem*, Proc. Natl. Acad. Sci. USA **76**, 6062 (1979).

[39] J. C. Slater, *A simplification of the hartree-fock method*, Phys. Rev. **81**, 385 (1951).

[40] O. K. Andersen, *Linear methods in band theory*, Phys. Rev. B **12**, 3060 (1975).

[41] D. D. Koelling and G. O. Arbman, *Use of energy derivative of the radial solution in an augmented plane wave method: application to copper*, J. Phys. F: Met. Phys. **5**, 2041 (1975).

[42] P. M. Marcus, *Variational methods in the computation of energy bands*, Int. J. Quantum. Chem. **1**, 567 (1967).

[43] D. D. Koelling and B. N. Harmon, *A technique for relativistic spin-polarised calculations*, J. Phys. C: Solid State **10**, 3107 (1977).

[44] G. H. Wannier, *The structure of electronic excitation levels in insulating crystals*, Phys. Rev. **52**, 191 (1937).

[45] N. Marzari and D. Vanderbilt, *Maximally localized generalized wannier functions for composite energy bands*, Phys. Rev. B **56**, 12847 (1997).

[46] I. Souza, N. Marzari and D. Vanderbilt, *Maximally localized wannier functions for entangled energy bands*, Phys. Rev. B **65**, 035109 (2001).

[47] F. Freimuth, Y. Mokrousov, D. Wortmann, S. Heinze and S. Blügel, *Maximally localized wannier functions within the flapw formalism*, Phys. Rev. B **78**, 035120 (2008).

[48] A. A. Mostofi, J. R. Yates, Y.-S. Lee, I. Souza, D. Vanderbilt and N. Marzari, *wannier90: A tool for obtaining maximally-localised wannier functions*, Comput. Phys. Commun. **178**, 685 (2008).

[49] B. Hardrat, *Ballistic transport in one-dimensional magnetic nanojunctions: A first-principles wannier function approach*, Ph.D. thesis, University of Kiel (2012).

[50] R. Wang, E. A. Lazar, H. Park, A. J. Millis and C. A. Marianetti, *Selectively localized wannier functions*, Phys. Rev. B **90**, 165125 (2014).

[51] M. Bode, S. Heinze, A. Kubetzka, O. Pietzsch, X. Nie, G. Bihlmayer, S. Blügel and R. Wiesendanger, *Magnetization-direction-dependent local electronic structure probed by scanning tunneling spectroscopy*, Phys. Rev. Lett. **89**, 237205 (2002).

[52] A. Matos-Abiague and J. Fabian, *Anisotropic tunneling magnetoresistance and tunneling anisotropic magnetoresistance: Spin-orbit coupling in magnetic tunnel junctions*, Phys. Rev. B **79**, 155303 (2009).

[53] A. N. Chantis, K. D. Belashchenko, E. Y. Tsymbal and M. van Schilfgaarde, *Tunneling anisotropic magnetoresistance driven by resonant surface states: First-principles calculations on an fe(001) surface*, Phys. Rev. Lett. **98**, 046601 (2007).

[54] J. D. Burton, R. F. Sabirianov, J. P. Velev, O. N. Mryasov and E. Y. Tsymbal, *Effect of tip resonances on tunneling anisotropic magnetoresistance in ferromagnetic metal break-junctions: A first-principles study*, Phys. Rev. B **76**, 144430 (2007).

[55] S. Schröder, *First-principles study of non-collinear magnetism and spin-orbit driven physics in nanostructures at surfaces*, Ph.D. thesis, University of Kiel (2013).

[56] N. M. Caffrey, S. Schröder, P. Ferriani and S. Heinze, *Tunneling anisotropic magnetoresistance effect of single adatoms on a noncollinear magnetic surface*, J. Phys. Condens. Matter **26**, 394010 (2014).

[57] A. Sokolov, C. Zhang, E. Y. Tsymbal, J. Redepenning and B. Doudin, *Quantized magnetoresistance in atomic-size contacts*, Nature Nanotechnology **2**, 171 (2006).

[58] S.-F. Shi and D. C. Ralph, *Atomic motion in ferromagnetic break junctions*, Nature Nanotechnology **2**, 522 (2007).

[59] W. F. Egelhoff Jr., L. Gan, H. Ettedgui, Y. Kadmon, C. J. Powell, P. J. Chen, A. J. Shapiro, R. D. McMichael, J. J. Mallett, T. P. Moffat, M. D. Stiles and E. B. Svedberg, *Artifacts that mimic ballistic magnetoresistance*, J. Magn. Magn. Mater. **287**, 496 (2005).

[60] K. I. Bolotin, F. Kuemmeth and D. C. Ralph, *Anisotropic magnetoresistance and anisotropic tunneling magnetoresistance due to quantum interference in ferromagnetic metal break junctions*, Phys. Rev. Lett. **97**, 127202 (2006).

[61] M. Viret, M. Gabureac, F. Ott, C. Fermon, C. Barreteau, G. Autes and R. Guirado-Lopez, *Giant anisotropic magneto-resistance in ferromagnetic atomic contacts*, Eur. Phys. J. B **51**, 1 (2006).

[62] G. Autès, C. Barreteau, D. Spanjaard and M.-C. Desjonquères, *Electronic transport in iron atomic contacts: From the infinite wire to realistic geometries*, Phys. Rev. B **77**, 155437 (2008).

[63] G. Autès, C. Barreteau, M.-C. Desjonquères, D. Spanjaard and M. Viret, *Giant orbital moments are responsible for the anisotropic magnetoresistance of atomic contacts*, Eur. Phys. Lett. **83**, 17010 (2008).

[64] M. Häfner, J. K. Viljas and J. C. Cuevas, *Theory of anisotropic magnetoresistance in atomic-sized ferromagnetic metal contacts*, Phys. Rev. B **79**, 140410 (2009).

[65] D. Jacob, J. Fernández-Rossier and J. J. Palacios, *Anisotropic magnetoresistance in nanocontacts*, Phys. Rev. B **77**, 165412 (2008).

[66] Y. Mokrousov, *Ab* initio *all-electron full-potential linearized augmented plane-wave method for one-dimensional systems*, Ph.D. thesis, RWTH Aachen (2005).

[67] J. C. Tung and G. Y. Guo, *Systematic ab initio study of the magnetic and electronic properties of all* 3*d transition metal linear and zigzag nanowires*, Phys. Rev. B **76**, 094413 (2007).

[68] J. Kröger, N. Néel and L. Limot, *Contact to single atoms and molecules with the tip of a scanning tunnelling microscope*, J. Phys. Condens. Matter **20**, 223001 (2008).

[69] Y. Mokrousov, G. Bihlmayer, S. Heinze and S. Blügel, *Giant magnetocrystalline anisotropies of* 4*d transition-metal monowires*, Phys. Rev. Lett. **96**, 147201 (2006).

[70] P. Bruno, *Tight-binding approach to the orbital magnetic moment and magnetocrystalline anisotropy of transition-metal monolayers*, Phys. Rev. B **39**, 865 (1989).

[71] N. N. Negulyaev, J. Dorantes-Dávila, L. Niebergall, L. Juárez-Reyes, G. M. Pastor and V. S. Stepanyuk, *Alloying route to tailor giant magnetic anisotropy in transition-metal nanowires*, Phys. Rev. B **87**, 054425 (2013).

[72] E. Abate and M. Asdente, *Tight-binding calculation of* 3*d bands of fe with and without spin-orbit coupling*, Phys. Rev. **140**, A1303 (1965).

[73] J. Schöneberg and N. Néel, private communication (2015).

[74] M. Polok, D. V. Fedorov, A. Bagrets, P. Zahn and I. Mertig, *Evaluation of conduction eigenchannels of an adatom probed by an stm tip*, Phys. Rev. B **83**, 245426 (2011).

[75] S. Sanvito, *Molecular spintronics: The rise of spinterface science*, Nature Physics **6**, 562 (2010).

[76] N. Atodiresei, J. Brede, P. Lazić, V. Caciuc, G. Hoffmann, R. Wiesendanger and S. Blügel, *Design of the local spin polarization at the organic-ferromagnetic interface*, Phys. Rev. Lett. **105**, 066601 (2010).

[77] C. Barraud, P. Seneor, R. Mattana, S. Fusil, K. Bouzehouane, C. Deranlot, P. Graziosi, L. Hueso, I. Bergenti, V. Dediu, F. Petroff and A. Fert, *Unravelling the role of the interface for spin injection into organic semiconductors*, Nature Physics **6**, 615 (2010).

[78] A. R. Rocha and S. Sanvito, *Resonant magnetoresistance in organic spin valves (invited)*, J. Appl. Phys. **101**, 7845 (2007).

[79] A. R. Rocha, V. M. Garcia-suarez, S. W. Bailey, C. J. Lambert, J. Ferrer and S. Sanvito, *Towards molecular spintronics*, Nature Materials **4**, 335 (2005).

[80] D. Waldron, P. Haney, B. Larade, A. MacDonald and H. Guo, *Nonlinear spin current and magnetoresistance of molecular tunnel junctions*, Phys. Rev. Lett. **96**, 166804 (2006).

[81] K. Horiguchi, T. Sagisaka, S. Kurokawa and A. Sakai, *Electron transport through ni/1,4-benzenedithiol/ni single-molecule junctions under magnetic field*, J. Appl. Phys. **113**, 144313 (2013).

[82] R. Yamada, M. Noguchi and H. Tada, *Magnetoresistance of single molecular junctions measured by a mechanically controllable break junction method*, Appl. Phys. Lett. **98**, 053110 (2011).

[83] J. R. Petta, S. K. Slater and D. C. Ralph, *Spin-dependent transport in molecular tunnel junctions*, Phys. Rev. Lett. **93**, 136601 (2004).

[84] S. Schmaus, A. Bagrets, Y. Nahas, T. K. Yamada, A. Bork, M. Bowen, E. Beaurepaire, F. Evers and W. Wulfhekel, *Giant magnetoresistance through a single molecule*, Nature Nanotechnology **6**, 185 (2011).

[85] M. Grünewald, M. Wahler, F. Schumann, M. Michelfeit, C. Gould, R. Schmidt, F. Würthner, G. Schmidt and L. W. Molenkamp, *Tunneling anisotropic magnetoresistance in organic spin valves*, Phys. Rev. B **84**, 125208 (2011).

[86] J.-J. Li, M.-L. Bai, Z.-B. Chen, X.-S. Zhou, Z. Shi, M. Zhang, S.-Y. Ding, S.-M. Hou, W. Schwarzacher, R. J. Nichols and B.-W. Mao, *Giant single-molecule anisotropic magnetoresistance at room temperature*, J. Am. Chem. Soc. **137**, 5923 (2015).

[87] G. Schull, T. Frederiksen, A. Arnau, D. Sanchez-Portal and R. Berndt, *Atomic-scale engineering of electrodes for single-molecule contacts*, Nature Nanotechnology **6**, 23 (2011).

[88] J. Brede, N. Atodiresei, S. Kuck, P. Lazić, V. Caciuc, Y. Morikawa, G. Hoffmann, S. Blügel and R. Wiesendanger, *Spin- and energy-dependent*

tunneling through a single molecule with intramolecular spatial resolution, Phys. Rev. Lett. **105**, 047204 (2010).

[89] L. Chen, Z. Hu, A. Zhao, B. Wang, Y. Luo, J. Yang and J. G. Hou, *Mechanism for negative differential resistance in molecular electronic devices: Local orbital symmetry matching*, Phys. Rev. Lett. **99**, 146803 (2007).

[90] S. Lei, W. Feng, B. Li, Q. Li, A. Zhao, B. Wang, J. Yang and J. G. Hou, *Orbital-selective single molecule rectifier on graphene-covered ru(0001) surface*, Appl. Phys. Lett. **102**, 163506 (2013).

[91] V. Iancu, K.-F. Braun, K. Schouteden and C. Van Haesendonck, *Inducing magnetism in pure organic molecules by single magnetic atom doping*, Phys. Rev. Lett. **113**, 106102 (2014).

[92] J. Wang, P. H. Acioli and J. Jellinek, *Structure and magnetism of vnbzn+1 sandwich clusters*, J. Am. Chem. Soc. **127**, 2812 (2005).

[93] Y. Mokrousov, N. Atodiresei, G. Bihlmayer, S. Heinze and S. Blügel, *The interplay of structure and spin–orbit strength in the magnetism of metal–benzene sandwiches: from single molecules to infinite wires*, Nanotechnology **18**, 495402 (2007).

[94] H. Weng, T. Ozaki and K. Terakura, *Revisiting magnetic coupling in transition-metal-benzene complexes with maximally localized wannier functions*, Phys. Rev. B **79**, 235118 (2009).

[95] S. H. Vosko, L. Wilk and M. Nusair, *Accurate spin-dependent electron liquid correlation energies for local spin density calculations: a critical analysis*, Can. J. Phys. **58**, 1200 (1980).

[96] B. W. Heinrich, L. Limot, M. V. Rastei, C. Iacovita, J. P. Bucher, D. M. Djimbi, C. Massobrio and M. Boero, *Dispersion and localization of electronic states at a ferrocene/cu(111) interface*, Phys. Rev. Lett. **107**, 216801 (2011).

[97] M. Ormaza, P. Abufager, N. Bachellier, R. Robles, M. Verot, T. L. Bahers, M.-L. Bocquet, N. Lorente and L. Limot, *Assembly of ferrocene molecules on metal surfaces revisited*, J. Phys. Chem. Lett. **6**, 395 (2015).

[98] S. R. Bahn and K. W. Jacobsen, *Chain formation of metal atoms*, Phys. Rev. Lett. **87**, 266101 (2001).

[99] N. Agraït, A. L. Yeyati and J. M. van Ruitenbeek, *Quantum properties of atomic-sized conductors*, Phys. Rep. **377**, 81 (2003).

[100] A. Thiess, Y. Mokrousov, S. Heinze and S. Blügel, *Magnetically hindered chain formation in transition-metal break junctions*, Phys. Rev. Lett. **103**, 217201 (2009).

[101] J. Fernández-Rossier, D. Jacob, C. Untiedt and J. J. Palacios, *Transport in magnetically ordered pt nanocontacts*, Phys. Rev. B **72**, 224418 (2005).

[102] A. Delin and E. Tosatti, *Magnetic phenomena in* 5*d transition metal nanowires*, Phys. Rev. B **68**, 144434 (2003).

[103] A. Smogunov, A. Dal Corso, A. Delin, R. Weht and E. Tosatti, *Colossal magnetic anisotropy of monatomic free and deposited platinum nanowires*, Nature Nanotechnology **1**, 22 (2008).

[104] A. Thiess, Y. Mokrousov and S. Heinze, *Competing magnetic anisotropies in atomic-scale junctions*, Phys. Rev. B **81**, 054433 (2010).

[105] V. M. Garcia-Suarez, D. Z. Manrique, C. J. Lambert and J. Ferrer, *Anisotropic magnetoresistance in atomic chains of iridium and platinum from first principles*, Phys. Rev. B **79**, 060408 (2009).

[106] A. Smogunov, A. Dal Corso and E. Tosatti, *Magnetic phenomena, spin-orbit effects, and landauer conductance in pt nanowire contacts: Density-functional theory calculations*, Phys. Rev. B **78**, 014423 (2008).

[107] L. Sandratskii, *Noncollinear magnetism in itinerant-electron systems: theory and applications*, Adv. Phys. **47**, 91 (1998).

[108] S. Mühlbauer, B. Binz, F. Jonietz, C. Pfleiderer, A. Rosch, A. Neubauer, R. Georgii and P. Böni, *Skyrmion lattice in a chiral magnet*, Science **323**, 915 (2009).

[109] X. Z. Yu, Y. Onose, N. Kanazawa, J. H. Park, J. H. Han, Y. Matsui, N. Nagaosa and Y. Tokura, *Real-space observation of a two-dimensional skyrmion crystal*, Nature **465**, 901 (2010).

[110] S. Heinze, K. von Bergmann, M. Menzel, J. Brede, A. Kubetzka, R. Wiesendanger, G. Bihlmayer and S. Blügel, *Spontaneous atomic-scale magnetic skyrmion lattice in two dimensions*, Nature Physics **7**, 713 (2011).

[111] I. Dzyaloshinskii, *Thermodynamic thoery of "weak" ferromagnetism in antiferromagnetic substances*, Sov. Phys. JETP **5**, 1259 (1957).

[112] T. Moriya, *Anisotropic superexchange interaction and weak ferromagnetism*, Phys. Rev. **120**, 91 (1960).

[113] N. Romming, A. Kubetzka, C. Hanneken, K. von Bergmann and R. Wiesendanger, *Field-dependent size and shape of single magnetic skyrmions*, Phys. Rev. Lett. **114**, 177203 (2015).

[114] J. Tersoff and D. R. Hamann, *Theory and application for the scanning tunneling microscope*, Phys. Rev. Lett. **50**, 1998 (1983).

[115] J. Tersoff and D. R. Hamann, *Theory of the scanning tunneling microscope*, Phys. Rev. B **31**, 805 (1985).

[116] C. Kruse, *Stm simulationen von skyrmionen und antiskyrmionen in ultradünnen filmen*, B.Sc. thesis, University of Kiel (2014).

[117] C. Hanneken, *Observation of non-collinear magnetoresistance by scanning tunneling spectroscopy on skyrmions in pdfe/ir(111)*, Ph.D. thesis, University of Hamburg (2015).

[118] T. Schulz, R. Ritz, A. Bauer, M. Halder, M. Wagner, C. Franz, C. Pfleiderer, K. Everschor, M. Garst and A. Rosch, *Emergent electrodynamics of skyrmions in a chiral magnet*, Nature Physics **8**, 301 (2012).

[119] K. Everschor, *Current-induced dynamics of chiral magnetic structures*, Ph.D. thesis, University of Cologne (2012).

[120] K. von Bergmann, M. Menzel, D. Serrate, Y. Yoshida, S. Schröder, P. Ferriani, A. Kubetzka, R. Wiesendanger and S. Heinze, *Tunneling anisotropic magnetoresistance on the atomic scale*, Phys. Rev. B **86**, 134422 (2012).

[121] K. M. Seemann, F. Garcia-Sanchez, F. Kronast, J. Miguel, A. Kákay, C. M. Schneider, R. Hertel, F. Freimuth, Y. Mokrousov and S. Blügel, *Disentangling the physical contributions to the electrical resistance in magnetic domain walls: A multiscale study*, Phys. Rev. Lett. **108**, 077201 (2012).

[122] A. Fert, V. Cros and J. Sampaio, *Skyrmions on the track*, Nature Nanotechnology **8**, 152 (2013).

Veröffentlichungen und Konferenzbeiträge

Teile der vorliegenden Arbeit wurden veröffentlicht in:

- C. Hanneken, F. Otte, A. Kubetzka, B. Dupé, N. Romming, K. von Bergmann, R. Wiesendanger and S. Heinze
  Electrical detection of magnetic skyrmions by tunnelling non-collinear magnetoresistance
  Nature Nanotechnology **10**, 1039 (2015).

- J. Schöneberg, F. Otte, N. Néel, A. Weismann, Y. Mokrousov, J. Kröger, R. Berndt and S. Heinze
  Ballistic Anisotropic Magnetoresistance of Single-Atom Contacts
  submitted

- F. Otte, S. Heinze and Y. Mokrousov
  Molecular Anisotropic Magnetoresistance
  Physical Review B: Rapid Communications **92**, 220411 (2015).

Weitere Veröffentlichungen:

- V. Sessi, F. Otte, S. Krotzky, C. Tieg, M. Wasniowska, P. Ferriani, S. Heinze, J. Honolka, and K. Kern
  Complex trend of magnetic order in Fe clusters on 4d transition-metal surfaces. I. Experimental evidence and Monte-Carlo simulations
  Physical Review B **89**, 205425 (2014).

- F. Otte, P. Ferriani, and S. Heinze
  Complex trend of magnetic order in Fe clusters on 4d transition-metal surfaces. II. First-principles calculations
  Physical Review B **89**, 205426 (2014).

- B. Dupé, J. E. Bickel, Y. Mokrousov, F. Otte, K. von Bergmann, A. Kubetzka, S. Heinze, and R. Wiesendanger
  Giant magnetization canting due to symmetry breaking in zigzag Co chains on Ir(001)
  New Journal of Physics **17**, 023014 (2015).

Vorträge

- **28.03.2012** F. Otte, P. Ferriani and S. Heinze
  Exchange interactions in Fe clusters on Rh(111) and Ru(0001) from first-principles
  DPG-Frühjahrstagung der Sektion Kondensierte Materie (SKM) 2012, Berlin, Deutschland

- **14.03.2013** F. Otte, B. Hardrat, F. Freimuth, Y. Mokrousov and S. Heinze
  First-principles calculation of ballistic transport in single-atom contacts

DPG-Frühjahrstagung der Sektion Kondensierte Materie (SKM) 2013, Regensburg, Deutschland

- **04.09.2013** F. Otte, S. Krotzky, V. Sessi, M. Wasniowska, C. Tieg, P. Ferriani, J. Honolka, K. Kern, and S. Heinze
  Unexpected trend of exchange interactions in Fe clusters on Rh(111) and Ru(0001)
  International Conference on Nanoscale Magnetism 2013, Istanbul, Türkei

- **01.04.2014** F. Otte, Y. Mokrousov and S. Heinze
  Tuning the ballistic anisotropic magnetoresistance in single-atom contacts via the apex atom
  DPG-Frühjahrstagung der Sektion Kondensierte Materie (SKM) 2014, Dresden, Deutschland

- **05.03.2015** F. Otte, J. Schöneberg, N. Néel, A. Weismann, Y. Mokrousov, J. Kröger, R. Berndt and S. Heinze
  Ballistic anisotropic magnetoresistance of single-atom contacts
  APS March Meeting 2015, San Antonio, Texas, USA

Poster

- **30.10.2013** F. Otte, Y. Mokrousov and S. Heinze
  First-principles calculation of ballistic transport in single-atom contacts
  543. WE-Heraeus-Seminar: Electron Transport through Atoms, Molecules and Nanowires: Advances in Experiment and Theory, Bad Honnef, Deutschland

Seminarvorträge

- **22.08.2013** F. Otte, B. Hardrat, F. Freimuth, Y. Mokrousov and S. Heinze
  First-principles calculation of ballistic transport in single-atom contacts
  Sehlendorf-Seminar: Strukturforschung an Werkstoffen 2013, Christian-Albrechts-Universität zu Kiel, Sehlendorf, Deutschland

Danksagungen

Zuerst möchte ich mich bei Prof. Dr. Stefan Heinze für das Ermöglichen und die Betreuung meiner Arbeit bedanken. Durch seine Anleitung und Beratung habe ich sehr viel gelernt. Zugleich war sein Ideenreichtum und sein Engagement immer eine große Inspirationsquelle.

Des Weiteren danke ich Dr. Bertrand Dupé und Dr. Paolo Ferriani für die vielfältige Unterstützung und für das Korrekturlesen von Teilen dieser Arbeit. Bertrand möchte ich insbesondere für die Hilfe zum Rechnen mit dem `FLEUR`-Code auf dem Linux-Cluster des Rechenzentrums der Christian-Albrechts-Universität zu Kiel und für die schönen DFT-Rechnungen zum "TNCMR" danken. Außerdem danke ich ihm für die Einführung in das Toprope-Klettern und die Organisation der vielzähligen Arbeitsgruppen-Barbecues und anderer AG-Aktivitäten.

Dr. Björn Hardrat möchte ich für die Einführung in die 1D-Version des `FLEUR`-Codes und in den Transport-Code danken.

Dr. Patrick Ludwig und Herrn Grage danke ich für die Hilfe zu jeglichen IT-Problemen und Frau Doris Schulz danke ich für die Hilfe zu Formularen aller Art.
Dr. Simone Knief vom Rechenzentrum der Christian-Albrechts-Universität zu Kiel danke ich für die Hilfe bezüglich der Rechnungen auf dem Linux-Cluster.

Den Mitarbeitern des Instituts für Theoretische Physik und Astrophysik der Christian-Albrechts-Universität zu Kiel danke ich für die gute Arbeitsatmosphäre. Dabei danke ich besonders Dr. Hauke Thomsen und Igmar Schnell für die Organisation der "Kaffeeliste". Weiterhin danke ich insbesondere allen derzeitigen und ehemaligen Mitgliedern der Arbeitsgruppe "Spintronics Theory Group" von Prof. Dr. Stefan Heinze für jegliche Hilfe und die schöne Zeit.

Prof. Dr. Stefan Blügel danke ich für das Ermöglichen meiner Aufenthalte im Institutsbereich "Quanten-Theorie der Materialien" des Peter Grünberg Instituts am Forschungszentrum Jülich. Ebenso möchte ich mich bei Prof. Dr. Yuriy Mokrousov für die Unterstützung, für die Betreuung meiner Aufenthalte am Forschungszentrum Jülich und für das Ermöglichen etwas an der 1D-Version des `FLEUR`-Codes zu arbeiten bedanken. Auch hierdurch habe ich sehr viel gelernt. Dr. Frank Freimuth vom Peter Grünberg Institut danke ich für die Einführung in die Wannier-Funktionen. Guillaume Geranton danke ich für die parallelisierte Version des `Wannier90`-Codes. Frau Ute Winkler danke ich für die Organisation der Unterkunft während meiner Aufenthalte am Forschungszentrum Jülich. Außerdem danke ich noch allen Mitgliedern

der Arbeitsgruppe “Quanten-Theorie der Materialien” für die Gastfreundlichkeit während meiner Aufenthalte.

Besonders interessant und erkenntnisreich waren auch immer die Diskussionen und Kollaborationen mit Experimentatoren:

Bei Christian Hanneken, Dr. André Kubetzka, Niklas Romming, Dr. Kirsten von Bergmann und Prof. Dr. Roland Wiesendanger von der Universität Hamburg möchte ich mich für die gute Zusammenarbeit und die schönen experimentellen Ergebnisse bedanken.

Ebenso danke ich Johannes Schöneberg, Dr. Alexander Weismann und Prof. Dr. Richard Berndt von der Christian-Albrechts-Universität zu Kiel sowie Dr. Nicolas Néel und Prof. Dr. Jörg Kröger von der Technischen Universität Ilmenau für die gute Zusammenarbeit und die schönen experimentellen Ergebnisse.

Abschließend danke ich noch meiner Familie und meinen Freunden für die Unterstützung während meines Studiums und der Promotion. Dr. Florian Kirchschlager danke ich für das Korrekturlesen von Teilen dieser Arbeit.

Eidesstattliche Erklärung

Hiermit versichere ich an Eides statt, dass die vorliegende Dissertation – abgesehen von der Beratung durch meinen wissenschaftlichen Lehrer und der Verwendung der angegebenen Hilfsmittel – nach Inhalt und Form meine eigene ist.

Sie hat weder ganz noch teilweise an einer Stelle im Rahmen eines Prüfungsverfahrens vorgelegen. Die hier vorgestellten Ergebnisse sind in Teilen bereits in wissenschaftlichen Fachzeitschriften veröffentlicht worden. Eine ausführliche Publikationsliste findet sich auf S. 147 ff.

Diese Arbeit ist unter Einhaltung der Regeln guter wissenschaftlicher Praxis der Deutschen Forschungsgemeinschaft entstanden.

Kiel, den